Stratospheric sulphur:

MIPAS/Envisat measurements and chemical transport model simulations of carbonyl sulphide, sulphur dioxide, and sulphate aerosol

Zur Erlangung des akademischen Grades einer

DOKTORIN DER NATURWISSENSCHAFTEN

von der Fakultät für Bauingenieur-, Geo- und Umweltwissenschaften

des Karlsruher Instituts für Technologie (KIT)

genehmigte

DISSERTATION

von

Dipl.-Hyd. ANNIKA GÜNTHER

aus Gochsheim

Tag der mündlichen Prüfung: 15 December 2017

Referent: PD Dr. Thomas von Clarmann

Korreferent: Prof. Dr. Jan Cermak

Korreferent: Prof. Dr. André Butz

Karlsruhe 2017

Zusammenfassung

Stratosphärisches Aerosol, in dem Schwefel bei weitem das am häufigsten vorkommende Element darstellt, besitzt das Potential die Temperatur an der Erdoberfläche zu verringern, indem es einfallende Solarstrahlung zurückstreut. Dieses Vermögen sowie ein Anstieg der Aerosolbelastung in der Stratosphäre während des letzten Jahrzehnts führten in den letzten Jahren zu wachsendem Interesse an stratosphärischem Schwefel.

Die zwei wichtigsten Vorprodukte stratosphärischen Schwefelaerosols sind gasförmiges Carbonylsulfid (OCS) und Schwefeldioxid (SO_2). Von MIPAS/Envisat (Michelson Interferometer for Passive Atmospheric Sounding auf dem Environmental Satellite) gibt es für den Zeitraum Jul 2002–Apr 2012 Datensätze für OCS und SO_2. Auf den genannten Datensätzen sowie einem zusätzlichen neuen Datensatz von Aerosolvolumendichten basiert diese Arbeit. Der neue Aerosoldatensatz wurde im Zuge der vorliegenden Studie erstmals untersucht. Während dieser Arbeit wurde der Datensatz durch die Identifizierung und das Herausfiltern von Daten verbessert die durch andere Arten von Aerosol als Schwefelaerosol beeinflusst waren. Durch Validierung mit Ballon-Messungen wurde gezeigt, dass die MIPAS Profile nach Anwendung einer höhenabhängigen Offset-Korrektur gut mit den in situ Messungen übereinstimmen. Diese Korrektur basiert auf dem Vergleich zwischen MIPAS und in situ Profilen von Aerosolvolumendichten.

In einem isentropen Chemietransportmodell (CTM) wurde ein Schwefelschema implementiert, um die Übereinstimmung zwischen den MIPAS-Datensätzen der Schwefelsubstanzen mittels Modellsimulationen zu testen. Zudem sollte geprüft werden, ob dies mit unserem derzeitigen Verständnis stratosphärischen Schwefels in Einklang ist. In einer Fallstudie zu den Vulkanausbrüchen von Kasatochi im Jahr 2008 und Sarychev im Jahr 2009, die beide während des borealen Sommers bei ∼50°N ausbrachen, konnte bezüglich der vulkanischen Schwefelmasse und Transportmuster Konsistenz zwischen MIPAS SO_2 und Sulfataerosol gezeigt werden. Berechnungen der e-folding Lebensdauer stratosphärischen Schwefels vulkanischen Ursprungs für den Sarychev-Ausbruch zeigten eine durchschnittliche Lebensdauer von ungefähr drei Monaten. Während Sedimentation eine wichtige Rolle spielt, insbesondere bezüglich des Maximums in Schwefelaerosolgehalt sowie des Schwefels der langfristig im Modell verbleibt, zeigen Sensitivitätssimulationen mit dem CTM, dass der dominierende Prozess der die Schwefellebensdauer in der unteren Stratosphäre der Extra-Tropen nach den zwei Eruptionen regulierte Transport durch die Brewer-Dobson Zirkulation war. Zusätzlich wurden Teile des emittierten Schwefels in Richtung Äquator transportiert, wo sie in der „tropical pipe" aufstiegen.

Mehrere Muster die in den MIPAS-Daten unter nicht-vulkanischen Bedingungen gesehen wurden konnten durch Modellsimulationen bestätigt werden, wie die Abnahme von OCS in der Stratosphäre durch Photolyse, oder Bildung von SO_2 aus OCS in den Tropen bei ∼25–35 km. Manche Muster, die in den neuen MIPAS-Aerosoldaten zu sehen sind konnten Schwefel zugeschrieben werden, der aus OCS freigesetzt wurde. Der freigesetzte Schwefel führt zu erhöhten Aerosol-Molfraktionen in den Tropen oberhalb von 22 km, die sich in Richtung niedrigerer Höhen in hohen Breiten erstrecken. Bezüglich der stratosphärischen

Schwefelmasse wurde Konsistenz zwischen den MIPAS-Datensätzen für OCS, SO_2 und Schwefelaerosol gezeigt. Simulationen von Hintergrundbedingungen, mit OCS als einzige Schwefelquelle, in Zusammenspiel mit Simulationen vulkanischen Schwefels mit einer relativ hohen Häufigkeit von vulkanischen Injektionen (98 einzeln identifizierte Ausbrüche innerhalb von etwa 10 Jahren), können die stratosphärischen Schwefelmassen erklären, die aus MIPAS-Messungen abgeleitet wurden. Unter Hintergrundbedingungen ist die simulierte Sedimentation von Schwefelaerosol ein Hauptunsicherheitsfaktor mit relativ starken Auswirkungen auf die Absolutmenge an Sulfataerosol. Abschließend wurde die Bedeutung von relativ kleinen und mittelgroßen vulkanischen Beiträgen als Hauptquelle für kurzzeitige Variation bis hin zu Variation in dekadischen Zeiträumen während der MIPAS-Periode veranschaulicht.

Schlagwörter: Stratosphäre, Schwefel, MIPAS, CTM, OCS, SO_2, H_2SO_4, Schwefelaerosol, Vulkane

Abstract

Stratospheric aerosol, in which sulphur is by far the most common element, has the potential to exhibit a cooling effect on Earth surface temperatures by backscattering incoming solar radiation. This potential, and an increased stratospheric aerosol loading during the last decade, caused rising interest in stratospheric sulphur during the last years.

The main precursors of stratospheric sulphate aerosol are gaseous carbonyl sulphide (OCS) and sulphur dioxide (SO_2). From MIPAS/Envisat (Michelson Interferometer for Passive Atmospheric Sounding aboard the Environmental Satellite), data sets of OCS and SO_2 are available for Jul 2002–Apr 2012. This work is based on the mentioned data sets of OCS and SO_2, and additionally on a new data set of MIPAS aerosol volume densities that has been studied in this thesis for the first time. In the course of this thesis, the new data set has been improved by identifying and deselecting data that were influenced by other types of aerosol than sulphate aerosol. By validation with coincident balloon-borne data, MIPAS profiles have been shown to be in good agreement with the in situ measurements after applying an altitude-dependent offset-correction. This correction is based on the comparison between MIPAS and in situ aerosol volume density profiles.

In an isentropic chemical transport model (CTM) a sulphur scheme has been implemented with the purpose to test consistency between the sulphur species measured by MIPAS with the aid of model simulations, and to test if this is in line with our current understanding. In a case study on the volcanic eruptions of Kasatochi in 2008 and Sarychev in 2009, which both erupted during boreal summer at $\sim 50°$N, consistency between MIPAS SO_2 and sulphate aerosol could be demonstrated in terms of volcanic mass and transport patterns. Calculations of e-folding lifetimes of stratospheric volcanic sulphur after the eruption of Sarychev resulted in average lifetimes of roughly three months. While sedimentation plays an important role, especially in the peak amounts of volcanic sulphate aerosol and the sulphur that remains in the model on the long-term, sensitivity simulations with the CTM show that the dominant process governing the lifetime of sulphur in the extra-tropical lower stratosphere after the two eruptions was transport by the Brewer-Dobson circulation. Additionally, parts of the emitted sulphur were transported towards the Equator where they were lifted in the tropical pipe.

Several patterns of primarily non-volcanic stratospheric sulphur seen in the MIPAS data, such as decrease of OCS in the stratosphere by photolysis, or formation of SO_2 from OCS in the Tropics at ~ 25–35 km, could be confirmed by model simulations. Some patterns that are seen in the new MIPAS aerosol data, such as elevated sulphur mole-fractions in the Tropics at above 22 km, extending towards lower altitudes at high-latitudes, could be ascribed to sulphur released from OCS. In terms of stratospheric sulphur mass, consistency has been demonstrated between the MIPAS data sets of OCS, SO_2 and liquid-phase H_2SO_4. Simulations of background conditions with OCS as the only sulphur source, in combination with simulations of volcanic sulphur with a relatively high frequency of volcanic injections (98 individual identified eruptions within approximately 10 years), can explain the stratospheric sulphur masses which were derived from MIPAS retrievals. Under

background conditions, modelled sedimentation of sulphate aerosol is a main factor of uncertainty, with relatively strong impact on the absolute amounts of sulphate aerosol. Finally, the importance of relatively small and medium sized volcanic contributions as the main source of short-term to decadal scale variability over the MIPAS period has been illustrated.

Key words: Stratosphere, sulphur, MIPAS, CTM, OCS, SO_2, H_2SO_4, sulphate aerosol, volcanoes

Acknowledgements

Contents

List of Figures

List of Tables

List of Abbreviations

3D	**3 d**imensional
ACE-FTS	**A**tmospheric **C**hemistry **E**xperiment - **F**ourier **T**ransform **S**pectrometer
aero	**Aero**sol
AK	**A**veraging **k**ernel
AND	**A**erosol **n**umber **d**ensity
AoA	**A**ge **o**f **a**ir
ASMA	**A**sian **s**ummer **m**onsoon **a**nticyclone
AVD	**A**erosol **v**olume **d**ensity
ave	**Ave**rage
B15	Chemical transport model simulation (see Sect. 3.5)
bb	**B**ottom **b**oundary
BDC	**B**rewer-**D**obson **c**irculation
BGO	Chemical transport model simulation (see Sect. 3.5)
CKa08	Chemical transport model simulation (see Sect. 3.5)
CKa08$_{\text{switch:loc}}$	Chemical transport model simulation (see Sect. 3.5)
CKa08$_{\text{switch:loc\&day}}$	Chemical transport model simulation (see Sect. 3.5)
CObb$_{\text{const}}$	Chemical transport model simulation (see Sect. 3.5)
CSa09	Chemical transport model simulation (see Sect. 3.5)
CSa09$_{\text{switch:loc}}$	Chemical transport model simulation (see Sect. 3.5)
CSa09$_{\text{switch:loc\&day}}$	Chemical transport model simulation (see Sect. 3.5)
CTM	**C**hemical **t**ransport **m**odel
CTM_MTAC	Chemical transport model simulation (see Sect. 3.5)
CTM_MTAR	Chemical transport model simulation (see Sect. 3.5)
CTM$_{\text{sglin}}$	Chemical transport model simulation (see Sect. 3.5)
Da08	**D**alafilla 20**08**
DAE	**D**ay **a**fter **e**ruption
DJF	**D**ecember, **J**anuary, **F**ebruary
DMS	**D**i**m**ethyl **s**ulphide
DT_0	Chemical transport model time step
EMAC	ECHAM/**ME**SSy **A**tmospheric **C**hemistry model
Envisat	**Env**ironmental satellite
ESA	European **S**pace **A**gency
ESRad	**E**ffective **s**edimentation **rad**ius
G17	Chemical transport model simulation (see Sect. 3.5)
H$_2$O	Water
H$_2$SO$_4$	Sulphuric acid
H$_2$SO$_4$(liq)	Sulphate aerosol

hν	Energy of a photon
HR	**H**igh **R**esolution
HSO$_3$	bisulphite
IR	**I**nf**r**ared
JJA	**J**une, **J**uly, **A**ugust
Ka08	**Ka**satochi 20**08**
KIT-IMK	**K**arlsruhe **I**nstitute of **T**echnology - **I**nstitute of **M**eteorology and **C**limate Research
λ	Wavelength of electromagnetic radiation
lat	**Lat**itude
lon	**Lon**gitude
LPC	**L**aser **p**article **c**ounter
MAM	**M**arch, **A**pril, **M**ay
MD	**M**ass **d**ensity
MIPAS	**M**ichelson **I**nterferometer for **P**assive **A**tmospheric **S**ounding
MLS	**M**icrowave **L**imb **S**ounder
NH	Northern hemisphere
NCEP	**N**ational **C**enters for **E**nvironmental **P**rediction
nosedi	**No sedi**mentation
O	**O**xygen
O(^1D**)**	Electronically excited **o**xygen atom
OCS	**C**arb**o**nyl **s**ulphide
OH	**H**ydr**o**xyl radical
P1	MIPAS measurement **p**eriod **1**, 2002–2004
P2	MIPAS measurement **p**eriod **2**, 2005–2012
pptv	**P**arts **p**er **t**rillion by **v**olume
PSC	**P**olar **s**tratospheric **c**loud
PV	**P**otential **v**orticity
QBO	**Q**uasi-**b**iennial **o**scillation
Re09	**Re**doubt 20**09**
RR	**R**educed **R**esolution
S	**S**ulphur
Sa09	**Sa**rychev 20**09**
sedixum	**Sedi**mentation corresponding to an effective sedimentation radius of **x** **μm**
SH	Southern hemisphere
SMD	**S**ulphur **m**ass **d**ensity
SO$_2$	**S**ulphate di**o**xide
SO$_2$**mea**	MIPAS **SO**$_2$ retrieved from **mea**n limb-scans (Höpfner et al., 2013)
SO$_2$**sgl**	MIPAS **SO**$_2$ from **s**in**gl**e limb-scans (Höpfner et al., 2015)
SON	**S**eptember, **O**ctober, **N**ovember
SPARC	**S**tratosphere-troposphere **P**rocesses **A**nd their **R**ole in **C**limate
TTL	**T**ropical **t**ropopause **l**ayer
UTC	**U**niversal **T**ime **C**oordinated

UTLS	**U**pper **t**roposphere / **l**ower **s**tratosphere
VMR	**V**olume **m**ixing **r**atio
wt%	Percent by **weight**

1 Stratospheric sulphur

Sulphur (S) in the stratosphere has gained increasing attention as a consequence of its impact on Earth surface temperatures. Stratospheric aerosol, which is by far dominated by sulphate aerosol (Thomason and Peter, 2006; Kremser et al., 2016), has the potential to cool the Earth surface (Solomon et al., 2011; Andersson et al., 2015). This potential mainly arises from the ability of stratospheric aerosol, a suspension of small particles in gas, to backscatter incoming solar radiation. Additionally, a noted raise of stratospheric aerosol during the last decade (Hofmann et al., 2009; Neely et al., 2013) resulted in increasing interest in the topic of stratospheric sulphur. In 2006 an extensive assessment of stratospheric aerosol has been published (Thomason and Peter, 2006) as part of the project SPARC (Stratosphere-troposphere Processes And their Role in Climate), which is part of the World Climate Research Programme (WCRP). One part of the SPARC projects is SSiRC, investigating 'Stratospheric Sulfur and its Role in Climate'. Recently, a review on the related scientific developments since 2006 has been published by Kremser et al. (2016). In these two publications findings are summarised concerning stratospheric aerosol as well as their main precursor gases. Figure 1.1 (from Kremser et al., 2016) shows a schematic of the most relevant processes which dominate the life cycle and distribution of stratospheric aerosol. The main aspects of this schematic will be addressed in the present section, while further details can be taken from Kremser et al. (2016).

The main precursors for stratospheric sulphate aerosol are carbonyl sulphide (OCS) and sulphur dioxide (SO_2). The net flux of total sulphur across the tropopause entering the stratosphere is estimated to be 103 Gg S yr^{-1} (Sheng et al., 2015; excluding primary aerosol). 'Background', or non-volcanic aerosol is mainly maintained by OCS that is transported from the Earth surface to the stratosphere. The OCS budget is governed by release from the oceans and uptake by vegetation (Glatthor et al., 2015). OCS has a relatively long atmospheric lifetime of more than 2.8 yrs (Griffith et al., 1998), and can therefore reach the stratosphere. During ascent OCS is well mixed and enters the stratosphere primarily through the tropical tropopause layer (TTL) (Kremser et al., 2016). In addition, isentropic quasi-horizontal transport from the upper tropical troposphere towards the lowermost stratosphere can augment the stratospheric sulphur loading.

The essential role of OCS for stratospheric sulphur and stratospheric aerosol has first been stated by Crutzen (1976). During the last decades several studies agreed on a major contribution of carbonyl sulphide to the stratospheric aerosol loading (Sheng et al., 2015; Brühl et al., 2012; Thomason and Peter, 2006; Chin and Davis, 1995), with the magnitude of contribution still being under discussion, however. The stratospheric distribution of OCS shows highest values in the lower tropical stratosphere caused by broad up-welling, while volume mixing ratios (VMRs) of OCS show a substantial reduction towards higher altitudes and latitudes (Glatthor

et al., 2017). In the stratosphere, OCS can be destroyed mainly by photolysis ($\sim$80%) in the ultraviolet (UV), supported by its reaction with oxygen (O, $\sim$17%) and hydroxyl radicals (OH, $\sim$3%) (Sheng et al., 2015). The release of sulphur from OCS is most active in the tropics, at altitudes between $\sim$25–35 km (Brühl et al., 2012). As OCS is converted into SO_2, e.g., MIPAS/Envisat (Michelson Interferometer for Passive Atmospheric Sounding aboard the Environmental Satellite) measurements of SO_2 show a local maximum in this region (Höpfner et al., 2013).
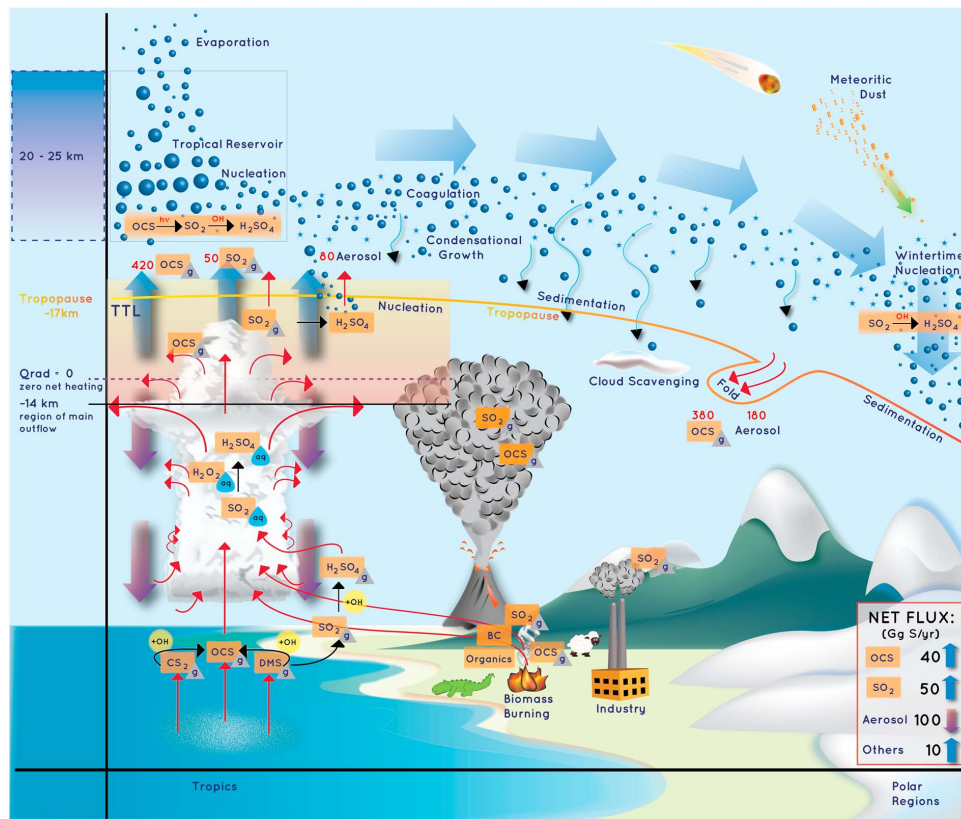
FIGURE 1.1: Schematic of the most relevant processes which dominate the life cycle and distribution of stratospheric aerosol, from Kremser et al. (2016) (license nr. 4213640845414, John Wiley and Sons and Copyright Clearance Center). Blue arrows: large-scale circulation; red arrows: transport processes; black arrows: chemical conversions; blue thin arrows: sedimentation of aerosol. Grey triangles: gaseous species; blue drops: aqueous species. Red numbers: flux of carbonyl sulphide (OCS), sulphur dioxide (SO_2) and aerosol (Gg S yr^{-1}, from model simulations by Sheng et al. (2015)). Grey box: approximate net flux of sulphur species that cross the tropopause (Sheng et al., 2015). 'Others' is mostly assigned to dimethyl sulphide (DMS) and hydrogen sulphide (H_2S). Note: as a consequence of its long tropospheric lifetime, OCS does not depend on deep convection for transport into the tropical tropopause layer (TTL) (as indicated in the figure). Abbreviations: CS_2 is carbon disulphide; H_2SO_4 is sulphuric acid; BC is black carbon.

Opposite to OCS, SO_2 has a rather short lifetime of few days in the troposphere (Eisinger and Burrows, 1998). In the dry stratosphere SO_2 can exist longer, with lifetimes in the order of several weeks (Höpfner et al., 2015; Eisinger and Burrows, 1998). This indicates that uplift of sulphur containing substances of natural or anthropogenic origin through air motion from the surface to the stratosphere is less important. Sulphur dioxide can be directly injected into the stratosphere by volcanic eruptions, which are an additional sulphur source to sustain stratospheric aerosol

and cause strongest variability in stratospheric sulphur. Especially eruptions with high explosivity and in regions of low tropopause heights have the potential for SO_2 emissions to cross the tropopause and enter the stratosphere.

Prominent examples of major volcanic eruptions that impacted the stratospheric aerosol loading and the Earth climate for up to several years are the eruptions of Krakatau in 1883, after which optical phenomena were first noted worldwide (Kremser et al., 2016), and Tambora in Indonesia, which erupted in 1815 and lead to the 'year without summer' in 1816. During the last two decades of the past century, two major eruptions occurred: El Chichón in Mexico in 1982 and Mount Pinatubo in 1991 in the Republic of the Philippines. The impact on the stratosphere exerted by Mount Pinatubo has been widely studied (e.g., Thomason and Peter, 2006, and references therein), as it is a major eruption with available satellite-borne measurements of aerosol. The eruption caused a rise of the stratospheric sulphur loading by a factor of 60 compared to background conditions, and in 1993 aerosol levels still were elevated by a factor of 10 (McCormick et al., 1995). The eruption of Mount Pinatubo in 1991 lead to the finding that strong volcanic eruptions can lower surface temperatures up to a few tenths of a degree Celsius (Kremser et al., 2016).

The negative radiative effect of stratospheric aerosol is discussed to have been one of the driving factors for the global warming 'hiatus' that we experienced during the last decade (Haywood et al., 2014; Santer et al., 2014; Fyfe et al., 2013). An increase in stratospheric aerosol levels has been observed by Hofmann et al. (2009), which they suggested to result from anthropogenic emissions. In newer studies (e.g., Neely et al., 2013), however, small and medium sized volcanic eruptions were demonstrated more likely to be the reason of this rise in aerosol loading, especially originating from tropical volcanoes. A number of volcanoes directly injected sulphur into the stratosphere during the first decade of this century, with injections reaching up to 20 km (Vernier et al., 2011b). Andersson et al. (2015) and Ridley et al. (2014) emphasise that not only tropical injections, but also volcanic eruptions in the mid- to high-latitudes play an important role for stratospheric aerosol. Their studies show the importance of volcanic aerosol in the lowermost stratosphere of the extra-tropics on the total forcing exerted by volcanic eruptions during the last decade. In many aerosol data sets the stratospheric altitudes below the 380 K isentrope ($\sim$15 km) are not represented. But following the studies by Andersson et al. (2015) and Ridley et al. (2014) these altitudes need to be considered in estimates of the global radiative forcing that is caused by extra-tropical volcanic eruptions.

As OCS, SO_2 and sulphuric acid (H_2SO_4) are sulphur species with increasing oxidation states in this order, OCS (via SO_2) and directly injected SO_2 are ultimately converted into H_2SO_4. In the free troposphere and lower stratosphere this conversion by oxidation of SO_2 is primarily caused by its reaction with hydroxyl radicals (OH) (Kremser et al., 2016). As can be reasoned by the mentioned main precursor gases for stratospheric aerosol OCS and SO_2, the by far most common element found in stratospheric aerosol is sulphur. It has already been stated by various studies several decades ago that stratospheric aerosol particles are dominated by H_2SO_4–H_2O (sulphuric acid and water) solution droplets, composed by about 75 percent by weight (wt%) H_2SO_4 (Hamill et al., 1977; Toon and Pollack, 1973; Rosen, 1971). As a consequence of the low saturation vapour pressure of gaseous sulphuric acid, H_2SO_4

can condense easily in the presence of H_2O and form aerosol. Other substances present in stratospheric aerosol are small amounts of, e.g., black carbon or organics (Kremser et al., 2016). Murphy et al. (2013) and Yu et al. (2016) demonstrated that besides sulphur, organic material also plays a role in the upper troposphere / lower stratosphere (UTLS) region.

Stratospheric aerosol forms by nucleation, via binary homogeneous nucleation preferably at low temperatures and surface areas, and high relative humidities (Kremser et al., 2016). In the presence of condensation nuclei, heterogeneous nucleation can occur, starting at lower saturation. Nucleation of stratospheric aerosol is predominantly occurring in the TTL and the polar middle stratosphere (Brock et al., 1995, and Campbell and Deshler, 2014, respectively). After formation, stratospheric aerosol grows by coagulation and condensation. During the process of coagulation, aerosols of different composition and size combine into a larger particle by collision, while growth by condensation means uptake of further water and sulphuric acid. Rather than by water, the condensational growth is controlled mainly by the amount of H_2SO_4 and thermodynamic properties of H_2SO_4, and the ambient temperature (Kremser et al., 2016).

While the microphysical processes of nucleation and coagulation are limited to a short period of time (Deshler, 2008), requiring large amounts of sulphuric acid to occur, condensation and evaporation as well as sedimentation have no such time restriction. As molecules can revert to their gaseous state at higher temperatures (evaporation) and as temperatures increase with altitude in the stratosphere, aerosol can evaporate. At altitudes above ~35 km, the amount of H_2SO_4 decreases, as the gaseous sulphuric acid can be photodissociated by visible light (e.g., Vaida et al., 2003; Lane and Kjaergaard, 2008). This destruction of sulphuric acid leads to formation of SO_2. An increase of SO_2 has been observed by Höpfner et al. (2013) in MIPAS measurements at altitudes above ~30–35 km, which can be associated with this newly formed SO_2.

During background conditions, Junge and colleagues observed a distinct layer of aerosol at stratospheric altitudes between 15 and 25 km by balloon measurements (Chagnon and Junge, 1961; Junge and Manson, 1961). This layer is found over a wide range of latitudes (Hofmann et al., 1975) with a peak at ~20 km (in particle number concentrations), and is often referred to as 'Junge layer'. Its lower boundary is usually associated with the tropopause, while the upper boundary is regulated mainly by sedimentation and evaporation (Hofmann et al., 1985; Kremser et al., 2016). In the tropical stratosphere, where uplift in the large-scale Brewer-Dobson circulation dominates transport, settling counteracts uplift (Kremser et al., 2016). In the extratropics, where subsidence is the dominant motion for stratospheric air, transport can be reinforced by sedimentation. Under background conditions, stratospheric aerosol radii typically lie below 0.2 μm (Thomason and Peter, 2006), but even though particles are small, sedimentation affects the aerosol distribution. Gravitational settling causes segregation, as sedimentation depends on the particle radius, with higher velocities associated to larger particles.

A certain interest in stratospheric aerosol is not only connected to its increased abundance during the last decade, sustained by naturally emitted OCS and SO_2, and possibly supported by some anthropogenic SO_2 emissions. Interest also arises due

to proposed geoengineering schemes, which suggest the use of sulphate aerosol to weaken the impact of climate change (Crutzen, 2006). Modelling studies investigate the possibilities and impact of injecting sulphur to the stratosphere (Niemeier and Timmreck, 2015; Laakso et al., 2016; Pope et al., 2012). Arguments against such suggestions are presented, e.g., by Robock (2008).

By now, several global data sets of OCS and SO_2 are available from space-borne measurements, as by MIPAS and ACE-FTS (Atmospheric Chemistry Experiment - Fourier Transform Spectrometer), which have already improved and are still improving our knowledge about processes that govern the stratospheric sulphur loading. The mentioned MIPAS data sets of the main gaseous precursors to stratospheric aerosol will be studied in this thesis. They were described by Glatthor et al. (2015, 2017) in the case of carbonyl sulphide, and by Höpfner et al. (2013, 2015) for the two available data sets of SO_2. The older SO_2 data set is more appropriate for studies of background conditions, while the more recent data set is of special value for analyses of volcanic SO_2. All data sets span a time period of approximately one decade, from Jul 2002–Apr 2012. During this thesis a new data set of aerosol volume densities, retrieved from MIPAS measurements at KIT-IMK (Karlsruhe Institute of Technology - Institute of Meteorology and Climate Research), is studied for the first time. In conjunction with chemical transport model (CTM) simulations of the sulphur species that are most relevant for the stratospheric sulphur loading, OCS, SO_2 and H_2SO_4, the consistency between the MIPAS data sets is tested in terms of quality and quantity, both for background and volcanically perturbed conditions.

In Chapter 2 the MIPAS data sets are described, with a more detailed introduction of the new data set of aerosol volume density profiles. This is followed by a presentation of the model implementations of a new sulphur module that includes OCS, SO_2, and H_2SO_4 in Chapter 3. In Chapter 4 the more recent MIPAS data set of sulphur dioxide and the new data set of sulphate aerosol are studied for volcanic contributions. In a case study on two volcanic eruptions (Kasatochi in 2008 – Ka08, Sarychev in 2009 – Sa09), the data sets are compared with the aid of model simulations of volcanic sulphur. This is followed by analyses of primarily non-volcanic sulphur, including the species OCS, SO_2, and sulphate aerosol (Chapter 5). The data sets are brought together for final analyses of the stratospheric sulphur burden in Chapter 6. The temporal evolution of measured stratospheric sulphur masses is assessed, together with a quantitative evaluation of the consistency between the MIPAS data sets by comparison to model simulations. Finally, Chapter 7 summarises the main findings of this thesis.

2 Michelson Interferometer for Atmospheric Sounding

In the present work, data sets as retrieved from MIPAS measurements (Jul 2002–Apr 2012) are analysed to study stratospheric sulphur. From MIPAS, data sets for two important sulphur species, carbonyl sulphide and sulphur dioxide, are available. Additionally, a new data set of aerosol volume densities has been provided at KIT-IMK for analyses during the present work. In this section, the MIPAS instrument and retrieval theory, as well as the data sets of OCS and SO_2 will be introduced shortly. This is followed by a description of the retrieval of aerosol volume densities. In Section 2.2 the new data set is compared against in situ data, and post-retrieval processing (offset correction and filters) is presented, aiming at an improvement of the aerosol data.

Observational data sets analysed in this work have been retrieved from measurements performed with the Michelson Interferometer for Passive Atmospheric Sounding (MIPAS) aboard the Environmental Satellite (Envisat). MIPAS (Fischer et al., 2008) was a limb emission sounder that measured in the infrared (IR) wavelength region, and operated on the European Space Agency's (ESAs) sun-synchronous polar orbiting satellite Envisat.

The instrument, a Fourier-transform spectrometer, measured high-resolution spectra of the radiation emitted by the constituents of the atmosphere. Its spectral region was 685–2,410 cm^{-1} or 4.15–14.6 µm. Due to relatively strong atmospheric signals, as the Planck function for atmospheric temperatures finds its maximum close to 10 µm, this spectral region is suitable to observe a wide variety of species (Fischer et al., 2008). Measured atmospheric radiance spectra are inverted to vertical volume mixing ratio profiles with the aid of characteristic lines of emission and absorption (absorption coefficients) of trace gases. The intensity of radiation that crosses the atmosphere is decreased by absorption and scattering of matter, and increased by emission by matter and scattering into the direction of the beam.

The general retrieval strategy for MIPAS at KIT-IMK is based on constrained inverse modelling of limb radiances, with a fit of calculated to measured limb radiances of entire limb-scans. The retrieval strategy has been described, e.g., in von Clarmann et al. (2003, 2009) and Höpfner et al. (2013), and is based on the following equation, a variant of the formulation by Rodgers (2000):

$$x_{i+1} = x_i + (K_i^T S_y^{-1} K_i + R)^{-1} \cdot [K_i^T S_y^{-1}(y_{\text{meas}} - y(x_i)) - R(x_i - x_a)] \qquad (2.1)$$

The atmospheric and instrumental parameters that need to be determined are incorporated in vector x. x_a contains a priori profiles, and $x_{i=0}$ are initial guess

profiles. These are generally chosen to be constant with altitude or climatological values. The volume mixing ratio profiles are gridded at 1 km vertical spacing and VMRs vary linearly with height between these altitudes. The averaged radiances of all tangent altitudes of one limb-scan, as measured by MIPAS and provided as level 1b calibrated radiances by ESA, are contained in y_{meas}. S_y represents the co-variance matrix of measurement noise, while y_i contains simulated spectral radiances (radiative transfer model KOPRA, Stiller, 2000), calculated from the results x_i obtained in iteration number i. The Jacobian matrix K_i includes the partial derivates $\partial y(x_i)/\partial x_i$. These are calculated along with y_i at each iteration step. R is a regularisation matrix that leads to smoothing of the retrieved profiles, but is chosen not to bias the retrieved volume mixing profiles (Höpfner et al., 2013). The regularisation is a first-order smoothing constraint following $R = \gamma L^T L$. Here, L is a first-order finite differences operator (Steck, 2002; Tikhonov, 1963), and γ a regularisation parameter. Line-by-line calculations are making use of molecular spectroscopic data, such as HITRAN (e.g., HITRAN 2012, Rothman et al., 2013). HITRAN is a high-resolution transmission molecular absorption database containing spectroscopic parameters.

Envisat orbited the Earth at an altitude of $\sim$800 km about 14 times per day, and provided data at around 10am and 10pm local time. Generally, MIPAS measured more than 1,000 limb sequences per day. As the instrument detected limb emission spectra, MIPAS scanned the horizon, under various elevation angles. The geometry of MIPAS is displayed in Fig. 2.1. The instrument measured trace gas emissions on a relatively long optical path through the atmosphere, along its line of sight, tangentially to the Earth surface. The minimal distance between the line of sight for a certain elevation angle and the Earth surface is called tangent height, while the point on Earth closest to the tangent point is named geolocation. The layer above this altitude provides most information for the measured spectrum, as the optical path within this layer is longest (Haenel, 2017). At the tangent point, the field of view covered by MIPAS was 3 x 30 km (vertical x horizontal), with MIPAS measuring the integral of radiances over this field of view. The instrument measured in different modes, which were designed for a number of scientific purposes. In the present work, retrieved data are based on measurements in the Nominal (most profiles), and Upper Troposphere / Lower Stratosphere (UTLS) mode. A more detailed description of the instrument and retrieval method can be found in various publications (e.g., Fischer et al., 2008; von Clarmann et al., 2003), and lie beyond the scope of this thesis.
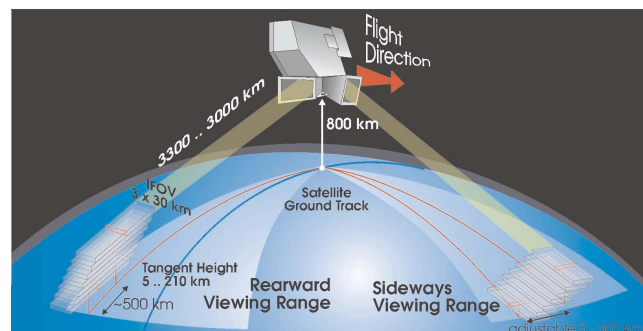
FIGURE 2.1: Geometry of the MIPAS instrument abord Envisat (source: Fischer et al., 2008, CC-BY-3.0).

   MIPAS operated in two measurement periods, from June 2002 to April 2004 (P1), and from January 2005 to April 2012 (P2). Details on the differences between the periods are given in Table 2.1, with differences regarding the vertical measurement extent, spectral resolution, vertical sampling and latitudinal distance between two subsequent single limb-scans. During P2, the spectral resolution was degraded compared to P1, leading to a decrease in time needed per measurement, resulting in a higher horizontal and vertical resolution in P2.

TABLE 2.1: Technical details of MIPAS measurements for measurement period 1 with high resolution (P1 or HR) and period 2 with reduced resolution (P2 or RR). 'altitude': altitude range of measurements; 'spectr. res.': unapodized spectral resolution; 'vert. sampl.': vertical sampling step in the upper troposphere / lower stratosphere; 'lat. dist.': latitudinal distance between two subsequent limb-scans.

period	time	altitude	spectr. res.	vert. sampl.	lat. dist.
P1 (HR)	Jun 2002–Apr 2004	6–68 km	0.025 cm^{-1}	3 km	530 km
P2 (RR)	Jan 2005–Apr 2012	7–72 km	0.0625 cm^{-1}	1.5 km	420 km

2.1 OCS and SO₂

Three data sets of sulphur species for Jul 2002–Apr 2012 are used to study stratospheric sulphur. These data sets were retrieved from MIPAS measurements at KIT-IMK, and consist of one data set of OCS volume mixing ratios (VMRs), and two data sets of SO_2 VMRs. The 'first comprehensive global data set of upper tropospheric OCS' (Glatthor et al., 2015) has been retrieved from single limb-scans and covers the altitude range 8–50 km. In Höpfner et al. (2013) the 'first observations of vertically resolved SO_2 covering (1) nearly the entire stratosphere, (2) the whole globe and (3) a time period of about 10 yr' were presented. SO_2 VMRs were retrieved from temporally and spatially averaged spectra and data are available as monthly 10° latitude bins for the altitude region 15–45 km. A newer SO_2 data set (Höpfner et al., 2015) is complementary to the climatology of SO_2 profiles and consists of profiles retrieved from single limb-scans. The data set is available at altitudes between 10–23 km, covering the UTLS region. As this data set has a high temporal and spatial resolution, the newer data are more suited for analyses of volcanic SO_2 than its precursor. The data sets are shortly characterised in the following, based on the publications by Glatthor et al. (2015, 2017), and Höpfner et al. (2013, 2015). The older data set of SO_2 is named 'SO_2mea' (mean) throughout this work, while the more recent data are called 'SO_2sgl' (single).

   The data set of MIPAS carbonyl sulphide VMRs is presented in Fig. 2.2, exemplary as seasonal vertically resolved meridional distributions. In Glatthor et al. (2017) the MIPAS data set of OCS has been characterised in terms of retrieval characteristics and patterns. OCS profiles have a vertical resolution of 4 to 5 km at the altitudes 6–15 km, while resolution is worse at higher altitudes (15 km at 40 km). Given error estimates of the total error are 40–50 pptv (parts per trillion by volume) at 10–20 km, and 120 pptv at an altitude of 40 km. Compared to balloon-borne data, MIPAS OCS does not exhibit a systematic bias (differences mostly below -50 pptv),

but compared to satellite-borne data from ACE-FTS they show a systematic positive bias (up to 100 pptv at 13–16 km). In Glatthor et al. (2015) global distributions of OCS were studied, and it has been shown that the data set, even though being restricted to the upper troposphere and higher altitudes, is of use when analysing surface sources and sinks of OCS, and to improve models. Analyses of OCS patterns as seen in MIPAS data can be found in Glatthor et al. (2015, 2017), and are partly addressed in Chapters 5 and 6.
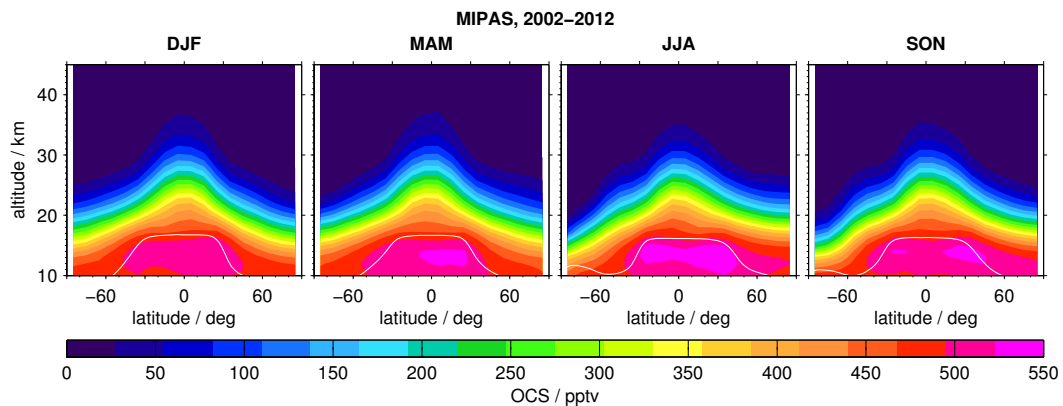
FIGURE 2.2: Seasonal MIPAS OCS volume mixing ratios, and tropopause heights. Vertically resolved zonal mean distributions (10° latitude bins). Data as in Glatthor et al. (2015, 2017). Seasonal means are calculated from a monthly climatology (from daily averages for 2002–2012). The white contour lines indicate seasonal tropopause heights (NCEP: National Centers for Environmental Prediction; 2002–2012) (Kalnay et al., 1996). Values exceeding the colour-scale are assigned with the limiting values.

The MIPAS data set of SO_2mea, retrieved from monthly and 10° zonal mean spectra (Höpfner et al., 2013) is shown in Fig. 2.3. Periods of obvious volcanic influence have been omitted in this Figure (see caption). Profiles have a vertical resolution of 3.5–4 km in the lower stratosphere, while the resolution is worse (6–10 km) at higher altitudes, due to lower pressure and reduced sensitivity, combined with wider sampling steps. The error estimates for single SO_2mea profiles is in the range of 5–20 pptv, with errors being caused especially by instrumental noise. The SO_2 profiles have been compared to the few available measurements of SO_2, and comparisons demonstrated general consistency to these data sets. With the data set of MIPAS SO_2mea, it was possible for the first time to confirm two patterns that had been suggested earlier by model simulations: SO_2 has a tropical maximum at ∼25–30 km, caused by sulphur release from OCS (Brühl et al., 2012). Further, SO_2-rich air from above is transported downwards to ∼25–30 km during polar winter, and destroyed when sunlight returns. Additionally, increased SO_2 loading in the upper stratosphere caused by photolysis of gas-phase H_2SO_4 could be confirmed (Mills et al., 2005; Vaida et al., 2003; Rinsland et al., 1995).
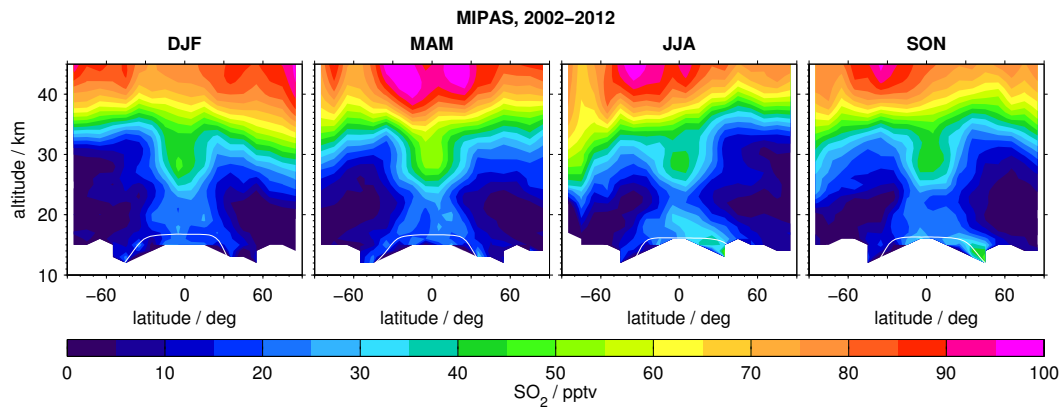
FIGURE 2.3: As Fig. 2.2, but for MIPAS SO$_2$mea. Data as retrieved from monthly and zonally averaged limb scans (10° latitude bins; Höpfner et al., 2013). Data for months with relatively strong volcanic influence (months as in Höpfner et al., 2013), are de-selected, at altitudes ≤25 km. These are: Oct–Dec 2002, Jul 2003, Jan–Jun 2005, May–Nov 2006, Oct 2007, Jul–Dec 2008, Jun–Dec 2009, Nov–Dec 2010, Jul–Sep 2011.
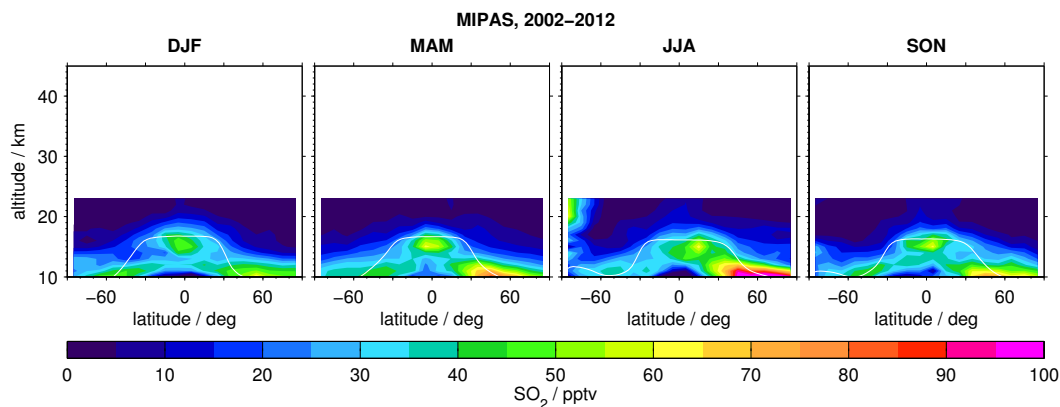
FIGURE 2.4: As Fig. 2.2, but for MIPAS SO$_2$sgl. Data as retrieved from single limb scans (Höpfner et al., 2015). Months with strong volcanic influence are de-selected as in Höpfner et al. (2015). These are: Oct–Dec 2002, Jul–Aug 2003, Jan–Aug 2005, May–Nov 2006, Oct–Nov 2007, Jul 2008–Jan 2009, Apr–Dec 2009, Nov–Dec 2010, Jun–Oct 2011.

Figure 2.4 shows MIPAS SO$_2$sgl volume mixing ratios, as retrieved from single limb-scans. Presented are seasonal means of primarily non-volcanic sulphur dioxide (omitted periods see caption). The total estimated error of the single profiles is around 70–100 pptv, dominated by instrument noise, and the vertical resolution is 3–5 km. Within ±50 pptv, the MIPAS data are consistent with independent observations from various aircraft measurement campaigns. During background conditions SO$_2$ VMRs have a bias of -10 to 20 pptv in the altitude region 10–20 km, with respect to satellite-borne ACE-FTS data. During volcanically perturbed periods, the bias lies in the range of -20 to 50 pptv, and varies with altitude. When compared to the natural variability of volcanically emitted SO$_2$, the bias is reasonably small. Höpfner et al. (2015) reported on problems during volcanically perturbed periods that have to be considered when working with the SO$_2$sgl data. Sampling artefacts due to aerosol interference may arise up to a few weeks directly after volcanic eruptions,

and the total SO_2 mass has been found to be strongly underestimated in several cases during these periods. Furthermore, saturation effects of spectral lines due to extreme amounts of SO_2 are thought to be a possible reason for the observed underestimations. For 30 volcanic eruptions that were identified in the UTLS region, SO_2 emissions have been derived for three altitude ranges covering 10–22 km. Further, lifetimes of SO_2 were derived for six of the strongest eruptions, within each altitude range. These data on volcanic SO_2 emissions and SO_2 lifetimes will be used or addressed in the present work.

2.2 Sulphate aerosol

2.2.1 Retrieval of aerosol volume densities from MIPAS limb-spectra

A new MIPAS data set of aerosol volume densities (AVDs) had been retrieved at KIT-IMK and was analysed for the first time as part of this thesis. MIPAS aerosol measurements in the IR depend only on the total aerosol volume density, when particles are sufficiently small in comparison to the measurement wavelength (d < ∼1 μm; Höpfner, 2004). Altitude profiles of aerosol volume densities can be derived from MIPAS measurements, as particles generally satisfy this criterion in the stratospheric aerosol. This holds true both during background and enhanced conditions, when medium sized volcanic eruptions are considered (e.g.,Deshler et al., 2003), as have occurred during the MIPAS measurement period (2002–2012). The assumed aerosol composition is a 75 percent by weight (75 wt%) H_2SO_4–H_2O solution, as typical stratospheric sulphuric aerosol compositions vary between 70–80% (e.g., Carslaw et al., 1995; Doeringer et al., 2012). This sulphate aerosol composition has been used in several studies, such as Gao et al. (2007), Kremser et al. (2016) and Kleinschmitt et al. (2017). The retrieval is based on optical constants by Niedziela et al. (1999) for a 75 wt% solution and a temperature of 230 K. Data are retrieved in an atmospheric window in the spectral region between 1,216.5 and 1,219.5 cm^{-1}. AVDs are given at altitudes between 10 and 33 km, and used from 10–30 km. While retrieved profiles are retrieved on a 1 km vertical grid, the actual vertical resolution is 3–4 km.

The retrieval method is described in more detail in Günther et al. (2018). Therein, an error analysis and information on the refractive indices used during the retrieval process are given (all provided by M. Höpfner, who retrieved the AVDs). In Günther et al. (2018), the leading error components are presented, for specified parameter uncertainties. The dominating error sources are the optical constants (10–20%), and uncertainties in the tangent pointing knowledge (5–15%). The total error is altitude-dependent, with an error of ∼20% or 0.09 μm^3 cm^{-3} at 10 km, and over 40% or 0.005 μm^3 cm^{-3} at 30 km. An additional error source, as, e.g., caused by straylight in the instrument (López-Puertas et al., 2009) can cause a tangent altitude dependent radiometric offset that has not been accounted for during the retrieval process.

To retrieve AVDs only spectra are considered that are not affected by optically thick clouds, applying the MIPAS cloud filter by (Spang et al., 2004) as basis for the selection of affected spectra. A relatively low threshold of 1.7 is chosen for the Cloud Index, intending not to filter out all spectra that are influenced by aerosol. As part

of this thesis, in the following section different artefacts caused by primarily non-sulphate aerosol, which were not captured by the low Cloud Index, will be described and filtered from the new data set.

2.2.2 Post-retrieval filters

Sulphate aerosol mole-fractions / volume mixing ratios, as derived from MIPAS aerosol volume density profiles for 2002–2012, are presented in Fig. 2.5. Shown are latitudinally resolved time series at altitudes of 10–24 km. Data are offset-corrected, as will be described in Sect. 2.2.3. Sulphate aerosol VMRs are calculated under the assumption that retrieved aerosol volume densities correspond entirely to a 75 wt% H_2SO_4–H_2O solution with an aerosol density of 1,700 kg m^{-3}.

Via the aerosol density and retrieved aerosol volume densities ($AVD_{H_2SO_4-H_2O}$, in μm^3 cm^{-3}), and the relation between density ρ, volume V, and mass m ($\rho = m/V$), the mass density of the H_2SO_4–H_2O binary solution ($MD_{H_2SO_4-H_2O}$, in kg m^{-3}) can be calculated (Eq. 2.2).

$$MD_{H_2SO_4-H_2O} = 10^{-12} \cdot 1,700 \text{ kg m}^{-3} \cdot AVD_{H_2SO_4-H_2O} \qquad (2.2)$$

Assuming only 75% of the mass density to be H_2SO_4, the H_2SO_4 volume mixing ratio can be calculated as follows:

$$VMR_{H_2SO_4} = 10^3 \cdot 0.75 MD_{H_2SO_4} \frac{R \cdot T}{p \cdot M_{H_2SO_4}} \qquad (2.3)$$

with T the temperature in K, p the pressure in Pa, R the ideal gas constant (8.314 J K^{-1} mol^{-1}), and the molar weight of H_2SO_4 ($M_{H_2SO_4}$ = 98.076 g mol^{-1}). The prerequisite to apply this equation, the ideal gas law, is not actually satisfied by sulphate aerosol, consisting of liquid- and not gas-phase H_2SO_4. In Eq. 2.3, the gas-phase equivalent that equals the sulphate aerosol in terms of mass is presumed.

The retrieval process does not provide any distinction between sulphate aerosol and other types of aerosols. Only parts of interfering aerosols are filtered out by the relatively loose cloud filter during the retrieval process (Sect. 2.2.1). Several very pronounced features are to be seen in the retrieved aerosol data (Fig. 2.5), which are not or only to a certain degree caused by sulphate aerosol. In the present section the intention is to identify and eliminate affected data.

At 10 to 12 km high aerosol loadings are retrieved, especially for the Northern hemisphere (NH) during boreal summer. These show an annual pattern or are influenced by volcanic eruptions. In the first MIPAS measurement period, however, enhancements are almost as high as elevated aerosol loadings caused by relatively strong volcanic eruptions, without being connected to such volcanic activity. No intense eruptions are known that could have caused such strong increases in sulphate aerosol during 2002–2004. Examples for clear volcanic signals in the Northern hemisphere are Kasatochi in 2008 and Sarychev in 2009 (Fig. 2.5). Furthermore, the root mean squared error (not presented here) shows regional patterns of high values at low altitudes during the first measurement period. A closer look into the retrieval (by M. Höpfner) revealed a connection of the enhancements during P1, both

in the retrieved data and errors, to interfering H_2O that was poorly resolved at low retrieval altitudes. Due to the different spectral and vertical resolution of MIPAS measurements during P2 (2005–2012), this problem is restricted to P1. For all further analyses, profiles of MIPAS aerosol before 2005 are considered above 12 km only.

At altitudes from about 14 to 20 km, MIPAS aerosol volume mixing ratios are unexpectedly high in the tropics. Further, during austral winter MIPAS aerosol shows strong enhancements in the polar region of the Southern hemisphere (SH), with a large vertical extent. In the Northern hemisphere similar enhancements are found during several boreal winters. In the Northern hemisphere, these elevated VMRs are of smaller horizontal, vertical, and temporal extent, however. All of these distinct features are most probably caused by non-sulphate aerosol influencing the retrieved aerosol volume densities.

The horizontal distribution of these features is presented in Fig. 2.6, which shows exemplary seasonal distributions of retrieved aerosol volume densities at 18 km. Chosen seasons are DJF 2007/08, MAM 2008, and JJA and SON 2010 (DJF: December, January, February; MAM: March, April, May; JJA: June, July, August; SON: September, October, November). These are periods with relatively weak volcanic influence at 18 km. Enhancements in the tropics at around 25°S–25°N are centred primarily above continental areas and in their vicinity, and above the Western Pacific. Furthermore, the enhancements above the polar region of the Southern hemisphere during austral winter are clearly identifiable, as well as weaker enhancements in the Northern hemisphere during boreal winter.

Enhancements in the tropics are strongest above and in the vicinity of continents and the Western Pacific. They also reach highest altitudes in these regions (not shown). These are areas of strong vertical motion and deep convective clouds (e.g., Xu and Zipser, 2012). Vertically resolved time series of MIPAS aerosol VMRs in the tropics (20°S–20°N; Fig. 2.7) show the altitude range of increased VMRs to be ∼13–21 km, with smallest vertical extent during boreal summer. Time series of MIPAS temperatures (temperatures at MIPAS locations, based on ECMWF analyses; European Centre for Medium-Range Weather Forecasts) are shown in the same way. Towards higher altitudes, a strong link between decreasing volume mixing ratios and increasing stratospheric temperatures is notable. This can be clearly seen in Fig. 2.8, where correlations between sulphate aerosol VMRs and temperatures are displayed (17–23 km). The decrease of VMRs with height has a strong gradient, and no upward motion of the pattern is observed. Due to the location of the enhancements, and the confinement to altitude regions with low temperatures without apparent upward transport, the retrieval is assumed to have been influenced by measurements of ice particles from thin cirrus clouds, which melt at higher temperatures.

MIPAS, without filters, with offset correction, 11 d running mean
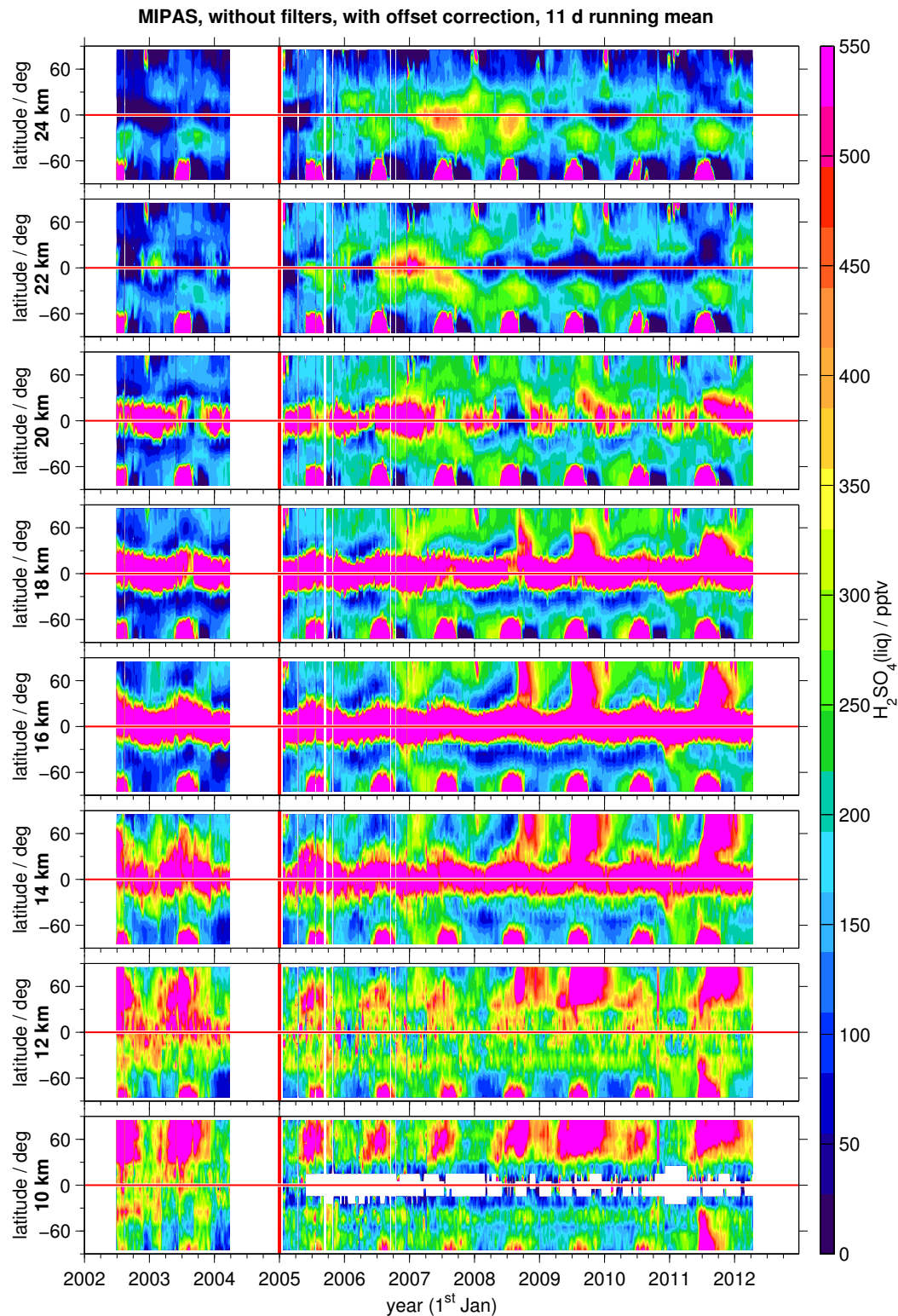
FIGURE 2.5: Offset-corrected, non-filtered MIPAS liquid-phase H$_2$SO$_4$ (H$_2$SO$_4$(liq)). Time series of latitudinally resolved zonally averaged VMRs for various altitudes (10–24km, 10° latitude bins). Offset correction as in Sect. 2.2.3. Values exceeding the colour-scale are assigned with the limiting values.
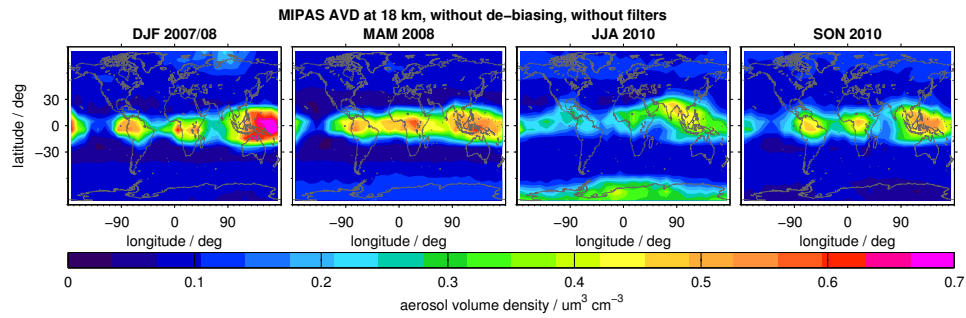
FIGURE 2.6: Influence of ice on the MIPAS aerosol retrieval: MIPAS aerosol volume densities as seasonal horizontal distributions at 18 km. Data are chosen for low volcanic influence and neither filtered nor de-biased. Values exceeding the colour-scale are assigned with the limiting values.
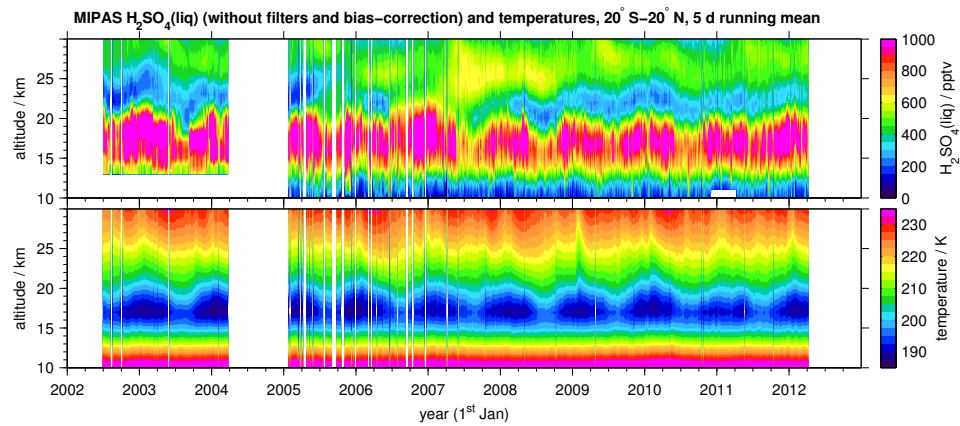
FIGURE 2.7: Influence of ice on the MIPAS aerosol retrieval: MIPAS sulphate aerosol and temperatures at 20°S–20°N (2002–2012). Vertically resolved time series of area weighted averages of 5 d running means. Aerosol data are neither filtered nor de-biased. Values exceeding the colour-scales are assigned with the limiting values.
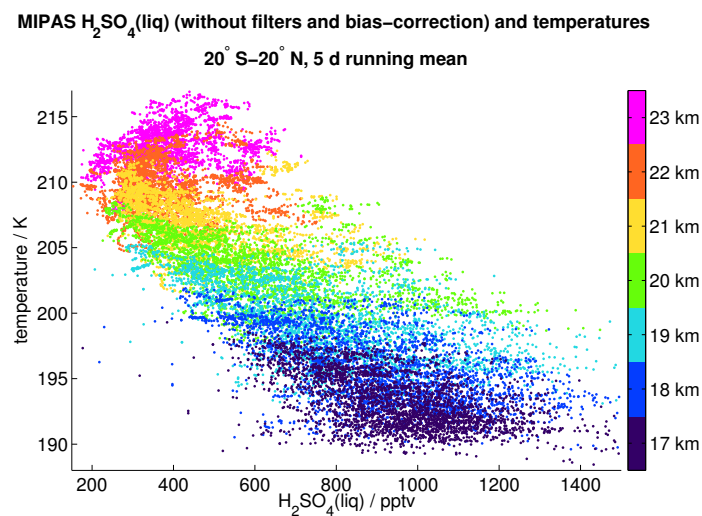
FIGURE 2.8: Correlation between MIPAS aerosol data (VMRs) and temperatures (20°S–20°S, 2002–2012) for 17–23 km. Data as in Fig. 2.7.

Griessbach et al. (2016) provided a method to identify MIPAS spectra that are influenced by ice. Their method consists of two steps to detect whether MIPAS spectra are influenced by a clear sky, ashes, ice, or aerosol (Griessbach et al., 2014, 2016). First, clouds and aerosols are identified by using a spectral window region, which is sensitive to clouds and aerosols. In a second step aerosols and ice clouds are separated by using spectral windows with contrasting behaviour regarding aerosols and ice. S. Griessbach (Forschungszentrum Jülich, FZJ) provided a data set of flags for MIPAS spectra at tangent heights below ~30 km, identifying measurements influenced by clear sky, ashes, ice, or aerosol. Based on this data set, the MIPAS AVDs are filtered to reduce the influence of ice on the retrieved data. From here on, only values retrieved at altitudes starting 4 km above the uppermost tangent height for which the measured spectrum was flagged to have been influenced by ice will be considered.

Figure 2.9 shows the ice filter, as seasonal horizontal distributions of the uppermost MIPAS tangent heights (plus 4 km) flagged to have been influenced by ice. Regions of high-reaching ice agree with the areas of enhanced aerosol loading in the new MIPAS aerosol data set (Fig. 2.6). Additionally, the percentage of MIPAS aerosol volume density profiles including spectra influenced by ice is shown as seasonal horizontal distributions (Fig. 2.9). The percentage distribution shows similar patterns, and reveals that on average the majority (up to 100%) of profiles in tropical continental areas and the Western Pacific, and the polar region of the Southern hemisphere during austral winter, are affected by the ice filter. In Fig. 2.10 the direct effect of the ice filter on MIPAS AVDs at 20 km can be seen exemplary for four days.

Simply filtering the new MIPAS aerosol data set based on a temperature threshold according to the existence temperature of ice under typical stratospheric conditions for H_2O did not have the desired effect. Discarding of data was limited to altitudes at which the temperature fell below the corresponding threshold. As the retrieved data contain information from surrounding altitudes, additional data would have needed to be discarded, as done when applying the ice filter.

Latitudinally resolved time series of the uppermost tangent heights flagged to have been influenced by ice (not shown) are consistent with MIPAS AVDs in terms of enhancements during boreal winter in the Northern hemisphere polar region, as described earlier. In boreal winters with high retrieved aerosol loading that is assigned to the presence of Polar Stratospheric Clouds (PSCs), the uppermost tangent heights influenced by ice are exceptionally high.

As has already been mentioned, patterns of high aerosol loading are visible in the presence of PSCs, which can form at low temperatures. H_2SO_4, which is next to nitric acid (HNO_3) and H_2O one of the three principle species that occur in the liquid-phase under stratospheric conditions Koop et al. (1997), can actually be contained in PSCs to some extent. Nevertheless, the extreme enhancements associated to PSCs will be filtered from the MIPAS data set of aerosol volume densities. As seen in MIPAS aerosol AVDs, PSCs form with higher frequency in the Southern hemisphere (Maturilli et al., 2005), as low temperatures needed for their formation are more frequent in the southern polar region. As the ice filter that has been applied to the MIPAS data, did not capture all profiles that are expected to have been influenced by PSCs, a second filter is used to improve the data set. Profiles are de-selected using

a temperature threshold of 195 K, the nitric acid trihydrate (NAT) existence temperature at around 20 km (Stein et al., 1999; Tabazadeh et al., 1996). Below that temperature, solid particles are thermodynamically more favoured than the gas-phase. When temperatures in the altitude range 17–23 km drop below 195 K polewards of 40°, from 15 Nov–15 Apr for the Northern hemisphere, and from 1 Apr–30 Nov for the Southern hemisphere, the entire profile is removed from the MIPAS aerosol data set.
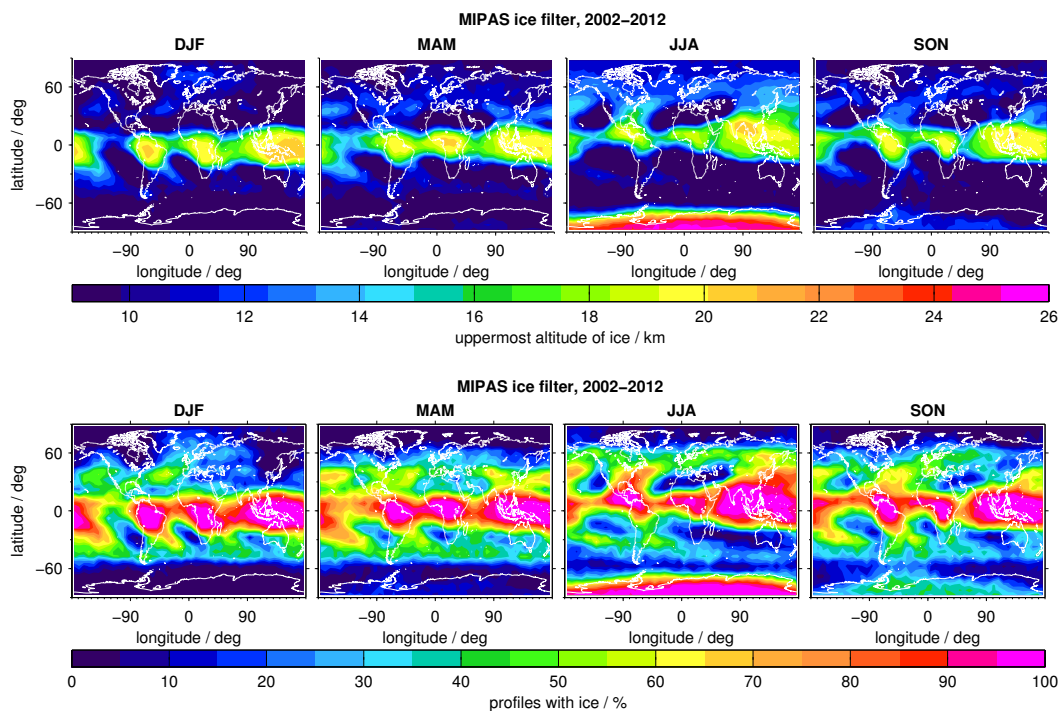
FIGURE 2.9: MIPAS ice filter. First row: mean seasonal distributions (10°lat x 10°lon) of the uppermost tangent height plus 4 km that is flagged to have been influenced by ice. Second row: mean seasonal distributions (10°lat x 10°lon) of the percentage of AVD profiles that are flagged to have been affected by ice at altitudes ≥10 km, when 4 km were added to the uppermost tangent height flagged positive for ice. The percentages are based on all available MIPAS AVD profiles, but do not consider whether AVD values were available at these altitudes. Seasonal values are calculated from a monthly climatology (from daily averages for 2002–2012). Values exceeding the colour-scale are assigned with the limiting values.

Figure 2.10 shows a comparison between the ice and PSC filter. Horizontal distributions of MIPAS AVDs are presented at 20 km for two examples of boreal winter conditions (13 Dec 2005, 18 Jan 2008), and two examples during austral winter (20 Jun 2009, 08 Aug 2010). In the examples for DJF, only on the 18 Jan 2008 the ice filter is active in the polar region, while the PSC filter is active on both days. For austral winter, the filters overlap in both examples, with the PSC filter being more stringent. As can be seen in these examples, the PSC filter overestimates the profiles with high aerosol loading in some cases. Nonetheless, as profiles with strong enhancements connected to PSCs persist when applying the ice filter only, and as no distinction between contributions of sulphate aerosol and other types of aerosol is possible in the MIPAS data set, the simple but effective PSC filter is used additionally.
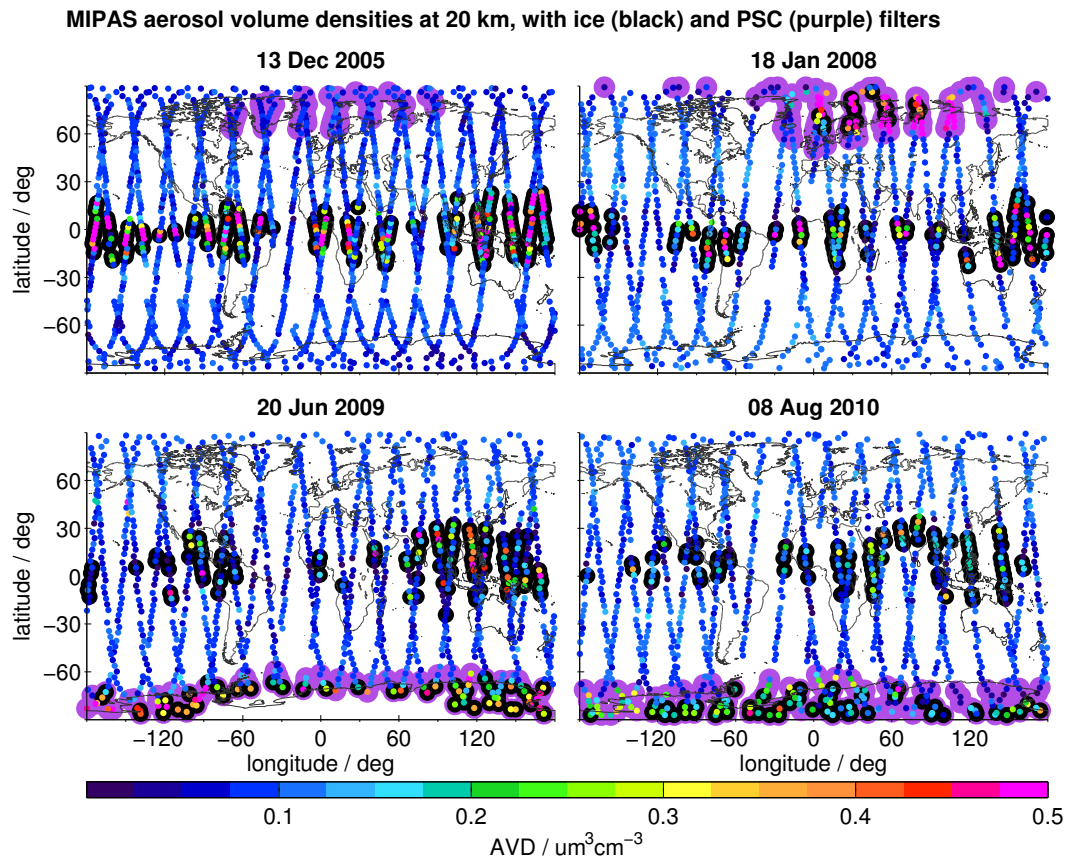
FIGURE 2.10: MIPAS aerosol volume densities at 20 km: examples for daily horizontal distributions of AVDs with indicated ice and PSC filters. Ice filter indicated by black circles, PSC filter by purple circles. Examples for boreal winter (13 Dec 2005, 18 Jan 2008) and austral winter (20 Jun 2009, 08 Aug 2010). AVDs are neither filtered nor offset-corrected. Values exceeding the colour-scale are assigned with the limiting values.

The retrieved aerosol volume densities are most probably also influenced by ash particles from volcanic eruptions, and mineral dust. Griessbach et al. (2014) provided a method to detect the influence of ash on spectra measured by MIPAS, based on an ash detection threshold function. MIPAS AVDs are filtered for ash in a similar way as for ice. Only retrieved data starting 4 km above the uppermost tangent height that was detected to have been influenced by ash are used from here on.

Figure 2.11 reveals the influence of the ash filter on the MIPAS aerosol profiles. Shown are latitudinally resolved time series of the uppermost tangent heights (plus 4 km) flagged to have been influenced by ash. Additionally, the percentage of affected profiles is presented. E.g., the volcanic eruptions of Kasatochi in 2008 and Sarychev in 2009 are visible in the time series of maximal altitudes affected by ash. Even though the maximal tangent heights where measurements were influenced by ash are more pronounced in the Northern hemisphere, and in the tropics during P1, the majority of filtered MIPAS AVD profiles are found after the eruption of Puyehue-Cordón Caulle in the Southern hemisphere. A large part of the structures seen in the data before 2005 (P1) are expected to be connected to the different vertical sampling step. In total, the ash filter has least impact on the retrieved MIPAS aerosol volume density profiles, compared to the ice and PSC filters described above.
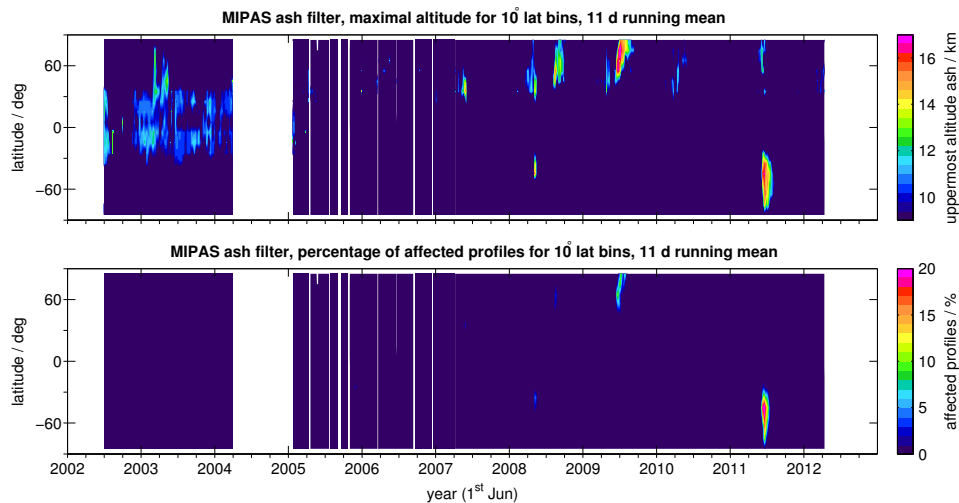
FIGURE 2.11: Latitudinally resolved time series of the ash filter for the new MIPAS aerosol data: upper-most tangent heights plus 4 km where ash has been detected, and percentage of affected profiles. Upper panel: maximal altitude per day and 10° latitude bin (11 d running means). Lower panel: percentage of affected profiles per 10° latitude bin (11 d running means), based on all MIPAS AVD profiles affected at altitudes ≥10 km. The percentages are based on all available MIPAS AVD profiles, but do not consider whether AVD values were available at these altitudes. Values exceeding the colour-scales are assigned with the limiting values.

Besides the omission of high values in the tropics, and the removal of PSC-affected profiles, the observed patterns are generally unchanged by the filters that were applied to the retrieved MIPAS aerosol profiles. Figures 2.12 and 2.13 show the filtered data, as comparisons to Fig. 2.6 and 2.7. In the tropics, parts of the high values remain. It is not clear to which extent these enhancements represent sulphate aerosol, or other types of aerosol. Having these uncertainties in mind, in total the data were improved and merely few non-sulphate aerosol is assumed to have per-sisted in the MIPAS data set of aerosol volume densities. For further analyses, the remaining data are therefore assumed to represent sulphate aerosol only, and gener-ally called MIPAS sulphate aerosol in the following sections. All MIPAS liquid-phase H_2SO_4 presented from here on is filtered for ice, ash, and PSCs, and additionally ex-cludes data below 13 km for 2002–2004. The final data set can be seen in Fig. 4.2 in a similar way as presented in Fig. 2.5 (non-filtered data).
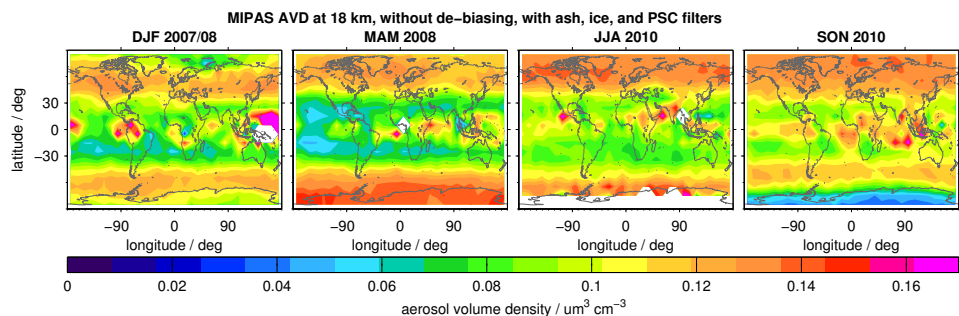
FIGURE 2.12: Effect of ice and PSC filter on MIPAS aerosol volume densities. As Fig. 2.6, but data are filtered for ice, ash, and PSCs. Data are not offset-corrected (Sect. 2.2.3).
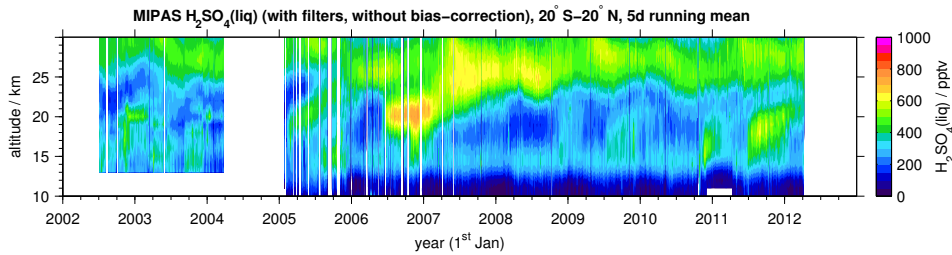
FIGURE 2.13: Time series of filtered MIPAS sulphate aerosol (2002–2012; 20°S–20°N). As Fig. 2.7. VMRs are filtered for ice, ash, and PSCs, but not de-biased. Values exceeding the colour-scale are assigned with the limiting values.

2.2.3 Validation with balloon-borne in situ data and offset correction

The new MIPAS data set of aerosol volume densities is validated by comparison to balloon-borne in situ data from Laramie, Wyoming (41°N/105°W). In situ data were measured by optical aerosol counters from the University of Wyoming, and consist of measurements of stratospheric aerosol at altitudes up to ∼30 km. Details on the measurements and data set are given in Deshler et al. (2003). Balloon flights usually started at around 6–9am, and measurements consist of size resolved aerosol concentrations. As presented in Günther et al. (2018), the validation is based on in situ measurements that were performed by Laser Particle Counters (LPCs). LPCs represent the latest of three instrument types, first used in 2006, and are the standard Laramie instruments since 2008. They measure particles in eight size classes, covering radii >0.08–4.2 μm. Unimodal or bimodal lognormal size distributions are fitted to the measurements. Further details on the fitting approach, aiming at finding the parameters of the lognormal distributions used to derive geophysical quantities from the in situ measurements, are given in Günther et al. (2018). In situ data have been provided by T. Deshler (University of Wyoming, UW). For comparison with MIPAS profiles, aerosol volume density estimates are considered, which have a precision of ± 40% (Deshler et al., 2003; Günther et al., 2018).

To validate MIPAS aerosol volume densities, comparisons to the balloon-borne in situ data are shown in Fig. 2.14. Profiles are presented for each day with available LPC and MIPAS profiles. Only MIPAS profiles in a restricted 5°latitude x 10°longitude distance from Laramie are considered, for the day of the corresponding balloon flight. MIPAS data consist of the primary retrieved aerosol volume densities (binary H_2SO_4–H_2O solution), that have been filtered as described in Sect. 2.2.2. MIPAS profiles are averaged over the restricted area, with the number of available profiles indicated in brackets, and their variability being displayed by their 1-σ standard errors.

Additionally, in Fig. 2.15(a)–(c) the mean profiles for the data shown in Fig. 2.14 are presented, excluding the 28 Jul 2011. The profiles on that day show large discrepancies between AVDs derived from MIPAS and LPC measurements, and at altitudes below ∼18 km the in situ profile shows the most intense vertical variability of all balloon-borne profiles. This variability is possibly connected to aerosol from the Nabro eruption (12 Jun 2011, 13.4°N/41.7°E). For the mean profiles, errors are given in Fig. 2.15(a) that are based on the measurement uncertainties of the single profiles.

In the case on the in situ profiles, these equal a 40% 1-σ uncertainty (Deshler et al., 2003), while the uncertainties for the daily MIPAS profiles include the noise errors of the underlying profiles, and additionally a 10% uncertainty for each profile. This 10% uncertainty represents the remaining errors (see Günther et al., 2018). Furthermore, Fig. 2.15(b) and (c) display the absolute and relative differences between the MIPAS and in situ mean profiles, with the uncertainty of the bias (difference between the mean in situ and mean MIPAS profile) indicated in (b).
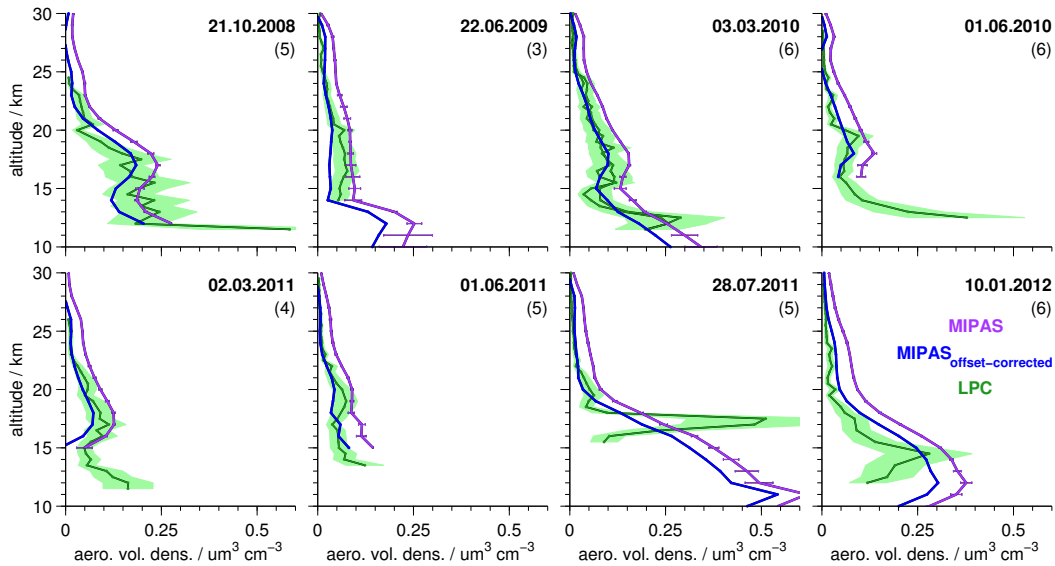
FIGURE 2.14: Comparison of aerosol volume density profiles from MIPAS and balloon-borne in situ measurements for Laramie, Wyoming (41°N/105°W). In situ profiles: from Laser Particle Counter (LPC) measurements. On the 3 Mar 2010 two instruments were flown. Green shaded areas show the 40% 1-σ errors for the in situ AVDs. MIPAS profiles: original (but filtered) MIPAS data in purple, and offset-corrected and filtered data in blue. MIPAS profiles are averages for the indicated day and a $\pm$ 5°lat x 10°lon distance from Laramie (number of available profiles in brackets). Horizontal lines (purple) show the 1-σ standard errors of the mean MIPAS profiles.

In general, the profiles of aerosol volume densities above Laramie, Wyoming, show relatively high values at lower altitudes, where air density is higher, and decrease towards zero with increasing altitude, while air density decreases exponentially. Due to the higher vertical resolution of the in situ data, and a certain smoothing of profiles retrieved from MIPAS measurements (e.g., Günther et al., 2018; Höpfner et al., 2013), the balloon-borne data show finer vertical structures. The MIPAS profiles are generally biased towards higher values, compared to the balloon-borne in situ data. The absolute bias decreases with increasing altitude and decreasing aerosol volume densities. This difference between MIPAS and in situ profiles is assumed to be caused by a tangent altitude dependent radiometric offset.

To compensate for this error, an offset correction is determined for the MIPAS AVDs, based on the observed differences to the balloon-borne data (Fig. 2.15(b)). At higher altitudes profiles are relatively smooth, and MIPAS profiles show a consistent variation with height, compared to the LPC measurements. The positive offset is not random, as shown by the relatively low spread of the uncertainties around the bias, and the clear distance of the limits of uncertainty from 0 μm^3 cm^{-3}. A subtractive linear bias correction is derived from the absolute differences between the mean

MIPAS and in situ profile (Fig. 2.15(b)). Based on the data between 18–30 km, a linear regression (least squares fit) is performed for the absolute differences. As the offset is assumed to be due to an additive error in the radiances (Günther et al., 2018), an additive, rather than a multiplicative offset correction is applied. Not only in the altitude region above 18 km, but also at lower altitudes, where the variation is stronger, the linear fit is reasonable. During offset correction, the aerosol volume densities corresponding to the linear regression (red line in Fig. 2.15(b)) are subtracted from each profile of the MIPAS AVD data set. No error weighting by inverse error variances has been considered in the calculation of mean profiles, as these variances, given as percentage uncertainties, depend on the atmospheric aerosol loading. Error-weighting would therefore produce a sampling artefact in both the estimated bias and linear regression. As can be seen in Fig. 2.15(d)–(f), changes when ex- or including the profiles on the 28 Jul 2011 are marginal above 18 km, which means that the offset correction is not affected. Agreement between MIPAS and in situ data is improved below 18 km, however, when excluding that day.

Even though in situ profiles were not only available from the third instrument type, only those were chosen for MIPAS validation. At altitudes above 20 km the positive bias of the MIPAS data is generally also consistent for the previous instrument type for which profiles for comparison were available (not shown). At lower altitudes, however, the in situ data diverge from each other, when two instruments were flown. The in situ data used in the present study are confined to LPC measurements, which permitted a simple altitude-dependent offset correction for MIPAS AVDs. The transition from the first to the second instrument type was published in Deshler et al. (2003), and a similar study for the transition from the second to third instrument is currently in progress (Günther et al., 2018).

In Figures 2.14 and 2.15 offset-corrected MIPAS profiles are shown. The mean de-biased profile agrees very well with the in situ data at altitudes above ∼16 km, and mostly lies in the range of the errors of the mean in situ profile at lower altitudes. Both absolute and relative differences are strongly reduced by the offset correction, and are generally below $\pm$ 25%. All results shown in the following are based on de-biased MIPAS aerosol volume densities. The final filtered and offset-corrected data set can be seen, e.g., in Fig. 4.2.
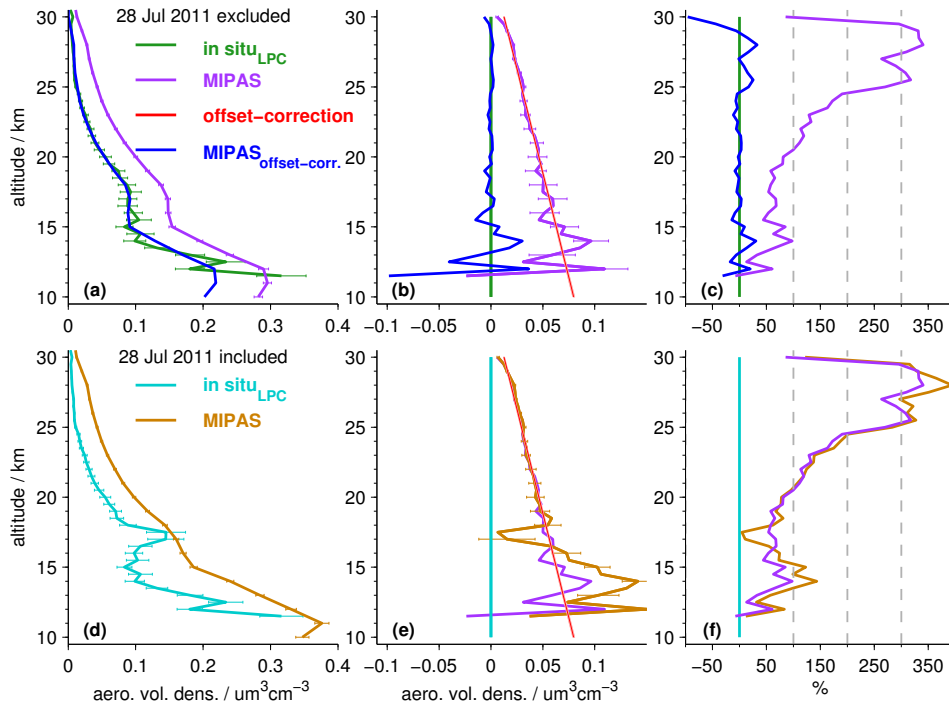
FIGURE 2.15: Comparison of aerosol volume density profiles for Laramie, Wyoming (41°N/105°W) from MIPAS and balloon-borne in situ measurements. Mean profiles from Fig. 2.14 (a), with absolute (b) and percentage (c) differences, and values for offset correction (b). Profiles in (a) are mean profiles for the data in Fig. 2.14, together with their 1-σ errors, which are based on estimated measurement uncertainties. The profiles measured on 28 Jul 2011 are excluded. Original data in purple, and mean over offset-corrected profiles in blue, both with all filters from Sect. 2.2.2 applied. As each day shall be weighted once, for the 3 Mar 2010 the average of the two available in situ profiles is considered. (b) and (c) show the absolute and relative differences between the average MIPAS and in situ profiles. The 1-σ uncertainties of the absolute difference between the average MIPAS and in situ profiles are indicated by horizontal purple lines (error propagation $\sqrt{x_1^2 + x_2^2}$ based on the errors x_1 and x_2 at a specific altitude, as in (a)). The red line in (b) represents a linear regression (least squares fit) to the purple MIPAS profiles in (b) – at 18–30 km – and indicates the offset correction for MIPAS AVDs. The equation of this correction is $y = 33.74 - 297.6x$, with x being the aerosol volume density, and y the altitude. The coefficient of determination is $r^2 = 0.98$. A narrow light red shaded area in (b) indicates the 1-σ uncertainty of the linear fit, based on the uncertainties of the parameters for the intercept and slope of the linear regression (generalised Gaussian error propagation). (d)–(f) are similar to (a)–(c), but for a comparison of profiles that include and exclude the 28 Jul 2011.

2.3 Short overview of analysed MIPAS data sets

In this work several MIPAS data sets for the sulphur species carbonyl sulphide, sulphur dioxide, and sulphuric acid are studied. These are the most important sulphur species determining the stratospheric sulphur loading. In the following chapters data will be analysed in terms of sulphur sources and removal, sulphur loading and distributions. Here, a short survey of the MIPAS data sets is presented, together with the identifiers of the data sets used throughout this work. Additionally given are the main sections of this thesis in which the data sets are studied.

- **OCS** (Glatthor et al., 2015, 2017): retrieved from single limb-scans (8–50 km; Chap. 5 and 6).

- **'SO$_2$mea'** (Höpfner et al., 2013): retrieved from monthly and zonally averaged limb-scans (10° latitude bins; 15–45 km; Chap. 5 and 6).

- **'SO$_2$sgl'** (Höpfner et al., 2015): retrieved from single limb-scans (10–23 km; Chap. 4 to 6).

- **Sulphate aerosol** (Günther et al., 2018): retrieved from single limb-scans (10–30 km; Chap. 4 to 6).

3 Chemical transport model

A three-dimensional (3D) isentropic chemical transport model is used to study stratospheric sulphur. This Eulerian model (e.g., Sinnhuber et al., 2003; Kiesewetter et al., 2010) is forced by temperatures, wind fields, and diabatic heating rates from the ERA-Interim reanalysis (Dee et al., 2011). While horizontal transport is calculated from wind fields, vertical transport between levels of constant potential temperature is derived from diabatic heating rates. The advection scheme employed by the model is the second order moments advection scheme by Prather (1986), which conserves the structures of trace species during motion by preserving the second-order moments of the areal spread of the species. The horizontal resolution of the CTM is $\sim 2.5°$ lat x $3.75°$ lon, on a Gaussian latitude grid (see below). The altitude range covered by 29 isentropic surfaces, i.e., levels of constant potential temperature, between 330 and 2,700 K is roughly 10–55 km. The model is run with a 30 min time step, while ERA-Interim data are updated every six hours, and interpolated linearly between the updates. Model output is generated once per day, at 12 UTC (Universal Time Coordinated). All model results shown in this work are based on simulated data after a model spin-up that has been adjusted to the specific simulation set-up and species. Long-lived species as OCS demand for longer spin-up periods. No model-spin up is considered when performing simulations with background concentrations of 0 pptv.

In the following, the vertical model grid, model age of air, and the quasi-biennial oscillation (QBO) are described. This is complemented by an introduction of the sulphur module that has been implemented in the CTM in the course of this work. The module comprises the most important sulphur species for stratospheric sulphur: OCS, SO_2 and H_2SO_4. These are consistent with the species available from MIPAS, while in the case of H_2SO_4 only the liquid part is available from MIPAS measurements. Model results are based on the following implementations: a bottom boundary of OCS, as sulphur source; photolysis of OCS, which forms SO_2; oxidation of SO_2 with OH, which forms H_2SO_4; sedimentation of the liquid part of H_2SO_4. Other implemented sulphur sources are volcanic emissions of SO_2, or emissions of H_2SO_4 for special analyses.

3.1 Vertical model grid

The vertical grid of the 3D-CTM consists of 29 isentropic surfaces, with the lowermost level starting at 330 K, and the uppermost level ending at 2,700 K. An isentrope is a surface of constant potential temperature, which is 'the temperature an unsaturated air parcel attains if it is brought adiabatically from its altitude down to a pressure of 1,000 mb' (Jacobson, 1999). 'Adiabatically' means that expansion

or compression of the air parcel does not include any heat exchange. Equation 3.1 shows the calculation of potential temperatures of dry air, considering the ambient temperature T (in K), and pressure p (in hPa). Even under moist conditions Eq. 3.1 is often used, as the error compared to the potential temperature of moist air can be neglected (Jacobson, 1999).

$$\theta = T \left(\frac{1,000 \, \text{hPa}}{p} \right)^{\kappa} \tag{3.1}$$

Here κ is the ratio of the gas constant of dry air ($R = 287 \, \text{J kg}^{-1} \, \text{K}^{-1}$) to the specific heat capacity at constant pressure ($c_p = 1,005 \, \text{J kg}^{-1} \, \text{K}^{-1}$). As shown, e.g., by Diallo et al. (2012) and Meijer et al. (2004), the transport is in general represented more realistically on isentropes, compared to levels of constant altitude or pressure. As the 3D-CTM used in this study does not cover large parts of the troposphere, no problems due to levels of too low potential temperatures 'entering' the Earth surface arise from the use of an isentropic vertical grid.

In Fig. 3.1 the vertical distribution of grid box centres is shown for the 29 isentropes representing the vertical grid of the CTM. Levels are presented as latitudinally resolved annual means (2002–2012). The lowermost model levels show meridional curvature, with the lowermost model level (335 K) starting at around 10–11 km in the extra-tropics, while in the tropics it is situated at ∼7–8 km. Generally, the lower stratosphere up to around 30 km is better resolved vertically than the upper stratosphere. In the tropical troposphere the distance between two levels is relatively large, while the resolution improves drastically between ∼16–30 km. In the present study the focus lies mostly on stratospheric altitudes up to ∼30 km, which coincides with the region of highest vertical model resolution, except for the tropical tropopause. The lowermost model level contains the bottom boundaries for the different trace-species, and is therefore not considered in any analysis of model results.

The horizontal distribution of the lowermost two model level altitudes (grid box centres of 335 and 344.2 K isentropes) is shown in Fig. 3.2, as seasonal means over 2002–2012. In the tropics, the 335 K isentrope is at low altitudes throughout the year (∼7–8 km), and at elevated altitudes in the extra-tropics. The meridional extent of low altitudes in the tropics coincides with the migrating Inter Tropical Convergence Zone (e.g., Green et al., 2017). This is the zone where the trade winds from northeast and southeast converge and is influenced by the solar zenith angle and the distribution of water and land masses. The Inter Tropical Convergence Zone is a zone of low pressures and strong convection, as seen by strong cloud formation in tropical regions (2.2.2). The 344.2 K isentrope reflects the distribution of high pressures at around 30°, with grid cell altitudes being more elevated in the subtropical high pressure belt. Further, three features can be seen in the altitude distributions of the 335 K and 344.2 K isentropes. One is connected to the winter polar vortex, especially pronounced in the Southern hemisphere during austral winter and spring, with elevated level altitudes. The second feature is connected to the Asian Summer Monsoon Anticyclone (ASMA). During boreal summer the ASMA provokes the lowermost model levels to lie at relatively low altitudes. A third feature is found in the tropical Western Pacific, where the lowermost model levels are generally situated at relatively low altitudes.
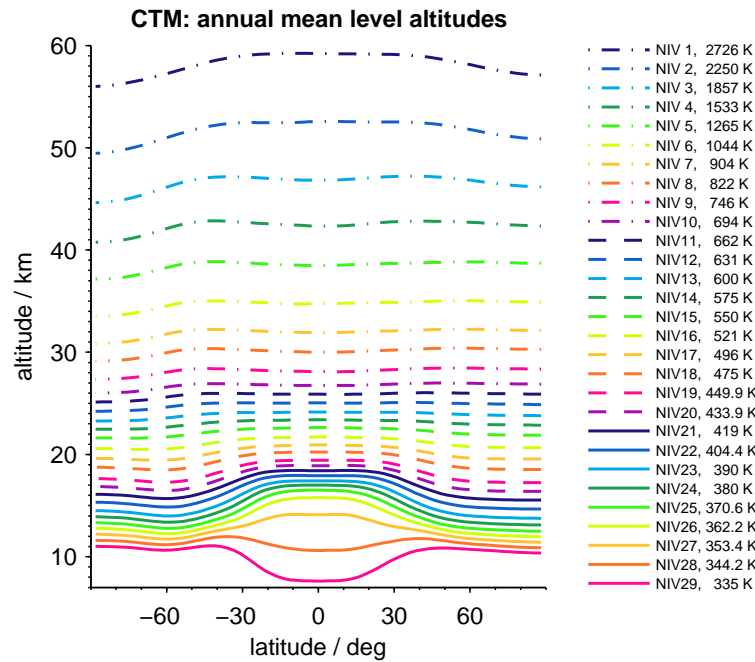
FIGURE 3.1: Vertical distribution of the isentropic 3D-CTM levels. Annual zonal mean altitudes of the grid box centres (2002–2012). Level numbers (NIV) and corresponding potential temperatures are denoted in the legend.
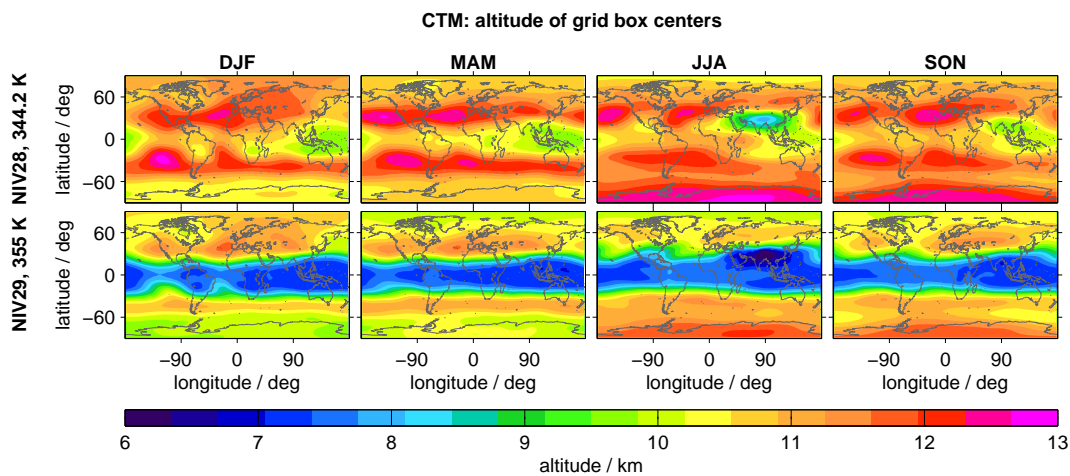
FIGURE 3.2: Seasonal horizontal distribution of grid box centre altitudes for the two lowermost CTM levels (2002–2012).

As the lower altitudes of the model are partly tropospheric and fast tropospheric uplift by convection (available from Aschmann et al., 2009) is not considered in the version of the model used during this thesis, a subroutine mixes the whole troposphere instantly in a simple approximation for tropospheric mixing (Aschmann, 2014). In the model, all grid cells per column up to a certain height above which air is considered stratospheric, are instantaneously mixed. The distinction of tropospheric and stratospheric air is based on the actual potential vorticity (PV) and potential temperature (thresholds: < 2 PVU and 350 K).

3.2 Age of air and Brewer-Dobson circulation

In the model, the implemented sulphur tracer-species are transported by advection, with calculations being based on the second order moments advection scheme by Prather (1986), and meteorological driving data from the ERA-Interim reanalysis (Dee et al., 2011). The transport direction, speed of motion, and mixing of air are important to determine distributions of trace-species in the atmosphere. This is obviously true for long-lived or inert trace-species, as well as for trace-species that are destroyed relatively fast by chemical processes or photo-dissociation. An easy example of transport time influencing trace-species concentrations of a substance that is affected by photolysis is slow transport through a region of intense photolysis, resulting in stronger decay of the substance, compared to fast transport through the same region.

Transport time can be described by the mean age of stratospheric air (AoA; e.g., Hall and Plumb, 1994; Waugh and Hall, 2002). This is a concept based on the knowledge of the stratospheric distribution of an inert substance / model tracer, that has a known linear increase of concentrations at its entry point to the stratosphere, the Tropical Tropopause Layer (TTL). This enables to calculate the average transit time it took the tracer or an air parcel to be transported to a certain point in the stratosphere, by referring the actual concentration at that point to the time when the same concentration has been observed in the TTL. This concept includes information about the speed of advection and the intensity of mixing of an air parcel or tracer. The distributions of AoA and trace-species are connected to the Brewer-Dobson circulation (BDC), the global residual stratospheric circulation. The BDC has been studied, e.g., in Plumb and Eluszkiewicz (1999), or reviewed by Butchart (2014).

While strong zonal winds lead to a fast zonal mixing of substances in the stratosphere, transport in the meridional and vertical directions is regulated by the BDC (Butchart, 2014; Holton et al., 1995). This residual circulation that is caused by wave breaking of upward propagating waves in the stratosphere has the following characteristics (Kremser et al., 2016): ascent in the tropics, transport towards the poles in the extra-tropics, and descent in high-latitudes, especially above the winter polar vortex. Additional transport occurs in the extra-tropics, characterised by two-way quasi horizontal stirring in the 'stratospheric surf zone' (McIntyre and Palmer, 1984). Following Holton et al. (1995), air that enters the stratosphere by slow diabatic ascent in the tropics can remain in the stratosphere for years when undergoing uplift in the ascending branch of the BDC. When air crosses the tropopause from the upper troposphere in the tropics to the lower stratosphere in higher latitudes by quasi-isentropic transport, however, the air subsides back into the troposphere within months.

Presented in Fig. 3.3 are seasonal vertically resolved meridional distributions of model AoA. A simulation has been performed to calculate the age of air at a certain location and time in the atmosphere, by allocating the model bottom boundary (335 K) with the actual date, per time step. From MIPAS, a data set of AoA is available (Haenel et al., 2015), calculated from retrieval results for the long-lived trace-species SF_6. These data (Haenel, 2017) are shown in Fig. 3.3 in comparison to the

model AoA. The model AoA shows a pronounced gradient between younger air in the tropics and older air in the extra-tropics, especially at altitudes above ∼20 km. Within the TTL meridional transport is rather effective, while above ∼18.5 km transport between low-latitudes and the extra-tropics is oppressed ('tropical pipe'; Plumb, 1996) or diminished ('tropical leaky pipe'; Neu and Plumb, 1999). This pattern is less pronounced in the MIPAS AoA. In the MIPAS data very high AoA is found in high-latitudes during polar winter and spring. This is connected to downward transport of SF_6-depleted air from the mesosphere, where SF_6 has a sink. This transport results in overestimated AoA in these regions (Haenel et al., 2015; Stiller et al., 2012). Model AoA is several years younger in this region. Overall, the model reproduces the large scale transport, as expressed by the age of air, sufficiently well that the CTM can be employed for the investigation of sulphur transport. Possible inaccuracies in the model transport speed need to be kept in mind, however, when analysing simulated species. Information on the ERA-Interim age of stratospheric air can be found in Diallo et al. (2012).
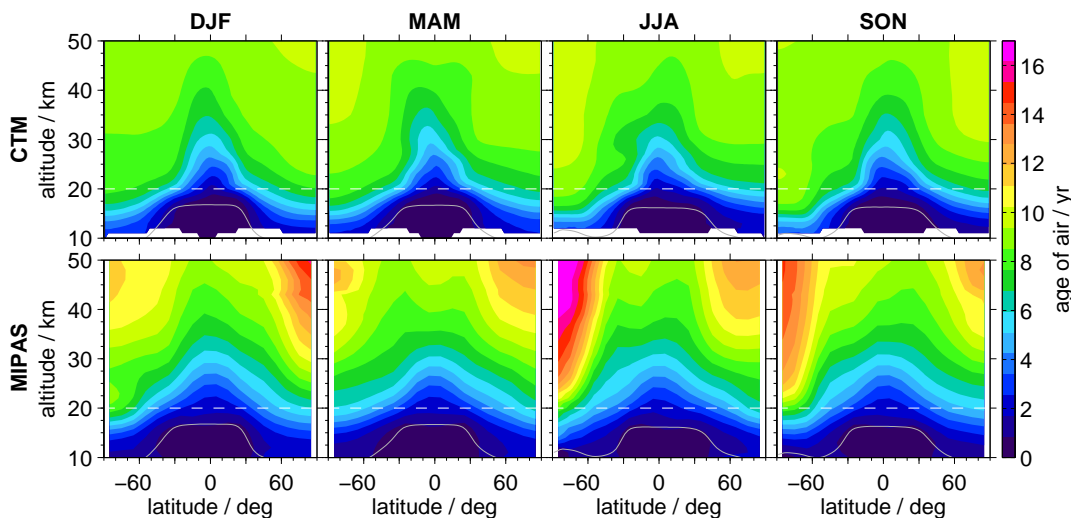
FIGURE 3.3: Mean age of air (2002–2012) from the CTM and MIPAS. Seasonal vertically resolved zonal means for 10° latitude bins. MIPAS AoA from Haenel (2017).

3.3   Quasi-biennial oscillation

In the tropical stratosphere in the vicinity of the equator, zonal wind shows a very distinct pattern of opposing phases, which propagate downwards with time. These phases of westerly (wind from the west, positive values) and easterly (wind from the east, negative phase) jets that are propagating downwards with a relatively constant amplitude and a rate of about 1 km per month (Brasseur and Solomon, 2006), persist for approximately two years (24–32 months, ∼28 months on average; e.g., Tweedy et al., 2017). This gives the phenomenon its name: quasi-biennial oscillation (QBO), which has been described, e.g., by Holton and Lindzen (1972), and reviewed in Baldwin et al. (2001). In the CTM, the QBO is included by the driving ERA-Interim reanalysis from Dee et al. (2011). A good representation of the QBO in the model is important, as it can influence trace-species distributions in the stratosphere (e.g.,

Tweedy et al., 2017; Schoeberl et al., 2008). Also stratospheric sulphur is influenced by the QBO (Sect. 5.1.2; Vernier et al., 2011b; Brühl et al., 2015). Information on the QBO in ERA-Interim can be found in Solomon et al. (2014).
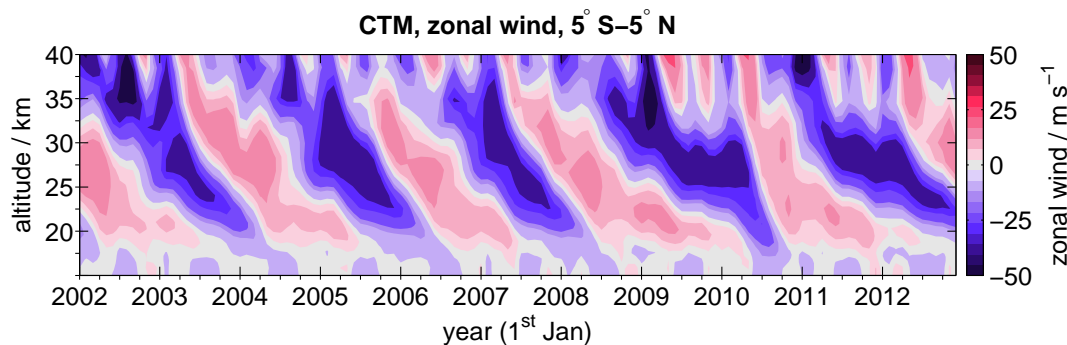
FIGURE 3.4: CTM: zonal wind at 5°S–5°N. Vertically resolved time series of monthly mean zonal wind for 2002–2012. Values exceeding the colour-scale are assigned with the limiting values.

3.4   Sulphur module

During this work, a sulphur module has been implemented in the 3D-CTM, covering the essential conversions of OCS to SO_2 and SO_2 to H_2SO_4, as well as sedimentation of sulphate aerosol. The different aspects of the sulphur module are:

- OCS

    – source: bottom boundary for OCS from MIPAS measurements

    – decay through photolysis, forming SO_2

- SO_2

    – bottom boundary (typically assumed as 0 pptv in this work)

    – sources:

        * sulphur released from OCS

        * volcanically injected SO_2

    – decay through oxidation by OH, forming H_2SO_4

- H_2SO_4

    – bottom boundary (here assumed to be 0 pptv)

    – source: sulphur released from SO_2

    – partitioning into gas- and liquid-phase, and removal of liquid-phase H_2SO_4 through sedimentation

In this study, two main types of simulations can be distinguished, once for background / non-volcanic conditions, and second for volcanically perturbed times. When simulating background conditions, OCS, SO_2, and H_2SO_4 are simulated. All sulphur released from OCS forms SO_2, and all sulphur released from SO_2 forms

H_2SO_4. The only sulphur source is a bottom boundary of OCS. When simulating volcanic sulphur, the only sulphur source is volcanically injected SO_2. Similar to the simulations for background conditions, all sulphur that is released from SO_2 forms H_2SO_4. Due to differing predominant aerosol radii during background conditions and for volcanic aerosol (Deshler, 2008), simulations are performed independently for these two conditions. The initial fields of SO_2 and H_2SO_4 are set to zero in the simulations of volcanic sulphur, while simulations of background sulphur need a model spin-up, to determine the initial trace-species fields. All aspects of the sulphur module are presented in more detail in the following sections.

3.4.1 OCS: bottom boundary

In the model, the bottom boundary of OCS is prescribed by OCS volume mixing ratios, based on MIPAS measurements. Data do not address any inter-annual or zonal, but intra-annual and meridional variability. As seen in Sect. 3.1, the lowermost model level is at around 8–11 km in the annual mean, with a certain seasonal variation. The bottom boundary is based on the meridional distribution of MIPAS OCS VMRs at 8–12 km. Per month and 10° latitude bin the maximum of the data at 8–12 km is chosen from the climatology of monthly MIPAS values (2002–2012). For the resulting meridional distribution of maxima, running means for 30° latitude bins are calculated. These are interpolated to the CTM horizontal grid and extended to high latitudes, where values are missing due to averaging, by simply assigning the last available value. The derived monthly data are interpolated linearly to daily distributions to prevent jumps in the simulations and are used as OCS bottom boundary in the CTM, if not denoted differently. Values are presented as monthly means in Fig. 3.5. The bottom boundary generally shows higher OCS VMRs and larger variability in the Northern hemisphere, and in the tropics during boreal spring and summer. Values in the tropics are in the range of $\sim$510–545 pptv.
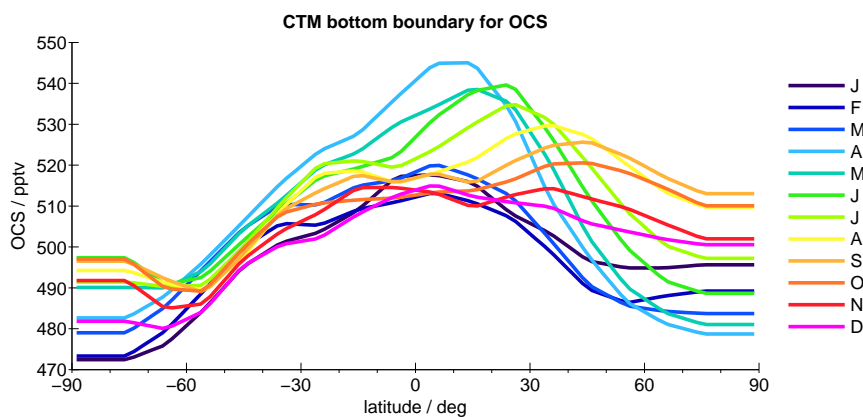
FIGURE 3.5: CTM bottom boundary of OCS, derived from MIPAS. Monthly meridional distribution of OCS volume mixing ratios.

3.4.2 OCS: destruction by photolysis

OCS in the model is removed by advective transport out of the model domain or photolysis, which is part of the newly implemented sulphur module. Photolysis rates for OCS are based on calculations by EMAC (ECHAM/MESSy Atmospheric Chemistry model; provided by G. Krysztoviak Tong, Université d'Orléans). Monthly photolysis rates are given on hybrid pressure levels and at a different horizontal resolution than used in the CTM. They are linearly interpolated to the CTM grid, and as for the OCS bottom boundary, monthly data are linearly interpolated to daily values. OCS photolysis rates in the CTM do not consider any inter-annual, but merely intra-annual variability. Zonal mean photolysis rates are used, as the EMAC output does not represent a snapshot of the horizontal distribution at a certain time of the day. The photolysis of OCS is presented in reaction R3.1 (Jacobson, 1999):

$$\underset{\textit{carbonyl sulphide}}{OCS} + h\nu \longrightarrow \underset{\textit{carbon monoxide}}{CO} + \underset{\textit{atomic sulphur}}{S} \qquad \lambda < 260 \, \text{nm} \qquad \text{(R3.1)}$$
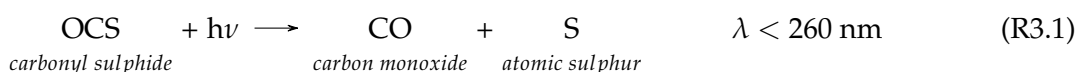
In reaction R3.1, $h\nu$ is the energy of a photon that depends on its frequency ν and the Planck's constant h, while λ is the wavelength of the electromagnetic radiation needed for the reaction to take place. The concentration of OCS after one model time step of $DT_0 = 30$ min (1,800 s) can be calculated from the photolysis rate (pr) as

$$[OCS] = [OCS]_0 \cdot e^{-DT_0 \cdot pr} \qquad (3.2)$$

Photolysis rates for OCS, as used in the CTM, and calculated OCS lifetimes ($\tau_{OCS} = pr^{-1}$), are presented in Fig. 3.6, as seasonal vertically resolved meridional distributions. Due to the strong vertical gradient values are shown in the logarithmic space. In this thesis, lifetime denotes the e-folding lifetime, which is the time needed for a species with exponential decay to decrease to e^{-1} of its initial concentration. The lifetimes calculated from OCS photolysis rates do not consider any transport induced decay. The photolysis rates depend on the availability of high energy electromagnetic radiation, with wavelengths smaller than 260 nm (ultraviolet and higher energetic radiation). Therefore, the photolysis rates decrease towards the Earth surface, and are smallest during polar winter. As the OCS lifetime is the reciprocal of the photolysis rates, OCS exists longest during polar winter and at low altitudes. In the troposphere and lower stratosphere OCS is a long-lived substance, while lifetimes decrease rapidly to below 0.1 yr at around 22–23 km in tropical latitudes. At the Earth surface interaction with the biosphere is an important process (Glatthor et al., 2015), affecting OCS lifetimes in the troposphere. In the model, as only covering the upper troposphere and the stratosphere, this is not considered.

An increase in the photolysis rates by a factor of x increases the loss rate by this factor, and consequently decreases the lifetime of OCS by x^{-1}. When pr is decreased by 10% ($x = 0.9$) the lifetime changes globally by +11%, while when pr is increased by 10% ($x = 1.1$) the lifetime changes globally by -9%.

(a) CTM mean seasonal OCS Jval / yr⁻¹

(b) CTM mean seasonal lifetime OCS / yr
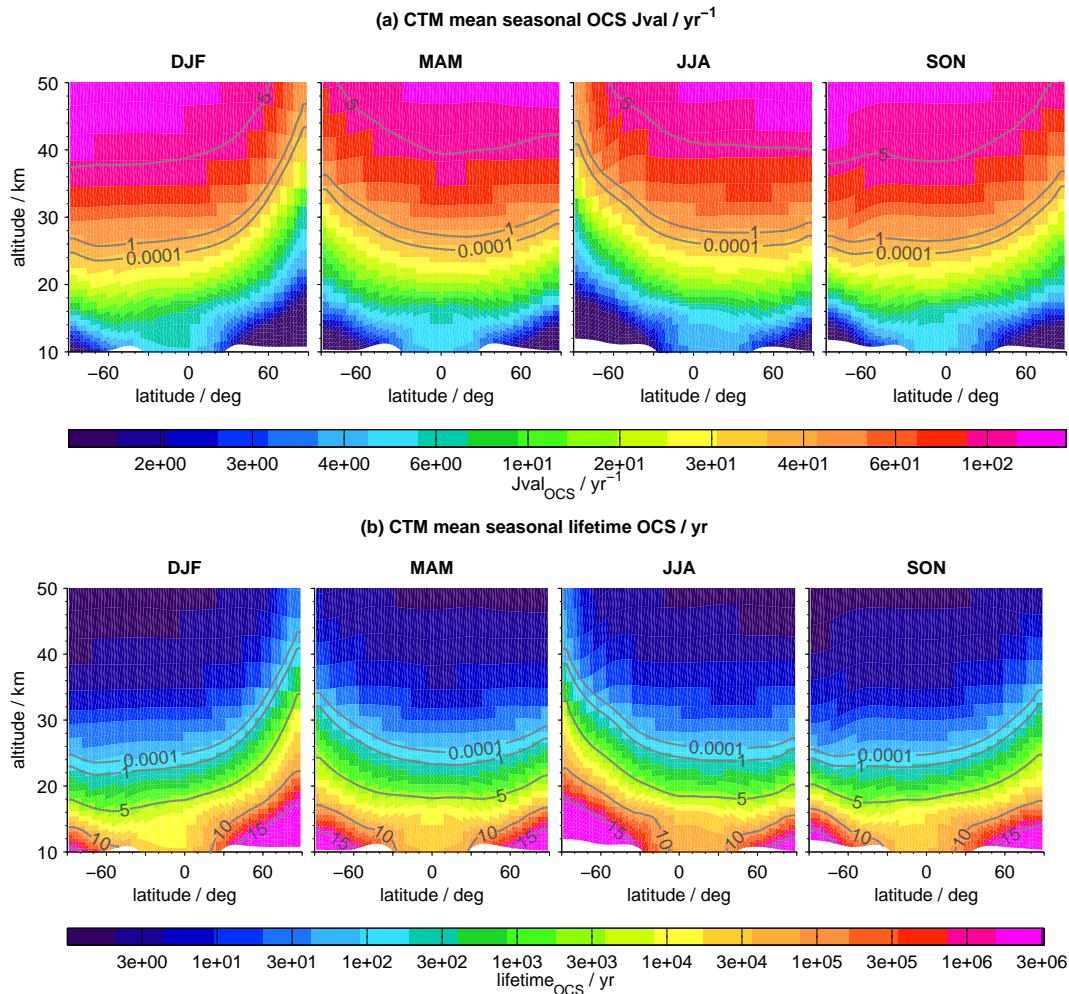
FIGURE 3.6: OCS photolysis rates as used in the CTM (a) and resulting e-folding lifetimes for OCS (b). Seasonal distribution of vertically resolved zonal means. Values are presented in the logarithmic space and based on the mean atmospheric state of the CTM for 2002–2012. Values exceeding the colour-scales are assigned with the limiting values, respectively.

3.4.3 SO$_2$: volcanic input

Volcanic emissions of SO$_2$ are implemented at the day of the eruption, instantaneously at 12 UTC. Two data sets are used to study volcanic sulphur. The first is a data set of volcanic SO$_2$ masses for 30 days by Höpfner et al. (2015), which is based on MIPAS SO$_2$sgl. Höpfner et al. (2015) provided SO$_2$ masses for three altitude ranges (10–14, 14–18, and 18–22 km). In several cases, the masses and injection heights were adapted during the present study for the CTM simulations to result in a better fit with MIPAS SO$_2$sgl, based on various simulations with differing masses and injection heights. The simulation including this modified data set is presented in the present work as 'G17'. The SO$_2$ masses and injection altitudes can be found in Tab. A.1. In the CTM, injected SO$_2$ masses are spread in the column of grid cells including the location of a certain volcano. Masses are injected homogeneously to the air mass in the corresponding altitude region. The method Höpfner et al. (2015) used to derive SO$_2$ masses, and the model set-up, will be described in more detail in Sections 4.3 and 4.2.

A second data set of volcanic SO_2 has been provided by C. Brühl (Max Planck Institut für Chemie, MPIC), consisting of SO_2 volume mixing ratios for 98 days during the MIPAS measurement period, as have been used as input to EMAC simulations in Brühl et al. (2015). Data have been interpolated from the EMAC model grid (hyprid pressure levels, and differing horizontal resolution) to the CTM grid, for the 98 days on which SO_2 emissions were provided, using the CTM atmospheric state at the eruption time, which has been chosen to be at 12 UTC. Further details on this simulation 'B15' are given in Section 4.2. Generally, when injecting volcanic SO_2 in the CTM, the current SO_2 field is not replaced, but volcanic SO_2 is added to the previously existing SO_2.

3.4.4 SO_2: oxidation by OH and formation of H_2SO_4

In the CTM, sulphur dioxide is removed by transport out of the model domain, or by oxidation with hydroxyl radicals (OH), as part of the newly implemented sulphur module. The reaction sequence forming H_2SO_4 from SO_2, due to the initial reaction of SO_2 with OH, is shown in R3.2 (following Jacobson, 1999). The gas-phase sulphuric acid that is formed by these reactions can then condense onto particles, forming aerosol with liquid water. As the interim reactions are relatively fast (Jacobson, 1999 for bisulphite - HSO_3), and the rate-controlling step in the reaction sequence is assumed to be the formation of HSO_3 from SO_2 (Hamill et al., 1977), no additional reaction is considered in the CTM.

$$SO_2 \xrightarrow{\text{+OH,M}} HSO_3 \xrightarrow{\text{+O2,--HO2}} SO_3 \xrightarrow{\text{+2H2O}} H_2SO_4$$
$$\quad\text{\textit{sulphur dioxide}} \qquad \text{\textit{bisulphite}} \qquad\qquad \text{\textit{sulphur trioxide}} \qquad\quad \text{\textit{sulphuric acid}}$$

$$\text{(R3.2)}$$
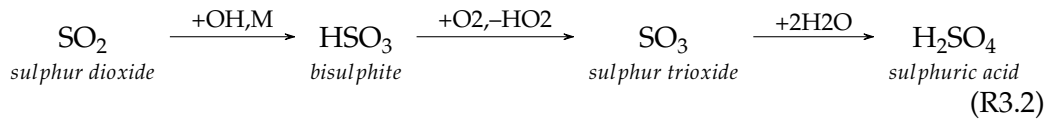
Reaction rates are needed to calculate SO_2 lifetimes, which are in turn used to derive SO_2 loss during one model time step. For the termolecular reaction (involving three chemical species) of SO_2 with OH, the calculation of the pressure-dependent reaction rate follows recommendations from JPL (Burkholder et al., 2015; Jet Propulsion Laboratory). Additional information on termolecular reactions and reaction rates is available from Brasseur and Solomon (2006) and Burkholder et al. (2015). The termolecular rate coefficient at low pressure $k_0(T)$ (low-pressure limit, in cm^6 molecule^{-2} s^{-1}) is

$$k_0(T) = k_0^{300} \left(\frac{T}{300} \right)^{-n} \tag{3.3}$$

with $k_0^{300} = 3.3 \cdot 10^{-31}$, $n = 4.3$, and T being the temperature (in K).

The bimolecular rate coefficient limiting the reaction at high pressure $k_\infty^{300}(T)$ (high-pressure limit, in cm^3 molecule^{-1} s^{-1}) is

$$k_\infty^{300}(T) = \left(\frac{T}{300} \right) \tag{3.4}$$

with $k_\infty^{300} = 1.6 \cdot 10^{-12}$.

The resulting effective second-order rate constant at a certain temperature and pressure is calculated from

$$k_f([M], T) = \left(\frac{k_0(T)[M]}{1 + \frac{k_0(T)[M]}{k_\infty(T)}} \right) \cdot x \tag{3.5}$$

with

$$x = 0.6^{\left(1 + \left[log_{10} \left(\frac{k_0(T)[M]}{k_\infty(T)} \right) \right]^2 \right)^{-1}} \tag{3.6}$$

[M] (Eq. 3.7) and [OH] (Eq. 3.8) are the number concentrations (or number densities) of air and OH (in molecules cm^{-3}).

$$[M] = \frac{VMR_{air} \cdot p}{k_b \cdot T} \cdot 10^{-6} = \frac{p}{k_b \cdot T} \cdot 10^{-6} \tag{3.7}$$

$$[OH] = \frac{VMR_{OH} \cdot p}{k_b \cdot T} \cdot 10^{-6} \tag{3.8}$$

p is the pressure in Pa, while k_b is the Boltzmann constant ($1.38 \cdot 10^{-23}$ m^2 kg s^{-2} K^{-1}) that relates the average kinetic energy of the particles in the gas with the temperature in the gas. The reciprocal of the loss rate, the e-folding lifetime of SO$_2$ (τ_{SO_2}, in s) for a certain temperature and concentration $[M]$ is

$$\tau_{SO_2} = (k_f([M], T) \cdot [OH])^{-1} \tag{3.9}$$

The concentration of SO$_2$ after one model time step of $DT_0 = 30$ min (1,800 s) can then be calculated as

$$[SO_2] = [SO_2]_0 \cdot e^{\frac{-DT_0}{\tau_{SO_2}}} \tag{3.10}$$

In this study no full chemistry runs were performed that included the mentioned sulphur species. The sulphur module is used as a stand-alone module, which does not interact with any other species. The chemical detergent OH needed for reaction with SO$_2$, has been derived from a separate full chemistry run of the CTM, for 2003–2006. A climatology of monthly values (at 12 UTC) was interpolated linearly to daily values. No inter-annual variability of OH is considered in this work. As the concentrations of the oxidising agent OH depend strongly on the availability of sunlight, it shows pronounced diurnal variation. In order to consider this diurnal variation, the OH fields used in the sulphur module, which represent OH at 12 UTC, are shifted longitudinally, corresponding to the model time of the day.

In the following, important reactions that control the availability of OH are presented, based on Jacobson (1999). Reaction R3.3 shows the predominant source of OH in the free troposphere and stratosphere. Further, in R3.4 the main reaction that is important for the availability of O(^1D) (electronically excited oxygen atom) in these atmospheric layers is presented. That reaction shows the photo-dissociation

of ozone (O_3) by solar radiation. Additional reactions that build OH in the stratosphere are shown in reactions R3.5 to R3.7. Apart from reaction R3.7, all mentioned reactions are included in the chemistry scheme of the CTM.

$$O(^1D) + H_2O \longrightarrow 2\,OH \tag{R3.3}$$

$$O_3 + h\nu \longrightarrow O_2 + O(^1D) \qquad \lambda < 310\,\text{nm} \tag{R3.4}$$

$$O(^1D) + CH_4 \longrightarrow CH_3 + OH \tag{R3.5}$$

$$O(^1D) + H_2 \longrightarrow H + OH \tag{R3.6}$$

$$HCl + O \longrightarrow Cl + OH \tag{R3.7}$$
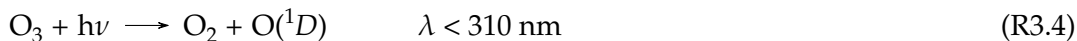
In the latter reactions, O_2 is molecular oxygen, CH_4 is methane and CH_3 is a methyl radical, H is hydrogen and H_2 is diatomic hydrogen, and Cl is chlorine while HCl is hydrogen chloride.

In Fig. 3.7 OH, temperatures, and calculated chemical e-folding lifetimes of SO_2 are displayed, as seasonal mean vertically resolved meridional distributions. Due to the strong gradient of OH volume mixing ratios, values are shown in the logarithmic space. OH VMRs increase towards higher stratospheric altitudes, and the OH loading in the lower stratosphere is especially small during polar winter, due to the absence of sunlight. The availability of water vapour is limited in the tropical tropopause layer, due to low temperatures and 'freeze-drying' of air in the TTL (Jensen et al., 1996), resulting in low OH concentrations at upper tropospheric altitudes. Further, the availability of OH in the dry stratosphere is low, compared to tropospheric levels, especially in the lower stratosphere (Eisinger and Burrows, 1998). Between models, there exists a rather large variability between simulated OH concentrations, and measurements are limited (Kremser et al., 2016). This results in uncertainties in simulations of SO_2. The distribution of SO_2 e-folding lifetimes calculated in the CTM reflects the low values of OH that are connected to a temperature minimum in the TTL, leading to a local maximum of SO_2 lifetimes in this region. Lifetimes of around 30 days in the upper troposphere (Fig. 3.7), and the relatively long SO_2 e-folding lifetimes in the TTL (> 100 d) are long enough for convective uplift to transport SO_2 to the TTL, and for SO_2 to enter the stratosphere by slow radiation-driven ascent through the TTL. Furthermore, a second prominent feature in the SO_2 lifetimes is caused by low availability and partly the absence of light during polar winter, resulting in longer SO_2 lifetimes. Additionally to the high values in the polar regions, calculated lifetimes of SO_2 show a strong increase at 42 km.

A positive change in OH by a factor of x increases the loss rate by this factor, and consequently decreases the chemical lifetime of SO_2, so the reciprocal of this loss rate, by x^{-1}. When OH_{VMR} is decreased by 30% ($x = 0.7$), the lifetime changes globally by +43%, and when OH_{VMR} is increased by 30% ($x = 1.3$), the lifetime changes globally by -23%.
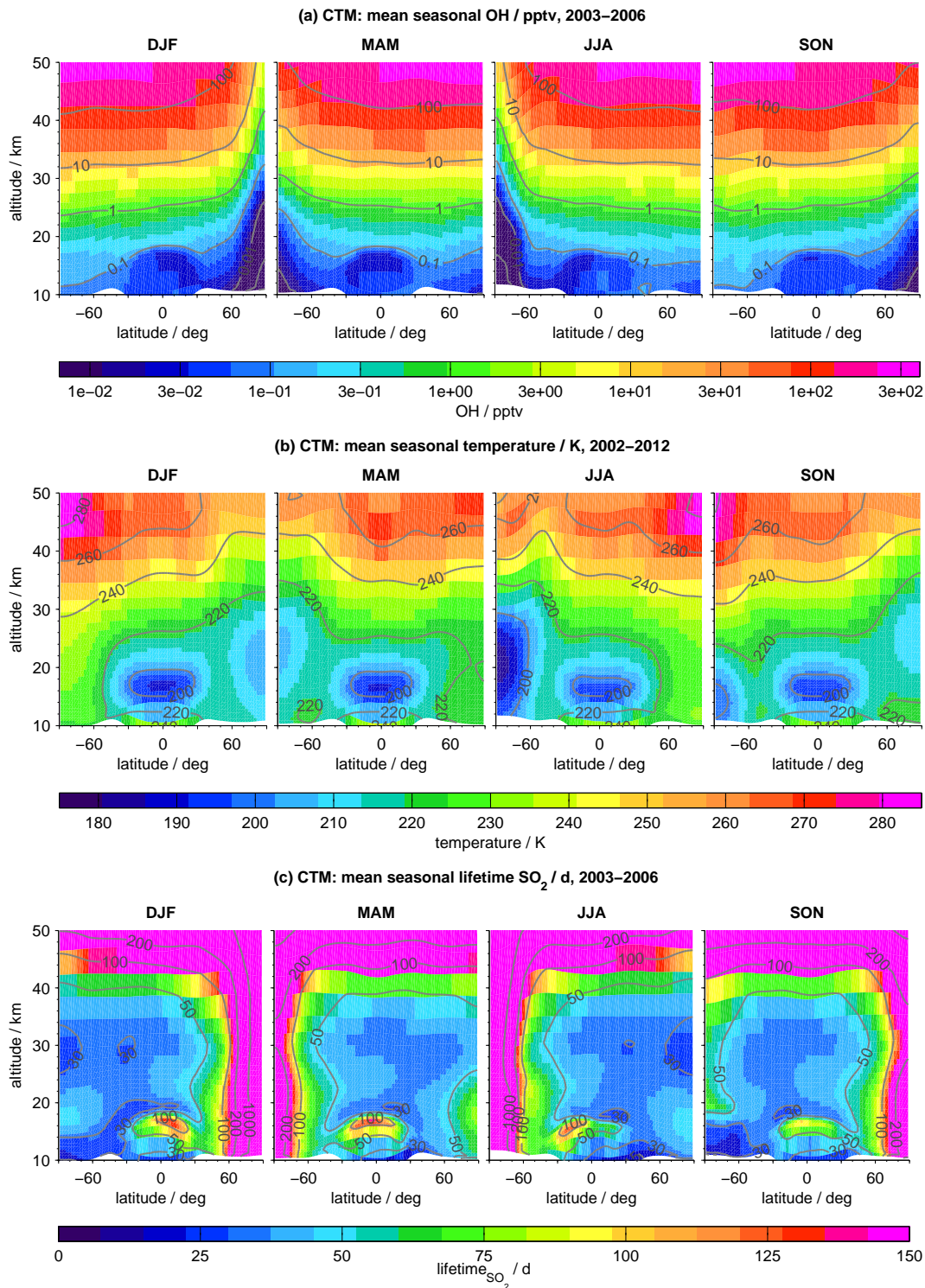
FIGURE 3.7: CTM: OH volume mixing ratios (a), temperatures (b) and SO_2 e-folding lifetimes (c). Seasonal vertically resolved meridional distributions per season. OH has been derived from a CTM full chemistry run (2003–2006). Temperatures (b) from the CTM are averaged over 2002–2012. Chemical SO_2 e-folding lifetimes are based on data in (a) and (b).

Höpfner et al. (2015) derived altitude-dependent SO_2 e-folding lifetimes (10–22 km) from MIPAS SO_2sgl, based on the measured decay of SO_2 masses after several volcanic eruptions. These are compared to CTM e-folding lifetimes of SO_2 in

Fig. 3.8. For the model vertical profiles are shown at the equator and 60° latitude. In the extra-tropics CTM lifetimes are remarkably larger, while in the tropics they are at the upper edge of lifetimes derived from MIPAS SO_2sgl. This difference can at least to a certain degree be explained by the fact that in the case of MIPAS transport and mixing processes are incorporated that can lead to reduced lifetimes. CTM lifetimes of SO_2 are chemical lifetimes due to oxidation with OH, which do not consider the mentioned processes. Following Höpfner et al. (2015), the lifetimes that were derived from MIPAS measurements are compatible with SO_2 lifetimes derived from other limb-sounders (Pumphrey et al., 2015). Compared to lifetime estimates from nadir sounders they are considerably larger, however, which Höpfner et al. (2015) attribute to the SO_2 detection limit and the dependence of decay times and instrument sensitivities on height.
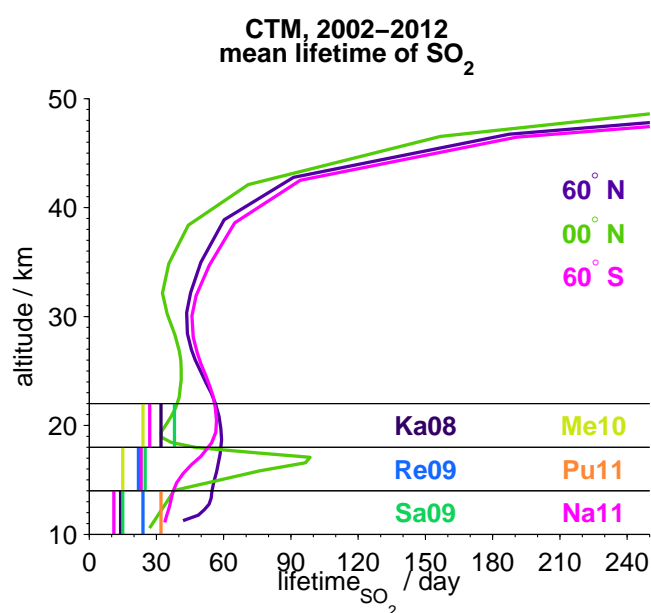
FIGURE 3.8: Profiles of chemical SO_2 e-folding lifetimes (CTM), in comparison to e-folding lifetimes of SO_2 by Höpfner et al. (2015), as derived from MIPAS SO_2sgl measurements. For MIPAS the lifetimes include removal by transport, while for the CTM only chemical loss by reaction with OH is considered. MIPAS: e-folding lifetimes derived for the eruptions of Kasatochi in 2008 (Ka08), Redoubt in 2009 (Re09), Sarychev in 2009 (Sa09), Merapi in 2010 (Me10), Puyehue-Cordón Caulle in 2011 (Pu11), and Nabro in 2011 (Na11), in the altitude regions 10–14, 14–18, and 18–22 km. CTM: annual mean chemical e-folding lifetimes at 0° and 60° (from Fig. 3.7).

3.4.5 H_2SO_4: equilibrium vapour pressure and aerosol density

In the CTM, all sulphur that is released from SO_2 by chemical reaction with OH forms H_2SO_4, which is transported by advection. Additionally the liquid part of H_2SO_4 is settled gravitationally. To determine the part of H_2SO_4 that remains in condensed phase, the H_2SO_4 equilibrium vapour pressure is calculated at each time step following the approach suggested by Ayers et al. (1980). All H_2SO_4 exceeding the current equilibrium partial pressure is assumed to reside completely in the liquid phase. Ayers et al. (1980) fitted a relationship for H_2SO_4 saturation vapour pressure over flat surfaces of sulphuric acid aqueous solutions to H_2SO_4 chemical potentials in liquid-phase, given by Giauque et al. (1960). The composition of

aqueous H_2SO_4 aerosol is determined following the scheme suggested by Carslaw et al. (1995), with the obtained binary solution density needed to derive terminal settling velocities of sulphate aerosol. Calculations of saturation vapour pressure and solution density are based on available CTM code that has been adapted for use in the sulphur module.

In the following equations p is the ambient pressure (in Pa), and T is the ambient temperature (in K). The pressure p_{atm} (in atm) is calculated as

$$p_{atm} = \frac{p}{101,300 \text{ Pa}} \tag{3.11}$$

and the partial pressure of a substance x (in atm) is $p_x = VMR \cdot p_{atm}$.

First, the mole fraction XSB of H_2SO_4 (in mole per mole) in the binary solution with water is calculated as:

$$XSB = \frac{-A - \sqrt{A^2 - 4B\left(47.004 - \frac{6,969.0}{T} - 4.6183 \cdot \ln(T) - \ln(p_{H_2O})\right)}}{2B} \tag{3.12}$$

with $A = -21.661 + 2,724.2/T$ and $B = 51.81 - 15,732.0/T$. In the sulphur module, H_2SO_4 that exceeds the H_2SO_4 saturation vapour pressure is hydrated based on the ambient water vapour loading, which is assumed to be 4.5 ppmv ($p_{H_2O} = 4.5 \cdot 10^{-6} \cdot p_{atm}$ atm). This value lies within MIPAS measurements for the lower / middle stratosphere (Wetzel et al., 2013). The weight fraction of H_2SO_4 in the aerosol ($W_{H_2SO_4}$, with the lower limit set to 41%) is calculated as

$$W_{H_2SO_4} = \frac{MS \cdot M_{H_2SO_4}}{1 + MS \cdot M_{H_2SO_4}} \tag{3.13}$$

with $MS = 55.51XSB/(1 - XSB)$ (in mole per kg of water) being the concentration of H_2SO_4 in the pure H_2SO_4–H_2O solution, and $M_{H_2SO_4}$ the molar mass of H_2SO_4 ($98.076 \cdot 10^{-3}$ kg mol^{-1}).

Following an approach suggested by Ayers et al. (1980), the H_2SO_4 equilibrium partial pressure (p_{eq,H_2SO_4}, in atm) is calculated as

$$p_{eq,H_2SO_4} = \exp\left(\frac{-10,156}{T} + 16.2590 - \frac{\mu_{H_2SO_4}}{R \cdot T}\right) \tag{3.14}$$

with the universal gas constant R (8.314 J K^{-1} mol^{-1}), and the chemical potential of H_2SO_4 ($\mu_{H_2SO_4}$; Eq. 3.15).

$$\mu_{H_2SO_4} = 4.184 \cdot (1.514 \cdot 10^4 - 286 \cdot (W_{H_2SO_4} - 40) +$$
$$1.080 \cdot (W_{H_2SO_4} - 40)^2 - \frac{3,941}{(W_{H_2SO_4} - 40)^{0.1}}) \tag{3.15}$$

All modelled H_2SO_4 per grid-cell for which $p_{H_2SO_4} \leq p_{eq,H_2SO_4}$ is assumed to be in the gas-phase, while exceeding H_2SO_4 is considered to be sulphate aerosol and undergoes gravitational settling.

The liquid solution density (ρ_{aero} in g cm^{-3}) of the binary solution of H_2SO_4–H_2O is calculated, considering the weight fractions of H_2SO_4 and H_2O in the solution, and their partial specific volumes. The weight fraction of H_2O in the binary solution is $W_{H_2O} = 1 - W_{H_2SO_4}$. The molar volumes of H_2SO_4 and H_2O are calculated as

$$V_{H_2O} = 2.393 \cdot 10^{-2} - 4.359 \cdot 10^{-5} \cdot T + 7.962 \cdot 10^{-8} \cdot T^2 \qquad (3.16)$$

and

$$\begin{aligned}
V_{H_2SO_4} = -0.199 + 1.396 \cdot 10^{-3} \cdot T - 2.021 \cdot 10^{-6} \cdot T^2 + \\
(0.517 - 3.054 \cdot 10^{-3} \cdot T + 4.505 \cdot 10^{-6} \cdot T^2) \cdot W_{H_2SO_4} + \\
(-0.301 + 1.840 \cdot 10^{-3} \cdot T - 2.722 - 6T^2) \cdot W_{H_2SO_4}^2 \quad (3.17)
\end{aligned}$$

The solution density (in g cm^{-3}) is $\rho_{aero} = 0.001/VM_{cal}$, with VM_{cal} defining the specific volume (sum of the partial specific volumes):

$$VM_{cal} = \frac{V_{H_2O} \cdot W_{H_2O}}{M_{H_2O}} + \frac{V_{H_2SO_4} \cdot W_{H_2SO_4}}{M_{H_2SO_4}} \qquad (3.18)$$

including the molar masses of H_2O and H_2SO_4 (18.0160 and 98.0800 g mol^{-1}). All model results presented in the following as sulphate aerosol are the H_2SO_4 model output reduced by its gas-phase fraction. Offline calculations of the partitioning into gas- and aqueous-phase of H_2SO_4 are similar to the ones presented in this section, using CTM pressure and temperature fields that correspond to the H_2SO_4 output.

Annual mean vertical distributions of zonally averaged H_2SO_4 equilibrium pressure, weight fraction of H_2SO_4, and H_2SO_4–H_2O aerosol density are presented in Fig. 3.9, together with ambient model temperature, air density and pressure. All data are based on CTM temperatures and pressures (2002–2012). The equivalent to the saturation partial pressure of H_2SO_4 in volume mixing ratios is presented, for better comparability to the measurements and model results shown in the following chapters. The saturation VMR of H_2SO_4 is extremely low below 30 km ($<$ 1 pptv), which indicates that H_2SO_4 can condense easily onto particles. Above 30 km the saturation VMR increases rapidly with altitude. The pattern of equilibrium VMR, as well as the patterns of weight fractions, and aerosol densities, generally reflect the temperature distribution, with a local minimum in the region of the Tropical Tropopause Layer, and increasing values in the stratosphere.

The extremely low saturation vapour pressures of H_2SO_4 at altitudes below $\sim$30 km indicate that it is of minor importance for the analysis of stratospheric sulphur at these altitudes that only liquid-phase H_2SO_4 is provided from MIPAS

measurements. As described in Sect. 2.2.1, the sulphate aerosol retrieved from limb-emission spectra measured by MIPAS is based on assumptions concerning aerosol density and weight fraction. These were chosen to be 1,700 kg m^{-3}, and 75 wt%. The altitude range that corresponds to these assumptions is indicated in Fig. 3.9. In the annual mean, the chosen aerosol density corresponds to a height of $\sim$24–26 km, and the chosen weight fraction is calculated for stratospheric altitudes of 18–24 km. Both air density and pressure, which are proportional to each other by $(R_d \cdot T)^{-1}$ (R_d: gas constant for dry air, T: temperature), decrease exponentially with increasing distance from the Earth surface.
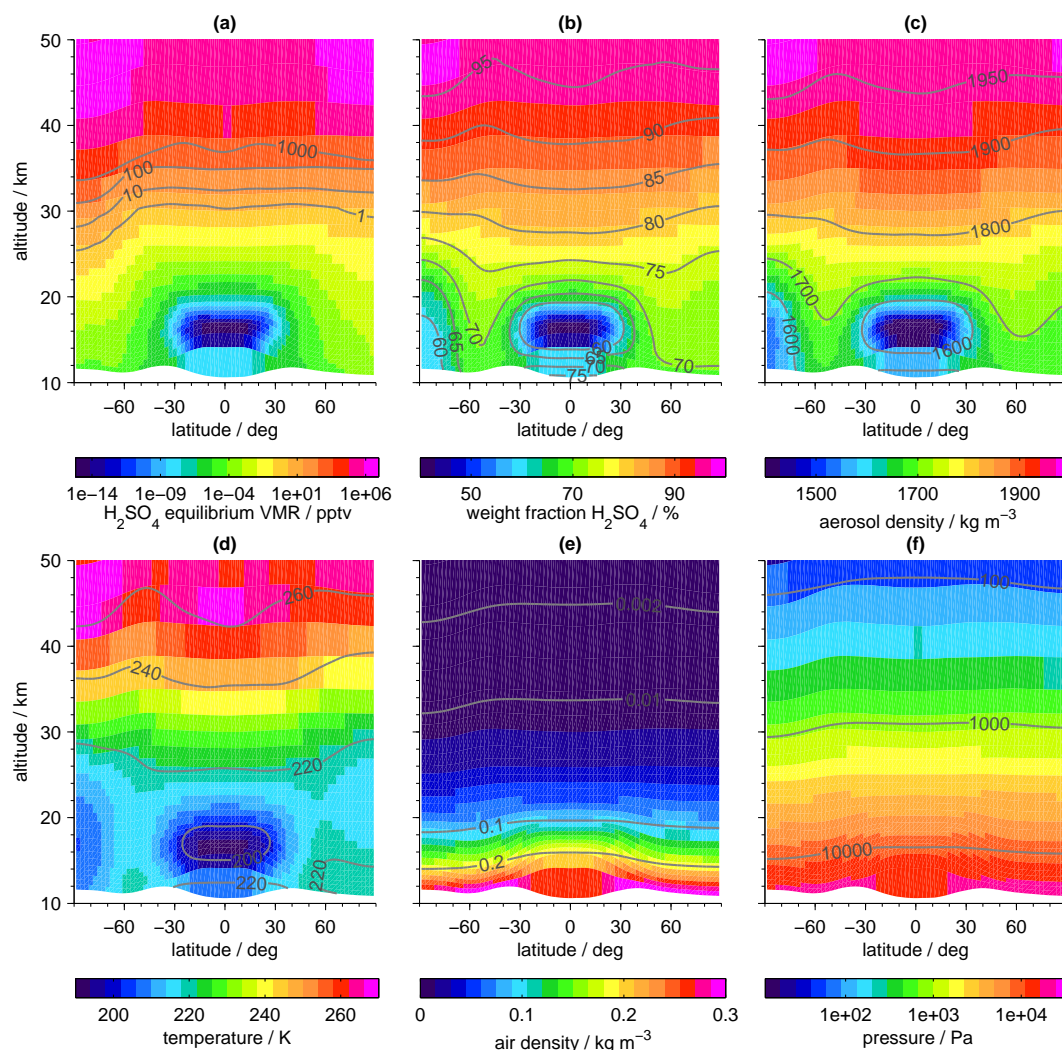
FIGURE 3.9: CTM: H$_2$SO$_4$ equilibrium volume mixing ratios (a), weight fractions of H$_2$SO$_4$ (b), H$_2$SO$_4$–H$_2$O aerosol densities (c), and ambient temperatures (d), air densities (e), and pressures (f). Annual mean vertical distributions of zonally averaged data, based on the average ambient model temperatures and pressures for 2002–2012. (a) and (f) shown in the logarithmic space.

3.4.6 H$_2$SO$_4$: sedimentation of sulphate aerosol

The model tracer H$_2$SO$_4$ contains both gas- and aqueous-phase H$_2$SO$_4$. Additionally to advective transport, the condensed part of the tracer is transported downwards by sedimentation, and can reach the grid box below, whenever the terminal settling

velocity is high enough. This velocity depends on the aerosol density determined in Sect. 3.4.5. Velocity calculations are based on equations given in Jacobson (1999). All sulphate aerosol is assumed here to be spherical. Sedimentation velocities (v, in m s^{-1}), which depend on the particle size and density, and the ambient pressure or density of air, are calculated using the ambient pressure p (in Pa), the ambient temperature T (in K), and

- $g = 9.801$ m s^{-2}, the gravitational acceleration

- $R_d = 287.05$ J K^{-1} kg^{-1}, the gas constant for dry air

- $k_B = 1.381 \cdot 10^{-23}$ m^2 kg s^{-2} K^{-1}, the Boltzmann's constant

- $m_{air} = 4.810 \cdot 10^{-26}$ kg molecule^{-1}, the mean mass of one air molecule

- r, the radius (fixed at a constant value, e.g., $r = 0.1 \cdot 10^{-6}$ m).

Even though the radius of sulphate aerosol varies throughout the atmosphere and in time (Deshler, 2008; Deshler et al., 2003), for simplification a constant 'effective sedimentation radius' (ESRad) is used in this study. Based on this ESRad, terminal fall velocities are determined, which are assumed here to be the average settling speed of aerosol particles that are variable in size. The effective sedimentation radius as used in this thesis shall not be mistaken as the effective radius that is defined as the ratio between the third and second moment of an aerosol size distribution (defined by Hansen and Travis, 1974), meaning the volume and surface area densities.

ρ_{air}, the density of air (in kg m^{-3}) that decreases exponentially with height, as pressure does, is:

$$\rho_{air} = \frac{p}{R_d \cdot T} \tag{3.19}$$

η_{air}, the temperature-dependent dynamic viscosity of air (in kg m^{-1} s^{-1}) is:

$$\eta_{air} \approx 1.8325 \cdot 10^{-5} \left(\frac{416.16}{T + 120} \right) \left(\frac{T}{296.16} \right)^{1.5} \tag{3.20}$$

v_{air}, the average thermal velocity of an air molecule (in m s^{-1}), which increases with rising temperature, is:

$$v_{air} = \sqrt{\frac{8 k_B T}{\pi m_{air}}} \tag{3.21}$$

λ_{air}, the mean free path of an air molecule (in m) that decreases with increasing air density, which provokes reduced distances between molecules, is:

$$\lambda_{air} = \frac{2 \eta_{air}}{\rho_{air} v_{air}} \tag{3.22}$$

Kn, the Knudsen number for air is:

$$Kn = \frac{\lambda_{air}}{r} \tag{3.23}$$

G_{Kn}, the Cunningham slip-flow correction is:

$$G_{Kn} = 1 + Kn \left[1.249 + 0.42 \cdot \exp \left(\frac{-0.89}{Kn} \right) \right] \qquad (3.24)$$

Given these values, and the aerosol density ρ_{aero} (in kg m^{-3}), the fall velocity v (m s^{-1}) for a spherical particle follows Eq. 3.25.

$$v = 2r^2 (\rho_{aero} - \rho_{air}) \frac{g}{9\eta_{air}} G_{Kn} \qquad (3.25)$$

Equation 3.25 is derived by equalising the equations for the vertical forces that act on particles (drag and gravity) (Jacobson, 1999). By scaling Stokes terminal velocity (first part of Eq. 3.25) with G_{Kn}, the formula becomes valid for both slip flow and Stokes flow. Slip flow denotes motion through air of particles smaller than λ_{air}, while Stokes flow corresponds to larger particles. As in the present study particles are sufficiently small, no Reynolds number-dependent iteration needs to be performed to derive the final fall velocity. Such an iteration applies to particles with diameters > 20 µm (Jacobson, 1999). For the size range addressed here for sulphate aerosol during non-volcanic and even volcanic periods, the assumption of sphericity is valid (Jacobson, 1999).

The part of sulphate aerosol that is removed from a certain grid-box by sedimentation is added to the grid-box below. This fraction depends on the available time, downward speed of the particle, and thickness of the grid-box. The more time is available, the faster the velocity of the falling aerosol, and the smaller the path it has to cover, the higher the fraction $frac = v \cdot DT_0 / tn$ of H$_2$SO$_4$, which is removed from a grid-box during one model time step. The thickness tn (in m; Eq. 3.26) of the grid-box from which sulphate aerosol is removed is derived by aid of the barometric formula for height.

$$tn = \frac{R_d T}{g} \ln \left(\frac{p_{lev}}{p_{lev-1}} \right) \qquad (3.26)$$

with p_{lev} and p_{lev-1} being the pressures at the grid-box interfaces (model levels are numbered from high to low altitudes).

Vertical profiles of sedimentation velocities are shown for various ESRad (0.01–10 µm) in Fig. 3.10. They are based on the annual mean CTM temperatures and pressures (2002–2012), and the equations that were introduced above. Further, they include aerosol densities as derived in the previous section (3.4.5). Profiles are presented for the equator and the poles. The smaller the particle, the longer it takes for the particle to fall a certain distance. Settling velocities generally show a logarithmic increase with altitude in the stratosphere, and are higher at the equator, compared to the poles. The rapid increase of terminal settling velocities is of minor relevance for sulphate aerosol at altitudes above approximately 30–35 km, due to the low H$_2$SO$_4$ saturation partial pressures at altitudes below, which result in primarily liquid-phase H$_2$SO$_4$. The presented sedimentation velocities compare well to values given in Mills (1996). As an example, a particle with a radius of 0.1 µm would settle with a velocity of 0.0034 cm s^{-1} (2.9 m d^{-1}) at 20 km at equatorial latitudes, and

0.0190 cm s^{-1} (16.4 m d^{-1}) at 30 km. A particle with a radius of 0.5 μm would settle faster, with velocities of 0.0210 cm s^{-1} (19.0 m d^{-1}) at 20 km, and 0.0990 cm s^{-1} at (85.5 m d^{-1}) 30 km.
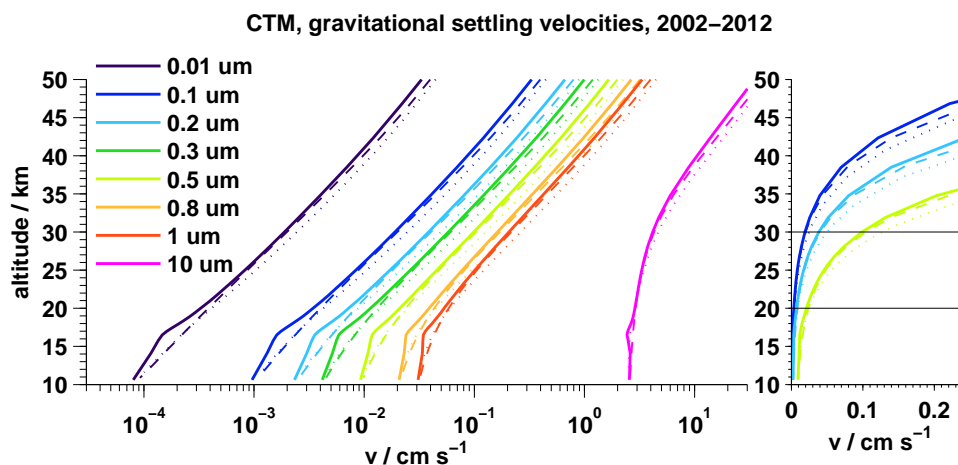
FIGURE 3.10: CTM: vertical profiles of terminal settling velocities if sulphate aerosol for various particle sizes. Solid lines are at 0°N, dashed lines at 90°N, and dotted lines at 90°S. Calculations based on the average annual ambient model temperatures and pressures for 2002–2012 (Fig. 3.9). Left panel: abscissae in logarithmic scale. Right panel: abscissae in linear scale.

3.4.7 H$_2$SO$_4$: sensitivity of partitioning and sedimentation to atmospheric H$_2$O and aerosol density

The equations for partitioning of H$_2$SO$_4$ into gas- and liquid-phase, and aerosol composition, were given in Sect. 3.4.5. For the terminal settling velocities of modelled sulphate aerosol calculations were presented in the previous section (3.4.6). Here, the sensitivity of the partitioning, aerosol composition, and settling velocities to the prescribed constant ambient water vapour loading (set to 4.5 ppmv) and to the online calculated aerosol densities are analysed.

In Fig. 3.11 vertical profiles of the H$_2$SO$_4$ equilibrium partial pressure (as VMR), weight fraction of H$_2$SO$_4$ in the aqueous solution, and aerosol density are given for varying water vapour loading (2.5, 4.5, and 7.5 ppmv). Furthermore, vertical profiles of resulting settling velocities are shown in Fig. 3.12. Uncertainties in the presumed water vapour loading are shown to be of minor impact on the model results. Changes in the sedimentation velocities are marginal. Only the partitioning, and therefore the part of H$_2$SO$_4$ that sediments, is influenced. The consequences of the change in partitioning are weak, however. When the H$_2$O vapour pressure is increased, reducing the weight fraction of H$_2$SO$_4$ in the aerosol, the transition region between dominating liquid-phase H$_2$SO$_4$ at lower altitudes and primarily gas-phase H$_2$SO$_4$ at higher altitudes, is slightly shifted upwards. The decrease of H$_2$SO$_4$ in the aerosol results in lower aerosol densities, which influences the settling velocities, but not the H$_2$SO$_4$ equilibrium pressure.

As part of the sulphur module, an online calculation of the binary solution density for sulphate aerosol has been implemented. The particle size and aerosol density affect the speed of the falling aerosol. This dependency is presented as terminal settling velocity profiles for various ESRad and aerosol densities in Fig. 3.12.

The chosen aerosol densities are the online calculated values, and constant densities of 1,700 kg m^{-3}, as used in the new MIPAS aerosol data set. Additionally, this latter density has been modified by $\pm$20% (2,040 and 1360 kg m^{-3}). At altitudes below ~22 km, an aerosol density of 1,700 kg m^{-3} leads to slightly faster settling, compared to online calculated values, while an opposite behaviour is observed at altitudes above. Considerably greater are differences when prescribing aerosol densities of 2,040 kg m^{-3}, or 1,360 kg m^{-3}. A reduced density, which corresponds to less H_2SO_4 in the aerosol, leads to slower sedimentation velocities, which results in weaker removal of sulphate aerosol from the stratosphere. These results indicate that it is more important for the simulation of sulphate aerosol to incorporate a good estimate of the solution density than of the ambient water vapour.
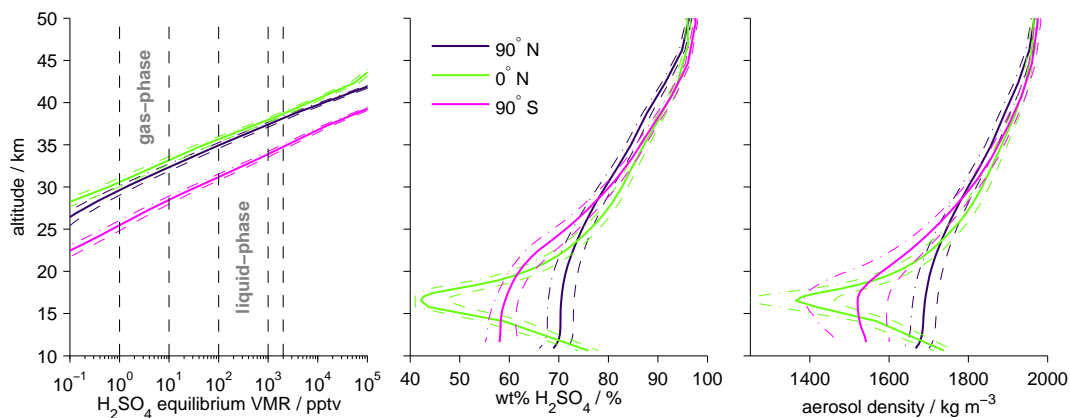
FIGURE 3.11: Sensitivity of predicted H_2SO_4 equilibrium partial pressure (as VMR; a), weight fraction of H_2SO_4 (b), and the H_2SO_4–H_2O aerosol density (c), on the prescribed H_2O vapour pressure. Mean annual profiles (2002–2012) at 90°N, 0°S, and 90°N, for 4.5 ppmv (solid line, as used in this study), and for 2.5 ppmv (dashed lines), and 7.5 ppmv (dashed-dotted lines). Calculations are based on the average ambient model temperatures and pressures for 2002–2012. (a) shown in logarithmic scale, with the abscissae limited to relevant VMRs. Indicated by dashed vertical lines are 1, 10, 100, 1,000, and 2,000 pptv (left to right).
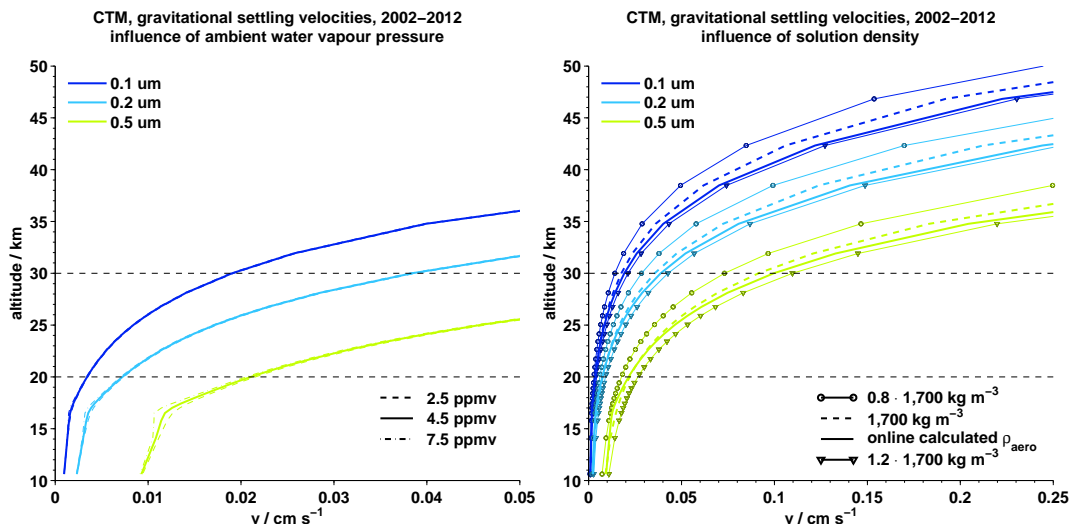
FIGURE 3.12: CTM: sensitivity of terminal settling velocities on the prescribed H_2O vapour pressure (left), and aerosol solution density (right). Mean annual velocity profiles (2002–2012) for ESRad of 0.1, 0.2, and 0.5 µm (colour coded). (left) for ambient H_2O of 4.5 ppmv (used in this study), 2.5 ppmv (right lines), and 7.5 ppmv (left lines). (right) for varying aerosol densities, as calculated online, and for $1,700\ kg\ m^{-3}$, and $0.8 \cdot 1,700\ kg\ m^{-3}$, and $1.2 \cdot 1,700\ kg\ m^{-3}$. Note the differing abscissae limits. All calculations are based on the average ambient model temperatures and pressures for 2002–2012.

3.5 Short overview of analysed CTM data sets

In this work several CTM simulations for the sulphur species carbonyl sulphide, sulphur dioxide, and sulphuric acid are studied. Here, a short survey of the simulations is presented, together with the identifiers of the simulations used throughout this work. Additionally given are the main sections of this thesis in which the simulation results are studied.

- Volcanic sulphur 2002–2012 (Chap. 4 to 6). The initial fields and bottom boundaries for SO_2 and H_2SO_4 are set to 0 pptv. The only sulphur sources included are SO_2 injections by various volcanoes per simulation (single injections at 12 UTC). Injected sulphur dioxide is added to the already existing SO_2. The sulphur dioxide is transformed to H_2SO_4 by oxidation with hydroxyl radicals. Liquid-phase H_2SO_4 is settled gravitationally, with effective sedimentation radii (ESRad) of 0.2, or 0.5 µm.

  - 'B15':
    Emitted SO_2 based on Brühl et al. (2015). SO_2 VMR fields that are added to the modelled SO_2 on 98 days are presented in Fig. A.1 to A.4.

  - 'G17':
    Volcanic SO_2 masses for 30 days partly based on Höpfner et al., 2015, but adapted in terms of injected mass and injection altitude ranges, for a better agreement between modelled SO_2 and MIPAS SO_2sgl. SO_2 masses for three altitude ranges are distributed homogeneously to the air mass within each altitude region, in the column of grid cells that include the

location of the specific volcano. SO_2 masses and altitude regions are given in Table A.1.

- Volcanic eruptions of Kasatochi (2008) and Sarychev (2009) (Sect. 4.3). As G17, but individual simulations per volcanic eruption.

    - **'CKa08'** (Sect. 4.3):
      Volcanic eruption of Kasatochi (7 Aug 2008; 52.2°N/175.5°W). Simulations without sedimentation of sulphate aerosol, and sedimentation with an ESRad of 0.1, 0.5, and 1 µm.

    - **'CSa09'** (Sect. 4.3):
      Volcanic eruption of Sarychev (12 Jun 2009; 48.1°N/153.2°E). Simulations without sedimentation of sulphate aerosol, and sedimentation with an ESRad of 0.1, 0.5, and 1 µm.

    - **'CKa08$_{switch:loc}$'** (Sect. 4.3.4):
      SO_2 mass from the eruption of Ka08 injected at the location of Sarychev (7 Aug 2008; 48.1°N/153.2°E). ESRad: 0.5 µm.

    - **'CSa09$_{switch:loc}$'** (Sect. 4.3.4):
      SO_2 mass from the eruption of Sa09 injected at the location of Kasatochi (12 Jun 2009; 52.2°N/175.5°W). ESRad: 0.5 µm.

    - **'CKa08$_{switch:loc\&day}$'** (Sect. 4.3.4):
      SO_2 mass from the eruption of Ka08 injected at the location and date of the Sarychev eruption (12 Jun 2009; 48.1°N/153.2°E). ESRad: 0.5 µm.

    - **'CSa09$_{switch:loc\&day}$'** (Sect. 4.3.4):
      SO_2 mass from the eruption of Sa09 injected at the location and date of the Kasatochi eruption (7 Aug 2008; 52.2°N/175.5°W). ESRad: 0.5 µm.

- Non-volcanic sulphur 2002–2012. Simulations with OCS as the only sulphur source for non-volcanic background. OCS input to the CTM is prescribed by a bottom boundary. Included in these simulations are OCS that is photolysed and forms SO_2, which is then oxidised to form H_2SO_4. Sulphate aerosol undergoes sedimentation with an ESRad of 0.1, or 0.2 µm. All initial fields are based on model spin-up, and bottom boundaries for SO_2 and H_2SO_4 are set to 0 pptv.

    - **'BGO'** (Chap. 5 and 6):
      Bottom boundary of OCS with meridional and intra-annual, but no inter-annual variability, which has been derived from MIPAS measurements.

    - **'CObb$_{trop}$'** (Sect. 5.1.3): Same bottom boundary as in BGO in the tropics, but with 0 pptv OCS prescribed polewards of 30°.

    - **'CObb$_{const}$'** (Sect. 5.1.3): Constant bottom boundary for OCS (mean over tropical bottom boundary from BGO).

- Analysis of a pattern of downward transport from the tropics towards higher latitudes seen in MIPAS sulphate aerosol (Sect. 5.2.2). The only sulphur source is sulphate aerosol, which is settled gravitationally, with an ESRad of 0.2 µm. The initial field and bottom boundary of H_2SO_4 are set to 0 pptv.

    – **'CTM$_{sglin}$':**
      The only sulphur source is sulphate aerosol from a single injection in the tropics, at around 27–30 km. Individual simulations for injections in January, April, July, and October.

    – **'CTM_MTAR':**
      The only sulphur source is sulphate aerosol from a variable source in the tropics, at around 27–30 km. Input is based on MIPAS measurements.

    – **'CTM_MTAC':**
      As CTM_MTAR, but for a constant source (mean over the source used in CTM_MTAR).

4 Stratospheric sulphur during volcanically perturbed periods

The major variability of the stratospheric sulphur loading is caused by volcanic eruptions (e.g., Höpfner et al., 2015 for SO_2; Kremser et al., 2016 for sulphate aerosol), which can directly inject sulphur dioxide into the stratosphere (e.g., Vernier et al., 2011b). Low tropopause heights and high explosivity of volcanic eruptions facilitate the entrance of volcanic sulphur into the stratosphere. This chapter aims on giving an overview of volcanic influence on SO_2 and sulphate aerosol, as seen in the MIPAS data sets of SO_2sgl and sulphate aerosol. Additionally, the consistency between the MIPAS data sets in terms of sulphur mass and sulphur distribution is analysed in a case study on the two Northern hemisphere mid-latitude eruptions of Kasatochi (7 Aug 2008) and Sarychev (Jun 2009). Parts of this case study are published in Günther et al. (2018).

4.1 Volcanic MIPAS SO_2 and sulphate aerosol 2002–2012

The distributions of SO_2 and sulphate aerosol, as retrieved from MIPAS measurements (2002–2012), are presented in Figs. 4.1 and 4.2. Figure 4.1 shows vertically resolved time series as 30° latitude bins, while in Fig. 4.2 the same data are presented as latitudinally resolved time series at various altitudes (10–24 km). In both data sets, strongest variability is caused by periodic volcanic eruptions with varying intensity and vertical extent. The volcanic impact is most pronounced in the tropics and Northern hemisphere.

In the following, the most important volcanic eruptions, as seen in the MIPAS data, are given together with the most affected areas and altitude regions, eruption dates and locations (locations see also Fig. 4.3):

- **Northern hemisphere mid- to high-latitudes** (30°N–60°N, and 60°N–90°N), at altitudes between ∼10–20 km:

    - *Kasatochi:* 07 Aug 2008, 52.2°N/175.5°W

    - *Sarychev:* 12 Jun 2009, 48. N/153.2°E

    - *Nabro:* 12 Jun 2011, 13.4°N/41.7°E

- **Tropics** (30°S–30°N), at altitudes above ∼16 km:

    - *Manam:* 27 Jan 2005, 4.1°S/145.0°E

    - *Soufrière Hills:* 20 May 2006, 16.7°N/62.2°W

    - *Rabaul:* 07 Oct 2006, 4.3°S/151.1°E

- **Southern hemisphere mid- to high-latitudes** (30°S–60°S, and 60°S–90°S), at altitudes below ~14/15 km:

    - *Puyehue-Cordón Caulle:* 04 Jun 2011, 40.6°S/72.1°W

As the volcanically emitted sulphur dioxide is converted into stratospheric sulphate aerosol, if not removed too rapidly from the stratosphere, the distributions of the two species show strong similarities. Differences in the patterns arise especially from the fact that SO_2 has a relatively short lifetime in the stratosphere, compared to sulphate aerosol. While SO_2 has an e-folding lifetime of only few weeks (e.g., Höpfner et al., 2015 and references therein), the lifetime of stratospheric aerosol is about one year (Rasch et al., 2008). The lifetime of H_2SO_4 depends on advective removal and gravitational sedimentation, which in turn depends on the particle size and aerosol density. The influence of the particle size will be analysed in more detail in Sect. 4.3.1 and 4.3.2. Additionally, as sulphate aerosol is formed from sulphur dioxide over time, the curve of in- and decrease of H_2SO_4 is generally flatter and broader, compared to SO_2, and the curve peaks at a later point in time.

In the Northern hemisphere the eruptions of Kasatochi in 2008 and Sarychev in 2009 (Sect. 4.3), and the eruption of Nabro in 2011 produced the strongest enhancements in the MIPAS measurements of SO_2 and sulphate aerosol. Even though Nabro is a tropical volcano (13.4°N), a major part of the emitted sulphur affected the entire Northern hemisphere.

In the tropics the strongest signals in the measurements of SO_2 are due to a series of eruptions that started in January 2005 (Manam), and continued in May and October 2006 (Soufrière Hills and Rabaul). The first two eruptions produced a pronounced signal in the MIPAS SO_2sgl measurements at altitudes up to 22–23 km, which disappeared after few months. The retrieved aerosol, however, is affected for many months, and a distinct pattern of upward transport can be seen. A similar pattern of uplift in the tropics has been observed in aerosol extinction ratios presented in Vernier et al. (2011b). Extinction ratios are based on measurements performed with the Stratospheric Aerosol and Gas Experiment II (SAGE II), the Cloud-Aerosol Lidar and Infrared Pathfinder Satellite Observations (CALIPSO) and the Optical Spectrograph and InfraRed Imager System (OSIRIS) onboard Odin.
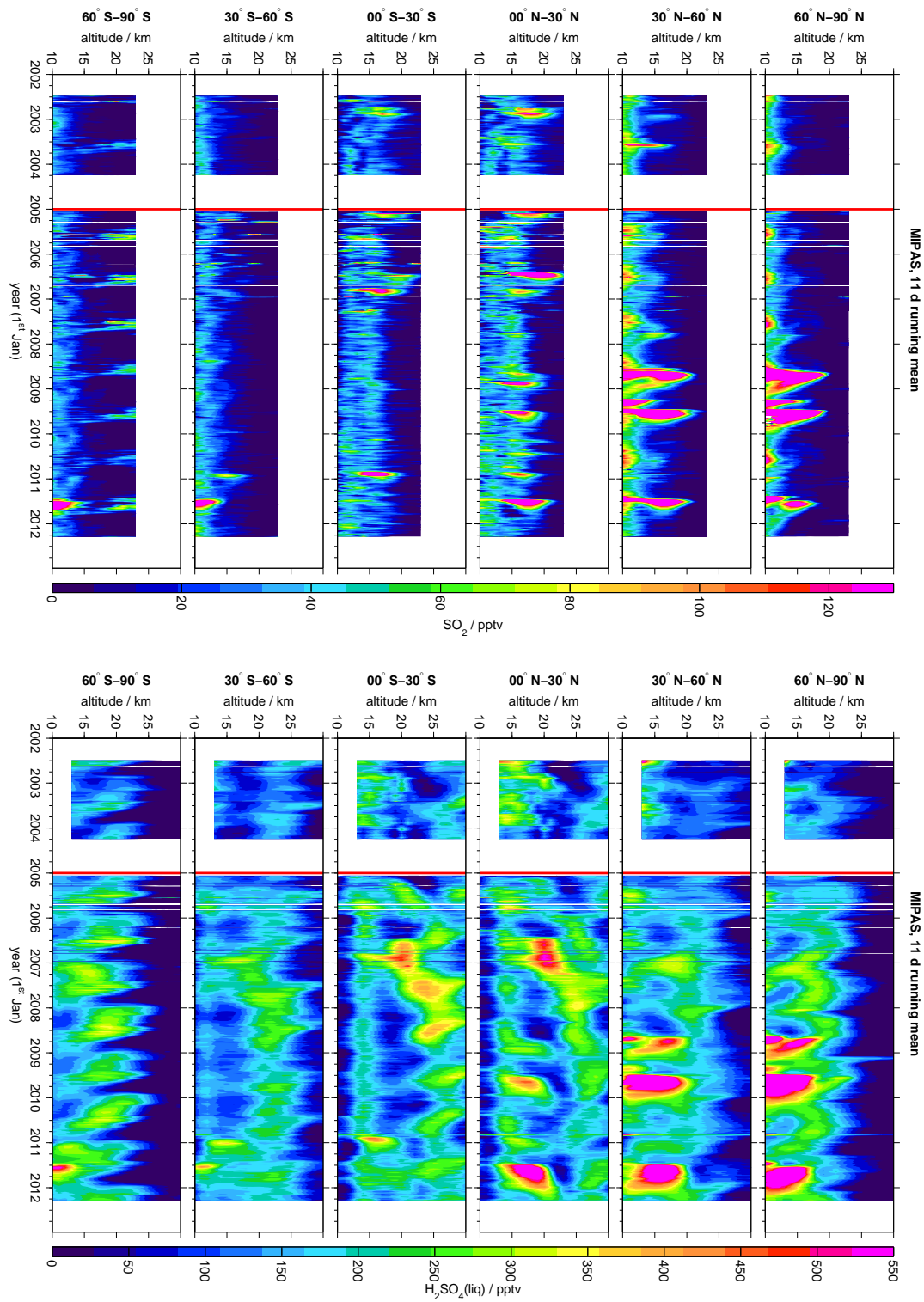
FIGURE 4.1: [Figure rotated by 90°] Time series (2002–2012) of MIPAS SO$_2$sgl (left) and sulphate aerosol (right). Vertically resolved volume mixing ratios for 30° latitude bins (area weighted averages; 11 d running means). A vertical red line indicates the transition between measurement periods P1 and P2. Values exceeding the colour-scales are assigned with the limiting values.
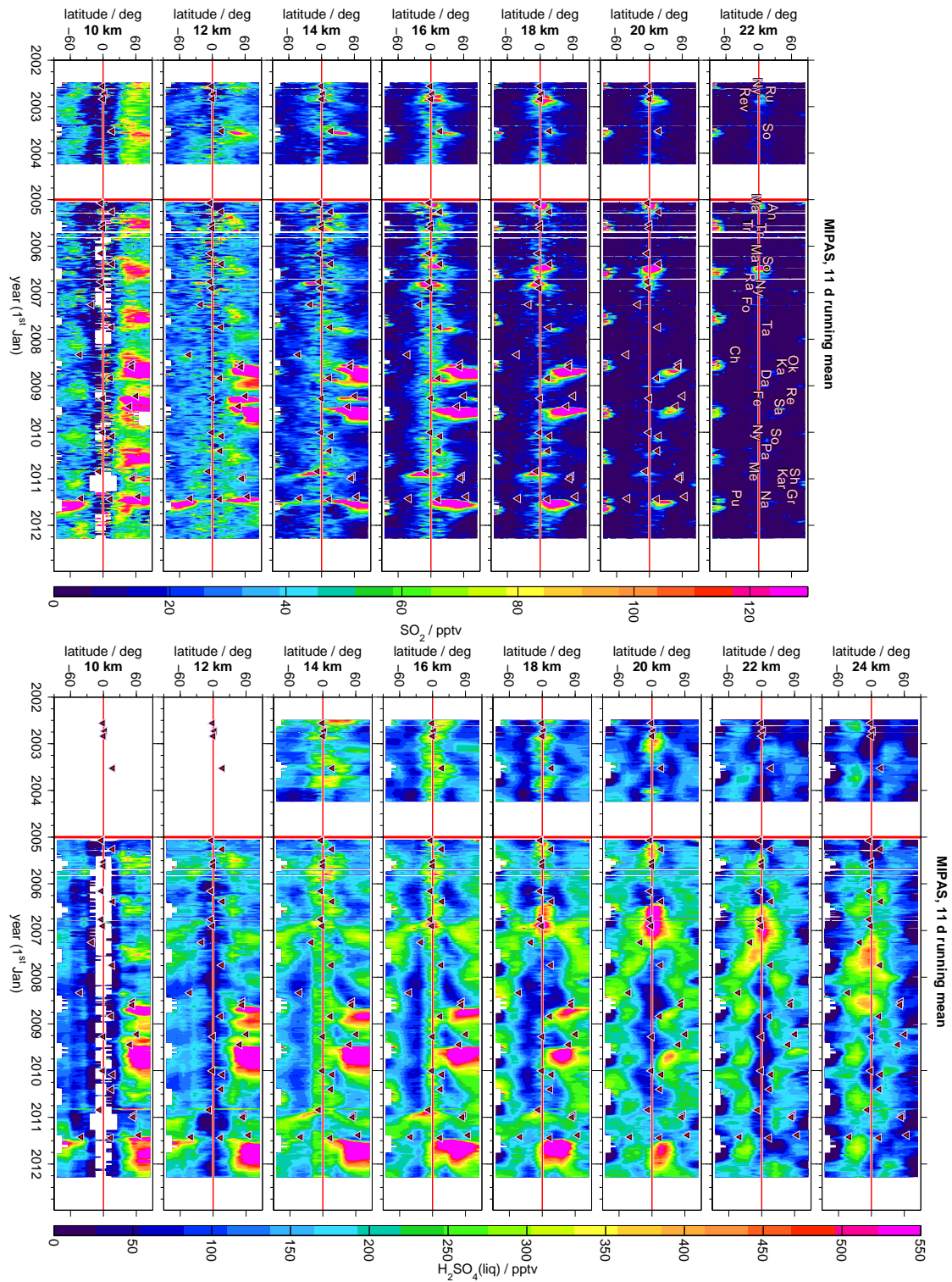
FIGURE 4.2: [Figure rotated by 90°] Time series of MIPAS SO$_2$sgl (left) and liquid-phase H$_2$SO$_4$ (right) volume mixing ratios (2002–2012) at various altitudes (10–24 km). Latitudinally resolved 11 d running means for 10° latitude bins. Triangles indicate volcanic eruptions (abbreviations in Table A.2). Values exceeding the colour-scales are assigned with the limiting values.
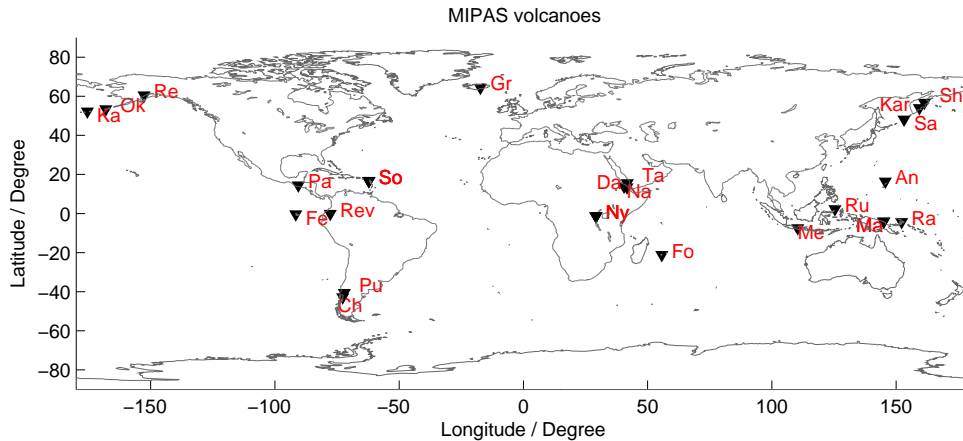
FIGURE 4.3: Locations of the volcanoes seen in Fig. 4.2. For the full names and eruption dates (2002–2012) see Table A.2.

4.2 Simulated volcanic sulphur 2002–2012

MIPAS measurements of SO_2 and liquid-phase H_2SO_4 show strong enhancements caused by various volcanic eruptions. In this section simulations of volcanic sulphur dioxide and sulphate aerosol are presented for the entire MIPAS measurement period (2002–2012). These simulations are based on two data sets of volcanic SO_2, as provided by Höpfner et al. (2015), and Brühl et al. (2015).

Höpfner et al. (2015) provided a list of volcanic SO_2 masses for 30 eruption days, as observed by MIPAS (SO_2sgl). They derived estimates of volcanic SO_2 masses for three altitude regions (10–14, 14–18, 18–22 km) by exponential extrapolation of the SO_2sgl masses back to the eruption day. This method has been applied in consequence of the underestimation of SO_2sgl masses in the first month after an eruption, connected primarily to sampling artefacts, caused by masking of measurements by volcanic ash (Höpfner et al., 2015). The derived SO_2 masses have rather large uncertainties, which depend on the fit period.

Brühl et al. (2015) provided a list of volcanic SO_2 masses injected into the stratosphere for 98 eruption days during the MIPAS measurement period. Basis for the SO_2 masses in Brühl et al. (2015) are measurements performed with instruments aboard several satellites. These are the Ozone Monitoring Instrument (OMI) and Total Ozone Mapping Spectrometer (TOMS), for which data are included in a SO_2 database by NASA (National Aeronautics and Space Administration, `http://so2.gsfc.nasa.gov`), MIPAS (SO_2sgl), the Microwave Limb Sounder (MLS; Pumphrey et al., 2015), the Smithsonian database (`http://www.volcano.si.edu`) and the Stratospheric Aerosol and Gasses Experiment (SAGE II; update of Thomason and Peter, 2006; Thomason et al., 2008). For the present study, C. Brühl (MPIC) provided the input dat of SO_2 volume mixing ratios, as used for simulations presented in Brühl et al. (2015). This input consists of latitudinally and vertically resolved distributions of SO_2 VMRs (no zonal variation), on the vertical and horizontal model grid used in their study. Simulations in their study were performed with the ECHAM/MESSy Atmospheric Chemistry (EMAC) model, which uses hybrid pressure coordinates as

vertical grid and a different horizontal resolution than the CTM. Data were interpolated to the CTM grid for further use. The vertical interpolation from pressure levels to isentropic levels considers the CTM pressure fields at the eruption day and is performed in the logarithmic space. In Fig. A.1 to A.1 the input data are presented as meridional distributions of SO_2 volume mixing ratios per CTM level and eruption day.

The CTM simulations of volcanic sulphur for 2002–2012 are based on the two data sets of volcanic emissions described above. They do not include any other sulphur sources than volcanically injected SO_2. The first data set (Höpfner et al., 2015) has been adapted in terms of injected masses and injection heights, to improve the agreement between measured (SO_2sgl) and modelled SO_2, based on various simulations with differing SO_2 masses and injection altitudes. The modified data set ('G17') is presented in Table A.1. Simulations with the second data set (based on Brühl et al., 2015) are named 'B15' throughout this thesis. Simulation results of modelled SO_2 and sulphate aerosol (ESRad 0.2 and 0.5 μm) are presented in Fig. 4.4 to 4.6, as time series of vertically resolved zonal means over 30° latitude bins. Simulations G17 and B15 show relatively large differences. These are especially caused by the higher eruption frequency considered in B15 (98), compared to G17 (30). Both sulphur species show values close to zero over long periods of time when including only 30 volcanoes, which is not true for B15. Even though the lifetime of SO_2 is short compared to sulphate aerosol, most of the data (2002–2012) are influenced by volcanoes for both species in simulation B15. Simulated sulphate aerosol is clearly influenced by the chosen effective sedimentation radius, with higher aerosol loading and longer residence times for the smaller ESRad. Smaller aerosol particles that settle less rapidly, can reside in the stratosphere over longer periods, and tropical aerosol is simulated to be lifted in the tropical pipe (Fig. 4.5). The simulations of volcanic sulphur will be further discussed in the following chapters (Chap. 5 and 6).
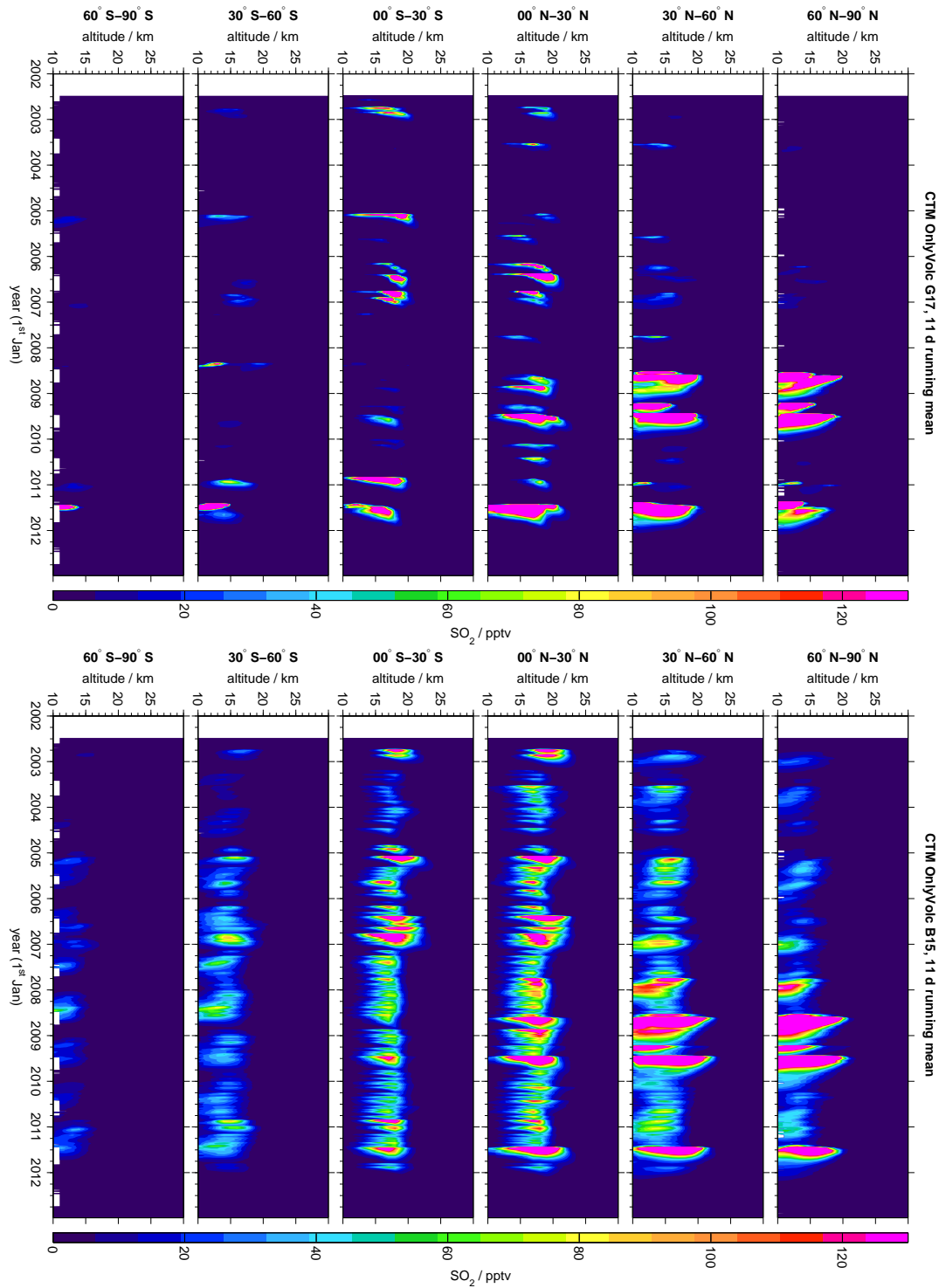
FIGURE 4.4: [Figure rotated by 90°] Time series of volcanic SO$_2$ volume mixing ratios (2002–2012) from CTM simulations G17 (left) and B15 (right). Vertically resolved time series for 30° latitude bins (area weighted averages). The only sulphur source are volcanic emissions of SO$_2$ (background: 0 pptv). All data are 11 d running means. Values exceeding the colour-scales are assigned with the limiting values.
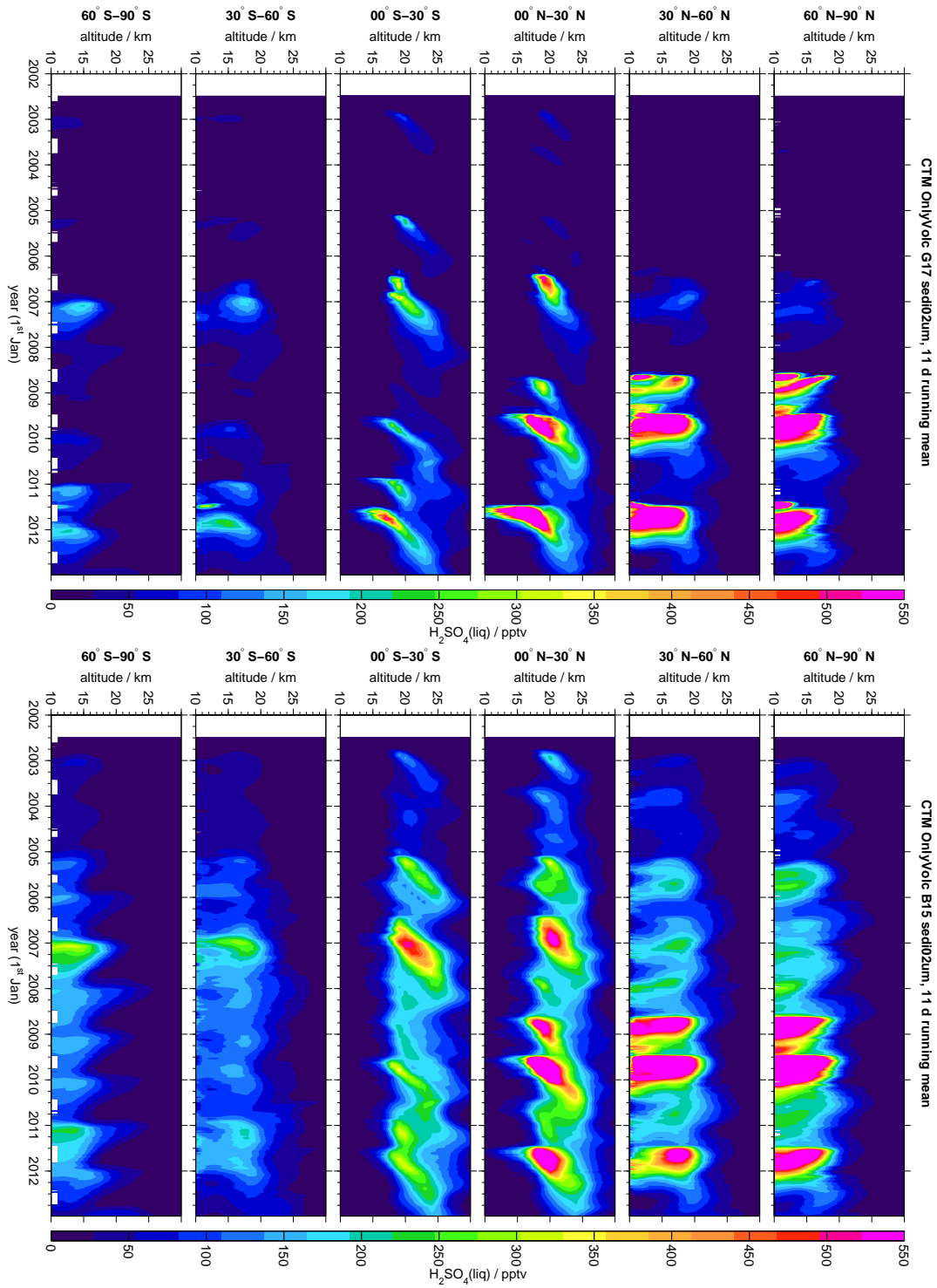
FIGURE 4.5: [Figure rotated by 90°] As Fig. 4.4, but for modelled volcanic sulphate aerosol (ESRad = 0.2 μm).
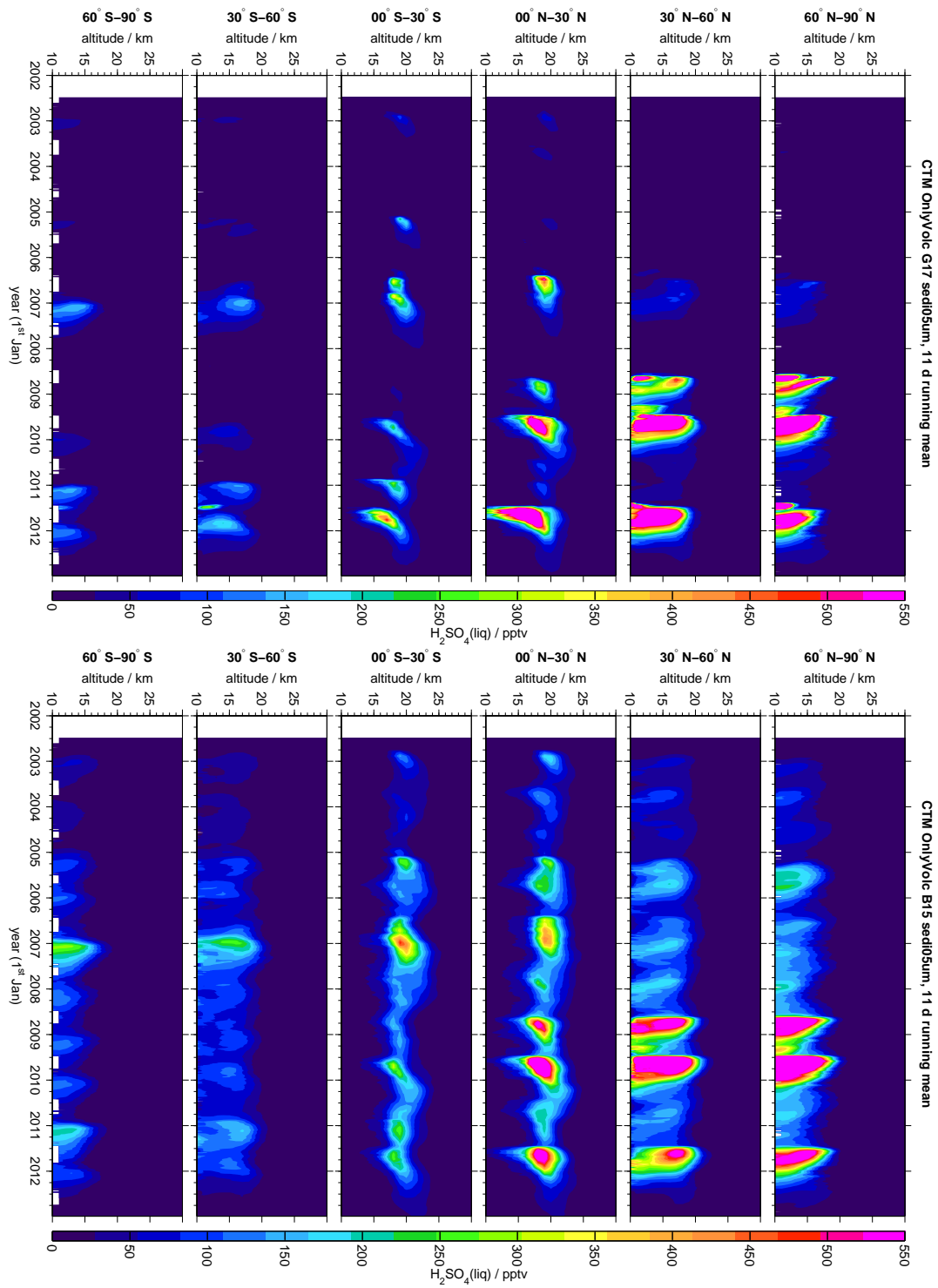
FIGURE 4.6: [Figure rotated by 90°] As Fig. 4.4, but for modelled volcanic sulphate aerosol (ESRad = 0.5 μm).

4.3   Volcanic eruptions of Kasatochi (Aug 2008) and Sarychev (Jun 2009)

In this section the MIPAS data set of SO_2sgl and the new MIPAS aerosol data set are studied for two volcanic eruptions. These are the eruptions of Kasatochi on the 07 Aug 2008 (52.2°N/175.5°W) and Sarychev on the 12 Jun 2009 (48.1°N/153.2°E). The two volcanic eruptions had a strong impact on the stratospheric sulphur loading of the Northern hemisphere. The volcanoes are located relatively close to each other, with a latitudinal distance of only 456 km and an absolute distance of 2,256 km. Furthermore, both volcanoes erupted during boreal summer.

One of the main purposes of this case-study is to analyse whether the two MIPAS data sets are consistent with each other, both in terms of quality and quantity. In Sect. 4.3.1 the measured enhancements caused by the two volcanoes are studied in terms of sulphur mass. With the aid of CTM simulations it is possible to assess if the amplitude of increased sulphur and its evolution with time are in agreement for the two data sets. Additionally, the predominant removal processes of SO_2 and liquid-phase H_2SO_4 are studied with the help of the measurements and model simulations. The transport patterns of the volcanically injected sulphur are analysed in Sect. 4.3.2 to 4.3.4, and the e-folding lifetime of volcanic stratospheric sulphur after the eruptions is derived in Sect. 4.3.5.

As the main focus lies on the volcanic sulphur per eruption, no other sulphur sources but volcanic SO_2 from one eruption are included in the simulations. The model-background and bottom boundary are set to zero for both species and do therefore not necessitate model spin-up. All simulations shown in the case-study start on the last day of the month preceding the eruption, and are restricted to 365 d.

4.3.1   Sulphur mass in the Northern hemisphere extra-tropics

The sulphur mass contained in sulphur dioxide and sulphate aerosol as derived from MIPAS measurements is compared to model simulations for the eruptions of Kasatochi in 2008 and Sarychev in 2009. As the volcanic sulphate aerosol is formed from the emitted SO_2, good agreement between measured and simulated sulphur dioxide is essential to study, with the help of the CTM, whether the new data set of MIPAS sulphate aerosol is qualitatively and quantitatively consistent with MIPAS SO_2sgl.

Various volcanically injected SO_2 masses and injection height limits were tested to acquire model results that match the measured SO_2. Analyses of the match were based on time series of SO_2, with comparisons starting about one month after the respective eruption, as SO_2 masses tend to be underestimated by MIPAS SO_2sgl up to about one month after the eruption, primarily due to masking of measurements by volcanic ash (Höpfner et al., 2015). Simulations presented in the following are based on SO_2 masses and injection heights that resulted in best agreement. In the case of Kasatochi the best match for injected SO_2 is achieved with the lower limits given by Höpfner et al. (2015). As noted in the previous section (4.2), Höpfner et al. (2015) provided estimates of volcanic sulphur dioxide masses from MIPAS SO_2sgl measurements for three altitude regions covering 10–22 km, with relatively large

error bars. For Sarychev, the best estimate is smaller than the error limits given in Höpfner et al. (2015). As upper injection limit an altitude of 19 km is implemented for both eruptions, based on comparisons with MIPAS SO_2sgl distributions.

The SO_2 masses used in the CTM simulations presented in this case-study are given in Table 4.1, together with sulphur dioxide masses from various publications. For both eruptions the majority of SO_2 is injected into the altitude range 10–18 km, while only few percent directly reach higher altitudes. The spread of SO_2 masses from different studies and various data sets shows that it is difficult to determine accurate SO_2 masses for volcanic eruptions. Values presented in Table 4.1 for various publications are not derived for the same altitude regions, however, adding to differences in the masses. The SO_2 masses derived in the present study and by Höpfner et al. (2015) and Brühl et al. (2015) are partly based on the same data, and are therefore not independent from each other. Generally, in the case of Kasatochi, the mass used in the present work is below other estimates found in the literature, with Brühl et al. (2015) representing the only exception. For Sarychev, the total mass lies in the range of SO_2 masses derived in other publications.

TABLE 4.1: Volcanically emitted SO_2 masses for Kasatochi (2008) and Sarychev (2009), from various publications and as used in the present work ('Present study'). For Pumphrey et al. (2015) pressure levels denoting the maximal pressure for vertical integration are given. The total error noted here for the SO_2 masses by Höpfner et al. (2015) is the sum of uncertainties for all heights.

Kasatochi (7 Aug 2008)			Sarychev (12 Jun 2009)		
	SO_2 / Gg	Height		SO_2 / Gg	Height
G17	677	10–19 km	**G17**	768	10–19 km
	518	10–14 km		401	10–14 km
	124	14–18 km		362	14–18 km
	35	18–19 km		5	18–19 km
Höpfner et al. (2015)	898	10–22 km	Höpfner et al. (2015)	1,474	10–22 km
	± 221			± 357	
	645	10–14 km		888	10–14 km
	± 127			± 293	
	210	14–18 km		542	14–18 km
	± 86			± 60	
	43	18–22 km		44	18–22 km
	± 8			± 4	
Pumphrey et al. (2015)	1,350	215 hPa	Pumphrey et al. (2015)	571	147 hPa
	± 38			± 42	
Karagulian et al. (2010)	1,700			1,160	215 hPa
				± 180	
Brühl et al. (2015)	376		Brühl et al. (2015)	562	
Clarisse et al. (2012)	1,600		Clarisse et al. (2012)	900	
Carn et al. (2016)	2,000		Carn et al. (2016)	1,200	
Prata et al. (2010)	1,200		Haywood et al. (2010)	1,200	
				± 200	
Kristiansen et al. (2010)	1,000				
Krotkov et al. (2010)	2,200				
Corradini et al. (2010)	900–2,700				
Thomas et al. (2011)	1,700				

Time series of sulphur mass are presented in Fig. 4.7, separately for SO_2 and sulphate aerosol (first row), and integrated over both species (second row). The mass is shown integrated over the Northern hemisphere mid- to high-latitudes (30°N–90°N) and three altitude ranges, from 10.5–14.5, 14.5–18.5, and 18.5–22.5 km. For liquid-phase H_2SO_4 model results are shown for simulations without sedimentation and effective sedimentation radii of 0.1, 0.5, and 1 µm. The view on the sulphur mass per species and integrated over both species, together with simulations with and without sedimentation, allows to study exclusively the influence of chemistry, advection and sedimentation. In the model, sulphur can decrease in a confined vertical and horizontal region by advection (SO_2, H_2SO_4), chemical interaction (SO_2) or sedimentation (liquid-phase H_2SO_4). In the case of the CTM, the evolution of the total volcanic sulphur mass excludes the effect of chemistry, as all sulphur that is released from SO_2 by chemical reaction with OH is consequently included in the sulphate aerosol, if not removed by advection.

In the case of SO_2 and simulated sulphur aerosol, the sulphur mass contained in a species is calculated from its volume mixing ratios. The mass density (MD, mass per unit volume) is calculated based on the ideal gas law (Eq. 4.1), and reduced by the mass of the non-sulphur atoms (Eq. 4.2). As an example, the sulphur mass density for sulphur contained in sulphur dioxide (SMD_{SO_2}, in kg m^{-3}) is calculated as follows:

$$MD_{SO_2} = 10^{-3} \cdot \frac{VMR_{SO_2} \cdot M_{SO_2} \cdot p}{R \cdot T} \tag{4.1}$$

$$SMD_{SO_2} = \frac{M_S}{M_{SO_2}} \cdot MD_{SO_2} \tag{4.2}$$

with the volume mixing ratio VMR_{SO_2} (in $\frac{mol}{mol}$), the pressure p (in Pa), and the temperature T (in K). R is the gas constant (8.314 kg m^2 s^{-2} K^{-1} mol^{-1}), and M_S and M_{SO_2} the molar weights of sulphur and sulphur dioxide ($M_S = 32.0650$ g mol^{-1}, $M_{SO_2} = 64.0638$ g mol^{-1}).

In the case of MIPAS sulphate aerosol, sulphur mass densities ($SMD_{H_2SO_4}$, in kg m^{-3}) are calculated from the primary retrieval product, the aerosol volume densities ($AVD_{H_2SO_4-H_2O}$, in µm^3 cm^{-3}), under the assumption that all aerosol is 75 wt% H_2SO_4–H_2O, with a binary solution density of 1,700 kg m^{-3}.

$$SMD_{H_2SO_4} = \frac{M_S}{M_{H_2SO_4}} \cdot 0.75 MD_{H_2SO_4-H_2O} \tag{4.3}$$

with

$$MD_{H_2SO_4-H_2O} = 10^{-12} \cdot 1,700 \text{ kg m}^{-3} \cdot AVD_{H_2SO_4-H_2O} \tag{4.4}$$

and the molar weight of H_2SO_4 ($M_{H_2SO_4} = 98.076$ g mol^{-1}).
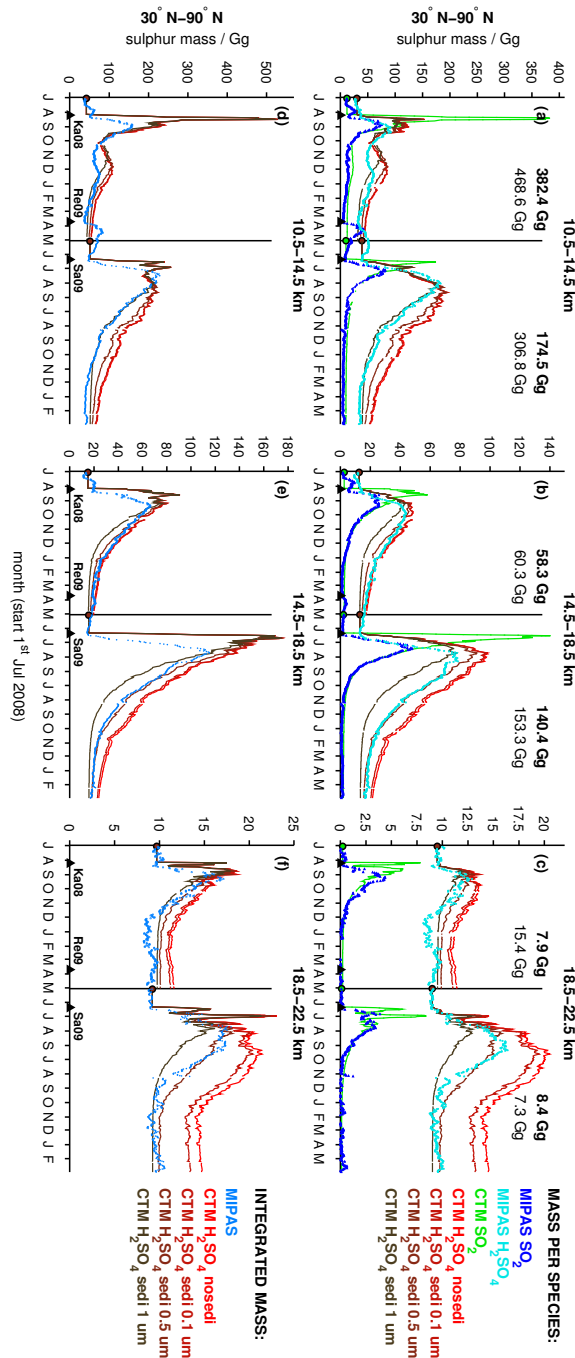
FIGURE 4.7: [Figure rotated by 90°] Time series of sulphur mass after Kasatochi (07 Aug 2008) and Sarychev (12 Jun 2009), from MIPAS measurements and CTM simulations. Integrated sulphur masses contained in sulphur dioxide and sulphate aerosol for 30°N–90°N in the altitude regions 10.5–14.5, 14.5–18.5 and 18.5–22.5 km. Mass calculated from running means over 5 d for SO_2 (MIPAS: SO_2sgl) and sulphate aerosol (per species: a–c, integrated for both species: d–f). Black triangles indicate the eruption dates of Kasatochi (07 Aug 2008, 52.2°N/175.5°W), Redoubt (23 Mar 2009, 60.5°N/152.7°W; not included in the CTM), and Sarychev (12 Jun 2009, 48.1°N/153.2°E). Simulations CKa08 and CSa09 are based on the volcanic emissions of SO_2 in Table 4.1 ('Present study') as the only sulphur source (background is 0 pptv). Simulations for Kasatochi and Sarychev are separated by a vertical black line (May 2009). Four simulation results are shown for sulphate aerosol (without sedimentation and ESRad of 0.1, 0.5 and 1μm). To ease visual comparison a constant background loading (red and green dots) is added to the simulated results, based on MIPAS measurements prior to Ka08 and Sa09, per altitude range. In (a)–(c) the peak values of simulated sulphur mass (SO_2) are given, calculated for all available model data (standard) and for locations with available MIPAS data (bold).

For the analysis of the agreement between measured and modelled data, calculations are based on equal databases. Therefore, the data sets are re-sampled onto a common grid, with a 1 km vertical gridwidth. The horizontal gridwidth equals that of the CTM ($\sim$2.5°lat x 3.75° lon). Merely 'grid-cells' with data available both for MIPAS and the CTM (per species) are considered. As when calculating integrated masses it is essential to have a good spatial data coverage to prevent underestimation, sulphur masses are derived from 5-days running zonal means. To further reduce biasing of the zonal averages due to inhomogeneities in the zonal data coverage, a method of increasing area averaging (see Appendix A.1) is applied when calculating zonal means. This method is not only used for sulphur masses, but for all zonal means presented in this thesis. Integrated sulphur masses are calculated by multiplication of the sulphur mass densities (kg m^{-3}) with the corresponding volumes of air, for 10° latitude bins (1 km x $\sim$10° lat x 360° lon).

To ease visual comparison between the modelled and measured anomalies caused by the two volcanic eruptions, a constant background mass is added to the simulated masses (Fig. 4.8). This background is chosen to match the MIPAS measurements during the time prior to the eruption, per altitude range, and is not necessarily representative for normal background conditions.

A strong underestimation of measured SO$_2$sgl is observed during the first few weeks after the eruption, when comparing SO$_2$sgl to modelled sulphur masses (Fig. 4.7). Likewise Höpfner et al. (2015) found that MIPAS underestimated SO$_2$ in comparison to sulphur dioxide from the Microwave Limb Sounder (MLS) onboard Aura (Pumphrey et al., 2015). The primary reason for this underestimation is that in the presence of particles MIPAS measurements of SO$_2$ are hindered (Höpfner et al., 2015). A large amount of ash released to the atmosphere by a volcanic eruption can produce data gaps in the SO$_2$ data retrieved from MIPAS spectra. A sampling-bias towards air parcels that are less volcano-affected can therefore be favoured (Höpfner et al., 2015). The presented comparisons to CTM simulations confirm an underestimation by SO$_2$sgl, even with measured and modelled data being re-sampled to a common grid and using the same basis of available data. The time scale of underestimation for about one month found by Höpfner et al. (2015) is consistent with presented model results.

The decay of measured and simulated SO$_2$ agrees well (Fig. 4.7), when starting comparisons about one month after each eruption. In the model, removal of SO$_2$ is caused by transport out of the region of interest, or by oxidation with hydroxyl radicals. No other processes, such as additional decay by photolysis or reaction with oxygen, are considered. As shown by the good agreement between measurements and simulations, in the time-scale of several months and larger spatial scales, the decay is explained adequately by the two mechanisms implemented in the CTM, and other processes can be neglected. Further, model results show that possible mechanisms in volcanic plumes, such as chemistry interactions, which lead to changed SO$_2$ lifetimes (Bekki, 1995), can be neglected at the temporal and spatial scale of interest. Following Bekki (1995) the speed of depletion might be reduced when high concentrations of sulphur dioxide react with OH, and thereby decrease the availability of hydroxyl radicals. In the CTM, an OH climatology is used for reaction with SO$_2$, derived from a CTM full-chemistry run, and no chemistry feedbacks on the available

concentrations of hydroxyl radicals are considered in the sulphur module.

As described earlier, data presented in Fig. 4.7 are based on locations on the horizontal CTM-grid and 1 km vertical grid, where both MIPAS and CTM data are available. As this omits information, especially for the model at altitudes above 13 km, above which model results have total coverage, and as this omission can lead to biased results, additional information is provided in the case of modelled SO_2. For comparison, peak values of SO_2 for the reduced data basis and all available model data are given in Fig. 4.7. Differences between the peak values lie between -49–15%, with negative values meaning a negative bias of the peak value for co-located data.

The effect of sedimentation can be analysed by comparing model simulations with and without sedimentation of sulphate aerosol. In the model, removal of sulphate aerosol is caused by advection or sedimentation. At each time step a certain fraction of liquid-phase H_2SO_4 is removed from a grid-cell and added to the grid-cell below. This fraction depends on the settling velocities of the particles, and therefore on the particle size. Results from simulations without sedimentation and with ESRad 0.1, 0.5 and 1 μm are shown in Fig. 4.7. Deshler et al. (2003) and Deshler (2008) derived aerosol size distributions from balloon-borne in situ measurements during volcanically perturbed times, and the chosen ESRad for CTM simulations are generally in the range of these distributions, with 1 μm being at the upper limit. Particle size distributions of aerosol depend on the available sulphuric acid, on the volcanic eruption and time after the eruption, due to nucleation, growth, and removal processes of the aerosol. None of these processes is considered in the sulphur module implemented in the CTM.

In general, the larger the particle the stronger the impact of sedimentation, and the higher the altitude the faster the terminal fall velocity. The stronger effect of sedimentation on model results for larger particles is clearly visible in Fig. 4.7. The time needed for removal and the mass that persists in the model over a relatively long period of time increases with decreasing droplet-size. While in the case of the two volcanic eruptions sedimentation with an effective settling radius of 0.1 μm shows relatively little impact on the simulation results, compared to a simulation without sedimentation, ESRad of $\geq$0.5 μm show a clear effect. Agreement between simulations and measurements is best for an ESRad of 0.5 μm, at altitudes above 14.5 km. In the lowermost altitude region studied here, an ESRad of ~1 μm compares better. This is possibly connected to the fact that bigger and heavier particles settle faster, and can be removed more rapidly, while small particles may float at a certain altitude or even undergo ascent, depending on the motion of air. As stratospheric air generally ascents in the tropics and subsides in the extra-tropics (Brewer-Dobson circulation, Sect. 3.2) the probability of upward motion of particles is higher in the tropics. It has to be kept in mind that data coverage is lowest in the lowermost altitude range, however. The aerosol masses simulated with an ESRad of 1 μm 'level out' relatively fast in the uppermost altitude range (18.5–22.5 km), compared to smaller particles and to the altitudes below. As only little aerosol is present at these higher altitudes and large particles can be removed faster, and as terminal velocities are increasing with height, the volcanic aerosol can be removed relatively fast. Model results compare reasonably well with MIPAS data for an ESRad of 0.5 μm in terms of maximal aerosol mass and removal. Therefore, this

radius is chosen for the studies of sulphur transport after the two volcanic eruptions presented in Sections 4.3.2 to 4.3.4.

Strongest effects of sedimentation are seen in the beginning and end of the simulations of volcanic sulphate aerosol. Sedimentation affects the peak amount of available sulphate aerosol and the amount of aerosol at which the model is 'levelling out' in a certain altitude region. CTM simulations show, however, that the dominating process for the long-term evolution of sulphate aerosol after the two eruptions is transport out of the studied region (extra-tropics, 10.5–22.5 km) towards the troposphere by the Brewer-Dobson circulation. This can be concluded as simulations with and without sedimentation show a relatively parallel decrease with time. Regarding the removal of total sulphur the same is true, as SO_2 is converted into sulphate aerosol relatively fast after the eruptions. Nevertheless, consideration of sedimentation improves the conformity between modelled and measured data.

The presented model results compare well with MIPAS measurements both for SO_2sgl and liquid-phase H_2SO_4. Hence, with the aid of the CTM it could be demonstrated that in the case of the two eruptions, the amplitude of the volcanically caused anomalies in the stratospheric sulphate aerosol loading in the Northern hemisphere extra-tropics that has been retrieved from MIPAS measurements, is in agreement with MIPAS SO_2sgl. Furthermore, the removal of both species is well reproduced by the simulations. This leads to the conclusion that both qualitatively and quantitatively the new data set of MIPAS sulphate aerosol is consistent with MIPAS sulphur dioxide measurements after the two eruptions.

Two additional features can be seen in Fig. 4.7. Downward transport of sulphur from the eruption of Kasatochi causes a peak in Nov / Dec 2008 in the lowermost altitude region. This will be discussed in more detail in the following section (Sect. 4.3.2). Furthermore, the eruption of Redoubt in Mar 2009 produced a signal in the MIPAS measurements but is not included in the CTM simulations analysed in this case-study, neither studied here.

To finalise this section on the temporal evolution of volcanic sulphur mass in the mid- to high-latitudes of the Northern hemisphere, after the eruptions of Kasatochi in August 2008 and Sarychev in June 2009, the main findings are summarised:

- The MIPAS data set of SO_2sgl and the new MIPAS data set of sulphate aerosol are consistent after the two eruptions, both in quality and quantity.

- MIPAS SO_2sgl underestimates the volcanic SO_2 in the first month after the eruptions.

- The decay of SO_2 is well explained by its reaction with OH.

- Removal of the bulk of volcanic sulphate aerosol and total volcanic sulphur is dominated by the Brewer-Dobson circulation.

- Agreement of modelled sulphur and sulphate aerosol with MIPAS data is improved when sedimentation is considered (ESRad $\sim$0.5 µm).

4.3.2 Vertical, meridional, and zonal sulphur transport

In Section 4.3.1 the temporal evolution and vertical distribution of sulphur mass contained in sulphur dioxide and sulphate aerosol has been discussed for the eruptions of Kasatochi in 2008 and Sarychev in 2009. Masses were integrated over the mid- and high latitudes of the Northern hemisphere (30°N to 90°N). Both volcanoes erupted during boreal summer (7 Aug 2008 and 12 Jun 2009), at $\sim$50°N. Data retrieved from MIPAS measurements for SO_2sgl, and liquid-phase H_2SO_4 were shown to be consistent with model results in terms of mass. For simulated sulphate aerosol, an effective sedimentation radius of 0.5 μm gives satisfactory agreement with MIPAS data. Hence, the simulations of sulphate aerosol shown in the present section are generally based on this ESRad. Here, particularities of the transport of the volcanic plumes are studied for the entire Northern hemisphere, including both MIPAS measurements and model results.

MIPAS data of SO_2sgl and sulphate aerosol, and model results for the eruptions of Kasatochi (CKa08) and Sarychev (CSa09), are shown as time series of vertically resolved volume mixing ratios for 30°N–90°N in Fig. 4.8. Additionally, the distributions of integrated sulphur (SO_2 plus liquid-phase H_2SO_4) are presented. After the eruption of Kasatochi, in the extra-tropics a vertical split into an upper and lower part of the volcanic plume is observed in the MIPAS measurements, both for sulphur dioxide and sulphate aerosol. The upper part of the plume subsides by the Brewer-Dobson circulation, which leads to a second increase of the sulphur loading at low altitudes that has already been noticed in the time series of sulphur mass (Fig. 4.7). The lower part of the plume descents and disappears relatively fast from the altitude range of observations. Both the split into an upper and lower part of the plume, and the downward transport are likewise present in the modelled distributions. The lowermost part of the plume contains a major part of the injected SO_2. In the CTM 77% (518 Gg) of the sulphur dioxide is injected at altitudes between 10–14 km (Table 4.1). This part of the SO_2 is available for conversion into sulphate aerosol for a relatively short period of time only, as the SO_2 is transported downwards via the Brewer-Dobson circulation. The effect can be seen in the comparably low amount of sulphate aerosol that is formed. This pattern of a 'double-plume' is in very good agreement with findings by Andersson et al. (2015). In their study, aerosol scattering as measured by the Cloud-Aerosol Lidar and Infrared Pathfinder Satellite Observations (CALIPSO) has been analysed. More details on the vertical split of the Kasatochi plume will be given in Section 4.3.4.

The eruption of Sarychev (Fig. 4.8) shows similar subsidence with time. However, a separation of the plume is neither measured nor simulated, as vertically sulphur is distributed rather homogeneously. In the simulations of Sarychev 48% (367 Gg) of the SO_2 is injected to altitudes above 14 km. This results in a higher measured and simulated sulphate aerosol loading, compared to Kasatochi.
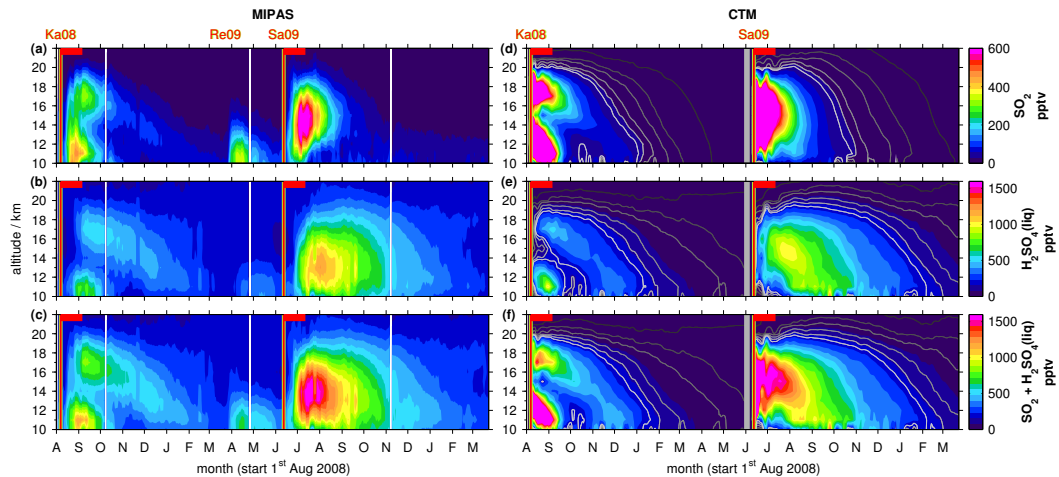
FIGURE 4.8: Time series of MIPAS and CTM SO_2, sulphate aerosol, and total sulphur (SO_2 + H_2SO_4(liq)) after Ka08 and Sa09, at 30°N–90°N. Vertically resolved zonal mean volume mixing ratios (area weighted, 5 d running means). MIPAS (left): SO_2sgl; CTM (right): CKa08 and CSa09 (ESRad 0.5 µm; simulations separated by a vertical grey line in May / Jun 2009). The eruption dates of Kasatochi (07 Aug 2008), Redoubt (23 Mar 2009, not included in the model) and Sarychev (12 Jun 2009) are indicated. The first 30 d after Ka08 and Sa09 are indicated by horizontal red lines. Contour lines in panels d–f represent (from dark to bright): for SO_2 1, 5, 10, 20, 30, and 40 pptv, and for sulphate aerosol and total sulphur 5, 25, 50, 100, 150, and 200 pptv. Values exceeding the colour-scales are assigned with the limiting values.

Similar to Fig. 4.8 for the northern extra-tropics, in Fig. 4.9 vertically resolved time series of volcanic sulphur are shown for the northern tropics (0°N–30°N). It becomes obvious that parts of the sulphur that has been emitted at ∼50°N is transported southwards after both eruptions and reaches the tropics. Especially the longer-lived volcanic sulphate aerosol persists at lower latitudes for several months, while concentrations of sulphur dioxide decay faster. In the 'tropical pipe' (terminology follows, e.g., Plumb, 1996) the sulphur ascends slowly with time, following the predominant vertical motion in the tropical lower stratosphere. The pattern of upward motion is observed in the MIPAS measurements and CTM simulations. Wu et al. (2017) found the ascent speed of volcanic aerosol from the Sarychev eruption in their study to be in good agreement with the water vapour ascent speed, which they derived from observations by Glanville and Birner (2017).

The aerosol pattern in the tropics, with competing ascent motion of air parcels and downward transport of aerosol by sedimentation, depends on the aerosol sizes. The larger the particles the higher the probability of effective downward transport in the tropics rather than uplift. Data presented in Fig. 4.9 are based on an effective sedimentation radius of 0.5 µm. In Fig. 4.10 the impact of the chosen ESRad on the pattern of uplift is shown, for a simulation without sedimentation, resulting in enhanced uplift, and a larger ESRad of 1 µm, causing upward motion of modelled sulphate aerosol to be suppressed. The ascent in the tropics as measured by MIPAS is best reproduced by the simulation with an ESRad of 0.5 µm.
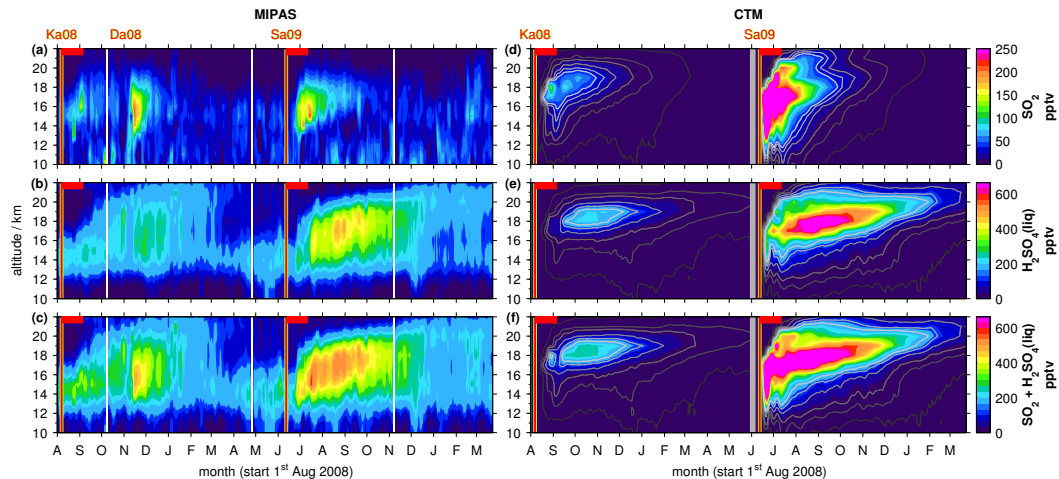
FIGURE 4.9: As Fig. 4.8, but for 0°N–30°N. The eruption date of Dalafilla is indicated (Da08, 3 Nov 2008, not included in the model).

Generally, it has to be noted that modelled ascent speeds are fraught with uncertainties (e.g., Liu et al., 2013; Pommrich et al., 2010). Therefore, a similar study with a different model that uses a different transport scheme, or the use of differing meteorological data for the calculation of vertical motion, may lead to varying best estimates of the effective sedimentation radius. Further, a constant radius, as implemented in the sulphur module of the present work, is a strong simplification as aerosol radii cover a large range of sizes, and size distributions are not constant in time and location (e.g., Deshler et al., 2003). The model neither considers different building and growth processes of aerosols, such as nucleation, coagulation or condensation.
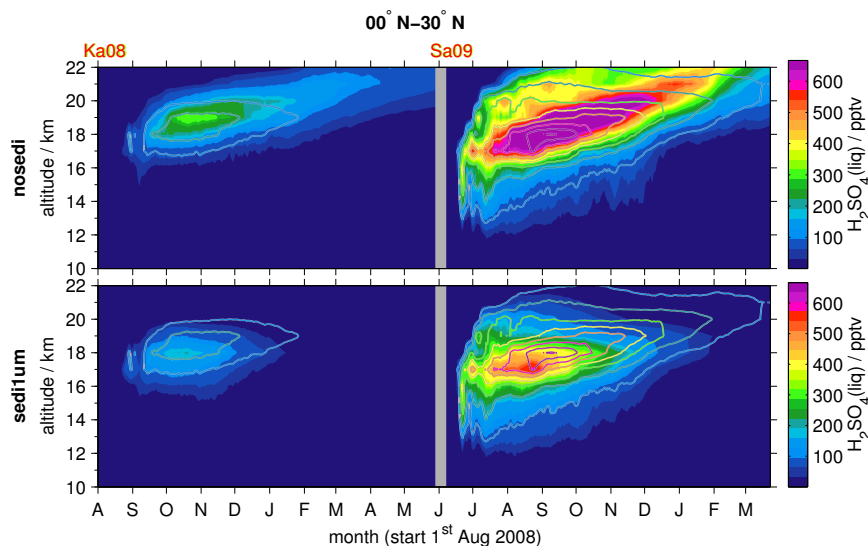
FIGURE 4.10: Vertically resolved time series of modelled sulphate aerosol after Ka08 and Sa09 at 0°N–30°N, without sedimentation (first row), and with and ESRad of 1 µm. Contour lines indicate results for an ESRad of 0.5 µm (as in Fig. 4.9), for 100 pptv steps, starting at 100 pptv. Data are area weighted averages. Two simulations are shown (CKa08, CSa09), separated by a bold grey line (May / Jun 2009). Values exceeding the colour-scale are assigned with the limiting values.

Relatively high values are measured in the tropics at ~13–16 km (Fig. 4.9). Such enhancements are not seen in the simulations, as they are not connected to the volcanically emitted sulphur from Kasatochi and Sarychev. There is a clear transition from a relatively high sulphur loading in the troposphere, to lower values in the stratosphere. The tropopause in the tropics is at a rather constant altitude of around 16–17 km throughout the year. More details on this feature are given in Section 5.2.

The extent to which the increased sulphur loading measured in the tropics results from the eruptions of Kasatochi and Sarychev cannot clearly be identified. Simulations indicate that in the case of Kasatochi volcanic sulphur is mainly confined to the altitude region above ~16 km. Measured enhancements are overlaid by the eruption of Dalafilla at 13.8°N after the 3 Nov 2008. In the case of Sarychev the model suggests that sulphur at tropospheric altitudes of 12 km, and at higher altitudes, can be attributed to the eruption. However, there is a clear difference between the measured and modelled maxima after the eruption of Sarychev in the tropics.

When analysing daily horizontal distributions of measured and modelled volcanic enhancements, differences in the data coverage and extent of the plumes get obvious. As an example, distributions at 16 km are shown in Fig. 4.11 and 4.12, for various days after the eruptions (5–25 days). Due to differences in the wind fields, the simulated plume stays in a relatively confined area for several days and is then spread zonally and towards the north after the eruption of Kasatochi, while a fast meridional transport of the Sarychev plume is simulated. Therefore, it takes parts of the simulated Sarychev plume only 7–8 days to reach 15°N at ~12–16 km, and all latitudes of the Northern hemisphere are affected after less than 20 days. Such a strong transport towards the equator is not found in the measurements. However, at 16 km, missing MIPAS data complicate the analysis of the agreement between the extent and location of the volcanic plumes in the model and observations. Especially in the data set of MIPAS sulphate aerosol coverage is sparse in certain areas due to the filtering connected to icy cirrus clouds (Sect. 2.2.2). Zonal averages, as presented in Fig. 4.9 may be biased towards low sulphur loading when data are missing in the areas of the volcanic plume. In Höpfner et al. (2015) such a biasing towards lower non-volcanic values has also been observed in the case of MIPAS SO_2sgl after volcanic eruptions. For the CTM only at altitudes below 12–13 km data coverage is sparse. Generally, for MIPAS SO_2sgl coverage is particularly sparse in the tropics ($\leq$ 15–16 km) or at altitudes up to around 17 km in the area of the Asian Monsoon Anticyclone (ASMA). Sulphate aerosol measurements are primarily filtered in the tropics ($\leq$ 18–19 km) or at altitudes up to around 20 km in the area of the ASMA. Furthermore, MIPAS aerosol data have been filtered for PSCs in the polar regions (Sect. 2.2.2).
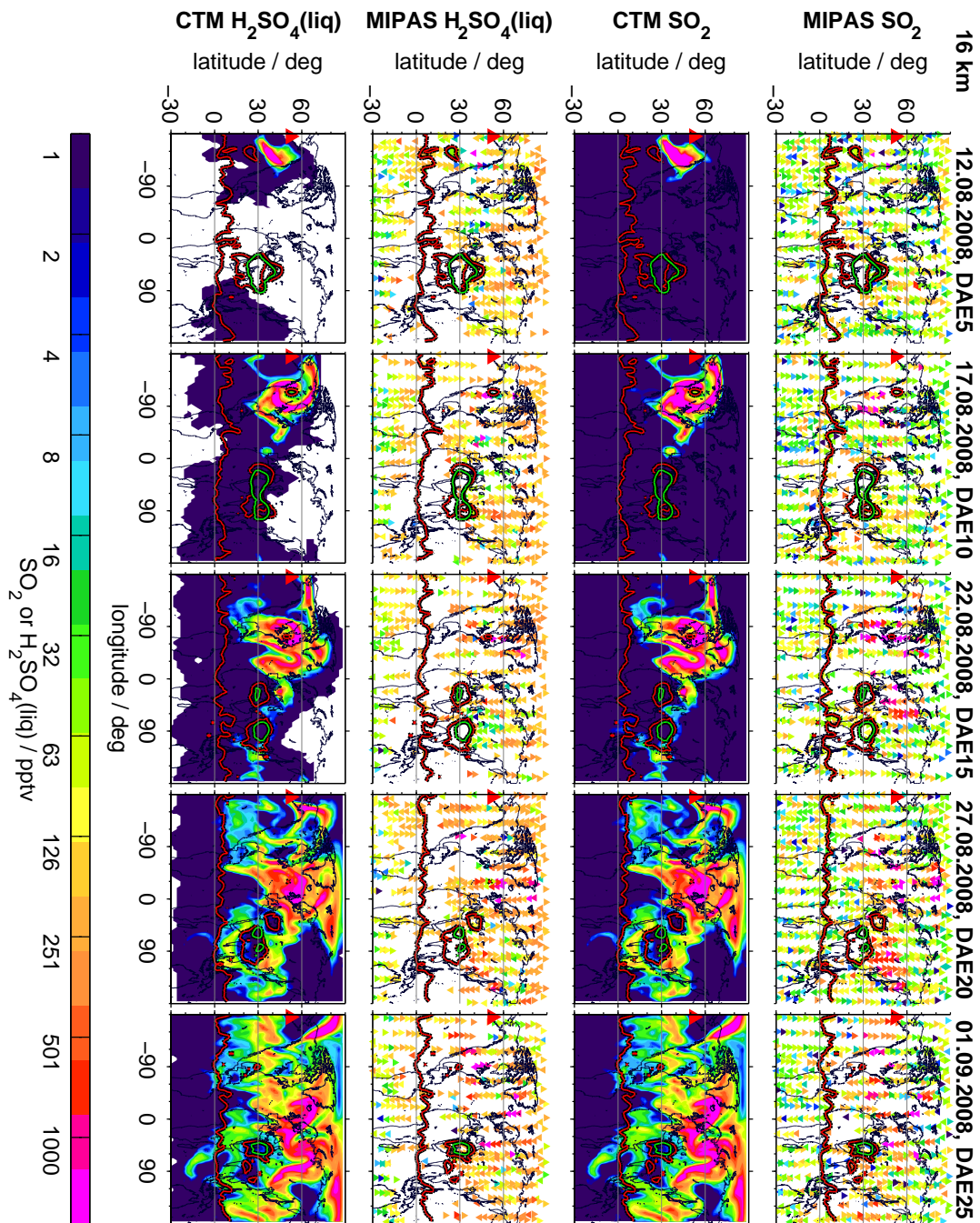
FIGURE 4.11: [Figure rotated by 90°] Daily horizontal distributions of sulphur dioxide and sulphate aerosol at 16 km after the eruption of Kasatochi (7 Aug 2008). MIPAS: SO$_2$sgl; CTM: simulation CKa08 (ESRad 0.5 μm). The barrier of the Asian Summer Monsoon Anticyclone is indicated as 14.32 m geopotential height on the 150 hPa level (green) and as 1.8 PVU on the 370 K isentrope (red). Indicated are the date and DAE (Days after eruption). A red triangle shows the location of Kasatochi. The colour-scale is logarithmic, with exceeding values being assigned with the limiting values. For simulated aerosol white areas represent 0 pptv.
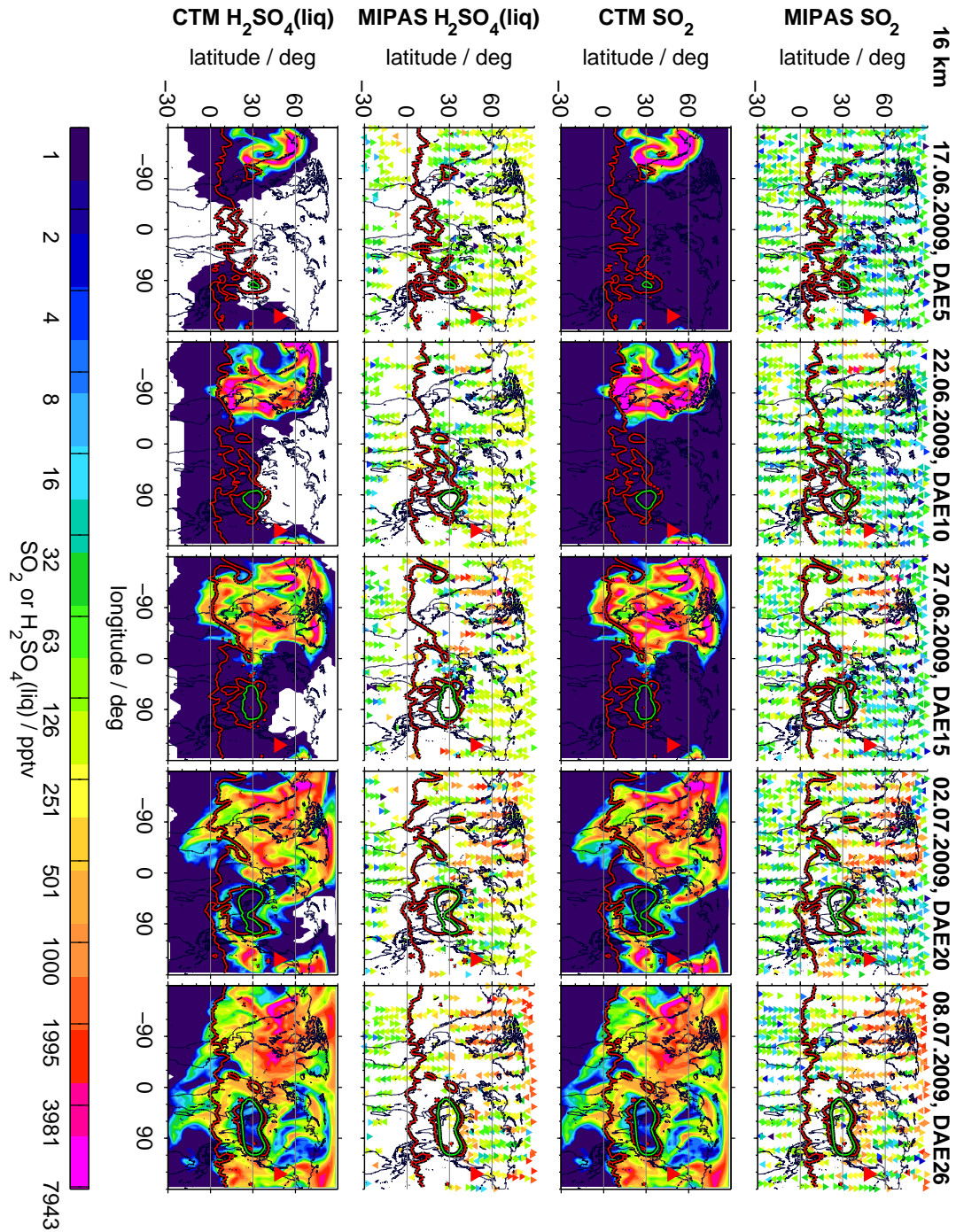
FIGURE 4.12: [Figure rotated by 90°] As Fig. 4.11, but for Sarychev (12 Jun 2009).

As has been stated before, the wind fields provoke differences in the evolution of the volcanic plumes from the Kasatochi (2008) and Sarychev (2009) eruptions. For 0 to 15 days after the eruptions, horizontal distributions of wind speed and direction in the Northern hemisphere are shown at 14–18 km in Fig. 4.13 and 4.15, together with the wind speed of the zonal component of the wind. Additionally, in Fig. 4.14 and 4.16 monthly mean distributions of the wind are presented. The zonal wind speed is generally lower at 18 km, compared to 14 km, with some exceptions especially in the Northern hemisphere tropics, where the north-eastern trade winds flow from east to

west. Zonal wind speed is lower in the regions of the subtropical highs ($\sim$30°N), and Polar front ($\sim$60°N). In the mid-latitudes westerlies dominate the wind pattern, including the subtropical jet (close to 30°N), currents of fast flowing air, which can form close to tropopause heights and the interface between the Ferrel (mid-latitudes) and Hadley (tropics) circulation cells (Hudson, 2012).

The subtropical jet strengthened few days after the eruption of Kasatochi, and a prevailing eastward wind can be seen in the mid-latitudes at 14–16 km, leading to the simulated eastward transport of sulphur. In the case of Sarychev, it gets obvious that it erupted north of a relatively strong subtropical jet, and northeast to the Asian Summer Monsoon Anticyclone. Furthermore, the prevailing eastward wind north of the ASMA, and westward wind south of the anticyclone are to be seen, with interconnecting winds at the western and eastern edges of the ASMA. The wind fields few days after the eruption of Sarychev additionally show the reason for the strong simulated equatorward transport of the plume (west of $\sim$90°W).
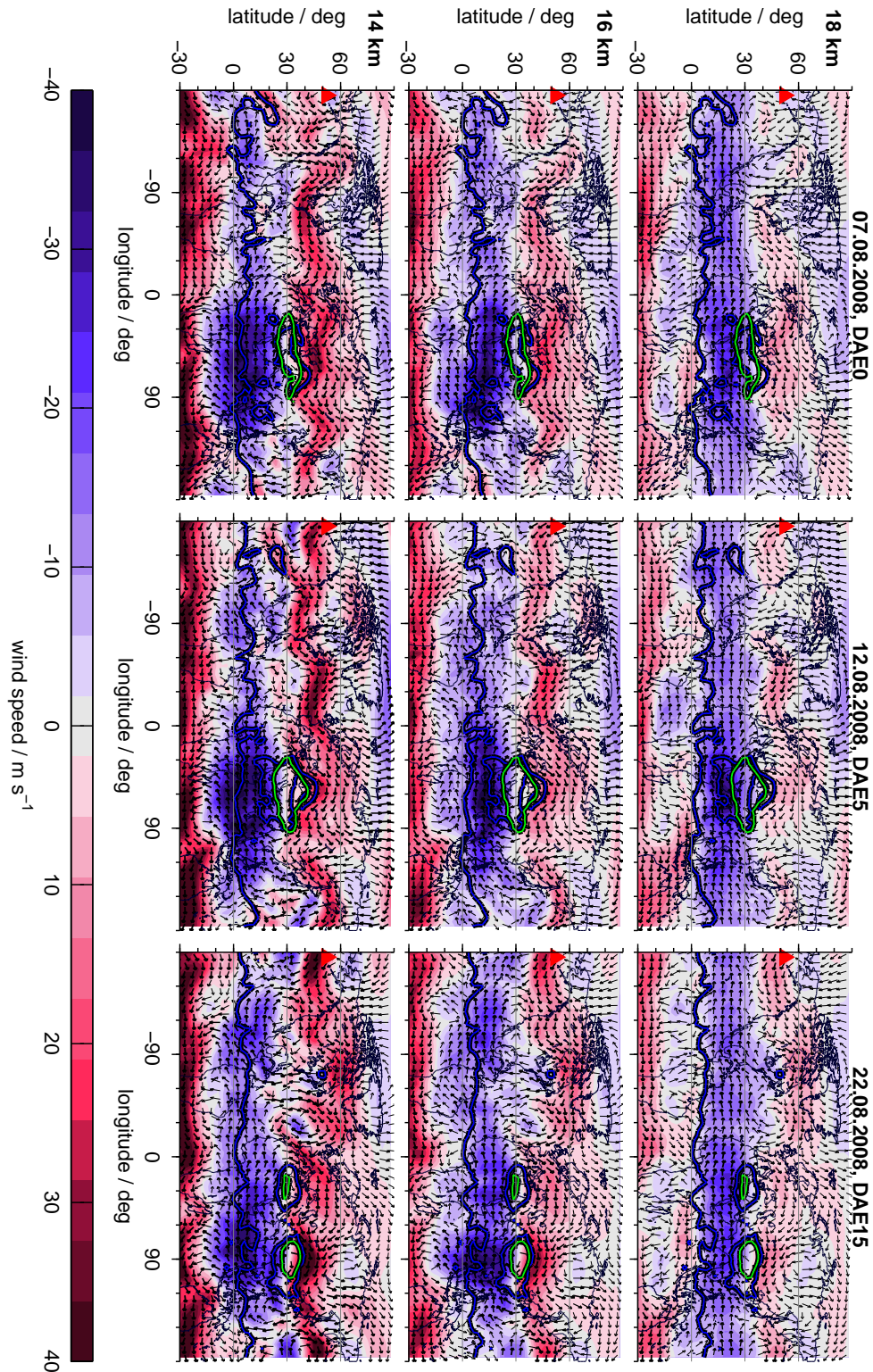
FIGURE 4.13: [Figure rotated by 90°] Daily horizontal distributions of wind speed and direction at 14, 16, and 18 km after the eruption of Kasatochi (7 Aug 2008), and zonal wind speed. Arrows represent wind speed (length and line width) and direction, while the zonal wind speed is colour-coded (positive values: eastward). Values represent CTM wind fields at 12 UTC, with model input being ERA-Interim wind fields. The barrier of the Asian Summer Monsoon Anticyclone is indicated as 14.32 m geopotential height on the 150 hPa level (green) and as 1.8 PVU on the 370 K isentrope (blue). Indicated are the date and DAE. A red triangle shows the location of Kasatochi. For better visualisation, the maximum wind speed shown by arrows is limited to 15 m s^{-1}, with all faster wind velocities being assigned with this value. Values exceeding the colour-scale are assigned with the limiting values.
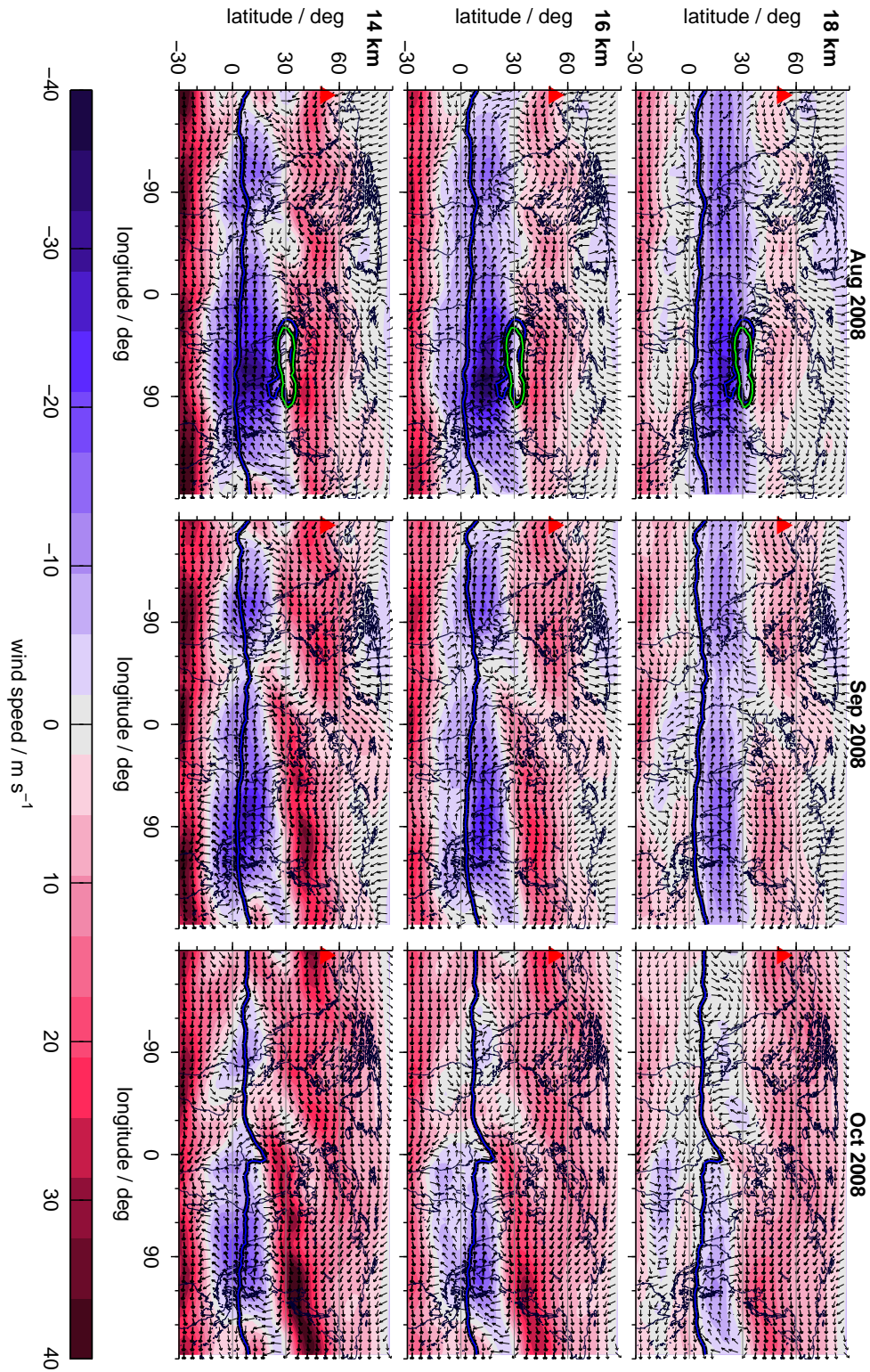
FIGURE 4.14: [Figure rotated by 90°] As Fig. 4.13, but for monthly averages (Aug, Sep, and Oct 2008).
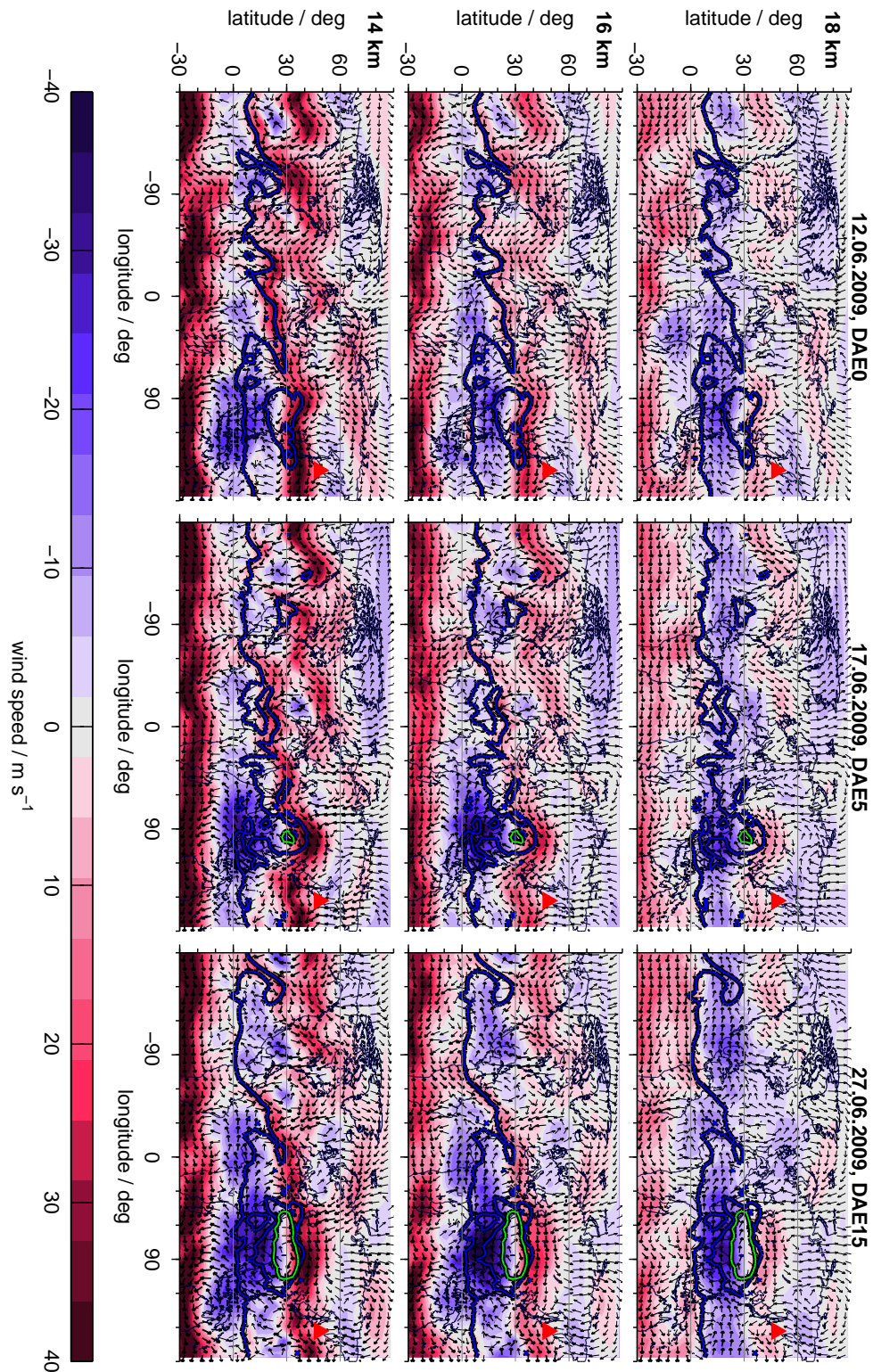
FIGURE 4.15: [Figure rotated by 90°] As Fig. 4.13, but for the eruption of Sarychev (12 Jun 2009).
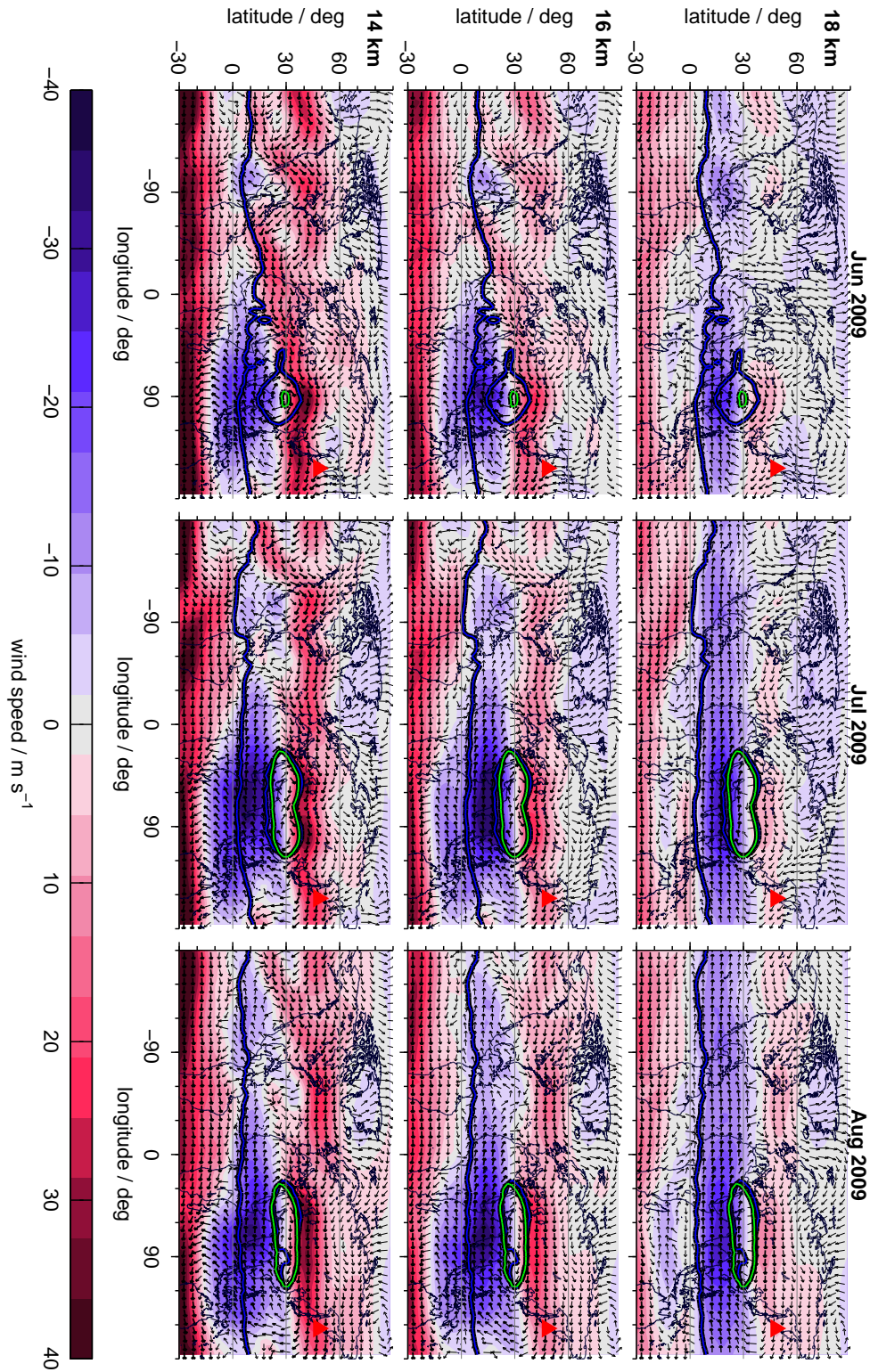
FIGURE 4.16: [Figure rotated by 90°] As Fig. 4.13, but for monthly averages (Jun, Jul, and Aug 2009).

To get a clearer picture of the temporal evolution of the latitudinal transport of the sulphur plumes after the eruptions of Kasatochi and Sarychev, latitudinally resolved time series of SO_2 and sulphate aerosol are presented for the Northern hemisphere in Fig. 4.17 and 4.18 for various altitudes, spanning 10–22 km. At altitudes below ∼16 km the majority of sulphur stays in the Northern hemisphere mid- to high-latitudes, north of ∼30°N. This is true for both the measurements and simulations, except for simulated sulphur after the eruption of Sarychev, where the fast transport towards the equator increases the sulphur loading in the tropics. Descent of sulphur in the extra-tropics is seen, as has already been noted in Fig. 4.8. At low altitudes, mixing is suppressed at around 30°N, leading to a relatively strong gradient between the tropics and extra-tropics. This mixing-barrier is stronger at low altitudes, where mixing is reduced due to the subtropical jet stream. At around 16–18 km and 30°N, primarily in the longer-lived sulphate aerosol, a 'tongue' of higher values compared to the surrounding latitudes can be seen that exists for a relatively long time.
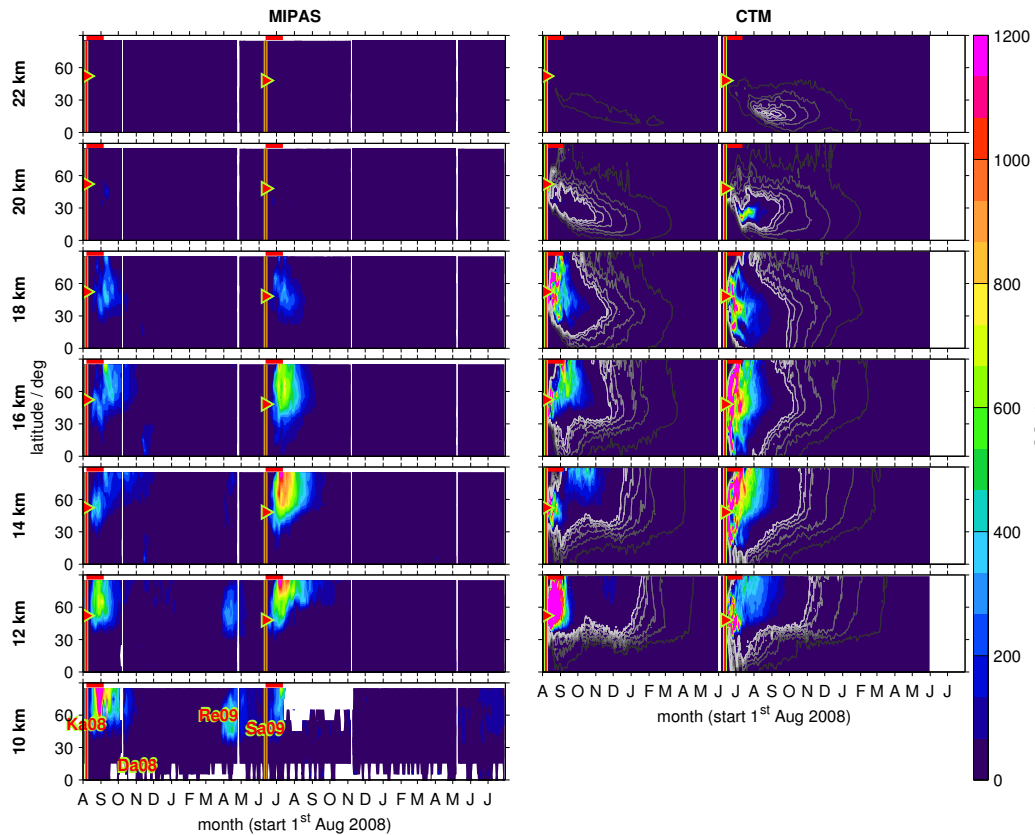
FIGURE 4.17: Sulphur dioxide as latitudinally resolved time series at 10–22 km, after Ka08 and Sa09: MIPAS SO_2sgl (left) and CTM simulations CKa08 and CSa09 (right). Time and latitude of the eruptions are indicated by red triangles. The eruptions of Dalafilla (2008) and Redoubt (2009) are indicated additionally (not included in the CTM). MIPAS: zonally averaged volume mixing ratios as 5 d running means for 10° latitude bins; CTM: daily values for 2.5° latitude bins. Simulations CKa08 and CSa09 are separated by a grey line. Black to white contour-lines show 1, 5, 10, 20, 30, and 40 pptv. The simulated distribution at 10 km is not shown, due to sparse data availability. The first 30 d after Ka08 and Sa09 are indicated by horizontal red lines. Values exceeding the colour-scale are assigned with the limiting values.
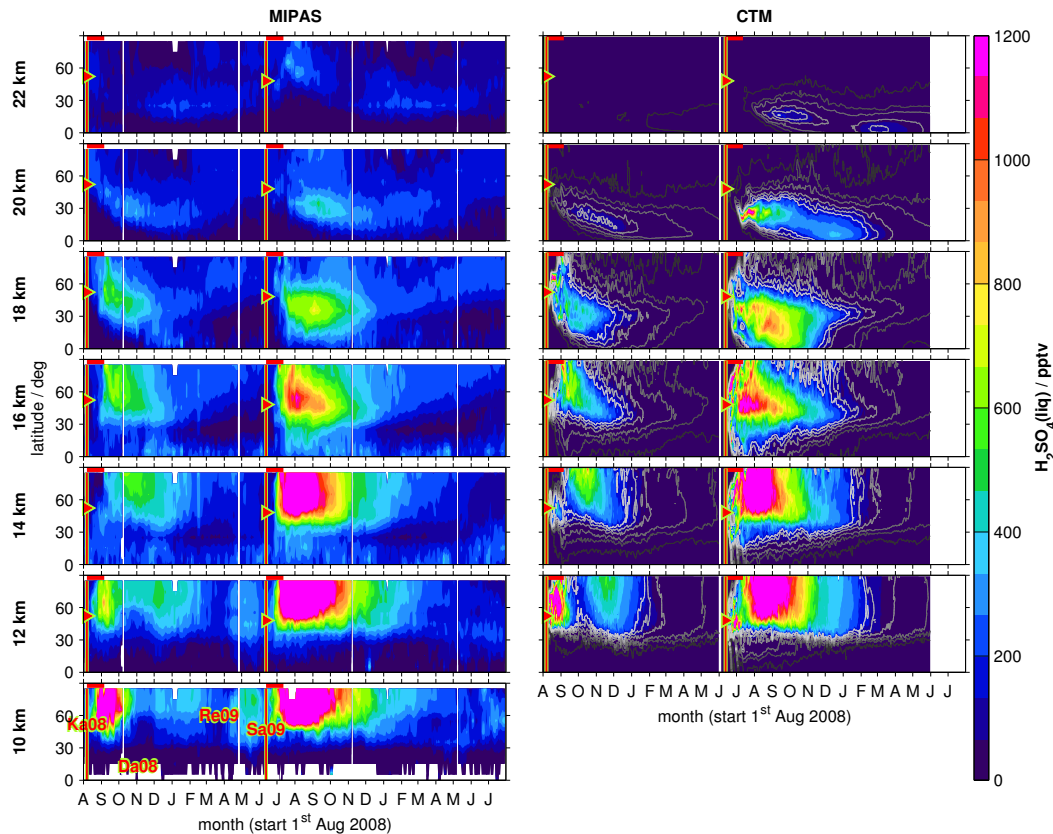
FIGURE 4.18: As Fig. 4.17, but for sulphate aerosol (ESRad = 0.5 µm). Dark to bright contour-lines show 5, 25, 50, 100, 150, and 200 pptv.

At altitudes above ∼17 km after the eruption of Kasatochi, and ∼15 km after the eruption of Sarychev, MIPAS measurements and CTM simulations show transport of volcanic sulphur from the mid-latitudes towards the equator. Sulphur reaches the tropics and the equator primarily as aerosol, where it undergoes slow ascent in the 'tropical pipe' (see also Fig. 4.9). The volcanic sulphur can hereby be transported into the stratospheric 'overworld' (terminology follows, e.g., Hoskins, 1991), the altitude region in the stratosphere in which isentropes lie entirely above the tropopause. Even though the amounts of sulphur reaching the equator are relatively small, compared to the sulphur emitted during the eruptions, Northern hemisphere mid-latitude eruptions are thereby shown to possibly impact the sulphur loading in the Southern hemisphere. Bourassa et al. (2012) studied stratospheric optical depths as measured by the Optical Spectrograph and InfraRed Imager System (OSIRIS) on-board Odin. These observational data also show that the effect of the eruptions of Kasatochi and Sarychev extended to lower latitudes. The dispersion of the plumes few months after the eruptions and the observed 'tongue' of relatively high volume mixing ratios is clearly visible in the horizontal distributions of measured and simulated sulphur dioxide and sulphate aerosol at an altitude of 18 km between ∼70–150 days after the eruptions, as presented in Fig. 4.19 and 4.20. The MIPAS SO_2sgl shows additional enhancements after the 3 Nov 2008 due to the eruption of Dalaffilla at 13.8°N that is not included in the model simulation.
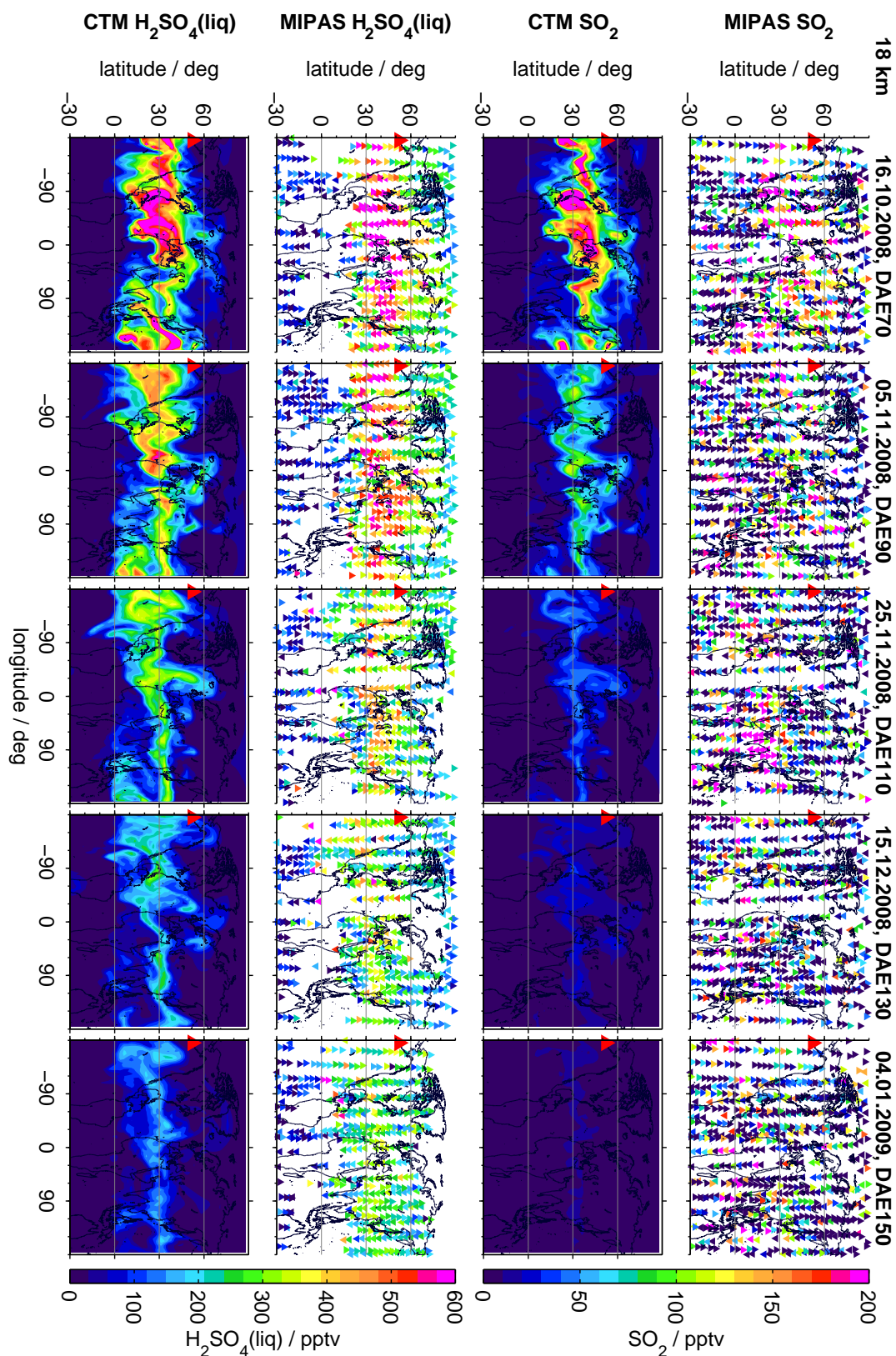
FIGURE 4.19: [Figure rotated by 90°] Daily horizontal distributions of sulphur dioxide and sulphate aerosol at 18 km after the eruption of Kasatochi (7 Aug 2008). MIPAS: SO$_2$sgl; CTM: simulation CKa08 (ESRad 0.5 μm). Indicated are the date and DAE. A red triangle shows the location of Kasatochi. Values exceeding the colour-scales are assigned with the limiting values.
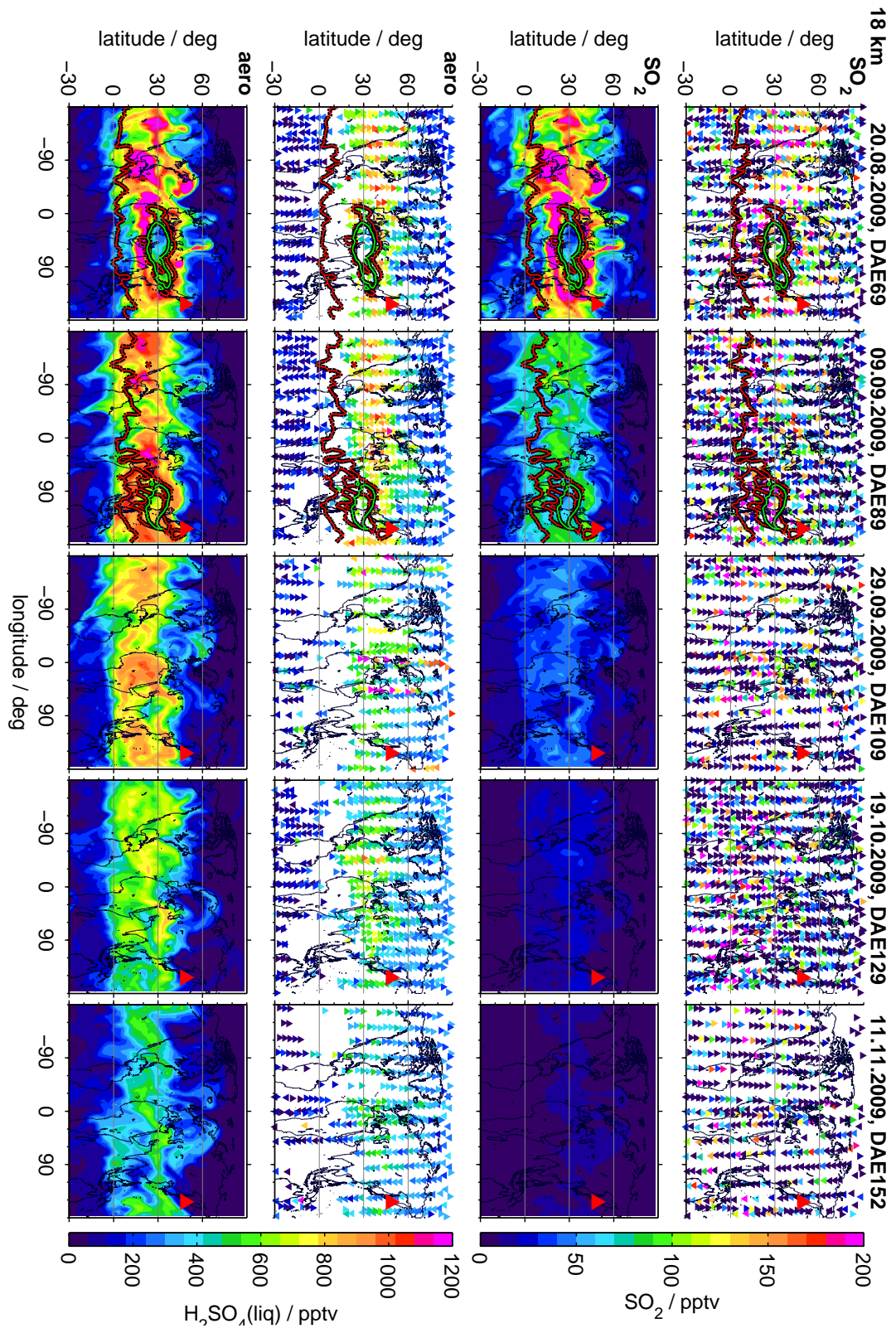
FIGURE 4.20: [Figure rotated by 90°] As Fig. 4.19, but for Sarychev (12 Jun 2009). The barrier of the Asian Summer Monsoon Anticyclone is indicated as 14.32 m geopotential height on the 150 hPa level (green) and as 1.8 PVU on the 370 K isentrope (red), for DAE 69 and 89.

As has been demonstrated above, sulphur emitted by the eruptions of Kasatochi and Sarychev reaches the tropics. To conclude this section, Fig. 4.21 shows the volcanic contribution to the tropical and Southern hemisphere sulphur loading in terms of mass, both for the CTM and MIPAS. It is clear that the majority of the volcanic mass stays in the Northern hemisphere extra-tropics and is removed by subsidence by the Brewer-Dobson circulation, and by sedimentation. After the eruption of Sarychev simulated masses are enhanced in the altitude range 14.5–18.5 km, as could be seen in modelled sulphur volume mixing ratios (Fig. 4.12). Simulation results show that the integrated mass in these altitudes in the NH tropics reach peak values that are only ∼20% smaller than in the same altitude region in the NH extra-tropics. Up to a few months after the eruption MIPAS shows lower values, by a factor of ∼2. After this period of large differences, however, the simulated and measured masses are similar. After the eruption of Sarychev, the strong modelled transport towards the equator further leads to a signal in the Southern hemisphere. It is not clear, whether such enhancements would have been observed if more MIPAS data were available in the tropics.

After the eruption of Kasatochi simulated and measured impacts on the NH tropics are consistent in terms of maxima and removal, with simulated peak values at 14.5–18.5 km being 85% smaller than in the extra-tropics at equal altitudes. Only at higher altitudes simulated masses corresponding to larger effective sedimentation radii (ESRad 0.5 and 1 μm) show a negative offset.

MIPAS data and CTM simulations confirm similarities between the transport patterns of sulphur after the eruptions of Kasatochi in 2008 and Sarychev in 2009. Haywood et al. (2010) likewise noticed similarities that arise from the fact that the volcanoes are located at a small distance in latitude, had similar injection altitudes, and both erupted during boreal summer. However, besides the mentioned conformities between the eruptions, both volcanic eruptions also showed their own characteristics. Two differences will be discussed in the following sections (4.3.3 and 4.3.4).
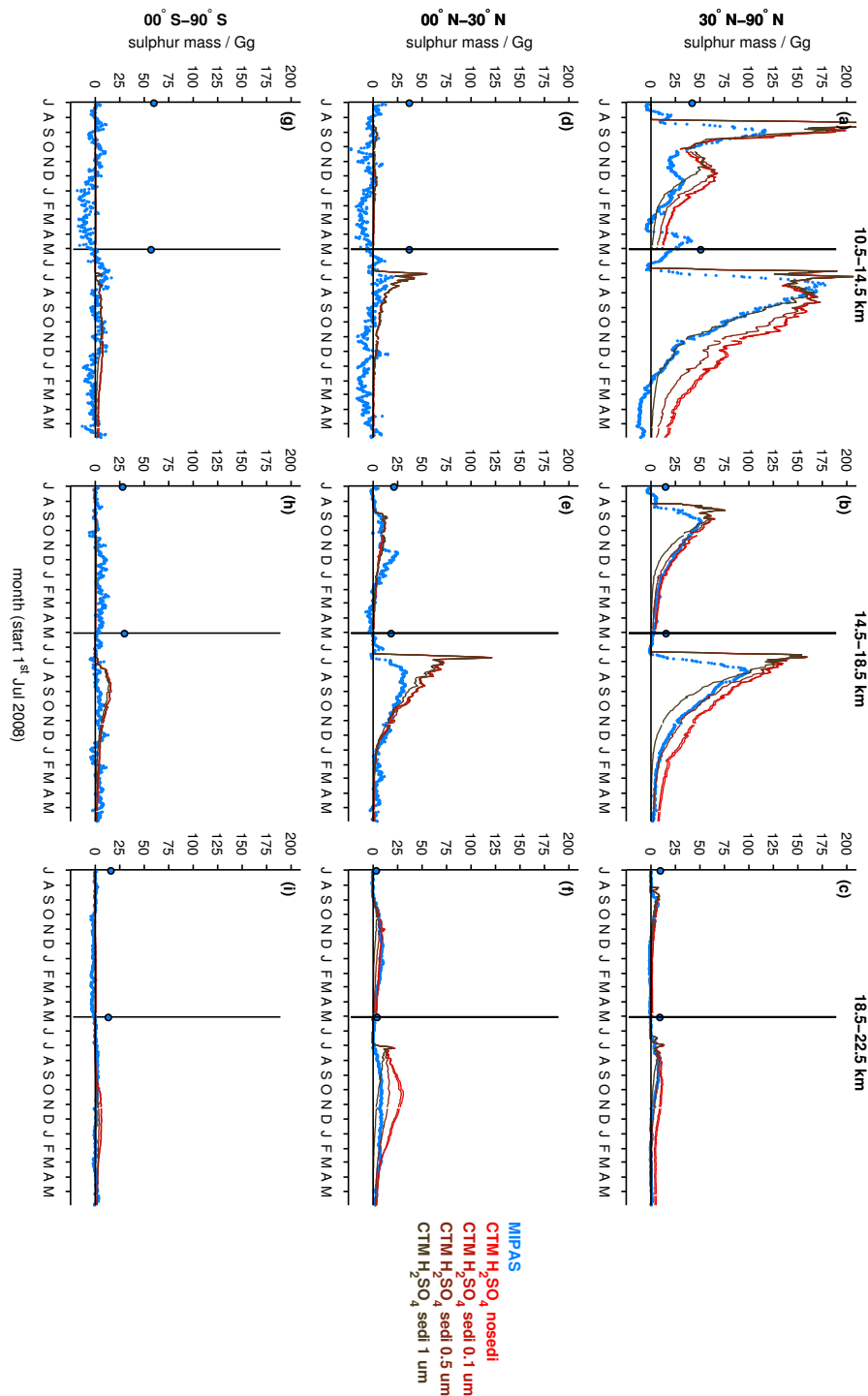
FIGURE 4.21: [Figure rotated by 90°] Time series of measured and simulated sulphur mass after Kasatochi (07 Aug 2008) and Sarychev (12 Jun 2009). Integrated sulphur masses as contained in sulphur dioxide and sulphate aerosol for 30°N–90°N, 00°N–30°N, and 00°S–90°S, in the altitude regions 10.5–14.5, 14.5–18.5 and 18.5–22.5 km. Mass calculated from running means over 5 d for SO$_2$ (MIPAS: SO$_2$sgl) and sulphate aerosol. Black triangles indicate the eruption dates of Kasatochi (07 Aug 2008, 52.2°N/175.5°W), Dalaffilla (3 Nov 2008, 13.8°N/40.5°E; not included in the CTM), Redoubt (23 Mar 2009, 60.5°N/152.7°W; not included in the CTM), and Sarychev (12 Jun 2009, 48.1°N/153.2°E). Simulations CKa08 and CSa09 are based on the volcanic emissions of SO$_2$ in Table 4.1 ('Present study') as the only sulphur source (background is 0 pptv). Simulations for Kasatochi and Sarychev are separated by a vertical black line (May 2009). Four simulation results are shown for sulphate aerosol (without sedimentation and ESRad of 0.1, 0.5 and 1μm). To ease visual comparison a constant background loading (blue dots) has been removed from the measured data, based on MIPAS measurements prior to the eruptions of Ka08 and Sa09, per altitude range.

4.3.3   Asian summer monsoon

Wu et al. (2017) studied the dispersion of the Sarychev plume and its equatorward transport, as well as the impact of the Asian summer monsoon anticyclone on its dispersion. They found that the equatorward transport at the 360 to 400 K isentropes (13–18 km at 30°N) has primarily been due to anticyclonic breaking of Rossby waves, strengthened by the Asian summer monsoon. They show that in the ASMA aerosol concentrations are low ('aerosol hole'), compared to the surrounding sulphur-rich air. As stated by Wu et al. (2017), such southward transport would be hindered by a strong subtropical jet, combined with Rossby wave breaking events, for an eruption during boreal winter.

Horizontal patterns of volcanic sulphur from the Sarychev eruption, as simulated by the CTM, clearly show the impact of the ASMA. Horizontal distributions are shown for the period 12 Jul 2009–24 Aug 2009 at an altitude of 17 km. The approximate location of the outer barrier of the ASMA is indicated by the 14.32 m geopotential height on the 150 hPa level (Randel and Park, 2006) and as 1.8 PVU on the 370 K isentrope (Ploeger et al., 2015; Wu et al., 2017), both derived from CTM fields. The CTM results show both a sulphur dioxide and sulphate aerosol hole in the Asian summer monsoon anticyclone, and a certain transport around the anticyclone. Inside the ASMA the 380 K isentrope (approx. tropopause height in the tropics) is at elevated altitudes, leading to higher reaching tropospheric air (Ploeger et al., 2015). MIPAS measurements are sparse, but suggest a rather strong gradient between high aerosol loading outside the anticyclone, towards the north, and low values inside the ASMA. Towards the south MIPAS aerosol data are very rare. Monthly wind fields (Fig. 4.16) show the circulation pattern of the ASMA, with predominant eastward wind at its northern edge, and westward wind at its southern edge, and interconnections at its western and eastern flanks. Furthermore, in Fig. 4.15 the subtropical jet at 14–16 km is located south of the eruption, and the ASMA southwest to Sarychev, both influencing the transport of volcanic sulphur emitted by Sarychev in June. In the measurements of MIPAS OCS (Glatthor et al., 2017) likewise detected transport of mid-latitude air masses around the ASMA towards the equator, at about 17–18 km altitude.
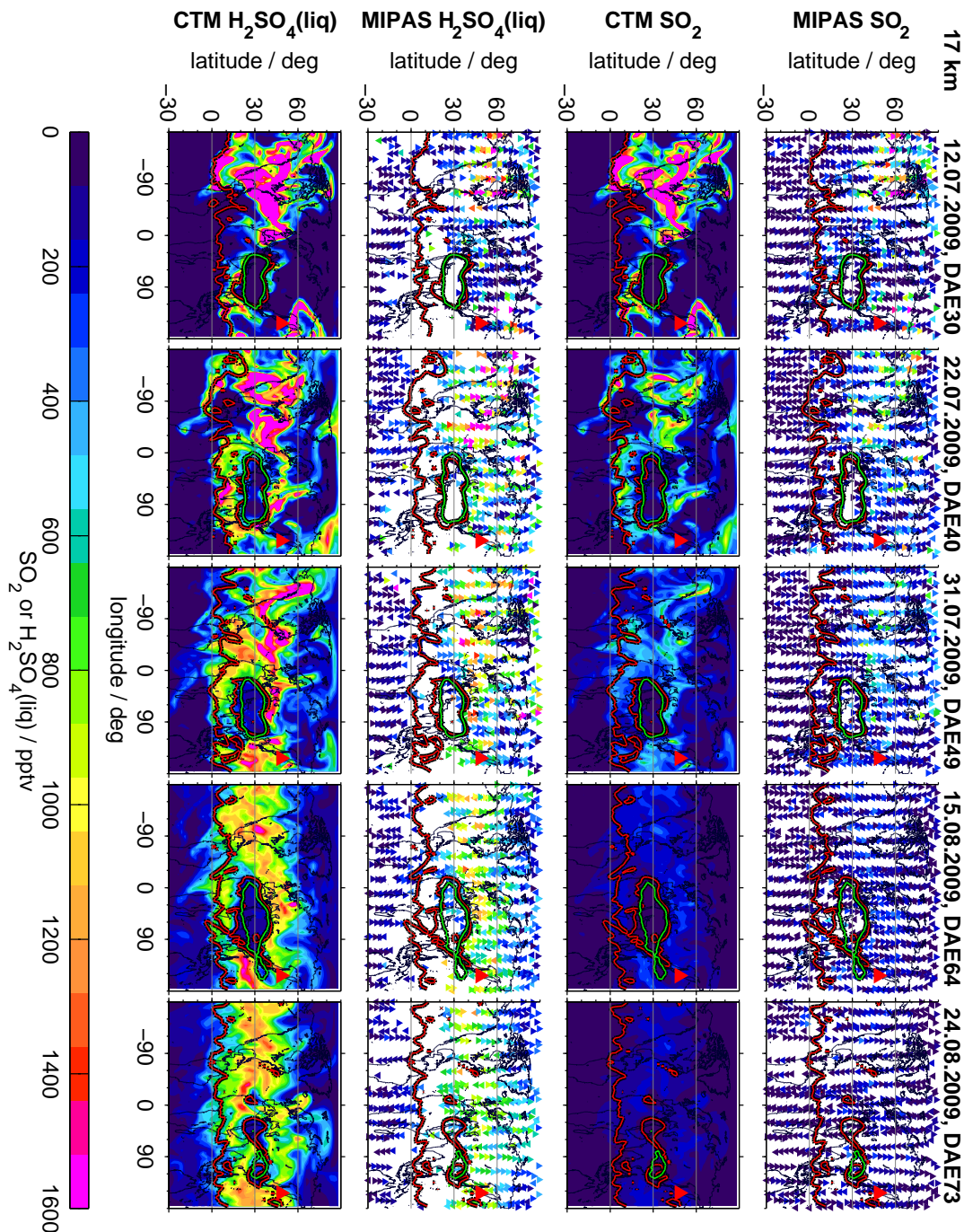
FIGURE 4.22: [Figure rotated by 90°] Horizontal distributions of sulphur dioxide and sulphate aerosol at 17 km after the eruption of Sarychev (12 Jun 2009), showing the influence of the Asian Summer Monsoon Anticyclone. MIPAS: SO$_2$sgl; CTM: CSa09 (ESRad 0.5 μm). The barrier of the Asian Summer Monsoon Anticyclone is indicated as 14.32 m geopotential height on the 150 hPa level (green) and as 1.8 PVU on the 370 K isentrope (red). Indicated are the date and DAE. Values exceeding the colour-scales are assigned with the limiting values.

The dispersion of the volcanic sulphur plume towards the south after the eruption of Kasatochi is weaker and starts at higher altitudes, compared to the Sarychev plume. The eruption of Kasatochi happened in the beginning of August, while the eruption of Sarychev was in June, in the beginning of boreal summer. The temporal difference leads to a shorter influence of the ASMA on the sulphur transport

after the eruption of Kasatochi and is expected to contribute to the differences in the southward transport.

4.3.4   Vertical split of the sulphur plume after the eruption of Kasatochi

As has been shown in Fig. 4.8, the volcanic sulphur plume after the eruption of Kasatochi on the 7 Aug 2008 was separated into an upper and lower part. The causes for this 'double-plume' are further investigated in this section. In Fig. 4.23 measured and simulated sulphur dioxide and sulphate aerosol are presented as zonal distributions of vertically resolved averages over 30°N–90°N, for various days after the eruptions (DAE) of Kasatochi and Sarychev (DAE 0–30). As noted before, shortly after the eruptions differences between the measured and modelled sulphur are large. About half a month after the eruptions the agreement between simulated and measured patterns of enhanced sulphur loading improves. The simulation of volcanic sulphur emitted by Kasatochi reveals a stronger eastward transport of the bulk of sulphur at low altitudes($< \sim$15 km), compared to higher altitudes. The difference in strength of the westerlies in the mid-latitudes, depending on altitude, could be seen in Fig. 4.13 and 4.14, which show horizontal wind fields. The lower part of the plume surrounds the globe in about 13–14 days. The different transport speeds at higher and lower altitudes are one of the causes for the vertical split of the plume. Even though in the case of Sarychev a similar faster transport towards the east is observed and modelled at lower altitudes, the entire altitude region is covered by sulphur, which hinders a double-plume to appear. Haywood et al. (2010) did a model study on the eruption of Sarychev and found that sulphate aerosol surrounded the globe in $\sim$14 days. This is consistent with the time scale of the present findings at lower altitudes.

To further analyse the occurrence of a double-plume as seen in the case of the Kasatochi eruption in 2008, the following simulations were performed:

- 'switched locations'

  - 'CKa08$_{switch:loc}$': SO$_2$ mass from Kasatochi injected at the location of Sarychev (7 Aug 2008, 48.1°N/153.2°E)

  - 'CSa09$_{switch:loc}$': SO$_2$ mass from Sarychev injected at the location of Kasatochi (12 Jun 2009, 52.2°N/175.5°W)

- 'switched locations and dates'

  - 'CKa08$_{switch:loc\&day}$': SO$_2$ mass from Kasatochi injected on the date and at the location of Sarychev (12 Jun 2009, 48.1°N/153.2°E)

  - 'CSa09$_{switch:loc\&day}$': SO$_2$ mass from Sarychev injected on the date and at the location of Kasatochi (7 Aug 2008, 52.2°N/175.5°W)

For these simulations vertically resolved time series of area weighted zonal means are shown in Fig. 4.24 for 30°N–90°N, in comparison to Fig. 4.8. None of these simulations shows a clear separation into an upper and lower part of the plume, as has been simulated and observed for the 'real' eruption of Kasatochi. This is true even when injecting the Kasatochi SO$_2$ masses at the Sarychev location, which is at

a distance of only ∼2,260 km and at a comparable latitude. The CTM simulations reveal that a rather specific combination of prevailing transport – in the CTM calculated based on wind fields and heating rates – with a certain vertical distribution of injected SO_2 masses is needed to produce such a double-plume.
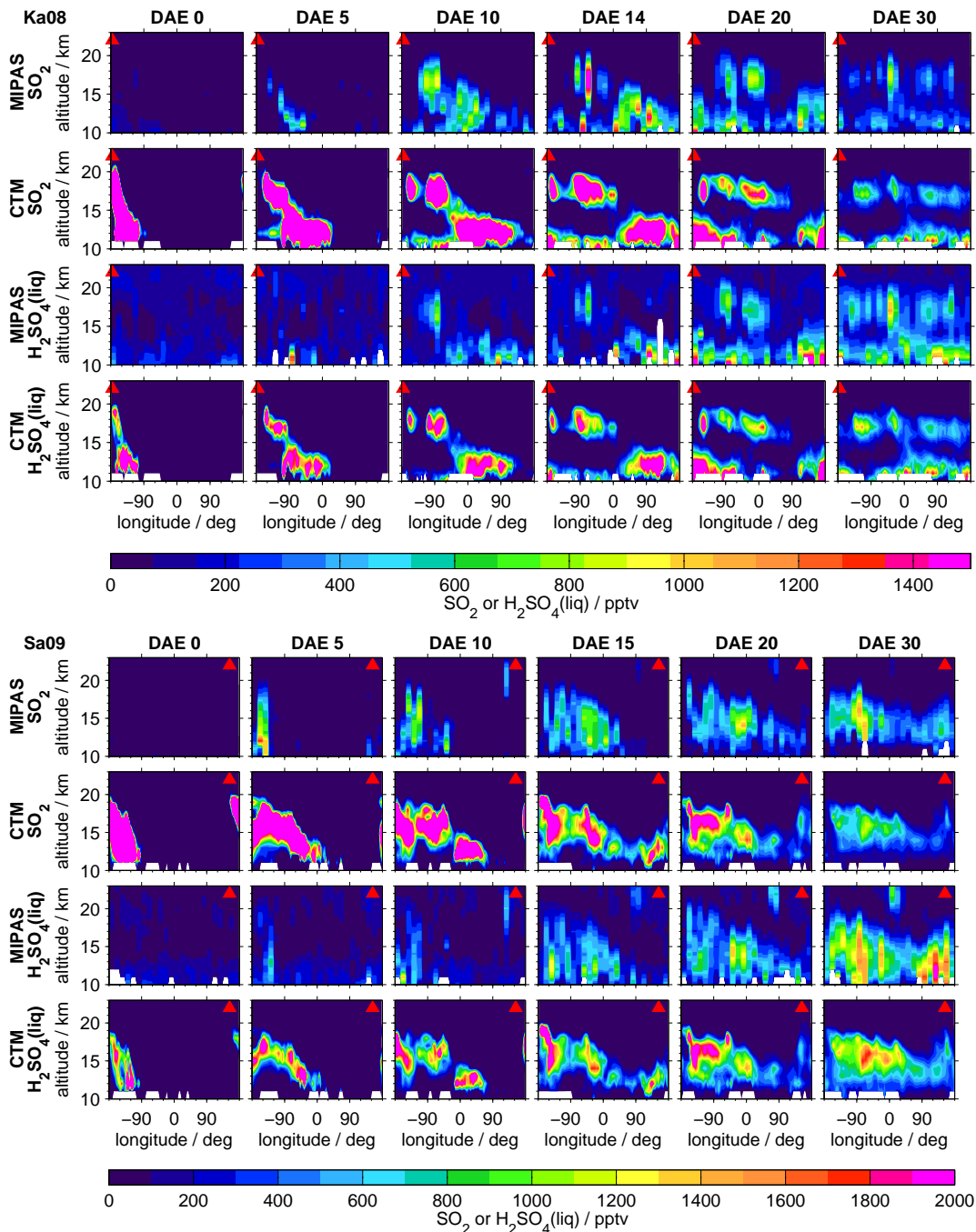
FIGURE 4.23: Vertical distributions of the volcanic plumes of Kasatochi (07 Aug 2008) and Sarychev (12 Jun 2009) at 30°N–90°N. MIPAS and CTM SO_2 and liquid-phase H_2SO_4 volume mixing ratios for various days after the eruptions. Vertically resolved longitudinal distributions of area weighted 3 d averages. Model results are 3.75° and measurements 15° longitude bins. MIPAS: SO_2sgl; CTM: simulations CKa08 and CSa09 (ESRad 0.5 μm). A red triangle shows the location of the volcanoes. Indicated are the days after eruption (DAE). Values exceeding the colour-scales are assigned with the limiting values.
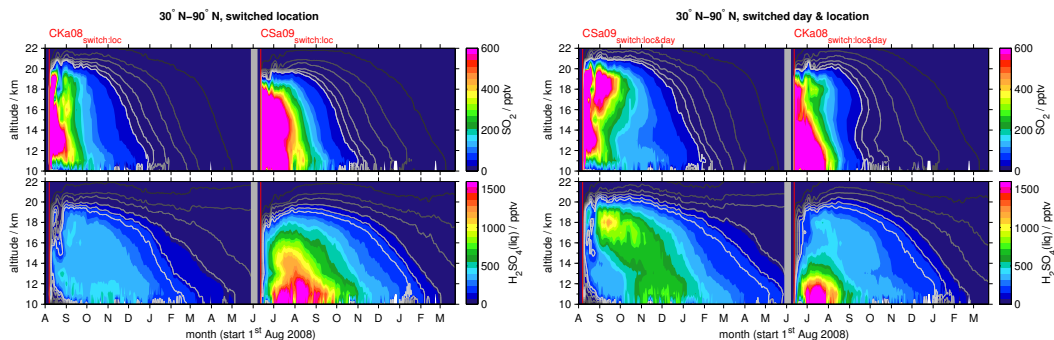
FIGURE 4.24: CTM: vertical distributions of volcanic plumes for simulations CKa08$_{\text{switch:loc}}$, CSa09$_{\text{switch:loc}}$, CKa08$_{\text{switch:loc\&day}}$, and CSa09$_{\text{switch:loc\&day}}$. Vertically resolved time series of simulated sulphur dioxide and sulphate aerosol (ESRad 0.5 μm) at 30°N–90°N (area weighted zonal means). Left panels: simulations with switched locations; right panels: simulations with switched days and locations (switch between Ka08 and Sa09). Simulations are separated by a vertical grey line. Values exceeding the colour-scales are assigned with the limiting values.

4.3.5   Lifetime of stratospheric sulphur

As could be seen in Fig. 4.7 for time series of sulphur mass after the eruptions of Kasatochi (2008) and Sarychev (2009), the mass of volcanically emitted sulphur decays with time, if no additional sulphur injections occur. From this decrease, e-folding lifetimes of volcanic sulphur in the stratosphere can be computed. Masses are calculated as described in Section 4.3.1, from data that is filtered for tropospheric values using NCEP tropopause heights (Kalnay et al., 1996), re-sampled to the CTM horizontal grid. Lifetimes are derived for the integrated sulphur mass contained in sulphur dioxide and sulphate aerosol between 9.5 and 23.5 km (only stratospheric values) and 30°N–90°N. The altitude limits correspond to the limited availability of MIPAS data (SO$_2$sgl). Due to the exponential decrease of air density with altitude, and a corresponding decay of sulphur mass densities, the sulphur contained at stratospheric altitudes above 23.5 km only has little effect on the integrated stratospheric sulphur mass. For the same reason the lower altitude limit is more important. Partly, tropospheric altitudes are not covered by the lower altitude limit of the observational data set, and additionally missing values due to filtering of the retrieved data at low stratospheric altitudes may impact the derived sulphur masses. Therefore, the presented data might imply a low bias.

The calculation of e-folding lifetimes from time series of stratospheric sulphur masses is adapted from Höpfner et al. (2015), where e-folding lifetimes were derived from MIPAS SO$_2$sgl masses for several volcanic eruptions. A linear least squares fit is performed to represent the time series of sulphur masses in the logarithmic space. To estimate the uncertainty of the lifetimes, various fitting intervals are chosen, during which decay in the logarithmic space is close to linear. As has been noted before (Sect. 4.3.1), in the first month after the eruptions MIPAS underestimated the sulphur mass. Therefore, the sulphur mass at the day of the eruption is chosen as the sulphur mass of the linear fit on the eruption day. This is shown in the first row of Fig. 4.25, as the intersect between the vertical black line that indicates the eruption day, and the exponential fitted curves. Lifetimes are indicated by vertical coloured lines.
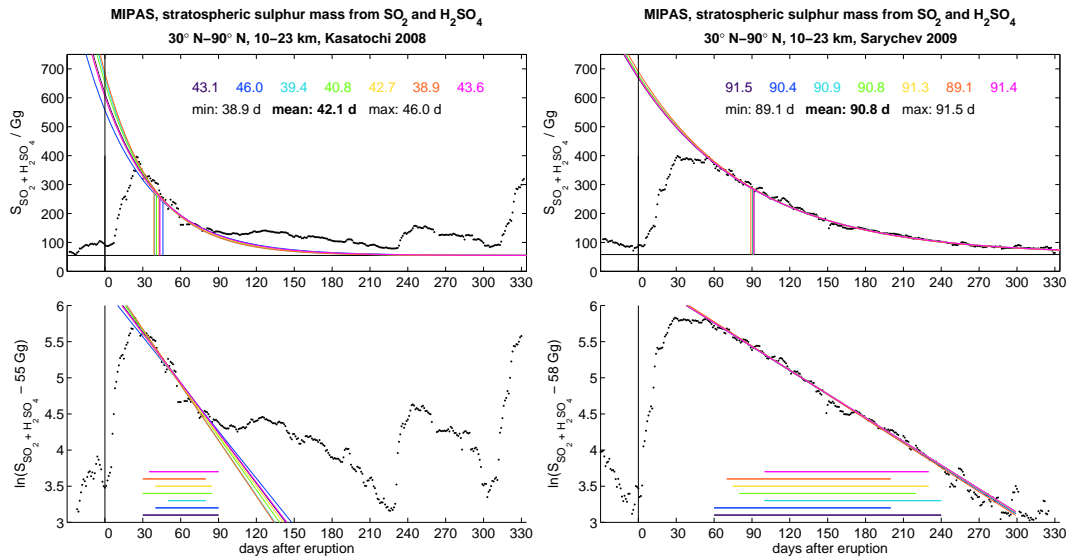
FIGURE 4.25: e-folding lifetimes of volcanic stratospheric sulphur after the eruptions of Kasatochi in 2008 (left) and Sarychev in 2009 (right). Shown are time series of measured (MIPAS) sulphur masses as contained in sulphur dioxide (SO_2sgl) plus sulphate aerosol, integrated over 30°N–90°N and 10–23 km. Masses are calculated as in Section 4.3.1, and filtered for tropospheric values using NCEP tropopause heights (on the CTM horizontal grid). First row: linear scale; second row: logarithmic scale. e-folding lifetimes are derived from a linear fit to the logarithmic sulphur masses (second row; reduced by a background mass, as indicated by a black horizontal line in the upper panels). The e-folding lifetimes are the number of days between the eruption day (sulphur mass S_{day_0}; vertical black lines) and the day when the sulphur mass reaches $\frac{1}{e}S_{day_0}$ (vertical coloured lines). Different fit-periods are indicated by coloured horizontal lines. e-folding lifetimes are given in the upper plots, together with their minimal, mean and maximal values.

In the case of Kasatochi, downward transport of the upper part of the volcanic plume (Sect. 4.3.2) leads to a second increase around 80–90 days after the eruption, and after ∼220–230 d the eruption of Redoubt additionally interferes with the measured sulphur masses from Kasatochi. This complicates the calculation of e-folding lifetimes. Time intervals for the fit are short, and as can be seen in Fig. 4.25 no good agreement can be achieved between the measured sulphur mass and fitted data. Calculated e-folding lifetimes for stratospheric sulphur after the eruption of Kasatochi are between 38.9 and 46.0 days, with the mean value being 42.1 d. These values have to be considered with precaution, however.

For the eruption of Sarychev Peak in 2009, it is possible to derive a good fit to the measured stratospheric sulphur loading, and resulting e-folding lifetimes are more reliable. Intervals can be chosen to be longer, as no other volcanic eruptions interfere strongly with the measurements, and due to the more homogeneous vertical distribution of sulphur (Sect. 4.3.2). The spread of e-folding lifetimes is low (89.1–91.5 d), and the average is 90.8 d. This is more than double the e-folding lifetime derived for the eruption of Kasatochi, which can be explained by the relatively fast removal of a major part of the injected sulphur after the eruption of Kasatochi, as the SO_2 has been injected at relatively low altitudes in the mid-latitudes (Sect. 4.3.2). As the lifetimes are based on measured sulphur as contained in SO_2 plus liquid-phase H_2SO_4, chemistry effects are low, but removal by transport dominates.

When applying the same method to simulated volcanic sulphur for simulation CSa09 (ESRad 0.5 μm), e-folding lifetimes are lower than for MIPAS data (Fig. 4.26). For the CTM they range between 79.1–85.7 d, and the average lifetime is 81.9 d. Fitting intervals are chosen differently, to improve the agreement between the fitted curves and the simulated data. When using the fit intervals from the CTM for MIPAS, the mean MIPAS e-folding lifetime is changed insignificantly, from 90.8 d to 89.8 d (lifetimes range between 88.6–90.9 d). The relatively low values simulated early after the eruption of Sarychev at 30°N–90°N (Fig. 4.26), are connected to the modelled southward transport of sulphur shortly after the eruption, as discussed in Section 4.3.2.
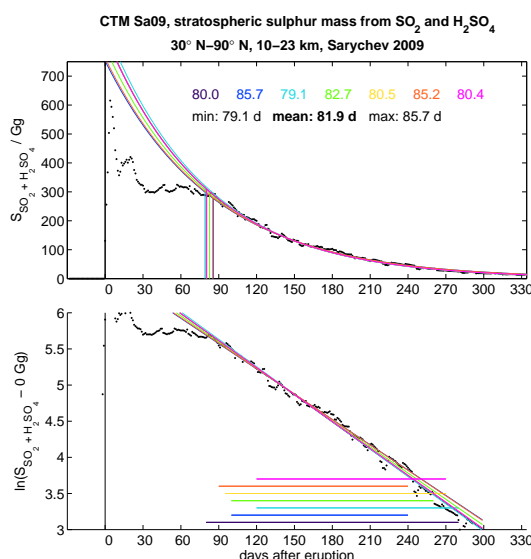
FIGURE 4.26: As Fig. 4.25, but for simulated sulphur after Sa09 (CSa09). No background is added, as the simulation background is 0 pptv.

Two publications shall further be mentioned here, regarding the impact on climate resulting from the eruptions of Kasatochi in 2008 and Sarychev in 2009. Interestingly, for the eruption of Kasatochi, in combination with the by far smaller eruption of Okmok that preceded only one month earlier at a very close distance (12 Jul 2008, 53.4°N/168.1°W), Kravitz et al. (2010) calculated a negligible climatic effect from an injected mass of 1.6 Tg SO_2. The reason for the low impact on surface temperature has been assigned to the eruption of Kasatochi having occurred too late in the year (7 Aug), resulting in too little insolation that could be backscattered by the volcanic aerosol. As Sarychev erupted earlier during the year (12 Jun), and due to the higher amount of aerosol that resides in the stratosphere for a rather long period of time, with stratospheric sulphur e-folding lifetimes of almost three months, the climatic effect of this eruption is expected to have had a higher impact on surface temperatures. However, also for the eruption of Sarychev, Haywood et al. (2010) stated that the cooling will 'likely not be detectable in the observational record', even though model simulations showed a radiative impact by the Sarychev aerosol in their study.

5 Stratospheric sulphur during 'non-volcanic' periods

In the present chapter the distribution and sulphur loading during non-volcanic / background conditions are assessed. As has been shown before, the main source for variability of stratospheric sulphur dioxide and sulphate aerosol are volcanic eruptions, and the stratospheric sulphur loading has been influenced by eruptions during the majority of the MIPAS measurement period (Jul 2002–Apr 2012). In the previous chapter (Chap. 4) the study mainly focused on volcanic perturbations, when SO_2 is injected into the atmosphere by volcanic eruptions and volcanic sulphate aerosol is formed. Consistency between MIPAS SO_2sgl and MIPAS sulphate aerosol in terms of mass and temporal evolution has been shown for the relatively intense eruptions of Kasatochi (2008) and Sarychev (2009). During background conditions not only sulphur dioxide and sulphate aerosol need to be considered, but additionally carbonyl sulphide (Thomason and Peter, 2006; Kremser et al., 2016). The OCS is mainly emitted at the surface (dominated by emissions from the oceans) and transported towards the stratosphere. As tropospheric OCS is relatively inert it has a long lifetime (atmospheric lifetime $\geq$ 2.8 years in Griffith et al., 1998; 2–6 yr in Barkley et al., 2008), largely affected by uptake by the biosphere (e.g., Glatthor et al., 2015, and references therein). The OCS can be well mixed in the troposphere and reach the stratosphere, primarily through the Tropical Tropopause Layer (TTL), the main region for air from below to enter the stratosphere (e.g., Kremser et al., 2016). Rather long time periods are needed for air to cross the tropopause, if not entering through special events, such as strong convection, explosive volcanic eruptions or strong pyrocumulonimbus clouds.

5.1 Carbonyl sulphide

Carbonyl sulphide volume mixing ratios have been retrieved from MIPAS measurements (single limb-scans) and were described by Glatthor et al. (2015, 2017). The MIPAS OCS data were further presented shortly in Section 2.1. In this chapter, MIPAS measurements of carbonyl sulphide and their contribution to stratospheric sulphur are discussed in combination with CTM simulations.

5.1.1 Measured and modelled OCS

Time series of MIPAS OCS are presented in Fig. 5.1, as latitudinally resolved volume mixing ratios at various altitudes (10–24 km), and vertically resolved data at different latitudes (30° latitude bins). Measured and simulated (BGO) OCS volume mixing ratios are shown in Fig. 5.3 as seasonal vertically and latitudinally resolved

distributions. Additionally, for better comparability of the absolute values and the differences between observed and modelled carbonyl sulphide, profiles of seasonal mean VMRs are presented in Fig. 5.4, for 30° latitude bins, together with their absolute differences (Fig. 5.5).

In the model (simulation BGO) a bottom boundary of OCS is considered as the only sulphur source (Sect. 3.4.1), which is based on MIPAS measurements at 8–12 km. Figure 5.2 shows the bottom boundary of OCS as time series of OCS VMRs for 30° latitude bins. The bottom boundary consists of a climatology of daily VMRs, and does not include any inter-annual or zonal variability. In the CTM, OCS is destroyed by photolysis, which is the dominant process releasing sulphur from OCS in the stratosphere (Brühl et al., 2012). The reactions of OCS with oxygen or hydroxyl radicals are not considered in the model, due to their minor importance.

OCS is distributed rather homogeneously in the troposphere. Tropical values are in the range ∼500–540 pptv at altitudes between ∼10–16 km, with the upper limit denoting roughly the tropical tropopause height. Highest stratospheric values are observed in the lower tropical stratosphere, as a consequence of broad up-welling (Glatthor et al., 2017). At higher altitudes OCS VMRs decrease towards 0 pptv with a strong gradient. During winter, relatively OCS-free air is transported downwards in the polar vortex, especially in the Southern hemisphere. In general, model results agree well with MIPAS OCS. OCS photolysis rates show a very strong increase from close to zero to ≥ 1 yr^{-1} at approximately 24–28 km (Fig. 3.6). This is reflected in the strong decrease of OCS VMRs in the stratosphere. Differences between MIPAS and the CTM are located especially in the tropics at low altitudes, with higher modelled OCS. Furthermore, at higher altitudes in the tropics simulated OCS decreases towards 0 pptv at lower altitudes, compared to MIPAS. CTM data were not convolved with MIPAS averaging kernels (AKs). During the retrieval process, a regularisation leads to smoothing of the profiles (Glatthor et al., 2017). A signal in a measured spectrum can lead to enhancements in retrieved VMRs at surrounding altitudes. Glatthor et al. (2017) present an example profile of MIPAS OCS, together with the corresponding AKs. These provide information about the contribution by signals from different altitudes to the retrieved profile. An AK that is symmetrically distributed to its middle value shows that information results from measurements at the nominal altitude. For the OCS profile presented in Glatthor et al. (2017) this is the case between 10–19 km. At stratospheric altitudes, however, the AKs are not centred at the nominal altitude but displaced towards lower altitudes (up to 2 km at 40 km). Therefore, the signal causing high retrieved OCS VMRs lies below the nominal altitude and lower OCS loading would be expected if AKs were symmetrically distributed. This suggests that the difference between MIPAS and the CTM in the tropics at above ∼32 km is due to non-centred AKs. Additionally, in the stratosphere, the vertical resolution of the OCS retrieval is lower (> 10 km in the upper stratosphere) than in the troposphere (4–5 km) (Glatthor et al., 2017).
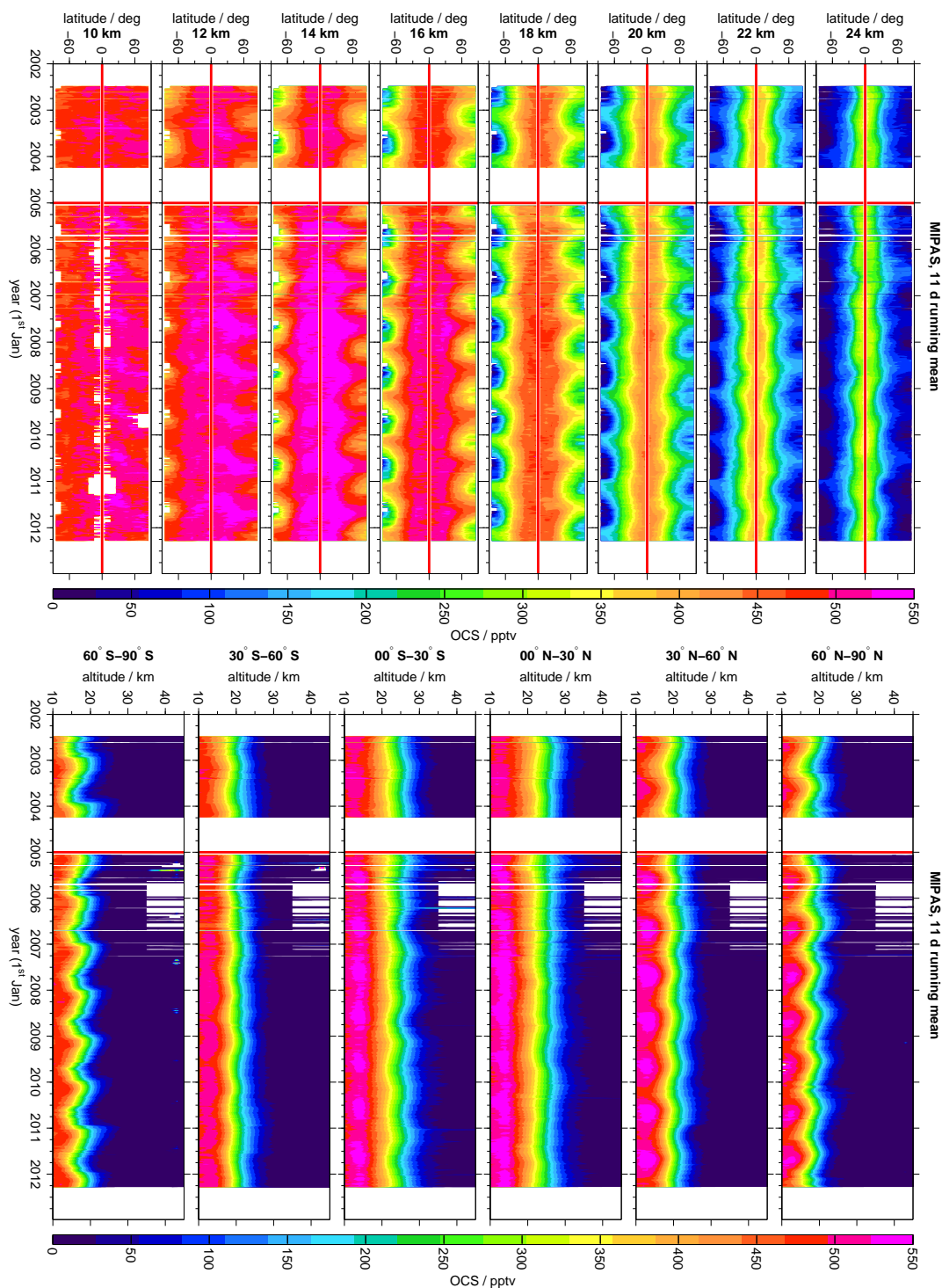
FIGURE 5.1: [Figure rotated by 90°] Time series of MIPAS OCS volume mixing ratios (2002–2012). Left panels: latitudinally resolved time series of zonal averages for various altitudes from 10–24 km. Right panels: vertically resolved time series for 30° latitude bins (area weighted averages). All data are 11 d running means. A horizontal red line indicates the equator and a vertical red line indicates the transition between the MIPAS measurement periods. Values exceeding the colour-scales are assigned with the limiting values.
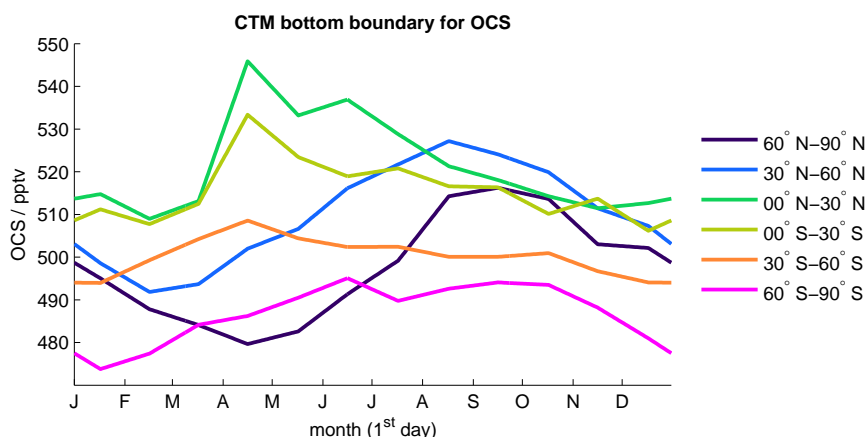
FIGURE 5.2: CTM: bottom boundary of OCS, as derived from MIPAS measurements. Mean OCS VMRs for 30° latitude bins (area weighted averages), as time series of daily values.
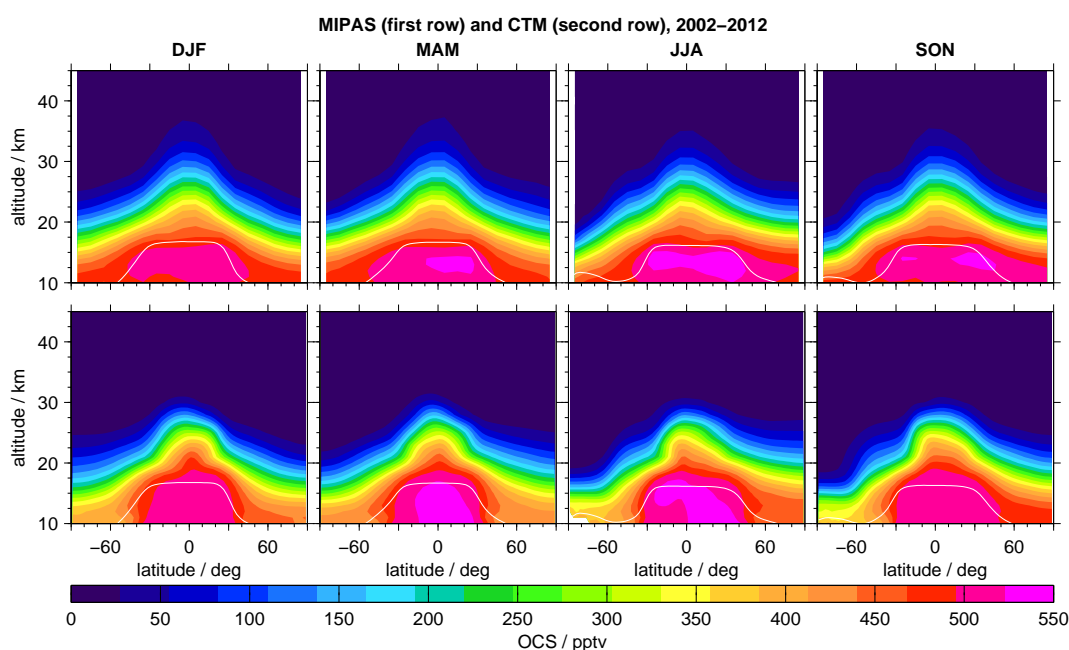
FIGURE 5.3: Seasonal MIPAS and CTM (BGO) OCS volume mixing ratios, and tropopause heights. Vertically resolved meridional distributions. Seasonal means are calculated from a monthly climatology for 2002–2012. The white contour lines indicate seasonal tropopause heights (NCEP, 2002–2012). MIPAS (first row): 10° latitude bins. CTM (second row): ∼2.5° latitude bins. Values exceeding the colour-scale are assigned with the limiting values.

Mostly, the absolute differences between MIPAS and CTM profiles of OCS are in the range of estimated errors for MIPAS OCS (40-50 pptv at 10–20 km, 120 pptv at 40 km) given in Glatthor et al. (2017). Larger differences are found in the Southern hemisphere, especially during austral winter and spring in the polar region (> 100 pptv, ∼15–20 km). As OCS is a long-lived trace-gas, its simulated distribution is strongly connected to the model age of air, a metric of the transport speed and mixing (see also Sect. 3.2). The CTM AoA has rather low values in the polar region of the Southern hemisphere during austral winter and a relatively strong gradient from low values in the tropics towards higher values in the extra-tropics at around

20 km (Fig. 3.3). Young air at polar latitudes means that the transport towards high latitudes is rather fast. Furthermore, compared to the AoA that has been derived from MIPAS measurements (Haenel et al., 2015), the tropical pipe seems to be more pronounced in the CTM, with a sharper transition to extra-tropical values of AoA. This distribution of AoA is reflected in modelled OCS. In the following (Sect. 5.2.2) it will be demonstrated that the extra-tropical differences observed between measured and modelled OCS are not of importance for the SO_2 that is formed from sulphur that is released by photolysis of OCS.
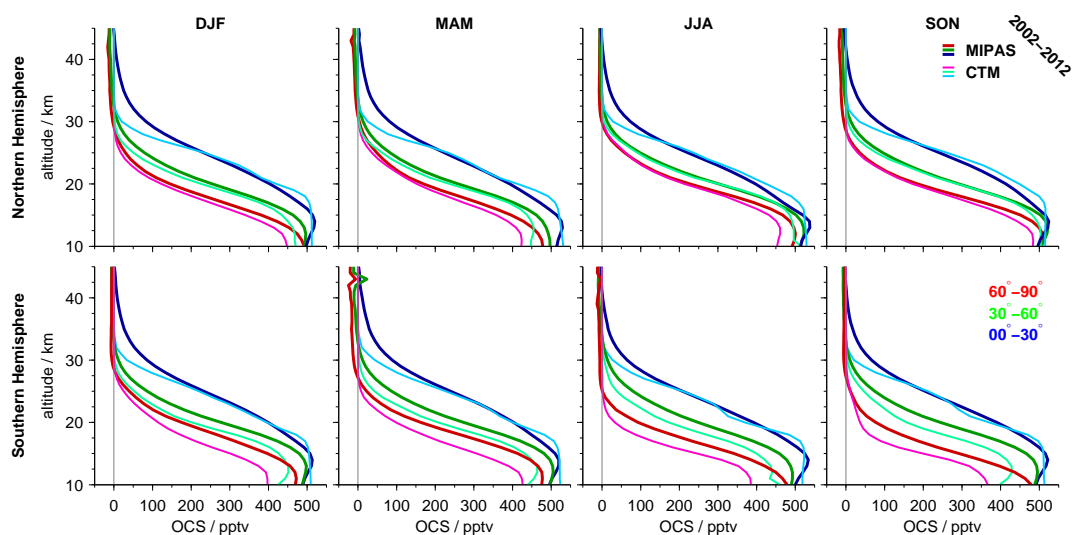
FIGURE 5.4: OCS data as in Fig. 5.3, but as vertical profiles per season and 30° latitude bin (area weighted averages). Columns: seasons; rows: northern and Southern hemisphere.
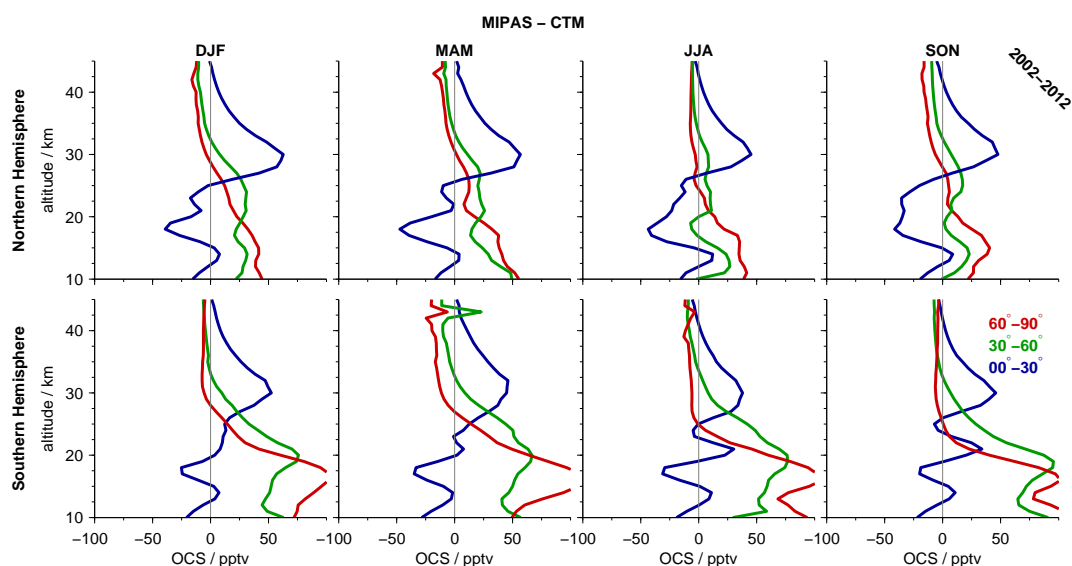
FIGURE 5.5: As Fig. 5.4, but for the absolute difference between measured and simulated OCS (MIPAS-CTM).

5.1.2 Modulation by the QBO

At the equator the prevailing direction of zonal wind changes with a phase of roughly two years (see Fig. 3.4, Section 3.3). This quasi-biennial oscillation between westerlies (positive phase) and easterlies (negative phase) develops at stratospheric altitudes (~35–37 km) and propagates downwards with time. The impact of changes in the main wind direction on available OCS in the tropical stratosphere is clearly visible in Fig. 5.6 and 5.8, both in the measurements and simulations. In Fig. 5.6 latitudinally resolved time series of OCS are presented for altitudes of 25 and 30 km, while in Fig. 5.8 time series of tropical OCS VMRs are shown for 15°S–15°N (25–30 km). In a similar way, the speed and direction of zonal wind are presented for 5°S–5°N in Fig. 5.7.

During the positive phase of the QBO, when the main wind direction is from the west and wind speed is generally lower, less OCS reaches high altitudes, while during the easterly phase, when wind speed is higher, OCS undergoes stronger uplift and can reach relatively high altitudes. Time series of zonal wind show a typical time shift of the phases of the QBO towards later times at lower altitudes, as the pattern of prevailing wind direction in the equatorial region is propagating downwards with time. Measurements and model results compare well in terms of the phase of the intensity of upwelling of OCS, while the amount of OCS shows some differences. At 25 km, improved agreement is found during the positive phase of the QBO when the OCS loading is lower, while at 30 km, constantly higher values are retrieved from MIPAS measurements, than simulated in the CTM. This difference at 30 km is most probably connected to smoothing applied during the retrieval process, as has been discussed in the latter section (5.1.1). Brühl et al. (2015) found a similar pattern of higher OCS VMRs during the negative phase of the QBO in simulations of OCS with EMAC.
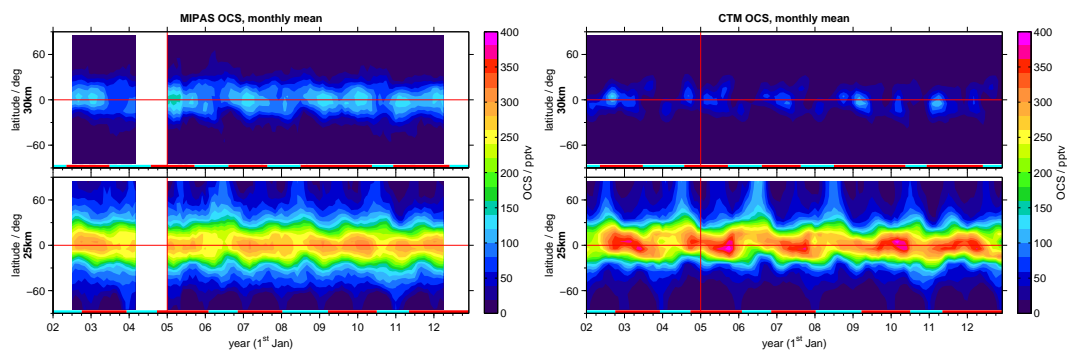
FIGURE 5.6: Influence of the QBO on OCS VMRs at 25 and 30 km. Latitudinally resolved time series (2002–2012) of OCS from MIPAS and CTM (BGO), as monthly means. Left panels: MIPAS; right panels: CTM. A horizontal red line indicates the equator, and a vertical red line indicates the transition between the MIPAS measurement periods. Indicated by blue and cyan horizontal lines is the phase of the QBO (blue: negative, cyan: positive). Values exceeding the colour-scale are assigned with the limiting values.
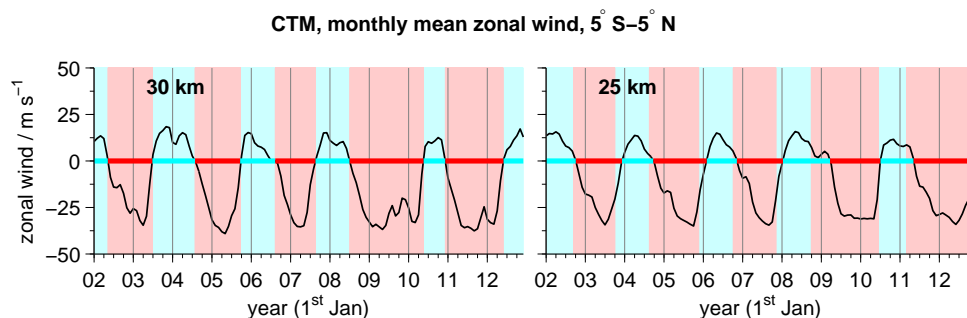
FIGURE 5.7: Tropical zonal wind speed and direction (from the CTM), as time series (2002–2012), at 25 and 30 km. Monthly zonal averages for 5°S–5°N (area weighted averages). Positive (negative) values denote prevailing eastward (westward) wind. Indicated by red and cyan shadings is the phase of the QBO (red: negative, cyan: positive).
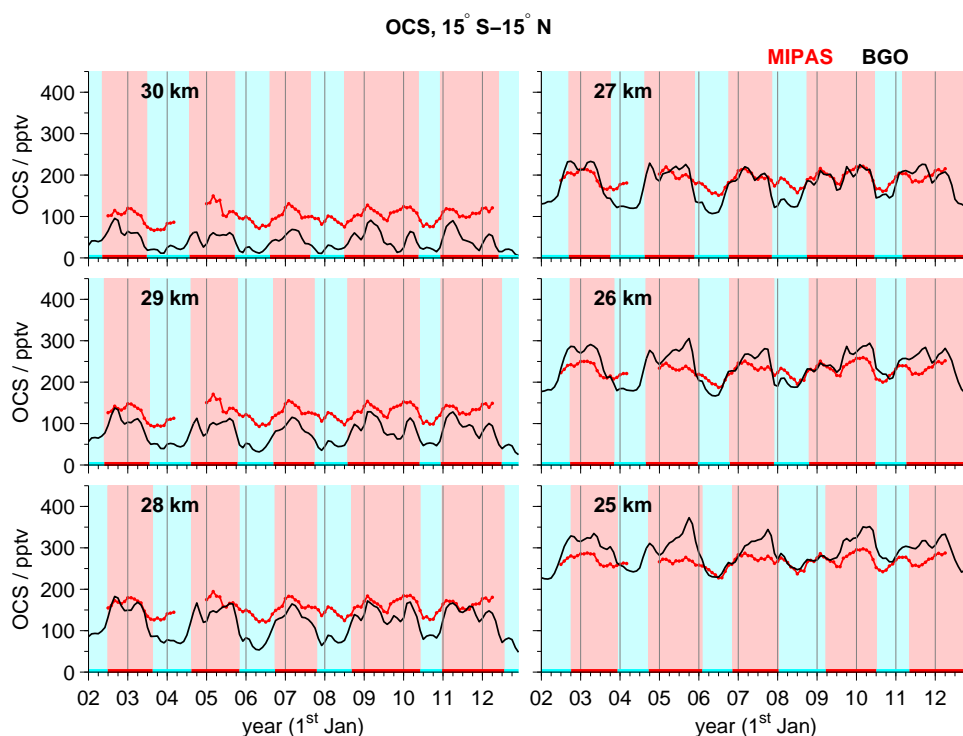
FIGURE 5.8: Time series of tropical measured (MIPAS, red) and modelled (CTM/BGO, black) OCS volume mixing ratios for 2002–2012. Monthly area weighted averages for 15°S–15°N at altitudes of 25 to 30 km. Indicated by red and cyan shadings is the phase of the QBO (red: negative, cyan: positive).

5.1.3 Effect of extra-tropical and seasonally variable tropospheric OCS on stratospheric OCS

The simulation BGO is based on a bottom boundary of OCS as the only sulphur source. This bottom boundary has been derived from MIPAS measurements and considers no inter-annual, but intra-annual variability. The variability is lowest in the Southern hemisphere and the amplitude at the equator between highest values in April and lowest values in February is approximately 33 pptv (∼512–545 pptv). A CTM simulation with constant bottom boundary for OCS shows that the effect of

the varying source strength of OCS in the troposphere, at the 335 K isentrope (centre of the lowermost model level), is restricted to altitudes below ∼18 km. Figure 5.9 shows globally averaged OCS (90°S–90°N) from a simulation with the standard bottom boundary derived from MIPAS, compared to a simulation with constant bottom boundary. The constant input of OCS is set to be 519 pptv, which is the mean tropical 'standard' bottom boundary. Model results are presented as time series of averaged volume mixing ratios for the altitude ranges 10.5–14.5, 14.5–18.5, and 18.5–22.5 km. The region of strongest sulphur release from OCS is in the tropics at ∼25–35 km (Brühl et al., 2012), when considering photolysis of OCS, and chemical reactions with oxygen (O), or OH. The SO_2 that is formed at these altitudes is not sensitive to the modulation of the OCS bottom boundary. As carbonyl sulphide is a relatively long-lived substance, it is well mixed during its transport through the troposphere. Therefore the amount of emitted OCS is important for stratospheric OCS, SO_2, and liquid-phase H_2SO_4, rather than the exact emission time.

Additionally, OCS is presented in a similar way in Fig. 5.9 for a simulation without OCS input polewards of 30°. In the extra-tropics, the bottom boundary is set to 0 pptv, while in the tropics, the standard bottom boundary from BGO is prescribed. Just as for a constant bottom boundary, the effect of the changed bottom boundary is only noticed at altitudes below ∼18 km, which confirms that the main entry pathway for OCS to the stratosphere is in the tropics. The main motion in the tropics is uplift, while in the extra-tropics subsidence via the Brewer-Dobson circulation is dominant. For the CTM a good representation of the bottom boundary in the extra-tropics is of minor importance.
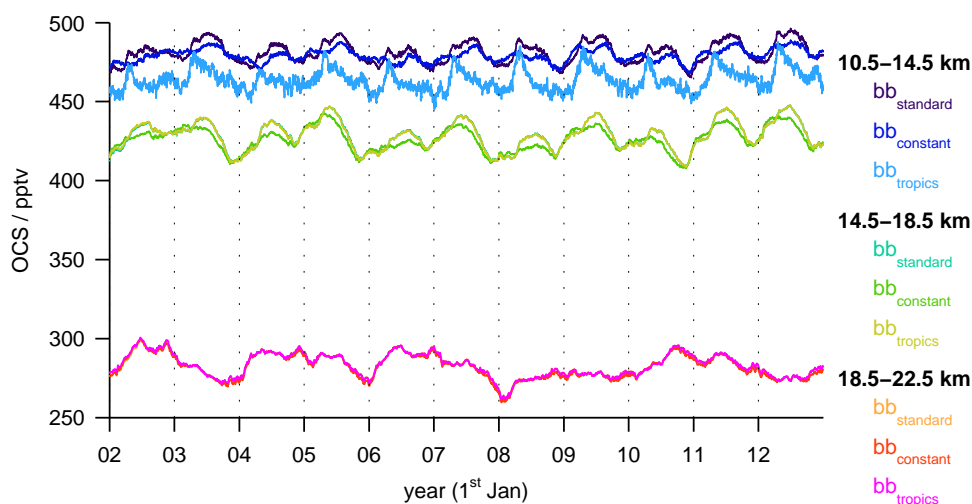
FIGURE 5.9: Influence of the CTM bottom boundary of OCS on stratospheric OCS. Comparison between a simulation with the 'standard' bottom boundary for OCS (BGO, 'bb$_{standard}$'), the same bottom boundary with 0 pptv OCS in the extra-tropics (CObb$_{trop}$, 'bb$_{tropics}$'), and a constant bottom boundary of 519 pptv OCS (CObb$_{const}$, 'bb$_{constant}$'). 519 pptv is the average of the standard bottom boundary at 30°S–30°N. Time series (2002–2012) of modelled OCS volume mixing ratios for 90°S–90°N, for various altitude ranges (10.5–22.5 km). Area weighted daily averages.

5.2   Sulphur dioxide and sulphate aerosol

In this section the main focus lies on sulphur dioxide and sulphate aerosol under background or non-volcanic periods. However, to some extent volcanic influence remains in the measurements presented as 'non-volcanic'. This is mainly due to the relatively high frequency of explosive volcanic eruptions, but also due to difficulties in correctly assigning enhanced sulphur loading to volcanic eruptions, and the possibility that sulphur from silent volcanoes, which are de-gassing over longer periods, reaches the stratosphere (Textor et al., 2004 and references therein). In the present section primarily three MIPAS data sets are studied. These are the SO_2 and liquid-phase H_2SO_4 data sets that have already been analysed in Chap. 4 for volcanic periods. Both consist of retrievals from single limb-scans. Additionally, a second MIPAS data set of SO_2 (SO_2mea) finds its use in the present section. SO_2mea has been derived from monthly and regionally averaged limb-scans (zonal averages for $10°$ latitude bins), and is more suitable for background conditions. The data cover almost the entire stratosphere, from altitudes of 15–45 km. In combination with MIPAS OCS, and CTM simulations, the distribution of background SO_2 and sulphate aerosol, and contributions from different sources, are analysed.

5.2.1   Distribution of primarily non-volcanic MIPAS SO_2 and liquid-phase H_2SO_4

The MIPAS data sets of SO_2sgl and liquid-phase H_2SO_4 are presented as time series of latitudinally resolved zonal means at various altitudes in Fig. 5.10. Additionally, the data set of SO_2mea derived from averaged limb-scans is shown as vertically resolved time series of $30°$ latitude bins in Fig. 5.11. For MIPAS SO_2, months with relatively clear volcanic signals are not considered in this section, unless when analysing time series. The de-selected months are indicated by red/black crosses in Fig. 5.10 and 5.11. These months were chosen as in Höpfner et al. (2013) and Höpfner et al. (2015), respectively. For SO_2mea only data up to 25 km are filtered for volcanic influence. In the case of liquid-phase H_2SO_4, it is not straight forward to select months with low volcanic impact on the sulphate aerosol without discarding too many data. This is connected to the longer residence time of sulphate aerosol, compared to SO_2. A different approach is used, to provide a data set of 'background' sulphate aerosol. For $20°$ latitude bins, data with apparent volcanic influence are deselected, with respect to altitude and time (as in Fig. A.5). These regions are marked by red/black crosses in Fig. 5.10.
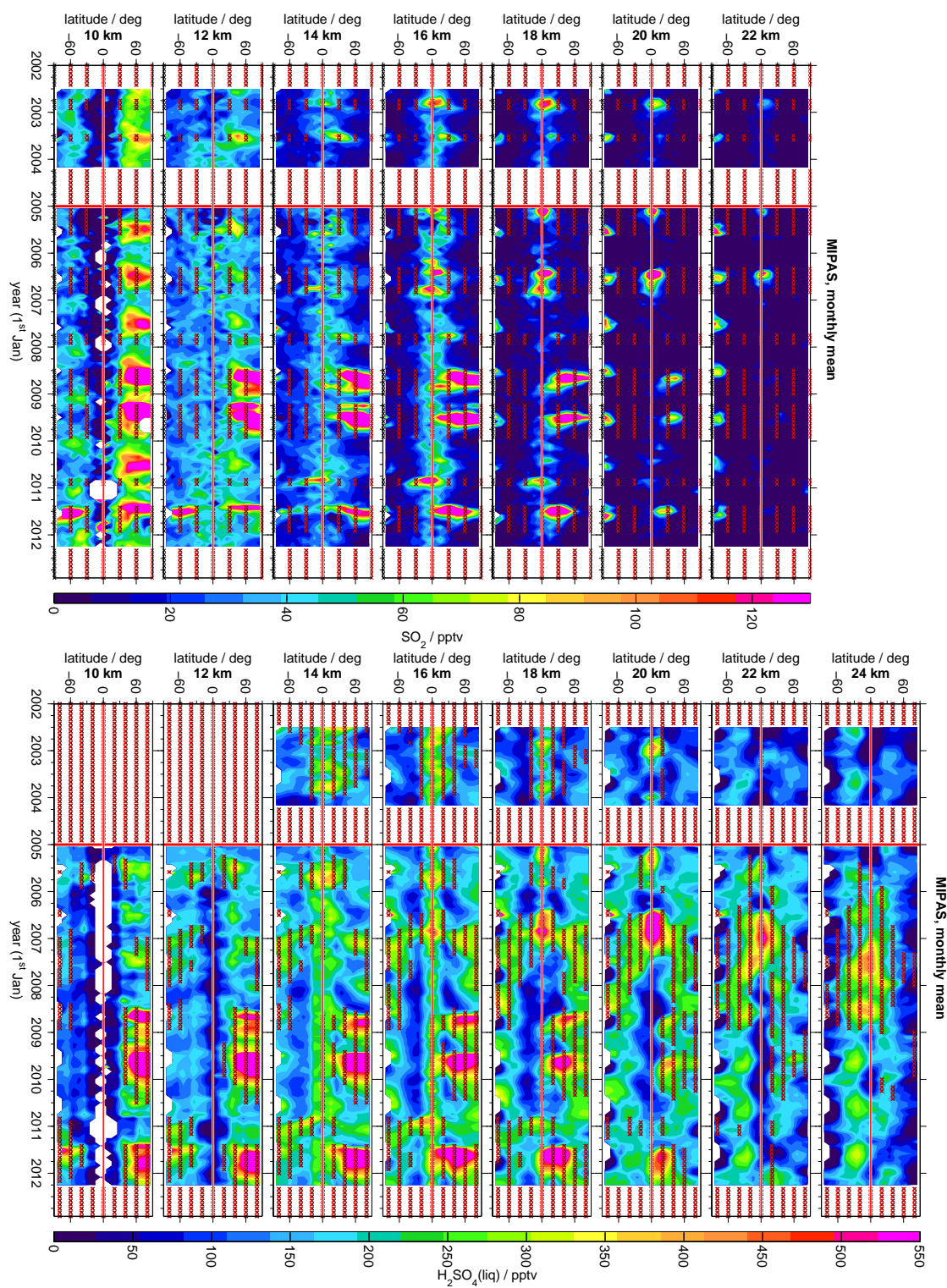
FIGURE 5.10: [Figure rotated by 90°] Time series of MIPAS SO$_2$sgl (left) and liquid-phase H$_2$SO$_4$ (right) volume mixing ratios for 2002–2012. Latitudinally resolved monthly means for 10° latitude bins at various altitudes (10–24 km). Periods that are not used for analyses of background conditions due to relatively strong volcanic influence are marked by red/black crosses. A horizontal red line indicates the equator. A vertical red line indicates the transition between the MIPAS measurement periods. Values exceeding the colour-scales are assigned with the limiting values.
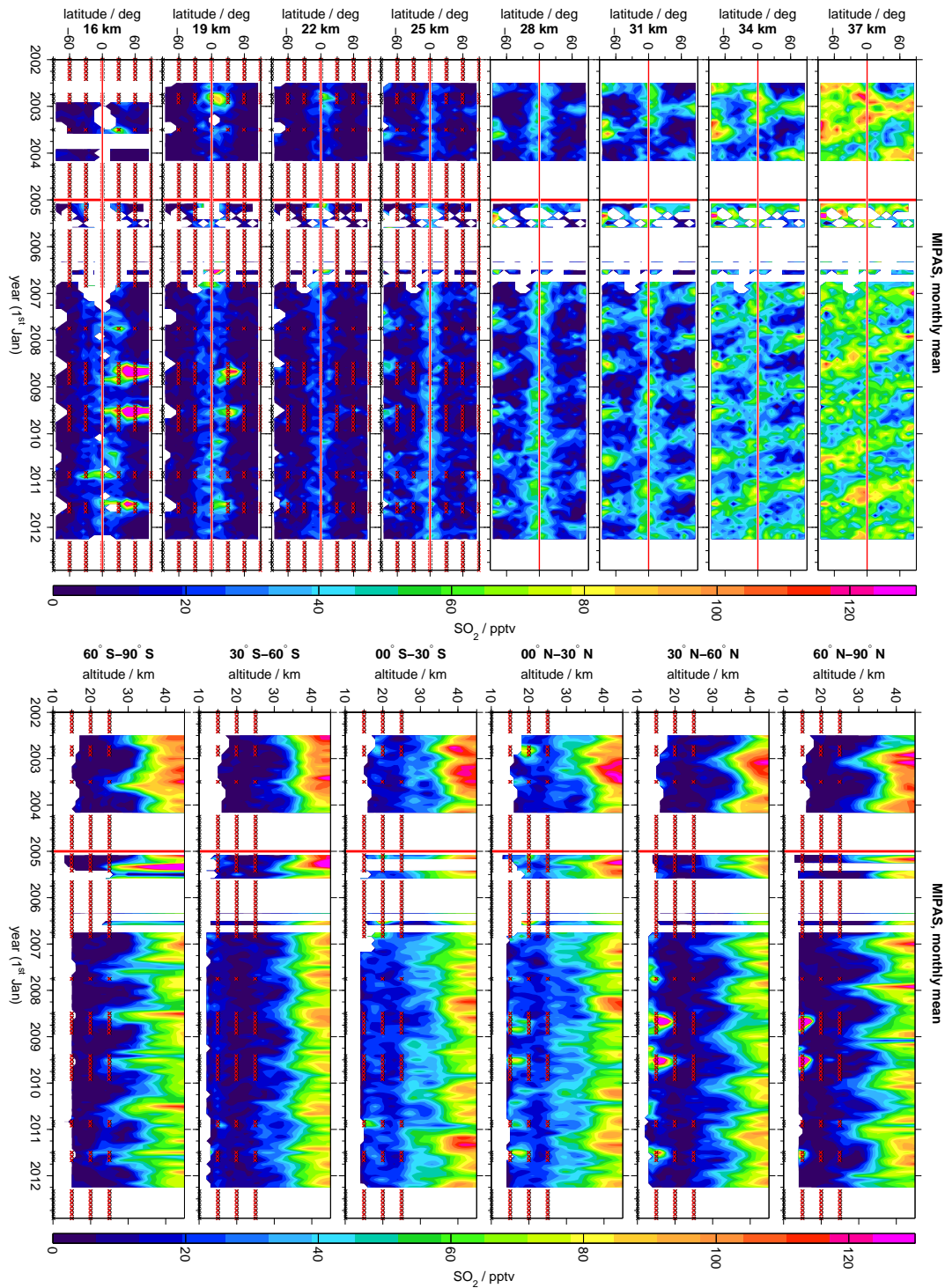
FIGURE 5.11: [Figure rotated by 90°] Time series of monthly MIPAS SO$_2$mea volume mixing ratios (2002–2012). Months that are not used for analyses of background conditions due to relatively strong volcanic influence are marked by red/black crosses. Left panels: latitudinally resolved time series of zonal averages for various altitudes from 16–37 km. Right panels: vertically resolved time series for 30° latitude bins (area weighted averages). A horizontal red line indicates the equator. A vertical red line indicates the transition between the MIPAS measurement periods. Values exceeding the colour-scales are assigned with the limiting values.

The seasonal mean distributions of MIPAS SO_2 and sulphate aerosol under background conditions are shown in Fig. 5.12 and 5.13, as vertically resolved zonal mean volume mixing ratios. Sulphur dioxide is averaged over the entire MIPAS measurement period (2002–2012), while the new data set of sulphate aerosol is shown individually for the first and second period (P1: 2002–2004; P2: 2005–2012).

MIPAS sulphur dioxide and sulphate aerosol distributions show several pronounced features, with approximately annual periodicity. For a clearer picture of several of the patterns, seasonal horizontal distributions of MIPAS SO_2sgl (2002–2012) and sulphate aerosol (2005–2012) are shown additionally in Fig. 5.14 and 5.15. Mainly, SO_2 shows enhanced values in the troposphere, and in the stratosphere close to the mean tropopause height. Further, especially in the tropics at ∼25–35 km SO_2 VMRs are elevated, and to a minor degree between the tropopause region and 25 km. Globally, MIPAS SO_2mea shows increasing values at altitudes above roughly 30 km, with varying lower altitude limits. MIPAS sulphate aerosol shows high values in the troposphere, and in the stratosphere close to the tropopause, similarly to SO_2sgl. Furthermore, sulphate aerosol VMRs are enhanced at 22–30 km in the tropics, with enhancements extending towards high-latitudes, where they span lower altitudes (∼10–25 km).
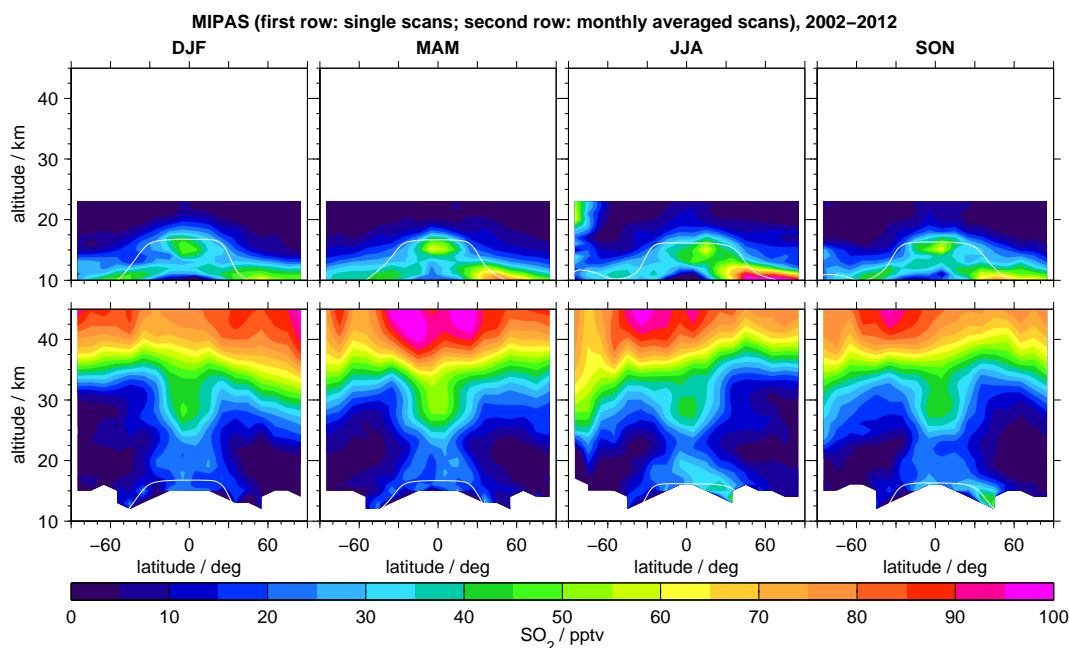
FIGURE 5.12: Seasonal primarily non-volcanic MIPAS SO_2 volume mixing ratios (upper panels: SO_2sgl; bottom panels: SO_2mea). Vertically resolved meridional distributions (10° latitude bins). Seasonal means are calculated from a monthly climatology for 2002–2012. The white contour lines indicate seasonal tropopause heights (NCEP, 2002–2012). Values exceeding the colour-scale are assigned with the limiting values.
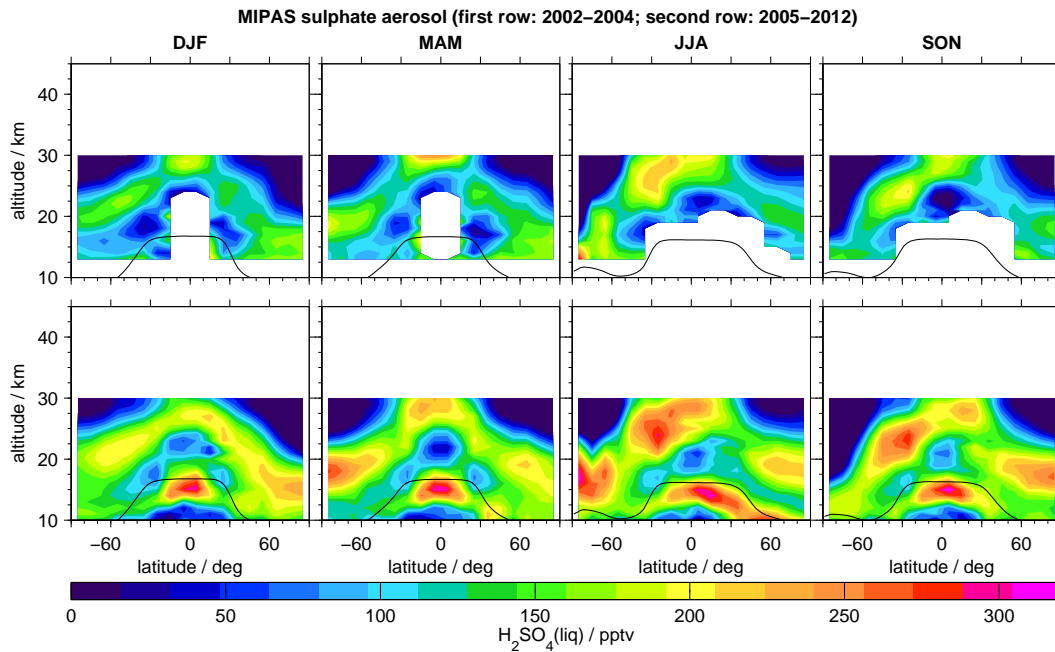
FIGURE 5.13: Seasonal primarily non-volcanic MIPAS sulphate aerosol volume mixing ratios (upper panels: P1; bottom panels: P2). Vertically resolved meridional distributions (10° latitude bins). Seasonal means are calculated from a monthly climatology for 2002–2012. The black contour lines indicate seasonal tropopause heights (NCEP, 2002–2012). Values exceeding the colour-scale are assigned with the limiting values.

In the following, the different patterns of MIPAS SO_2 and liquid-phase H_2SO_4 will be further described and certain features will be analysed in more detail in comparison to CTM results in the following sections (5.2.2 and 5.2.3).

- **Sulphur dioxide**

    (S1) Increased values of SO_2 centred in the tropics ∼25–35 km (Sect. 5.2.2).

    (S2) Increasing SO_2mea above approximately 30–35 km, with transport towards higher latitudes. During polar winter SO_2 subsides in the polar vortex. Down-welling is stronger in the Southern hemisphere, as is the polar vortex regime, due to lower winter temperatures. At stratospheric altitudes, where temperatures increase with altitude, H_2SO_4 exists in the gas-phase rather than as aerosol (mostly above ∼30 km), and the H_2SO_4 can be photolysed and form SO_2 (Höpfner et al., 2013; Vaida et al., 2003).

    (S3) High loading of SO_2 in the troposphere, especially in the tropics at around 14–16 km. Höpfner et al. (2015) already reported on the increased MIPAS SO_2sgl VMRs in the tropics, which are localised mostly in continental regions, and the Western Pacific. Further information are given in Section 5.2.3.

    (S4) Enhancements in mid- to high-latitudes, at altitudes of 10–12 km, primarily in the Northern hemisphere. Höpfner et al. (2015) reported on these enhancements. The pattern will be further discussed in Section 5.2.3.

(S5) Elevated values of SO_2sgl at 16–18 km in the region of the Asian Summer Monsoon during boreal summer. Höpfner et al. (2015) reported on this feature in the MIPAS data potentially being related to the Asian tropopause aerosol layer (ATAL; Vernier et al., 2011a).

- **Sulphate aerosol**

  (H1) Aerosol layer from the tropics at above ∼22 km, to high-latitudes at roughly 10–25 km, with seasonally variable vertical extent. During Northern hemisphere polar winter, down-welling of relatively aerosol-free air is observed in the polar region. A similar and more pronounced pattern of down-welling is measured by MIPAS in the Southern hemisphere during austral winter to spring. Thomason and Poole (1993) reported on observations of very low aerosol loading in the polar vortex, relative to surrounding non-vortex air. Low sulphate aerosol values may be explained by the formation of SO_2 from gas-phase H_2SO_4 above ∼30 km. Sulphur is transported polewards and subsides in the polar vortex in the form of SO_2 rather than in the form of sulphate aerosol. Due to low availability of sunlight SO_2 can exist for relatively long periods of time in the polar region during winter. A pattern of downward and southward propagation of high values from the tropics towards mid-latitudes is seen in the MIPAS measurements of sulphate aerosol. These aerosol enhancements will be further studied in Section 5.2.2.

  (H2) High values below the tropopause in the tropics (∼14–16 km), throughout the year, but with varying intensity. Similar enhancements are present in the MIPAS data of sulphur dioxide. Increased values are localised mostly in continental regions, and the Western Pacific, both for MIPAS sulphate aerosol and SO_2 (Fig. 5.14 and 5.15). See Section 5.2.3 for further discussions.

  (H3) Elevated values in the Northern hemisphere during boreal summer at low altitudes (∼10–12 km). Similar patterns are seen in MIPAS measurements of SO_2. These will be discussed in more detail in Section 5.2.3.

  (H4) Relatively low values of sulphate aerosol in the Southern hemisphere mid-latitudes at low altitudes. Further, low values in the tropics below ∼14 km, related to low VMRs especially in the eastern Pacific, in combination with data sparsity.

  (H5) Elevated values at 14–18 km in the region of the Asian Summer Monsoon during boreal summer. Possibly the pattern of enhanced aerosol loading is connected to the ATAL (Vernier et al., 2011a). However, as MIPAS data are sparse in this region (filtering for ice, Sect. 2.2.2), and due to enhancements of similar intensity in other tropical areas during the remaining seasons, it is not clear whether this feature is actually connected to the ATAL.
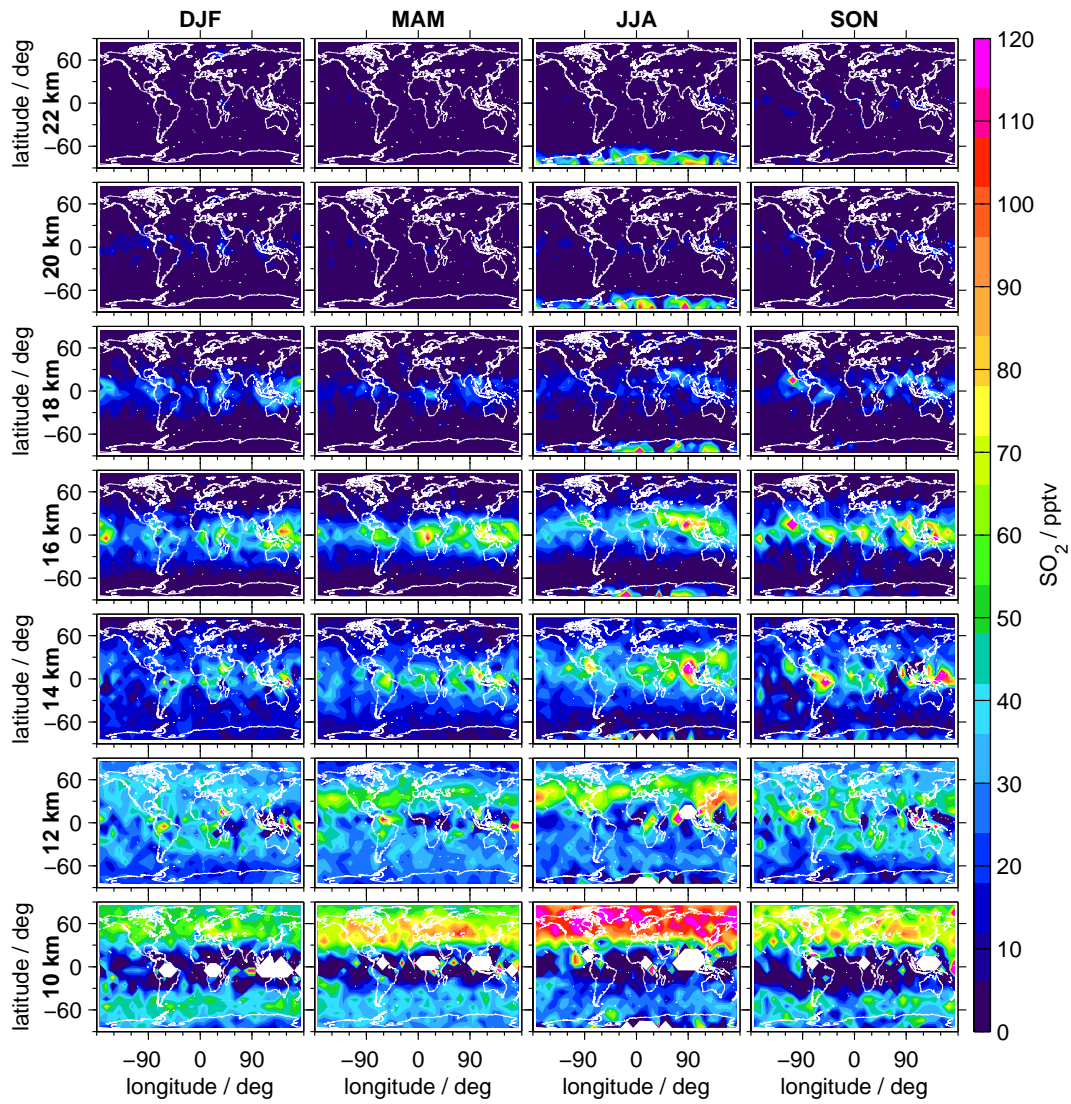
FIGURE 5.14: Primarily non-volcanic MIPAS SO_2sgl, as seasonal mean horizontal distributions at 10–22 km. Seasonal averages are calculated from a monthly climatology (2002–2012). Values exceeding the colour-scale are assigned with the limiting values.
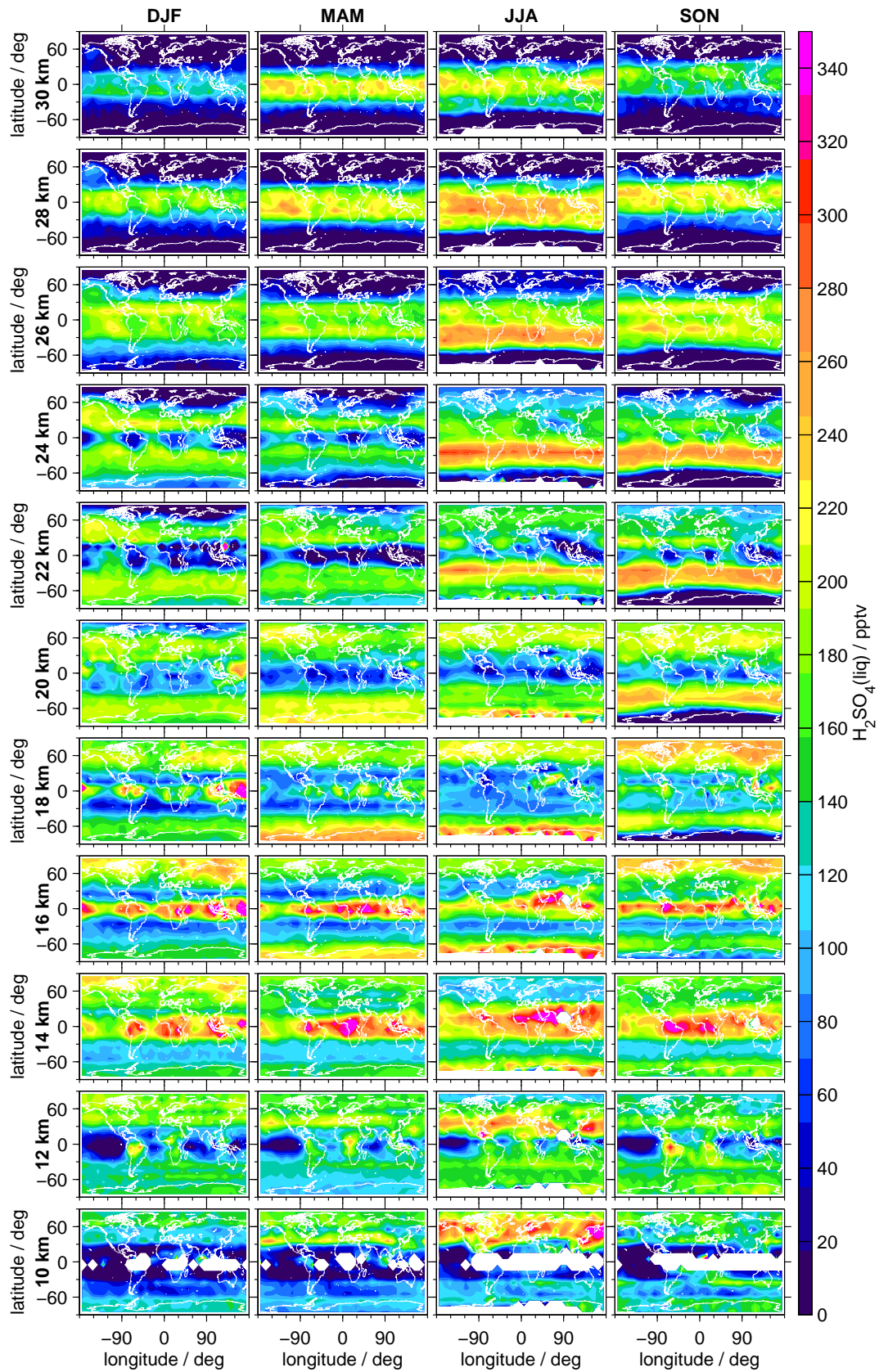
FIGURE 5.15: Primarily non-volcanic MIPAS sulphate aerosol (P2), as seasonal mean horizontal distributions at 10–30 km. Seasonal averages are calculated from a monthly climatology (2005–2012). Values exceeding the colour-scale are assigned with the limiting values.

In Fig. 5.13 seasonal sulphate aerosol has been presented individually for the first and second MIPAS measurement period. Generally, the features in the retrieved data are consistent between the two periods. One can observe a certain difference in the vertical location of enhancements at high altitudes in the tropics (upward-shift in P1). This is expected to be caused by a change in the vertical sampling between the measurement periods, as presented in Table 2.1. The more remarkable difference, however, is a low bias of sulphate aerosol VMRs during P1, compared to P2. The absolute and percentage bias between the two measurement periods is shown for the annual mean distributions of vertically resolved zonal means in Fig. 5.16. In a large region data from P1 show a low bias in the range of -20 to -100 pptv (-20 to -75%). As has been discussed in Section 2.2.3, MIPAS aerosol profiles are offset-corrected by comparison to balloon-borne in situ data. Comparing offset-corrected VMRs from P2 against non-offset-corrected data from P1 does not improve the agreement between the periods. No bias-correction to improve the agreement between the two periods is performed in this study. Most of the following analyses are based on the retrieval from P2 only, as data from P1 are fraught with problems at low altitudes due to interfering H_2O. Furthermore, only for MIPAS profiles from the longer second period a comparison to in situ data has been possible (see Sect. 2.2).
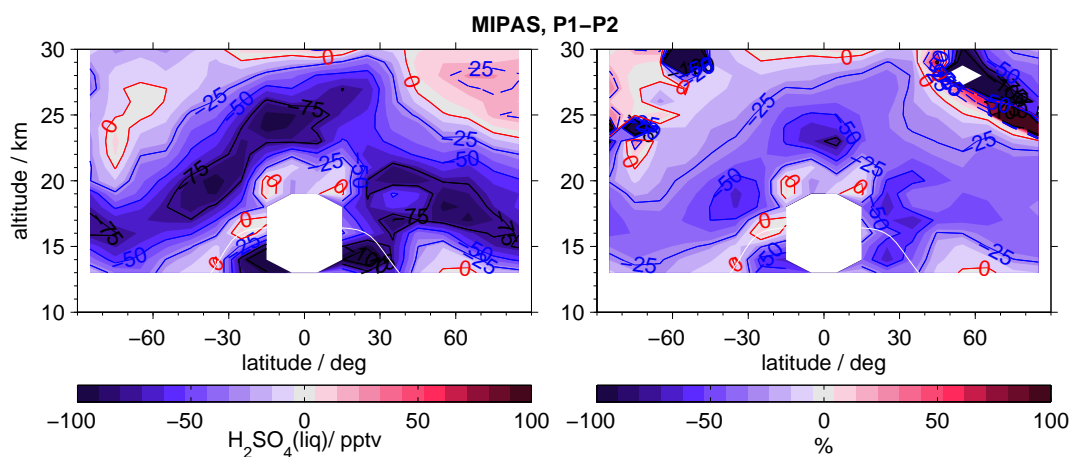
FIGURE 5.16: Absolute (left) and percentage (right) bias between primarily non-volcanic MIPAS sulphate aerosol VMRs for P1 and P2 (P1-P2). Annual vertically resolved meridional distributions. Values exceeding the colour-scales are assigned with the limiting values.

5.2.2 Upper part of aerosol enhancements

In this section the upper part of the MIPAS sulphate aerosol distribution (Fig. 5.13) will be analysed in comparison to CTM simulations. This aerosol layer extends from the tropics at above ∼22 km to high-latitudes at roughly 10–25 km, with seasonally variable vertical extent. The simulation BGO includes OCS from a bottom boundary derived from MIPAS measurements (Fig. 5.2 and 3.5) as the only sulphur source. OCS is destroyed through photolysis and SO_2 is formed. The SO_2 is destroyed by oxidation with OH, and H_2SO_4 is formed. Liquid-phase H_2SO_4 is settled gravitationally, with a constant effective sedimentation radius (ESRad).

In Fig. 5.17 and 5.18 simulated SO_2 and liquid-phase H_2SO4 are presented for the simulation BGO as seasonal vertically resolved zonal averages. For background conditions ESRad of 0.1 and 0.2 µm are chosen. These ESRad resulted in improved agreement between the measured and modelled data, when considering a set of simulations with various ESRad. Additionally, the mean annual distributions of simulated gas-phase H_2SO_4 that correspond to simulated sulphate aerosol that settles with these ESRad are presented in Fig. 5.19. For a better comparability of absolute values, simulated data are additionally shown in comparison to MIPAS as annual mean profiles for 30° latitude bins in Fig. 5.20. This figure also includes CTM results for a simulation without sedimentation of sulphate aerosol. It has to be kept in mind that data coverage at the lower edge of the profiles is sparse.
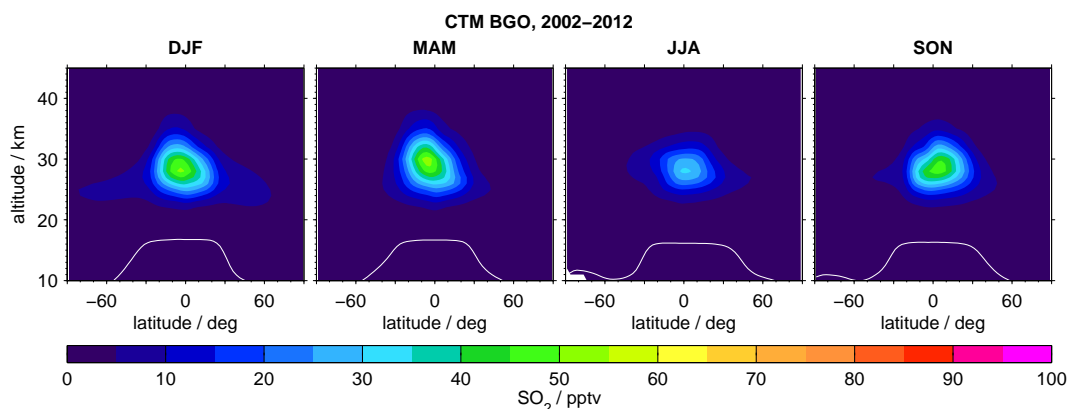
FIGURE 5.17: Seasonal simulated non-volcanic SO_2 volume mixing ratios as vertically resolved meridional distributions for simulation BGO. Seasonal averages are calculated from a monthly climatology (2002–2012). The white contour lines indicate seasonal tropopause heights (NCEP, 2002–2012). Values exceeding the colour-scale are assigned with the limiting values.

The Tropical Tropopause Layer is the main entry pathway for tropospheric OCS (e.g., Kremser et al., 2016). As shown in Section 5.1, OCS enters the stratosphere in the tropics with a value of about 530 pptv and decreases towards 0 pptv above, with a relatively strong gradient towards higher altitudes. Modelled SO_2, as formed by photolysis of OCS, is located mainly in the tropics at around 25–35 km, with highest values centred at ∼28–30 km. This is in agreement with findings by Brühl et al. (2012) regarding the main regions of sulphur release from OCS. This pattern of enhanced SO_2 is consistent with MIPAS SO_2mea (Fig. 5.12). No further effects of OCS on SO_2 are seen in the CTM. At higher altitudes no elevated SO_2 is simulated, as present in MIPAS S_2 mea. This is a consequence of the 'missing' implementation of SO_2 formation by photolysis of gas-phase H_2SO_4 at these altitudes. In the annual mean, the absolute modelled amount of SO_2 in the tropics at 28 km shows a low bias, compared to MIPAS SO_2mea, while on seasonal scale biases reach into both directions.

Modelled sulphate aerosol that results from OCS (simulation BGO) shows strongest enhancements at around 30 km in the tropics, and an aerosol layer extending from the tropics to lower altitudes in the mid- to high-latitudes. In general, the model results show agreement with MIPAS sulphate aerosol regarding the upper part of the distribution. However, in detail, the vertical distribution and absolute

values differ. The chosen ESRad has a rather strong effect on the available sulphate aerosol, with more aerosol being available for a smaller ESRad that results in weaker sedimentation. The ESRad also affects the distribution of simulated sulphate aerosol, but with minor differences, compared to the effect on the absolute values.
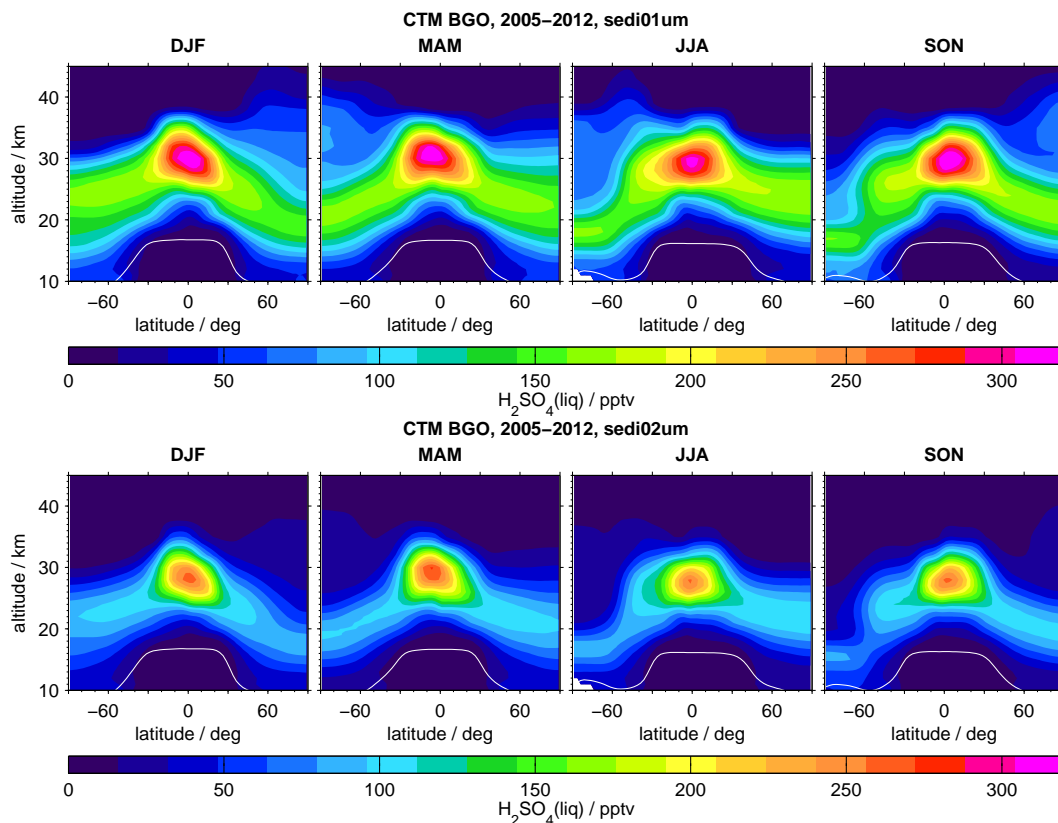
FIGURE 5.18: Seasonal simulated non-volcanic sulphate aerosol volume mixing ratios as vertically resolved meridional distributions for simulation BGO. Sedimentation with ESRad 0.1 (upper panels) and 0.2 μm (bottom panels). Seasonal averages are calculated from a monthly climatology (2002–2012). The white contour lines indicate seasonal tropopause heights (NCEP, 2002–2012). Values exceeding the colour-scale are assigned with the limiting values.
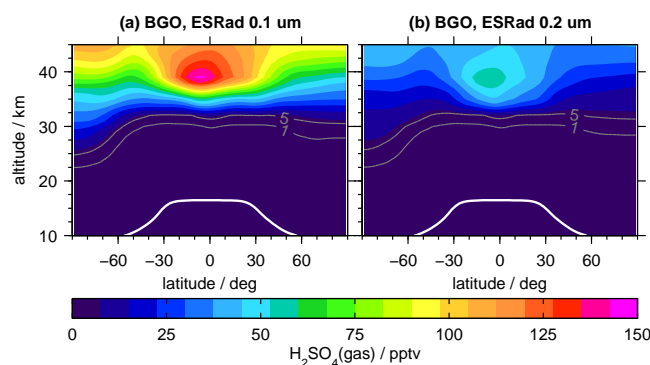
FIGURE 5.19: CTM data of gas-phase H_2SO_4 as annual mean vertically resolved meridional distributions (2005–2012). Simulation of non-volcanic (BGO, ESRad 0.1 and 0.2 μm) H_2SO_4. The white contour lines indicate the annual mean tropopause height (NCEP, 2002–2012). Values exceeding the colour-scale are assigned with the limiting values.
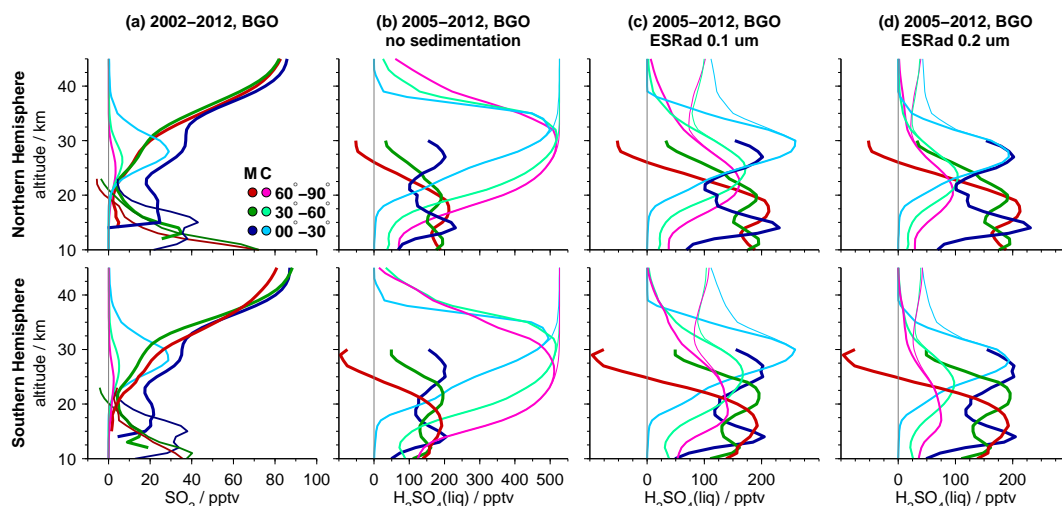
FIGURE 5.20: Vertical profiles of measured and modelled SO_2 (a) and liquid-phase H_2SO_4 (b)–(d), as mean annual averages per $30°$ latitude bin (area weighted averages). First row: Northern hemisphere; second row: Southern hemisphere. MIPAS (dark lines): SO_2sgl (thin lines up to 23 km), and SO_2mea (bold lines up to 45 km); CTM (bright lines): simulation BGO without sedimentation, and with ESRad 0.1 and 0.2 µm. Annual averages are calculated from a monthly climatology, with the time period of averaging displayed in the titles (valid for measurements and simulations).

On annual scale (Fig. 5.20) and for an ESRad of 0.2 µm, one can see very good agreement between the CTM and MIPAS regarding the location and absolute values of enhanced sulphate aerosol in the tropics ($\sim$28–30 km). Absolute values in the remaining areas are in better agreement, however, when considering an ESRad of 0.1 µm. Simulated sulphate aerosol decreases towards higher altitudes, due to the increase in temperature in the stratosphere, and a thermodynamic preference of the gas-phase rather than the liquid-phase of H_2SO_4. At the winter pole, where MIPAS measurements show down-welling of SO_2-rich and aerosol-free air, the model results show a rather opposite behaviour. Again, this is expected to result from the 'missing' implementation of photolysis of gas-phase H_2SO_4 at high altitudes. As no SO_2 is formed from gas-phase H_2SO_4 in the model, no SO_2 but H_2SO_4 subsides in the polar vortex, and due to the reduced temperatures above the winter pole, in the CTM this H_2SO_4 is assigned to sulphate aerosol again.

Model results that do not consider sedimentation of sulphate aerosol are not realistic. However, they elucidate that on the long term, when no other sulphur sources exist than tropospheric OCS, the maximum amount of total modelled H_2SO_4 in the upper stratosphere is limited by the mean model input of OCS in the tropics. Simulations illustrate the importance of sedimentation for the distribution and amount of stratospheric sulphate aerosol.

In Fig. 5.20 it becomes obvious that MIPAS sulphate aerosol is far below 0 pptv in the polar regions in the annual mean (above 25 km). This suggests a too strong offset correction (Sect. 2.2.3). This correction is based on comparisons with available balloon-borne in situ data at $41°$N, and seems to result in an over-correction in the polar regions.

Additionally to the seasonal distributions of SO_2 and liquid-phase H_2SO_4, time series of the two species are shown for tropical latitudes (SO_2: 10°S–10°N; H_2SO_4(liq): 15°S–15°N) at 25–30 km (Fig. 5.21 and 5.22). Modelled SO_2 (BGO) time series are generally consistent with the measurements (SO_2mea), especially in the centre of enhanced SO_2. At 25 km differences in the absolute values are higher than above, only during the second MIPAS measurement period, however.
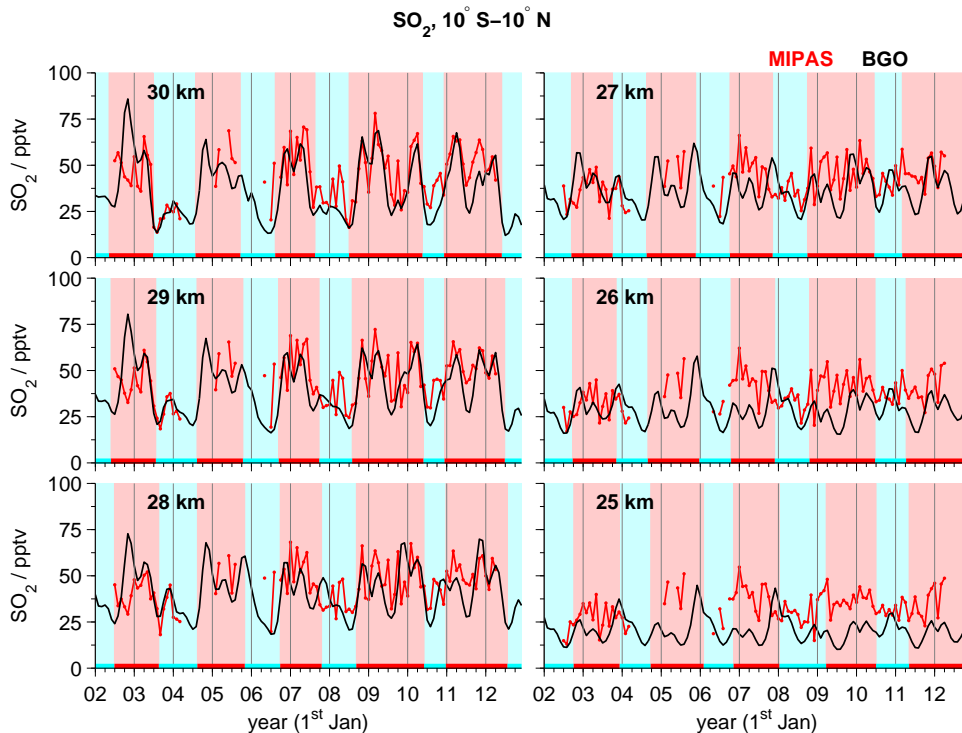
FIGURE 5.21: Time series of tropical measured (MIPAS SO_2mea) and modelled (CTM/BGO) SO_2 volume mixing ratios for 2002–2012. Monthly area weighted averages for 10°S–10°N at altitudes of 25 to 30 km. Indicated by red and cyan shadings is the phase of the QBO (red: negative, cyan: positive).

Time series of measured sulphate aerosol at 25–30 km (Fig. 5.22) reveal a strong variability in the MIPAS data. As discussed in Section 5.2.1, sulphate aerosol data for the first measurement period are generally lower than during P2. This is clearly visible at lower altitudes (Fig. 5.22), while above ∼28 km no general bias is observed for tropical aerosol. At lower altitudes (< ∼28 km) time series are influenced by high reaching volcanic sulphate aerosol (Manam, Soufrière Hills and Rabaul; e.g., Fig. 4.1). No volcanic emissions are included in the simulation (BGO). As noted before, agreement between modelled and measured sulphate aerosol is poorer, compared to the good agreement for OCS and SO_2.

When close to the main source region of sulphate aerosol, time series of simulated sulphate aerosol with ESRad 0.1 and 0.2 µm show little differences. For 2010–2012, during P2 and after the volcanic perturbations, measured and modelled data agree well at 25–26 km. At higher altitudes, differences between the simulations increase. In terms of absolute values in the tropics the simulation with ESRad 0.2 µm is at the level of MIPAS sulphate aerosol, while sulphate aerosol loading is higher

for 0.1 µm. Neither of the simulations shows the strong variability inherent to tropical MIPAS sulphate aerosol, however. MIPAS sulphate aerosol has a strong peak approximately every two years at 28–30 km, during the negative phase of the QBO. In the simulation with ESRad 0.2 µm such modulation is seen, but with a smaller amplitude.
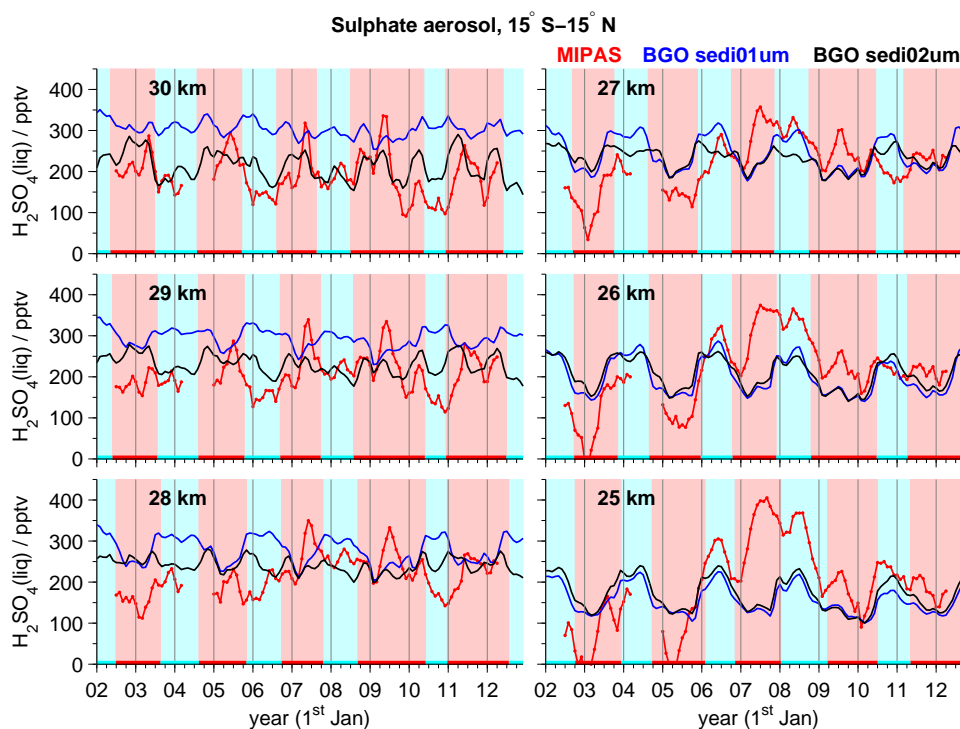
FIGURE 5.22: Time series of tropical measured (MIPAS) and modelled (CTM/BGO, ESRad of 0.1, and 0.2 µm) sulphate aerosol volume mixing ratios for 2002–2012. Monthly area weighted averages for 15°S–15°N at altitudes of 25 to 30 km. Indicated by red and cyan shadings is the phase of the QBO (red: negative, cyan: positive).
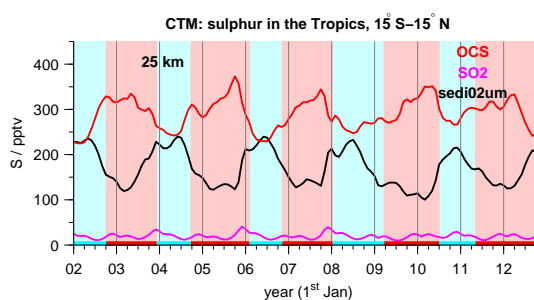
FIGURE 5.23: Time series of tropical simulated OCS, SO_2, and liquid-phase H_2SO_4 at 25 km (2002–2012; BGO, ESRad 0.2 µm). Monthly area weighted averages for 15°S–15°N at altitudes of 25 to 30 km. Indicated by red and cyan shadings is the phase of the QBO (red: negative, cyan: positive).

Glatthor et al. (2017) reported on a systematic positive bias of MIPAS OCS to ACE-FTS, with differences of up to 100 pptv at 13–16 km. However, reduced OCS as model input would result in worse agreement not only between OCS as modelled in the CTM and retrieved from MIPAS measurements, but also in the results presented here for SO_2 and sulphate aerosol.

Time series of modelled OCS, SO_2, and sulphate aerosol at 25 km are additionally displayed in Fig. 5.23 for easier comparability between the time series. Modelled sulphate aerosol and OCS are anti-correlated at ~25 km. Simulated sulphate aerosol is low during the negative phase of the QBO, while OCS is high. Generally, first OCS peaks during the negative phase of the QBO, then SO_2 at the end of the phase of strong up-welling, and finally sulphate aerosol is highest during the positive phase. This time shift between the maxima is a consequence of the time needed to form sulphate aerosol from OCS via SO_2.

The findings presented in this section until now suggest the follwing:

- Enhancements in the tropics (25–35 km), as seen in MIPAS SO_2mea, can be explained by photolytic sulphur release from OCS and consequent formation of SO_2, both in terms of pattern and absolute values.

- The distribution and absolute values of sulphate aerosol in the 'upper layer' seen in MIPAS sulphate aerosol is formed from sulphur that has been released from OCS.

- These findings are based on model simulations of OCS that are in good agreement with MIPAS OCS.

- Modelled sulphate aerosol loading depends strongly on the prescribed ESRad.

Model study on aerosol transport in the middle stratosphere

In the MIPAS aerosol volume mixing ratios a pattern of aerosol transport away from the equator towards higher latitudes has been seen, in combination with downward motion of aerosol. The pattern is stronger and has a clearer structure in the Southern hemisphere. This pattern, and in general sulphate aerosol transport initiated in the tropics at ~30 km, is studied here in further detail by various CTM simulations. In Fig. 5.24 time series of MIPAS sulphate aerosol VMRs are presented for 5° latitude bins, at 10°–15°, and 20°–25°, for both hemispheres. Additionally, MIPAS VMRs are shown for 2009–2012 as vertically resolved meridional distributions, averaged over two months, respectively (Fig. 5.25). The feature of downward moving aerosol is clearly visible, especially at 20–25°S. The pattern is observed each year, but with varying intensity and maxima. From around April to May, values in the tropics start to increase at ~28–30 km and maxima move downwards and polewards in the Southern hemisphere. High values reach an altitude of about 20 km in the extra-tropics after several months, and the aerosol loading decreases in the following. Maxima are stronger when initiating in Apr/May 2009 and 2011, compared to 2010.

Simulations studied to analyse the pattern of enhanced sulphate aerosol seen in MIPAS data at higher altitudes are described in the following, concerning the implemented sulphur sources:

- 'BGO' with an ESRad of 0.1 and 0.2 μm: OCS is included as the only sulphur source (bottom boundary as in Fig. 5.2).

- 'CTM_MTAR' (MIPAS Tropical Aerosol Real) with an ESRad of 0.2 μm: The only sulphur input is H_2SO_4 derived from MIPAS sulphate aerosol. In Fig. 5.27 this input is shown (black dashed line). It consists of monthly mean MIPAS sulphate aerosol for 28–30 km. When no measurements are available, climatological values (2002–2012) are used ('ave 28–30 km'). As the injection is done at model levels 7–9 ($\sim$27–30 km) in the tropics ($\sim$15°S–15°N), a gas-phase part of H_2SO_4 is assumed to be neglectable (see, e.g., Sect. 3.4.5). The H_2SO_4 tracer in the model is overwritten by the MIPAS input in each model time step, in the grid cells covering the region mentioned before and over all longitudes.

- 'CTM_MTAC' (MIPAS Tropical Aerosol Constant) with an ESRad of 0.2 μm: Similar to CTM_MTAR, but the H_2SO_4 input is held constant at 206 pptv, which is the mean over the time series used in CTM_MTAR.

- 'CTM$_{sglin}$' (single injection) with an ESRad of 0.2 μm: The only sulphur source considered in the simulations is a unique injection of 500 pptv H_2SO_4 in the tropics (levels 8–9, 7.5°S–7.5°N, all longitudes). Simulations are presented for four injection times: at 12 UTC on the last day of the month before January, April, July, and October (individual simulations of 365 d).

For all simulations mentioned above, bi-monthly mean distributions for 2009–2012 are presented in Fig. 5.26 to 5.30. The colour-scale limits are reduced, compared to MIPAS sulphate aerosol, as the focus lies on a pattern comparison, rather than a comparison of absolute values. Additionally, model results for BGO are shown as vertically resolved time series (Fig. 5.24), for comparison with the MIPAS data.

Simulations with single injections show the dominant transport of sulphate aerosol for different seasons and years:

- Injections in January (2009, 2010) lead to transport primarily towards the north, with visible transport starting in July / August. For 2011, the January injection shows transport towards the north, but starting in July a transport of parts of the aerosol towards the south is simulated, forming a 'bulge' of aerosol. In 2010 high concentrations of aerosol remain in the tropics, while in 2009 and 2011 concentrations decrease.

- When sulphur is injected in April, the primary transport direction is towards the south for all three injections (2009–2011), with a bulge forming in July to December. Simulations initiated in 2009 or 2011 show a stronger decrease of aerosol in the tropics, and stronger transport.

- Injections in July show strong inter-annual variability, with primary transport towards the south for July 2009 and 2011, and towards the north for July 2010. Again, it depends on the year, and therefore on the meteorological situation, how much aerosol remains in the tropics.

- October injections in 2009–2011 lead to transport of sulphate aerosol primarily towards the north.

In the time series of modelled sulphate aerosol (BGO) a downward transport is seen in both hemispheres, with a clearer pattern in the Southern hemisphere. This is consistent with the measurements. In the simulations the pattern is not as pronounced, and a certain time shift is suspected, however. In the measurements a relatively confined aerosol mass seems to be moved downwards and towards the south. Model simulations show more of a bulge that increases in extent from Jul–Dec. The different simulations show stronger transport towards the south and lower altitudes especially in 2011. The simulation with a single injection in April demonstrates differences between the years. Starting in 2009 or 2011, the aerosol decays in the tropics and a clearer movement of the aerosol towards the south and lower altitudes is seen. When the simulation is initiated in April 2010 the bulk of the aerosol remains in the tropics. Stronger simulated transport in 2009 and 2011 fits the measurements. The transport pattern is not primarily controlled by the amount of aerosol that is available in the tropics, as not only a simulation based on time series of MIPAS aerosol (CTM_MTAR), but also a simulation with constant input in the tropics (CTM_MTAC) results in similar transport patterns. Even though being based on H_2SO_4 input derived from MIPAS measurements, the simulated sulphate aerosol in CTM_MTAR is lower in the extra-tropics than observed by MIPAS. This difference is expected to be caused partly by the chosen injection area and partly by the simplicity of the sulphate aerosol scheme.

In conclusion, the patterns seen in the MIPAS aerosol data are not suspected to be retrieval artefacts, which could be caused, e.g., by interfering gases. Even though differing in detail, CTM simulations show that the dominant transport path, the inter-annual variability, and time scales of transport, are coherent with MIPAS data. Transport patterns do not depend primarily on a modulation of the aerosol in the tropics at ~30 km, but on the meteorological situation.
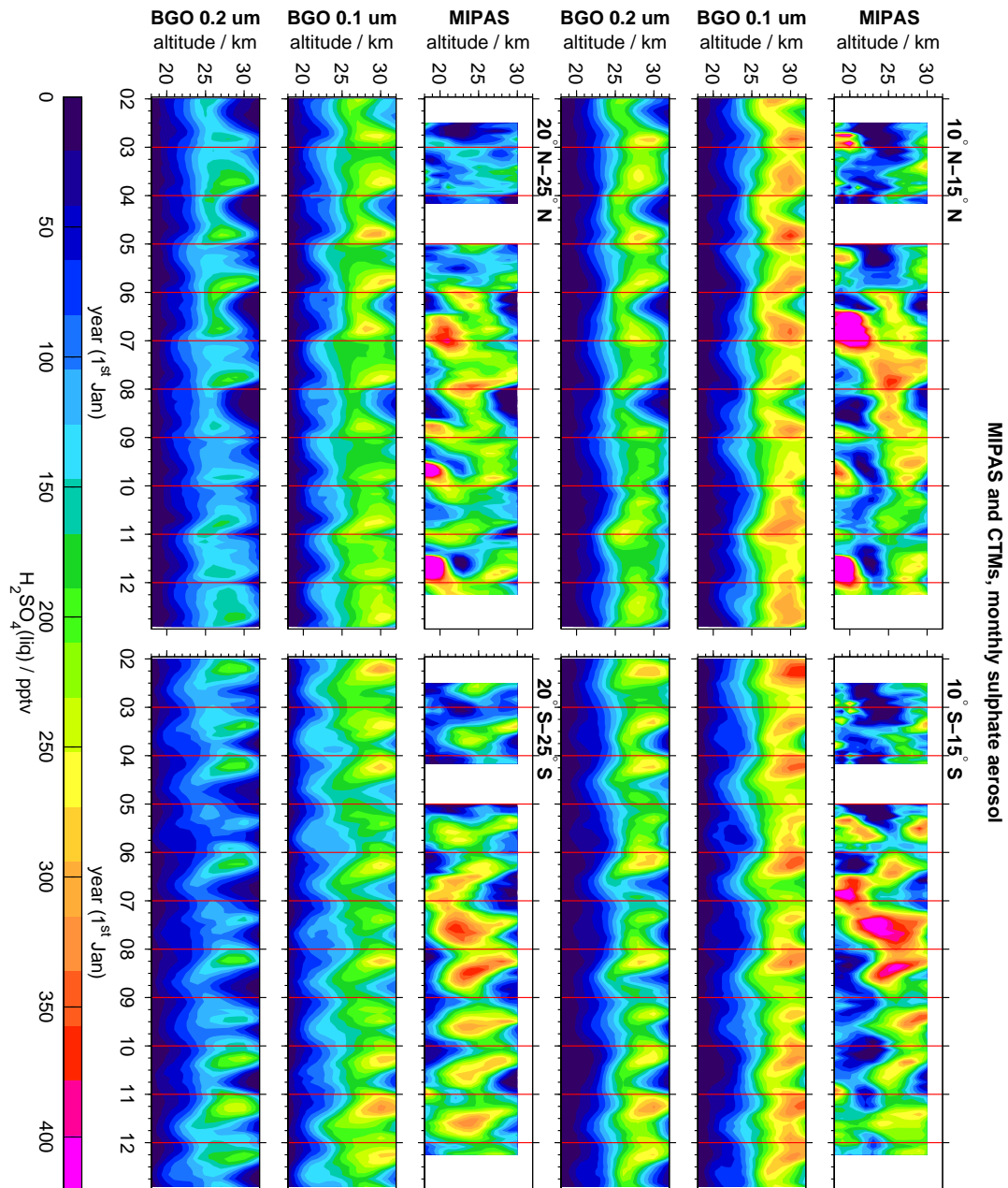
FIGURE 5.24: [Figure rotated by 90°] Time series of sulphate aerosol VMRs, from MIPAS and the CTM (BGO, ESRad 0.1 and 0.2 μm). Vertically resolved time series (2002–2012) of monthly and zonally averaged data for 5° latitude bins (rows 1–3: 10°–15°; rows 4–6: 20°–25°) for the Northern hemisphere (left) and Southern hemisphere (right). Red vertical lines mark the first day of each year. Values exceeding the colour-scale are assigned with the limiting values.
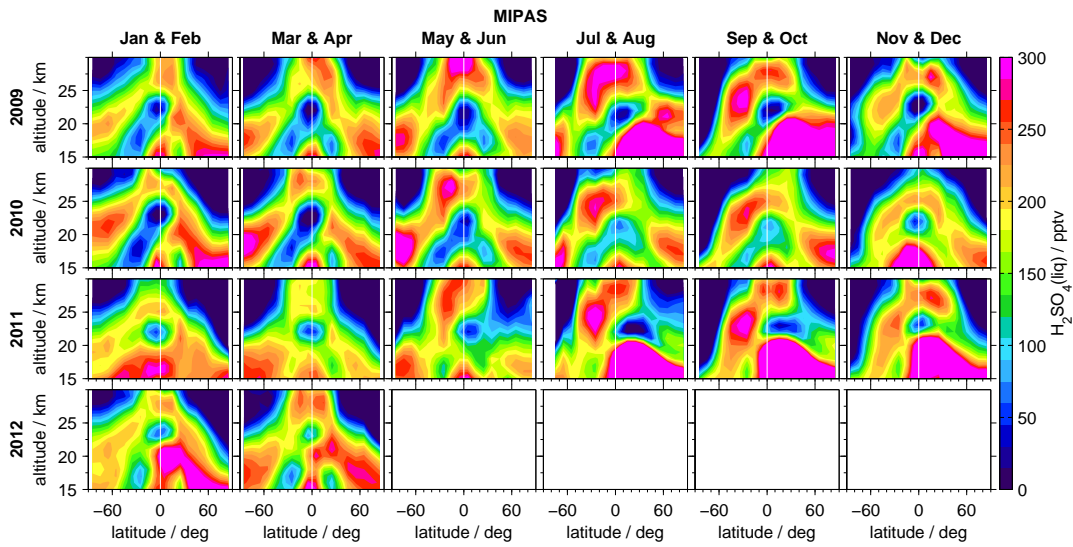
FIGURE 5.25: MIPAS sulphate aerosol as vertically resolved 2-monthly and zonally averaged VMRs (2009–2012). Values exceeding the colour-scale are assigned with the limiting values.
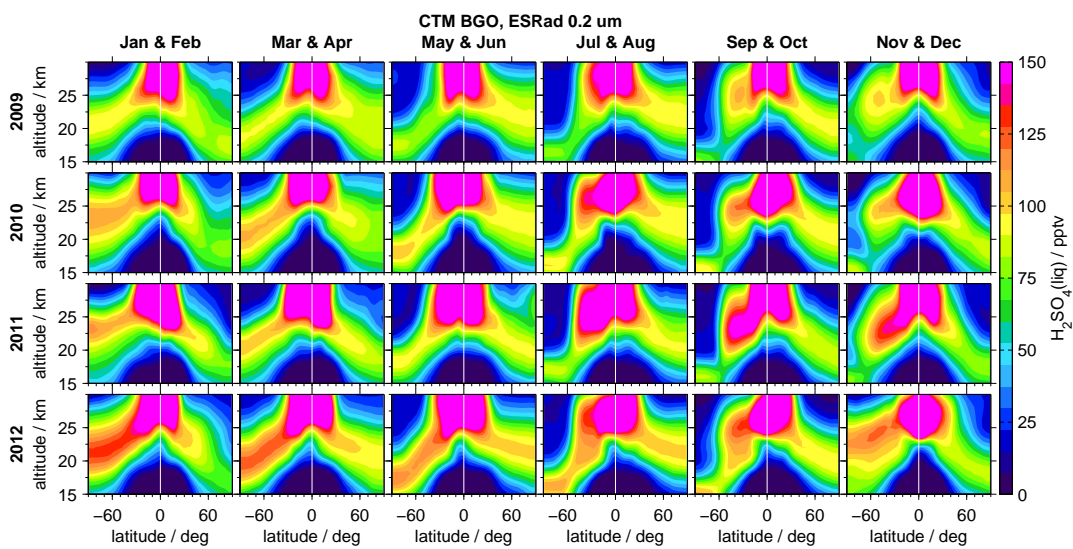
FIGURE 5.26: Simulated sulphate aerosol as vertically resolved 2-monthly and zonally averaged VMRs (2009–2012). CTM BGO, ESRad 0.2 μm. Values exceeding the colour-scale are assigned with the limiting values.
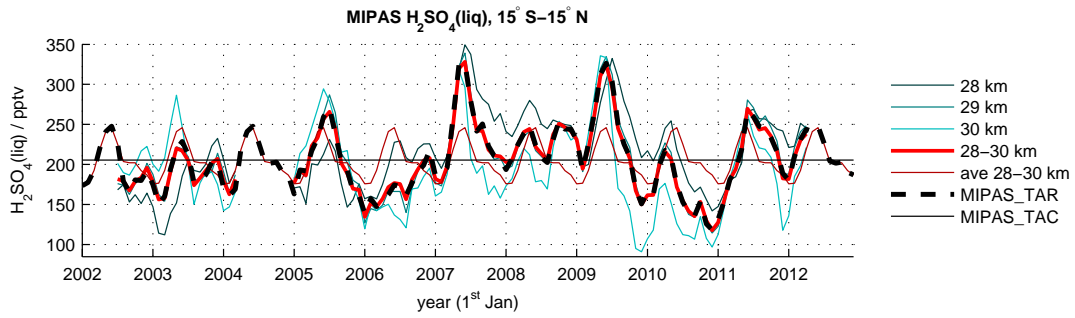
FIGURE 5.27: Input for simulations CTM_MTAR and CTM_MTAC. Time series of MIPAS sulphate aerosol at 15°S–15°N. Monthly mean area weighted averages per altitude for 28 to 30 km, and mean values. 'ave 28–30 km' is a climatology of monthly values, based on 2002–2012. Dotted black line: input for the CTM simulation CTM_MTAR; solid black line: input for the simulation CTM_MTAC.
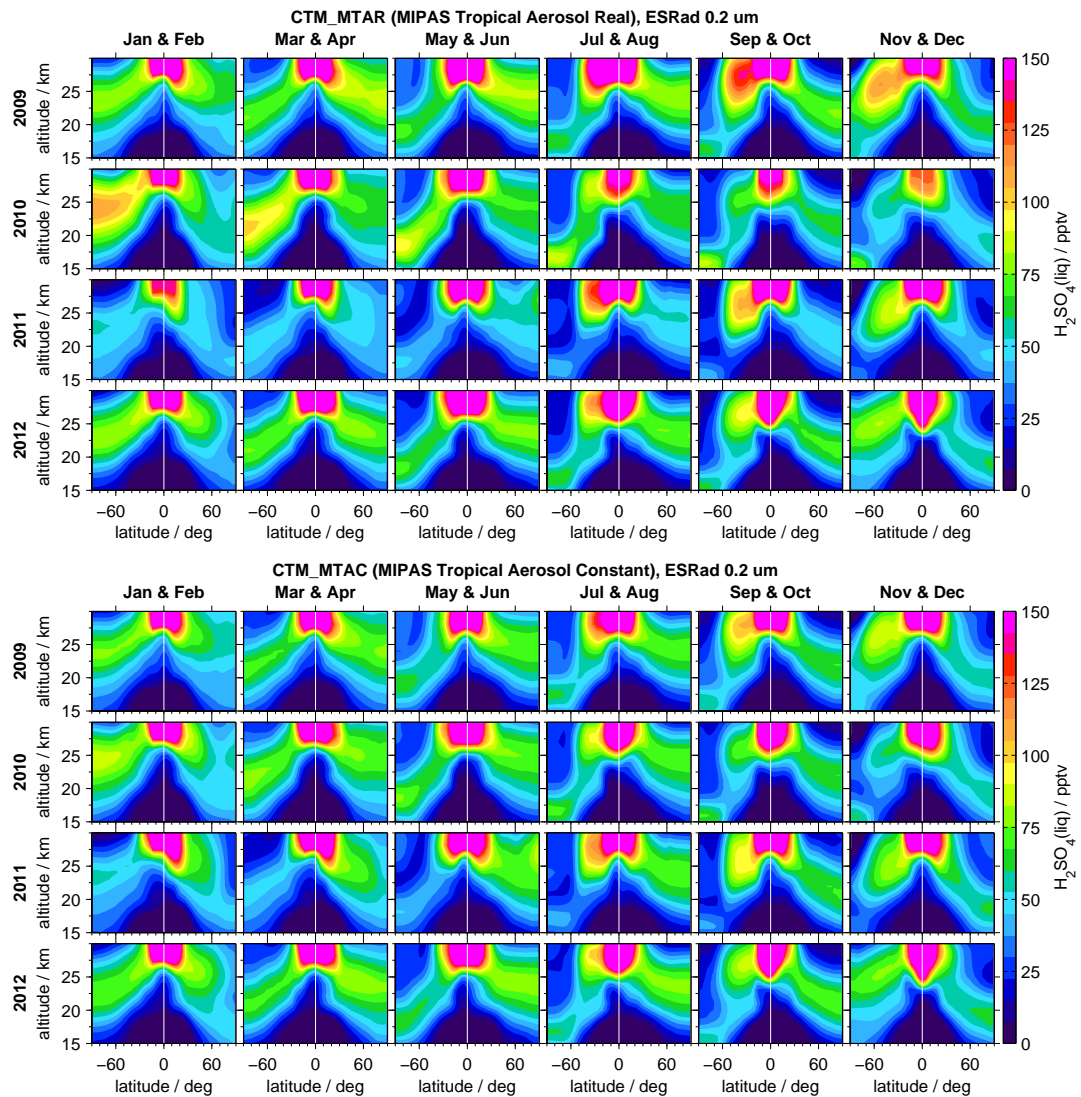
FIGURE 5.28: CTM_MTAR and CTM_MTAC (ESRad 0.2 μm): sulphate aerosol as vertically resolved 2-monthly and zonally averaged VMRs (2009–2012). Values exceeding the colour-scale are assigned with the limiting values. Input as in Fig. 5.27.
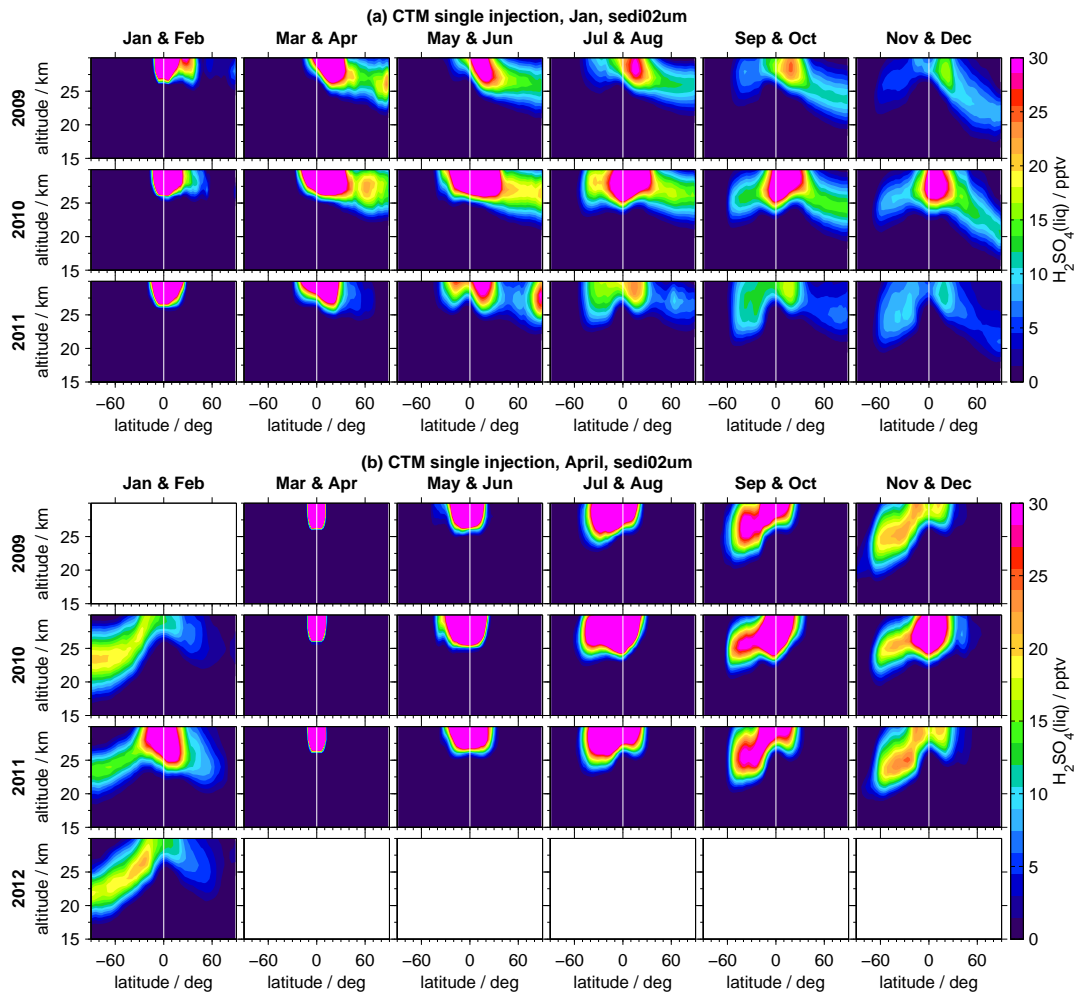
FIGURE 5.29: CTM$_{sglin}$ (ESRad 0.2 µm): sulphate aerosol as vertically resolved 2-monthly and zonally averaged VMRs (2009–2012). Simulations for single injections (Jan and Apr). For the April injection values for March are not included. Values exceeding the colour-scale are assigned with the limiting values.
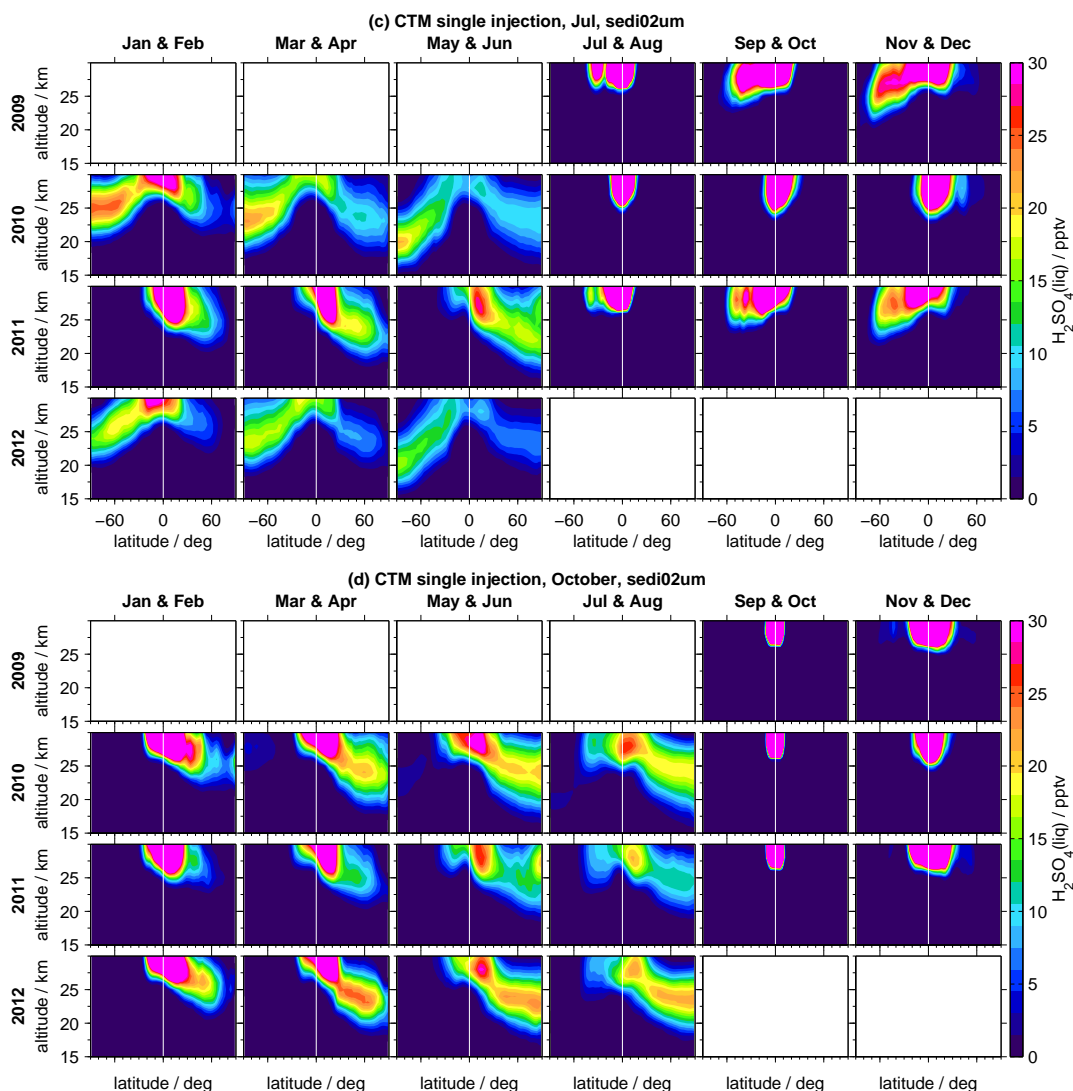
FIGURE 5.30: Continuation of Fig. 5.29. For the October injection values for September are not included.

5.2.3 Lower part of aerosol enhancements

In Fig. 5.31 the mean annual distributions of MIPAS SO_2 and sulphate aerosol for background conditions are shown, as vertically and latitudinally resolved volume mixing ratios. In the previous section, the upper part of the MIPAS sulphate aerosol distribution has been shown to be explained most probably, both in terms of pattern and absolute values, by sulphur input from OCS. Uncertainties in the analyses arise particularly from modelled sedimentation that is based on a rather simple approach, considering a constant effective sedimentation radius. Sulphur is released from OCS and forms SO_2 that is located mostly in the tropics at $\sim$25–35 km. Sulphur that is released from this tropical sulphur dioxide then forms sulphate aerosol, which is transported towards higher latitudes and is seen as the upper aerosol layer in the new MIPAS sulphate aerosol data set. Following the presented CTM results from a simulation with bottom boundary of OCS as the only sulphur source (BGO), OCS is not the source for enhancements seen in MIPAS SO_2 and liquid-phase H_2SO_4

at lower altitudes. These enhancements are studied in more detail in the present section.
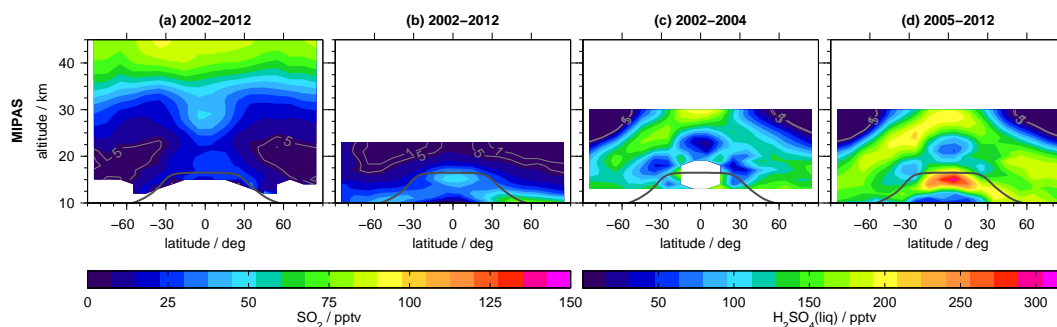
FIGURE 5.31: Primarily non-volcanic MIPAS data of SO_2 (sgl and mea), and liquid-phase H_2SO_4 (P1 and P2 individually). Annual mean vertically resolved meridional distributions. *(a)* SO_2mea (2002–2012); *(b)* SO_2sgl (2002–2012); *(c)* sulphate aerosol for P1 (2002–2004), and *(d)* for P2 (2005–2012). Annual averages are calculated from a monthly climatology. The grey contour lines indicate annual tropopause heights (NCEP, 2002–2012). Values exceeding the colour-scale are assigned with the limiting values.

In the Northern hemisphere mid- to high-latitudes at low altitudes (10–12 km), most pronounced during boreal summer, enhancements are seen in MIPAS SO_2sgl and MIPAS sulphate aerosol. These are presented in Fig. 5.32 as time series of monthly mean VMRs at 10–11 km, averaged over 30°N–90°N. Shown are monthly values from 2005–2012, without volcanic data being excluded. The feature in SO_2sgl has been discussed by Höpfner et al. (2015), where it was stated that due to missing availability of in situ measurements the increased SO_2 loading could not be confirmed by in situ measurements. It was not clear to them, whether these enhancements were retrieval artefacts or in fact caused by SO_2. Similar enhancements are present in the data set of MIPAS sulphate aerosol, which suggests that enhancements are a real feature. Monthly horizontal distributions (not shown) clarify that enhancements cover the Northern hemisphere without a distinct pattern. Also in the Southern hemisphere a seasonal cycle can be distinguished, by far weaker, however, with highest values during austral summer for SO_2, and during austral spring for liquid-phase H_2SO_4.

One possible reason for such enhancements are wild fires, that lead to the formation of pyrocumulonimbus clouds (e.g., Fromm et al., 2010) with strong uplift and a high vertical extent, connected to a strong transport of SO_2. E.g., Fromm et al. (2005, 2010), Cammas et al. (2009), and Damoah et al. (2006) reported on wild fire injection heights reaching the lower stratosphere. Höpfner et al. (2015) proposed a connection to elevated tropopause heights during summer, and a 'flushing' of the UTLS in mid- to high-latitudes by tropospheric air during late spring and summer (Gettelman et al., 2011). This has been proposed regarding the elevated levels of SO_2sgl, but is also a valid suggestion for sulphate aerosol that is produced from SO_2. Other possible explanations are industrial sources or volcanic influence, with the periodicity of the enhancements indicating that volcanic origin is less probable.
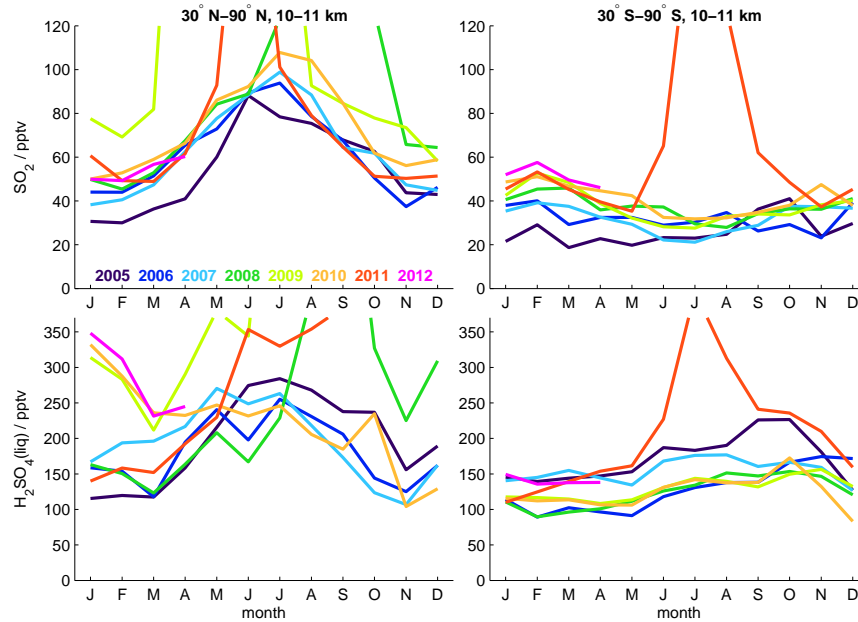
FIGURE 5.32: Enhancements of MIPAS SO$_2$sgl (upper panels) and sulphate aerosol (bottom panels) at 10–11 km altitude. Monthly mean VMRs per year (2005–2012). Data are averaged over 30°–90° latitude per hemisphere (left: Northern hemisphere; right: Southern hemisphere).

In the model one can distinguish easily between different sulphur sources, which is impossible in the case of the presented MIPAS measurements. To test the influence of volcanic sulphur on the presented background distributions, results from the simulations B15 and G17, which are based on volcanic SO$_2$ as the only sulphur source, are filtered in the same way as MIPAS SO$_2$sgl and MIPAS sulphate aerosol. Data marked in Fig. 5.10 are excluded, which also neglects months without MIPAS measurements. The resulting annual mean SO$_2$ is presented in Fig. 5.33, as vertically resolved meridional distributions. Included are the background simulation BG0, and the simulations G17 and B15, together with integrated SO$_2$ volume mixing ratios for background and volcanic simulations. Simulated sulphate aerosol is presented in a similar way in Fig. 5.34 and 5.35 for BG0 with ESRad 0.1 and 0.2 μm, and B15 and G17 with larger ESRad for volcanic aerosol (0.2 and 0.5 μm).

The influence of volcanic SO$_2$ that remains in the data sets after filtering is limited to altitudes below 20 km. For B15, which includes more frequent volcanic input, and which is in better agreement with MIPAS measurements during periods of low volcanic activity, the remaining SO$_2$ covers all latitudes. Highest values are found in the tropics, right above the mean annual tropopause. About 50 pptv SO$_2$ remain in the filtered data in this region, which is in agreement with MIPAS SO$_2$sgl. However, elevated SO$_2$ in MIPAS SO$_2$sgl is located below the tropopause. Further, as could be seen in time series of MIPAS SO$_2$ (Fig. 5.10), the pattern of enhancements is rather persistent in the tropics, at 14–16 km. Horizontal distributions (Fig. 5.14) reveal that these enhancements are localised above most of the continental areas, with varying seasonal intensities. In MIPAS SO$_2$sgl enhancements at low altitudes (10–12 km) in the Northern hemisphere also have an annual periodicity and are observed most pronounced during boreal summer.

These characteristics suggest both patterns of elevated MIPAS SO_2 to be not or only partly connected to volcanic activity. It is not clear to which extent the enhancements in the modelled and measured data sets are connected. Adding to the uncertainties, the volcanic input for simulation B15 that has been derived from various SO_2 measurement data sets might not completely exclude all non-volcanic SO_2. Nevertheless, besides the mentioned uncertainties, one can conclude from the presented analysis that volcanic contributions cannot be neglected in the MIPAS data studied for background conditions. In a recent study, Rollins et al. (2017) demonstrated some uncertainty in the MIPAS SO_2sgl data of the tropical UTLS for background conditions. A comparison of in situ, model, and satellite-borne profiles of SO_2 in the tropical UTLS region suggested that MIPAS SO_2sgl, averaged over times of low volcanic activity, are overestimating the SO_2 loading, and are not useful unless their uncertainties and temporal variability are correctly considered.

Simulated background sulphate aerosol for an ESRad of 0.1 µm results in reasonable agreement with MIPAS sulphate aerosol, even though showing a positive bias in the tropics ($\sim$25–35 km). An ESRad of 0.2 µm leads to better agreement in this region, but too little sulphate aerosol persists in the remaining stratosphere, compared to MIPAS. For volcanic aerosol an ESRad of 0.2 µm is rather small and simulation results represent a lower limit for volcanic sulphate aerosol. For the eruptions of Kasatochi (2008) and Sarychev (2009) an ESRad of 0.5 µm resulted in satisfying agreement between modelled and measured sulphate aerosol (Sect. 4.3). A combination of simulations BG0 with ESRad 0.1 µm and B15 with ESRad 0.5 µm shows rather good agreement with MIPAS sulphate aerosol, differing in detail.

Findings for SO_2, as stated above, prove to hold true for sulphate aerosol as well. In the Northern hemisphere MIPAS sulphate aerosol is elevated during boreal summer, with annual periodicity, when not interfered by volcanic eruptions, and MIPAS shows enhancements in the tropics at about 14–16 km, which are rather persistent throughout the measurement period. As could be seen in mean seasonal horizontal distributions of MIPAS sulphate aerosol (Fig. 5.15), enhancements at 14–16 km are highest in continental areas of the tropics. Partly, high values in the tropics might be connected to cirrus clouds that were not captured by the MIPAS ice filter (Sect. 2.2.2). Simulated sulphate aerosol from B15, with strong volcanic periods being omitted in the results, is elevated in the Northern hemisphere and in the tropics, where enhancements are located above the tropopause, however. Even though agreeing rather well with MIPAS sulphate aerosol in absolute terms, it is not clear to which degree these enhancements are from similar origin.
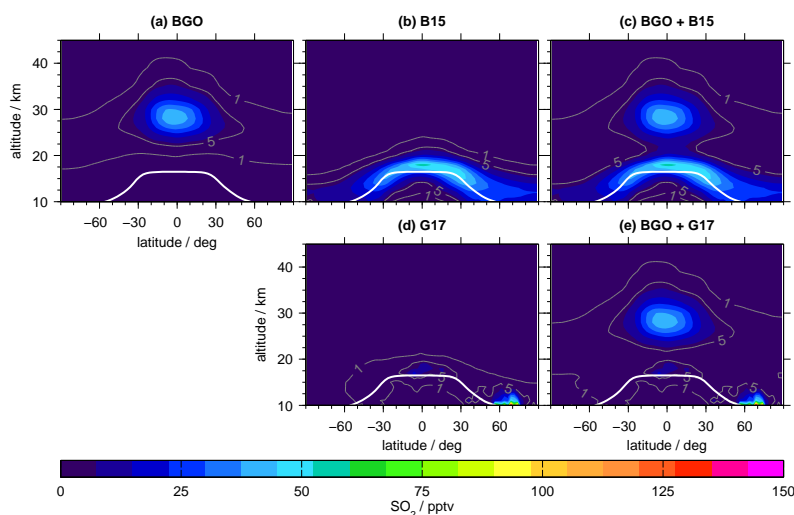
FIGURE 5.33: CTM data of SO_2 as annual mean vertically resolved meridional distributions (2002–2012). Simulation of non-volcanic (BGO), and volcanic SO_2 (B15 and G17, with MIPAS-filter for volcanic influence). Data per simulation in (a), (b), and (d). Integrated non-volcanic and volcanic sulphur dioxide in (c) and (e). The white contour lines indicate the annual mean tropopause height (NCEP, 2002–2012). Values exceeding the colour-scale are assigned with the limiting values.
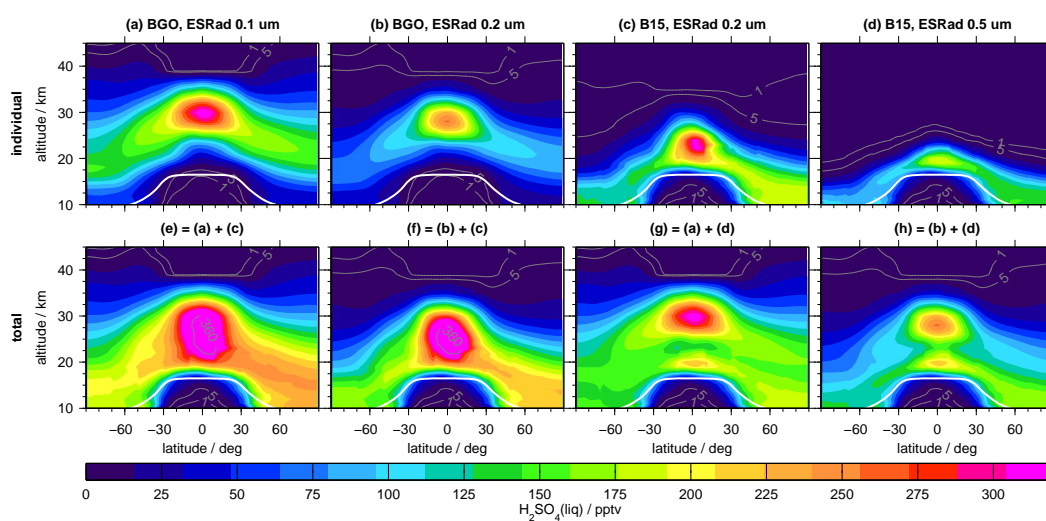
FIGURE 5.34: CTM data of liquid-phase H_2SO_4 as annual mean vertically resolved meridional distributions (2005–2012). Simulation of non-volcanic (BGO, ESRad 0.1 and 0.2 µm), and volcanic sulphate aerosol (B15 and G17, ESRad 0.2 and 0.5 µm, with MIPAS-filter for volcanic influence). Data per simulation in (a)–(d). Integrated non-volcanic and volcanic sulphate aerosol in (e)–(h). The white contour lines indicate the annual mean tropopause height (NCEP, 2002–2012). Values exceeding the colour-scale are assigned with the limiting values.
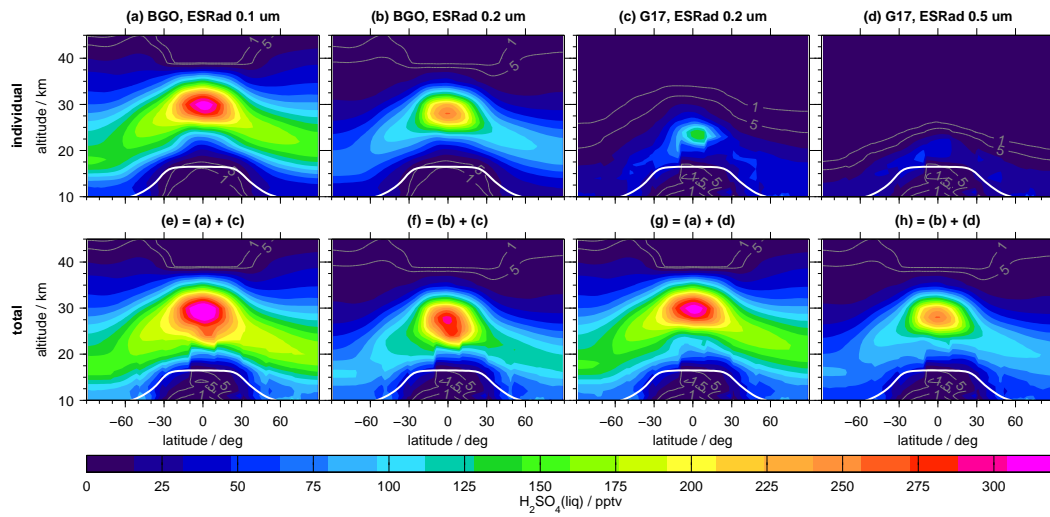
FIGURE 5.35: As Fig. 5.34, but for volcanic simulation G17.

6 Stratospheric sulphur burden

After the discussions of stratospheric sulphur during volcanically perturbed and background conditions in Chap. 4 and 5, based on MIPAS measurements and CTM simulations, the current chapter intends to combine the data sets for an analysis of the stratospheric sulphur burden. Time series of stratospheric sulphur mass for the main stratospheric sulphur species, OCS, SO_2, and liquid-phase H_2SO_4 are assessed. With the aid of the CTM it is tested whether the MIPAS data sets are consistent in terms of stratospheric mass, and the evolution of stratospheric mass is analysed for 2002–2012.

Figure 6.1 shows time series (2002–2012) of measured and modelled stratospheric sulphur, as contained in carbonyl sulphide, sulphur dioxide, and sulphate aerosol. All data sets are filtered for tropospheric values using NCEP tropopause heights (re-sampled to the CTM horizontal grid). At the lower edge of the altitude region for which data are available ($\geq$10 km), stratospheric values are partly missing, as in some cases the tropopause height lies below 10 km, and due to limited data coverage especially at low altitudes. Therefore, the presented integrated sulphur masses are expected to have a low bias, compared to values covering the entire stratosphere. Integrated masses are calculated as described in Section 4.3.1. Masses are integrated horizontally, from 90°S–90°N, and vertically over a specified altitude region. For MIPAS OCS this is restricted to 10–30 km, which is the altitude range of MIPAS sulphate aerosol data. MIPAS SO_2sgl covers 10–23 km. All model results are restricted to 10–30 km. Generally, the exponential decrease of air density with altitude leads to a decrease in sulphur mass densities with height, and a weaker contribution to the vertically integrated mass from higher altitudes, even if volume mixing ratios remain high.

CTM data presented here are OCS, SO_2, and liquid-phase H_2SO_4 (ESRad 0.1 and 0.2 μm) from the simulation BGO, with a bottom boundary of OCS as the only sulphur source. Furthermore, volcanic sulphur dioxide and sulphate aerosol (ESRad 0.2 and 0.5 μm) are analysed, as simulated in G17 and B15, which contain as the only sulphur source volcanically emitted SO_2. OCS is converted to SO_2 by photolysis, and H_2SO_4 is formed by oxidation of SO_2 with OH. The liquid part of sulphuric acid settles with a prescribed effective sedimentation radius. For G17 and B15, both including volcanic SO_2 emissions but no OCS, results are shown as integrated masses for BGO and the volcanic simulation, respectively.
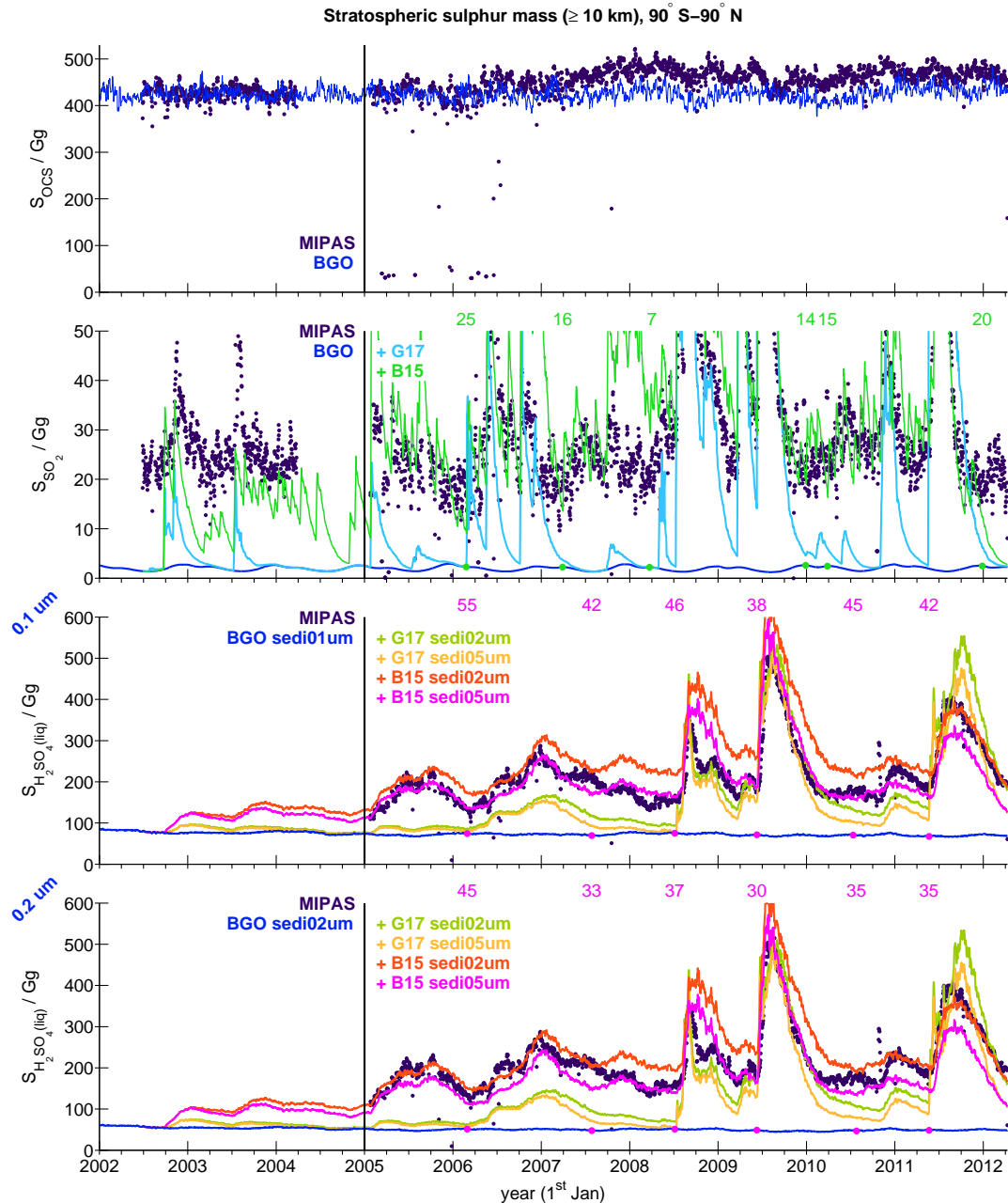
FIGURE 6.1: Time series of stratospheric sulphur masses from MIPAS and CTM (90°S–90°N; 2002–2012). MIPAS: OCS, SO_2sgl, liquid-phase H_2SO_4; CTM: OCS (BGO), SO_2 (BGO, G17, B15), liquid-phase H_2SO_4 (BGO with ESRad 0.1 and 0.2 µm, G17 and B15 with ESRad 0.2 and 0.5 µm). The sulphur masses are based on stratospheric data only (filtered with NCEP tropopause heights). Minimal available altitude: 10 km. Maximal altitude: for OCS and H_2SO_4(liq) 30 km, for SO_2sgl 23 km. Masses are calculated from 5 d running zonal means for ∼10° latitude bins, as in Section 4.3.1. Measured sulphate aerosol for P1 is not shown due to retrieval problems at low altitudes. Panel 1: sulphur mass in OCS from MIPAS and CTM (BGO). Panel 2: sulphur mass in SO_2 from MIPAS (SO_2sgl) and CTM (BGO, BGO + G17 and BGO + B15). Panels 3&4: sulphur mass in sulphate aerosol from MIPAS and CTM (BGO, BGO + G17 and BGO + B15). Panel 3: BGO with ESRad 0.1 µm, and G17 and B15 with ESRad 0.2 and 0.5 µm. Panel 4: BGO with ESRad 0.2 µm, and G17 and B15 with ESRad 0.2 and 0.5 µm. Volcanic masses are added to the masses from BGO in each case. Coloured numbers above panels 2–4 indicate the percentage of simulated background sulphur in total sulphur (BGO + B15) for the annual minima of total sulphur in 2006–2011, with colours indicating the corresponding time series of total sulphur, and coloured dots (on time series of BGO) indicating the corresponding time.
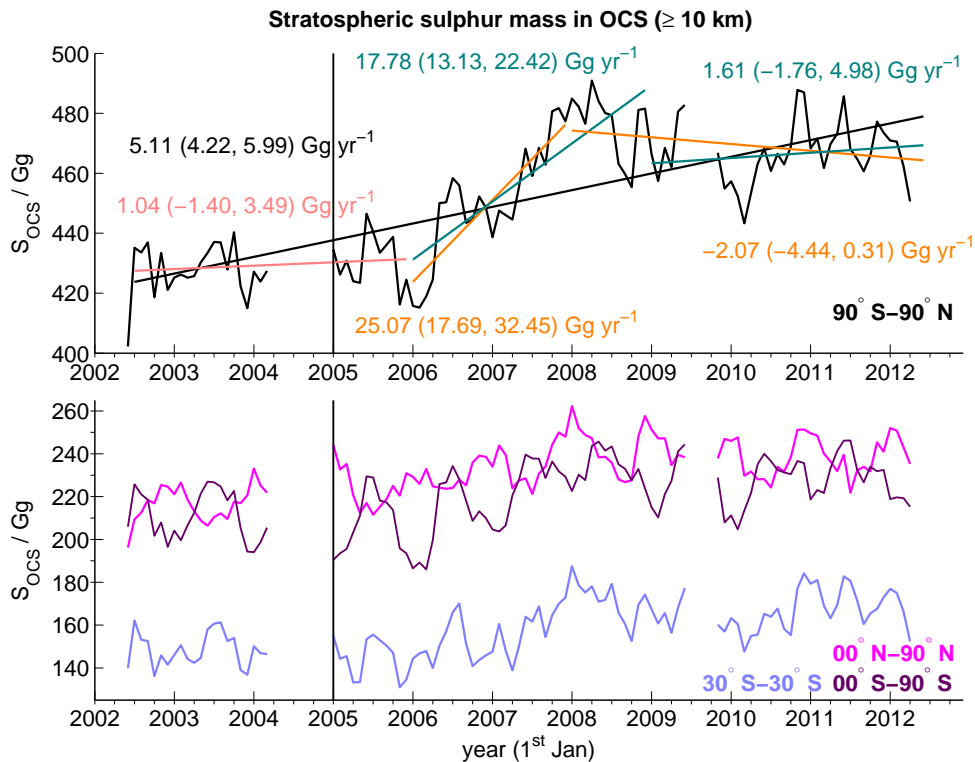
FIGURE 6.2: Time series of stratospheric sulphur masses in OCS (MIPAS), for various latitude bins. Data as in Fig. 6.1, but for differing latitude regions, and monthly mean masses. For 90°S–90°N linear regressions (least squares fits) are included for different fit-periods. Given are the change per year and 95% confidence bounds (2-σ uncertainties). Outliers were omitted from the 5 d running means: data were not considered (per 10° latitude bin), when the respective value differed more than twice the standard deviation from the median, both calculated over a period of ±5 d around the value. Furthermore, data for approx. Jul–Nov 2009 are excluded, as they showed a low bias (changed tangent heights during that period).

Compared to sulphur dioxide and sulphate aerosol, the variability of OCS masses is small. The total stratospheric amount of sulphur contained in OCS is roughly 400–500 Gg. Simulated OCS shows no trend, which is to be expected, as no inter-annual change of the bottom boundary has been implemented. Neither do the photolysis rates include any inter-annual variability. In the model a trend could merely result from changes in the meteorological conditions which drive the tracer transport. Measured OCS is at equal levels as the simulated values until the end of 2005, then increases until approximately 2008, and remains at a rather constant level later on, until the end of the measurements. As the increase starts in 2006, it is not connected to the change between high and reduced resolution measurements, which started in Jan 2005. In Fig. 6.2 stratospheric OCS masses are shown as monthly values, for different latitude regions. For globally integrated time series, linear regressions (least squares fits) are presented for different fit periods. The annual changes corresponding to the regression lines are presented in Fig. 6.2, together with their 95% confidence bounds (2-σ uncertainties). For 2002–2012 the change is 5.11 Gg yr^{-1}, or 51.1 Gg decade^{-1}. This is a remarkable change, regarding the total mass of OCS being less than 500 Gg, resulting in the change being larger than 10%. More accurate seems the division of the MIPAS measurements into several fit periods. Until the end of 2005 and after 2008 or 2009 changes are weak. During

the years 2006, 2007, and partly 2008, however, stratospheric masses of OCS derived from MIPAS measurements increase rapidly, by roughly 13.13–32.45 Gg yr^{-1}. As this change is very strong, no significance analysis has been performed. As stated in Glatthor et al. (2017) a positive trend in OCS would potentially result in increased stratospheric aerosol loading, causing a negative radiative effect. OCS itself is a strong greenhouse gas, however. Therefore, the exhibited net climate forcing is expected to be very small (Brühl et al., 2012). The reason for the observed increase of stratospheric OCS in both hemispheres (Fig. 6.2) is not studied here in detail. One possible explanation for the observed increase in stratospheric OCS masses could be a decrease in tropopause heights. The NCEP tropopause heights that were used to filter all profiles for tropospheric values, show decreasing annual maxima of the mean tropical tropopause heights (area weighted means over 30°S–30°N) for the years 2006–2008. The maxima in tropopause heights, present at the beginning of these years, decreased from 16.86 to 16.58 km. An argument against the influence of tropopause heights, however, is the fact that the same mask has been used to omit tropospheric values from the model results and measurements, resulting in simulated masses which do not reproduce the increase seen in the measurements.

Glatthor et al. (2017) also performed a trend analysis on MIPAS OCS data, using a different approach. Based on monthly zonally averaged 10° x 1 km bins analyses were performed per bin, and regression functions were fitted to time series of volume mixing ratios of OCS (2002–2012). These regression functions consisted of a conjunction of a 'linear trend, 8 sine and cosine waves with periods between 3 and 24 months and of 2 terms describing the QBO' (Glatthor et al., 2017; von Clarmann et al., 2010; Stiller et al., 2012). For the upper troposphere no significant trend was detected, pointing to a global balance between sources and sinks. In the middle stratosphere they found significant negative trends (up to -65 pptv decade^{-1}) in a wide region in the Northern hemisphere. These trends are mostly located above altitudes of approximately 20 km in the tropics and around 17 km in higher latitudes. A large region of weaker positive trends is obtained for the Southern hemisphere. Glatthor et al. (2017) suggested these trends to be caused by a change in the BDC. Differences in the results obtained in this thesis and the trend analysis by Glatthor et al. (2017) can most probably be attributed to the different approaches. Their analysis is based on volume mixing ratios that do not depend on air density, as do the masses studied in this thesis. In the present results VMRs at lower altitudes and closer to the equator have a higher contribution to the total estimated change. At low stratospheric altitudes the trends obtained by Glatthor et al. (2017) do not show such a clear picture of negative trends in the Northern hemisphere and positive trends in the Southern hemisphere as they do at higher altitudes.

For the last decade Lejeune et al. (2017) derived a positive trend in OCS for 2002–2008 (1.34±0.08% yr^{-1}) from tropospheric columns (in molecules cm^{-1}) above the Jungfraujoch, and no significant trend after 2008. For the stratosphere they derived a weak trend of 0.20±0.06% yr^{-1} (1995–2015), and therefore concluded that the change in tropospheric columns was mainly due to tropospheric processes. In their study, they analysed data from Fourier-transform infrared solar observations. These findings differ from the results presented here, as a stronger trend is found, even though omitting tropospheric concentrations of OCS. Kremser et al. (2015) calculated

positive trends from total column OCS (in molecules cm^{-1}) measured by ground-based Fourier-transform spectrometers at three stations in the Southern hemisphere (34.45°S–77.80°S). The trends were in the range 0.43±0.02% and 0.73±0.03% yr^{-1} (2001–2014), which lead to the conclusion that the budget of atmospheric OCS was not closed.

Sulphur dioxide and sulphate aerosol both show large variability caused by volcanic sulphur injections. The total amount of simulated sulphur mass in SO_2 (Fig. 6.1), as formed from OCS (BGO), ranges between 1.2 and 3 Gg, while measured SO_2 is roughly in the range of 15–30 Gg in times of low volcanic activity. The measured level of SO_2 is not reached when considering a limited number of 30 volcanoes (2002–2012), as done in simulation G17. The volcanic simulations G17 and B15 start with a prescribed background of 0 pptv SO_2. Even though showing differences in detail, simulation B15, with more frequent volcanic emissions (98 days), combined with the SO_2 formed from OCS (BGO), is sufficient to explain the level of measured SO_2 during the second measurement period. This period initiates with a series of relatively strong eruptions in the tropics, and SO_2 masses from MIPAS and the CTM are in agreement. As the total mass depends on the corresponding air volume, and therefore on the surface area, tropical volcanoes have a relatively strong influence on stratospheric SO_2 masses. 50% of the Earth surface is located between 30°S–30°N. Therefore, to derive good estimates of total sulphur mass, a good representation of the species in terms of volume mixing ratios is more essential at low- to mid-latitudes, which have higher weight in the integrated masses. To some degree this is counteracted by the higher tropical tropopause. Stratospheric SO_2 has a rather short lifetime, therefore the total simulated mass of SO_2 decreases rapidly towards simulated non-volcanic values after the last eruption considered in the model. As SO_2 is strongly influenced by episodic volcanic eruptions, a change in 'background' conditions is not easily detectable. In the case of simulated SO_2, the sulphur emitted from OCS accounts for only ∼7–25% of total sulphur (BGO + B15), when regarding the annual minima of total sulphur in 2006–2011 (Fig. 6.1).

As a consequence of the longer stratospheric residence time of sulphate aerosol, compared to SO_2, the sulphur mass contained in sulphate aerosol is accumulated and is therefore clearly higher than sulphur contained in SO_2 (Fig. 6.1). MIPAS measurements for the first period are not shown, due to retrieval difficulties by interfering H_2O at low altitudes, as discussed in Section 2.2.2. The sulphur mass in sulphate aerosol, as derived from MIPAS measurements, is greater than 100 Gg, with variability primarily being caused by volcanic eruptions. In the simulation BGO, considering OCS as the only sulphur source, the sulphur mass contained in stratospheric sulphate aerosol ranges between 67–88 Gg for an ESRad of 0.1 μm, and is lower (45–63 Gg) for a stronger sedimentation with an ESRad of 0.2 μm. When additionally considering volcanic sulphate aerosol, the sulphur mass increases to values that are at a similar level as mboxMIPAS data, in the case of B15. This is in agreement with the findings for SO_2, as presented above. Better agreement is achieved for an effective sedimentation radius of 0.5 μm for volcanic aerosol, compared to an ESRad of 0.2 μm. This is consistent with findings in Section 4.3.1 for the eruptions of Kasatochi in 2008, and Sarychev in 2009. In the case of simulated sulphate aerosol, the sulphur emitted from OCS accounts for ∼38–55% of total sulphur (BGO ESRad 0.1 μm + B15

ESRad 0.5 µm), when regarding the annual minima of total sulphur in 2006–2011 (Fig. 6.1). For a simulation of background sulphate aerosol with stronger removal by sedimentation in combination with volcanic sulphur (BGO ESRad 0.2 µm & B15 ES-Rad 0.5 µm), background sulphur represents only ∼30–45% of total sulphur during periods of lower volcanic influence in the years 2006–2011. As noted in Section 5.2.2, MIPAS data of sulphate aerosol are well below zero at polar latitudes in the annual mean (Fig. 5.20). Due to the higher weight of data at low- to mid-latitudes, this does not impair the agreement between the measured and modelled data, as can be seen in Fig A.6, where time series of masses are shown, integrated from 60°S–60°N. As seen in simulation B15, the stratospheric sulphate aerosol is influenced by volcanic sulphur throughout the entire MIPAS measurement time. During periods of weaker volcanic influence, values have increased from 2005–2012, connected to frequent and partly intense volcanic injections of SO_2. Vernier et al. (2015) also suggested an observed increased aerosol loading in the UTLS region during boreal summer to be connected to upward transport of anthropogenic pollution in the Asian summer monsoon.

Uncertainties in the results shown here for the comparison between integrated sulphur masses from MIPAS and CTM, arise from uncertainties in the trace-species distributions, as discussed in the two previous chapters (4 and 5). Depending on the meridional location of the vertical profiles of volume mixing ratios, the derived mass has a lower or higher weight. Furthermore, for sulphate aerosol sedimentation has a strong effect on the stratospheric mass. Simulations with different ESRad, meaning one spatial and temporal constant particle radius per simulation, which is a clear simplification and does not include various microphysical processes that determine the variable aerosol size distribution, illustrate the uncertainty of simulated sulphur mass. Nevertheless, the comparisons between the three MIPAS data sets, in combination with CTM results, as presented in Fig. 6.1, indicate consistency between the MIPAS data sets in terms of stratospheric sulphur mass. Furthermore, the importance of not only OCS as a primarily non-volcanic sulphur source, but also the relevance of volcanic SO_2, and an increase of MIPAS OCS and sulphate aerosol, has been demonstrated.

To finalise this chapter, time series of the entire stratospheric sulphur mass contained in carbonyl sulphide, sulphur dioxide, and sulphate aerosol, as derived from MIPAS measurements, are shown in Fig. 6.3, together with the partitioning into the three species. Only data from 2005–2012 are considered, as sulphate aerosol masses were not derived for the first MIPAS measurement period. To achieve a better presentation of the data, outliers are removed from the individual time series of sulphur masses. Outliers are detected using a limit of twice the standard deviation as derivation of the median, calculated over ±5 days around the tested value. The underestimation of SO_2 by MIPAS SO_2sgl and to a smaller degree by liquid-phase H_2SO_4 after volcanic eruptions, as discussed in Chap. 4, is not relevant for this analysis, as the focus lies on periods of relatively low volcanic influence.

MIPAS, partitioning of total stratospheric sulphur mass on OCS, SO$_2$ and H$_2$SO$_4$(liq)

MIPAS, percentage partitioning of total stratospheric sulphur mass on OCS, SO$_2$ and H$_2$SO$_4$(liq)
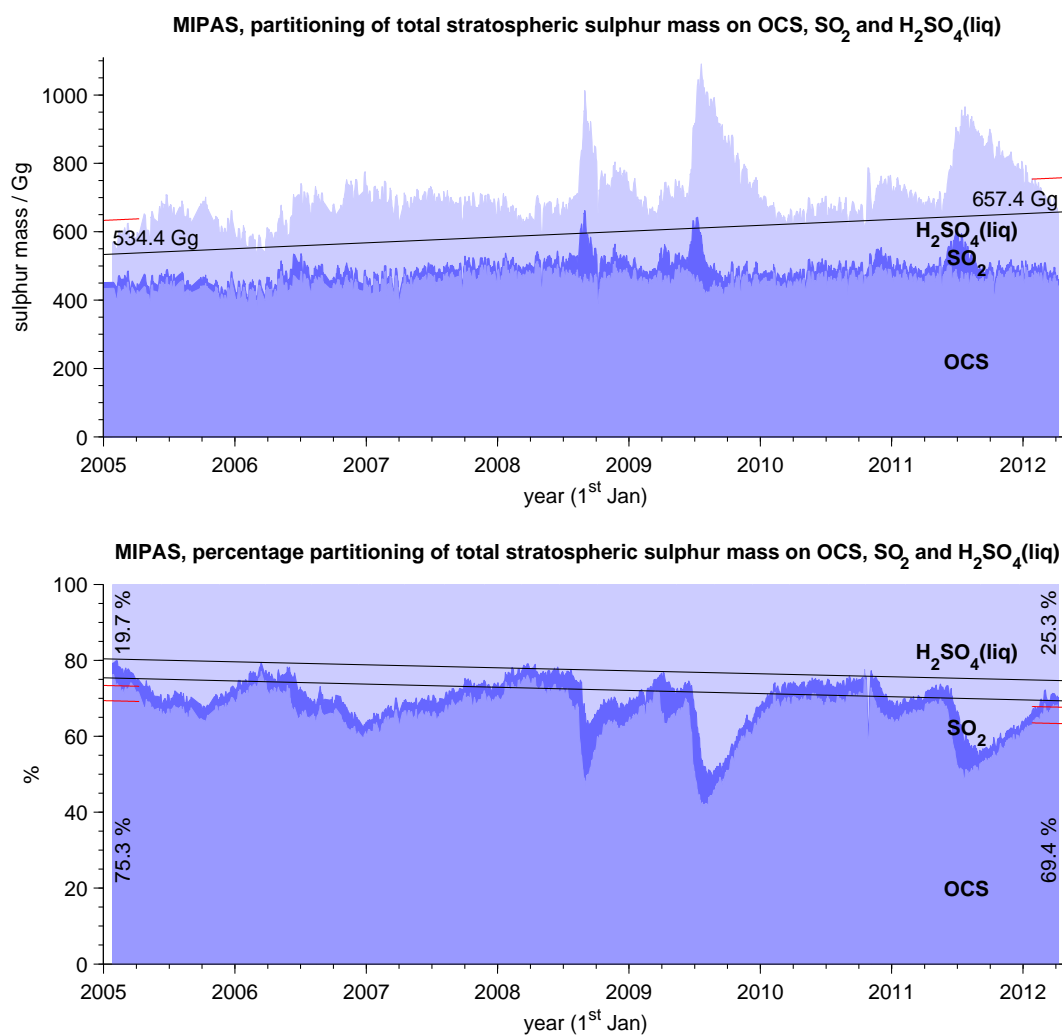
FIGURE 6.3: Time series of sulphur masses from MIPAS (as in Fig. 6.1), but as total stratospheric sulphur mass, and partitioning into the different species. Similar MIPAS data as in Fig. 6.1, but for 2005–2012 and corrected for outliers. Partitioning of stratospheric sulphur mass into the parts contained in OCS, SO$_2$, and liquid-phase H$_2$SO$_4$ (colour-coded). Upper panel: total values; lower panel: percentage values. Data are discarded (per data set), when the respective value differs more than twice the standard deviation from the median, both calculated over a period of ± 5 d around the value. Included are linear regressions (least squares fits) to the entire stratospheric sulphur mass, and the percentage partitioning. Calculated fits are indicated by red short lines. Black lines have the same slope, but are shifted towards less volcanically perturbed values. The numbers in the upper panel show the values of the linear regression (black) on the first and last day of the MIPAS data. In the bottom panel they indicate the partitioning on these days (black lines). Upper panel: 17.08 (15.76, 18.39) Gg yr^{-1}. Lower panel: partitioning OCS/SO$_2$/H$_2$SO$_4$(liq): 1 Jan 2005 75.3/4.00/19.7% (74.1/5.03/20.8%, 76.5/4.96/18.5%); 30. Apr 2012 69.4/5.32/25.3% (67.3/5.39/27.3%, 71.4/5.26/23.4%).

The entire stratospheric sulphur mass increased from around 534 to 657 Gg from Jan 2005 to Apr 2012. A linear least squares fit to the total sulphur mass reveals an increase of 158.4–184.8 Gg per decade. Following the MIPAS measurements, not only the total amount of sulphur has changed from 2005–2012, due to an increase measured in OCS and liquid-phase H$_2$SO$_4$, but also the ratio between the three species has changed. Regarding periods of relatively low volcanic activity, the part of sulphur mass contained in OCS decreased from 75.3 to 69.4% from Jan 2005 to Apr 2012, while the part retained in sulphate aerosol increased from 19.7 to 25.3%. Following

Thomason and Peter (2006), about 25% of the stratospheric sulphur mass resides in sulphate aerosol. This is in good agreement with the MIPAS data, especially towards the end of the measurements. This change in partitioning is related to volcanic emissions. For SO_2, an increase from 4.0 to 5.3% has been derived from the MIPAS measurements. Unfortunately, measurements ended during the removal phase of volcanic sulphur emitted by Nabro. The bulk of emitted sulphur had already been removed, but parts remained in the stratosphere at that time and impact the derived linear fits and are expected to increase their slope.

7 Summary and conclusions

This study focusses on the three main sulphur species that dominate the stratospheric sulphur loading. These are carbonyl sulphide, sulphur dioxide and sulphuric acid. The major part of OCS is emitted from the oceans throughout the year, and can reach the stratosphere as a consequence of its long tropospheric lifetime. In the stratosphere, OCS is destroyed and forms SO_2. Direct sources for stratospheric SO_2 are episodic volcanic eruptions that dominate the variability of the entire stratospheric sulphur loading. Sulphuric acid is formed from SO_2 and is found predominantly in the form of sulphate aerosol at altitudes below $\sim$30 km.

From the instrument MIPAS onboard Envisat data sets are available for the three main stratospheric sulphur species, from Jul 2002–Apr 2012, retrieved from infrared emission spectra at KIT-IMK. Data sets are provided as retrieved from single limb-scans (up to 1,300 profiles per day), covering the altitude ranges 8–50 km for OCS, 10–23 km for SO_2, and 10–30 km in the case of sulphate aerosol. For sulphur dioxide an additional data set is available, as retrieved from temporally and spatially averaged limb-scans. This latter data set is more suited for periods of low SO_2 loading and covers the majority of the stratosphere (15–45 km). The volume mixing ratio data sets of OCS and SO_2 were readily available for analyses during this thesis (Glatthor et al., 2015, 2017; Höpfner et al., 2013, 2015). The MIPAS data set of aerosol volume densities, however, has been retrieved more recently, and was first studied in this thesis.

The data set of AVDs demanded post-retrieval processing, as part of the present work. The retrieval is based on the assumption that all retrieved aerosol is sulphate aerosol with an aerosol composition of 75 wt% H_2SO_4 and 25% H_2O, and a binary solution density of 1,700 kg m^{-3}. As the AVDs appeared to contain strong signals from primarily non-sulphate aerosol in confined regions, the data set was filtered for several contributions of different types of aerosol. Identified and filtered from the retrieved data was the influence of cirrus clouds, polar stratospheric clouds, and ash.

A validation of the filtered aerosol volume density profiles from MIPAS against coincident balloon-borne in situ observations from Laramie, Wyoming (41°N), revealed a positive altitude-dependent bias of MIPAS AVDs. This bias is supposed to be a consequence of instrumental radiance baseline offsets. All MIPAS profiles were corrected for this positive bias, based on the comparison to in situ data. In general, de-biased MIPAS aerosol volume density profiles demonstrate good agreement with the in situ observations, with percentage differences being mostly below ±20% at $\sim$14–25 km.

Aiming at the analysis of consistency between the different MIPAS data sets, and on a general study of stratospheric sulphur, MIPAS observations have been analysed with the aid of simulations by an isentropic chemical transport model. As part of this

study, a sulphur module has been implemented into the CTM, which covers the essential conversions of OCS to SO_2 and SO_2 to H_2SO_4. The basic sulphur module consists of the following steps: photolysis of OCS forms SO_2 that is oxidised by OH and forms H_2SO_4. The condensed part of sulphuric acid is settled gravitationally, based on a spatially and temporally constant effective sedimentation radius. Terminal settling velocities depend on online calculated aerosol solution densities, and the partitioning between gas- and liquid-phase H_2SO_4 follows saturation vapour pressure calculations. The sulphur input considered in a simulation is chosen accordingly to the simulation aim. For analyses of non-volcanic sulphur the input is OCS from a bottom boundary (at 335 K potential temperature), based on MIPAS OCS. To study volcanic sulphur, no OCS is considered, but vertically resolved volcanic SO_2 injections are the only sulphur source.

MIPAS data sets of SO_2sgl and liquid-phase H_2SO_4 show strongest variability due to a number of eruptions that occurred between 2002 and 2012. Two of the most intense eruptions originated from the volcanoes Kasatochi (52.2°N/175.5°W) in August 2008, and Sarychev (48.1°N/48.1°E) in July 2009. In a case study on these eruptions the conformity between MIPAS SO_2sgl and MIPAS sulphate aerosol has been demonstrated with the help of model simulations, in terms of temporal evolution of volcanic sulphur mass and transport patterns. Simulated sulphate aerosol originating from the injected SO_2 (Kasatochi: 677 Gg; Sarychev: 768 Gg; at 10–19 km) agrees to within uncertainty levels with measured sulphate aerosol, with uncertainties arising, e.g., from the simulated sedimentation of aerosol. Furthermore, the agreement between simulated and measured SO_2 shows that the fast decay of SO_2 is well explained by its reaction with OH. This is the only removal mechanism included in the sulphur module, additionally to removal from a certain region by transport. The chemical lifetime of SO_2 is based on climatological values of OH without any feedbacks included that could arise from a possible depletion of OH in the presence of large amounts of SO_2. Further, the time-scale of formation of sulphate aerosol from SO_2 via oxidation with OH in the CTM is in agreement with the new MIPAS sulphate aerosol data set. The long-term removal of volcanic sulphur from the lower stratosphere in the extra-tropics following the two eruptions is shown to be dominated by transport via the Brewer-Dobson circulation, which leads to a general motion of subsidence polewards of ∼30°. The effect of sedimentation of sulphate aerosol cannot be neglected, however, and affects especially the peak values and the amount of aerosol that resides in the stratosphere on the long-term.

Transport patterns after the eruptions of Kasatochi and Sarychev show that most of the sulphur that has been emitted at ∼50°N impacts the Northern hemisphere mid- to high-latitudes. However, after the two eruptions parts of the sulphur at higher altitudes (16–22 km) also reach the tropics, mainly in the form of longer-lived sulphate aerosol. This holds true for measured and modelled volcanic sulphur. After the eruption of Sarychev, integrated masses for the altitude region 14.5–18.5 km show simulated peak values in the Northern hemisphere tropics that are only 20% smaller (lower limit) compared to equal altitudes in the NH extra-tropics. With 85%, differences are larger after the eruption of Kasatochi. In the equatorial stratosphere, upward motion of air dominates and counteracts sedimentation. Measurements and simulations show that sulphate aerosol is lifted in the tropical pipe, from where

the volcanic sulphur may influence both hemispheres. For these two eruptions it is demonstrated that sulphur that enters the stratosphere at 50°N can impact the sulphur loading of the entire hemisphere, and even the Southern hemisphere.

These findings regarding residence time and transport of sulphur, which show the potentially global effect of sulphur that is injected in the mid-latitudes, must be considered in proposed climate-engineering schemes using sulphate aerosol. Additional analyses including the CTM tested the consistency between MIPAS data sets, not only for SO_2sgl and liquid-phase H_2SO_4 after volcanic eruptions, but also for OCS and SO_2mea, and the already mentioned MIPAS data sets, over the entire MIPAS measurement period. The relatively constant input of OCS, compared to the highly variable volcanic emissions of SO_2, is known to be the most important sulphur source sustaining the stratospheric sulphur loading, when not considering volcanic sulphur injections. The relatively long-lived trace-species is transported from the surface to the stratosphere, where OCS enters mainly through the tropical tropopause layer, and is well mixed on its way. Model simulations of OCS, based on a bottom boundary of OCS derived from MIPAS as the only sulphur input, result in good agreement to MIPAS OCS, especially in the tropics (differences $< \pm 50$ pptv, compared to absolute amounts of $\sim$500–520 pptv). Photolysis of OCS leads to a strong gradient between higher OCS volume mixing ratios at tropopause heights, and low values above. At around 28–30 km the OCS has decayed to 0 pptv, while the released sulphur forms SO_2. The resulting pattern of enhanced SO_2 at 25–35 km in the tropics is seen in MIPAS and the CTM, with reasonable agreement. On annual scale the CTM shows a peak at 28 km that is $\sim$20% lower than for MIPAS SO_2mea, and time series at 28–30 km compare very well in terms of variability and absolute values.

From the enhanced sulphur dioxide loading in the tropics at around 25–35 km, which is formed by sulphur release from OCS, sulphate aerosol is formed and leads to an enhanced aerosol loading in this region, both in the measurements and simulations. In the data set of MIPAS sulphate aerosol, a pattern of enhanced VMRs covers all latitudes, from the tropics at higher altitudes (> 22 km) to high-latitudes at lower altitudes (< 25 km). Model simulations suggest this pattern in the new data set of MIPAS aerosol to be realistic and to originate from sulphur released from OCS. Absolute values of simulated sulphate aerosol depend strongly on the chosen effective sedimentation radius. Compared to MIPAS, an ESRad of 0.2 µm provides good model results in the tropics where the aerosol is formed, while a smaller ESRad of 0.1 µm - which implies weaker aerosol removal by sedimentation - results in better agreement in absolute values in the extra-tropics. Sedimentation is seen to be one of the main uncertainties in the presented results of simulated sulphate aerosol. In the case study on two single eruptions it had been shown that the removal of the bulk of injected sulphur was dominated by the Brewer-Dobson circulation rather than sedimentation. However, and especially important for aerosol under background conditions, sedimentation did indeed have a considerable effect on the peak values of simulated volcanic sulphate aerosol and on the amount of sulphur that remained in the modelled atmosphere after several months. For volcanic sulphur a larger ESRad of 0.5 µm was found as best estimate. Smaller particles during 'background' conditions, and larger particles after volcanic eruptions due to increased sulphur

availability, are in agreement with literature.

Patterns seen in MIPAS SO_2 and sulphate aerosol at lower altitudes could only partly be explained by model simulations. In the MIPAS data, these are primarily two patterns. The first pattern are enhancements in the tropics at 14–16 km that persist in the MIPAS data throughout the entire measurement time, whilst being of varying intensity. To some extent these are expected to be influenced by volcanic contributions, but also other origins are thought to play a role, reflected in their persistency. The second MIPAS pattern are elevated VMRs at 10–12 km in the Northern hemisphere during boreal summer, with annual periodicity. Again, some influence by volcanic sulphur may contribute to the enhancements, but the annual periodicity suggests a different origin, such as wild fires or industrial sources.

Regarding the stratospheric sulphur burden, simulations in- and excluding volcanic sulphur show that measured sulphur masses for the different species are in agreement, when considering input from OCS and volcanic SO_2 with a relatively high frequency of small volcanic eruptions (98 eruption days in $\sim$10 years). MIPAS OCS suggests a strong increase of stratospheric OCS from 2006–2008 (+ 13–32 Gg yr^{-1}), while the stratospheric OCS burden remained at a rather constant level before and after this period. One possible reason for this increase in stratospheric OCS might be caused by a decrease in tropopause heights during this period. Time series of sulphate aerosol mass further suggest an increase during periods of relatively weak volcanic influence. Additionally, comparisons between measured and simulated SO_2 and liquid-phase H_2SO_4 emphasise the importance of volcanic contributions to reach the levels of observed stratospheric sulphur masses.

In this thesis the studied MIPAS data sets of the main stratospheric sulphur compounds were shown to generally be consistent with each other in terms of mass and patterns. One of the advantages of retrieving profiles for the different species from the same instrument is the missing sampling bias due to varying geolocations and measurement times. To a certain degree data availability still differs as a result of filters that are applied during the retrieval process or to the retrieved data sets.

In continuation of this work the following 'refinements' would be desirable. Concerning the new MIPAS data set of sulphate aerosol, an update of the retrievals for the high-resolution measurement period (2002–2004) should be considered, as during this period interferences due to water vapour corrupted retrieved aerosol volume densities at low altitudes. To have a more continuous data set for the entire MIPAS measurement time, the bias between the two measurement periods should be corrected. Data quality might further be improved by filtering MIPAS spectra prior to the retrieval process, based on Griessbach et al. (2014, 2016), where methods were provided to detect MIPAS spectra affected by ice or ash. A more sophisticated PSC filter could limit the amount of de-selected data. The offset correction that is based on a globally constant altitude-dependent de-biasing, and on comparisons with in situ data at 41°N only, is thought to over-correct high-latitude profiles of MIPAS aerosol volume densities. Low data availability might hinder an improved offset correction, however. Aerosol composition retrievals would be desirable, and the combination of MIPAS aerosol volume densities with measurements from other sensors, such as the Scanning Imaging Absorption Spectrometer for Atmospheric CHartographY (SCIAMACHY) or the Global Ozone Monitoring by Occultation of

Stars (GOMOS) onboard Envisat, could help to constrain aerosol size retrievals.

Concerning the sulphur module that has been implemented in the CTM as part of the present work, several additional features could be included. The module could be refined in terms of species (e.g., DMS), and processes, such as decay of OCS by O or OH, and decay of SO_2 by photolysis could be added. Even though a more complex sulphur module might improve the agreement with MIPAS measurements, especially in the case of sulphate aerosol, the simple approach shown in this work has the advantage that one can easily study the influence of individual processes. Further, a complex model system does not necessarily imply better results. More important than the above mentioned model improvements are thought to be a consideration of photolysis of gas-phase H_2SO_4 in the middle to upper stratosphere, and a refinement of the sulphate aerosol scheme, to improve the simulation of the microphysical process of sedimentation.

Even without the refinements mentioned, the MIPAS data sets of the two main precursor gases of stratospheric aerosol, and stratospheric sulphate aerosol itself, were shown to provide a valuable basis for analyses of stratospheric sulphur. By combination with model results, the quality of the data sets has been demonstrated and further analyses based on the MIPAS measurements are encouraged, to raise our knowledge about stratospheric sulphur, e.g., in terms of sulphur budget, temporal evolution, patterns, or removal processes. The new MIPAS data set of sulphate aerosol is a step forward to close the sulphur budget for 2002–2012, and can be used to further constrain models, to quantify volcanic emissions, and to help improve our understanding of stratospheric sulphur and its effects on climate. Model simulations presented in this thesis showed agreement between the MIPAS data sets of SO_2sgl and sulphate aerosol after two volcanic eruptions, in terms of mass and transport patterns. Further, conformity has been demonstrated between the MIPAS data sets of OCS, SO_2mea & SO_2sgl, and liquid-phase H_2SO_4 under so-called 'background' conditions. Several patterns of background sulphur seen in the MIPAS data could furthermore be confirmed by CTM simulations. It has been demonstrated by model simulations that in the period 2006–2011 the sulphur released from OCS only accounted for about 7–25% of the stratospheric sulphur mass contained in SO_2 and for 30–55% of the stratospheric sulphur mass contained in sulphate aerosol, in both cases regarding periods of relatively low volcanic influence. The presented findings help to better understand the transformation between the three sulphur species, prove the importance of volcanic sulphur for the stratospheric sulphur loading, and encourage further use of the MIPAS data sets.

A Appendix

A.1 Method of increasing areas for zonal averages

As described in Günther et al. (2018), zonal averages are calculated using a method of increasing areas to diminish the influence of non-homogeneous data distribution. Calculations are based on the horizontal distribution of grid cells in the Chemical Transport Model used in the present work ($\sim 2.5°$ latitude x 3.75° longitude). In the case of the MIPAS measurements, daily arithmetic averages are derived per CTM-grid box from the single profiles. The grid box profiles are averaged longitudinally to 32 profiles of lat x 11.25° (with lat being $\sim 2.5°$ or a multiple of it) and the area is then further broadened by a factor of two per average, whereas the number of boxes averaged lessen by this factor (32 x 11.25° $\rightarrow$ 16 x 22.5° $\rightarrow$ 8 x 45° $\rightarrow$ 4 x 90° $\rightarrow$ 2 x 180° $\rightarrow$ 1 x 360°). In cases of total longitudinal data coverage the result is not changed, compared to standard averaging (sum of values divided by number of values). When averaging over a wide range of latitudes ($> \sim 11.25°$) are weighted averages are calculated (and in some cases also for smaller latitude ranges) to prevent biases towards values from high latitudes, as the surface decreases from the equator towards the poles.

A.2   Volcanoes

TABLE A.1: List of 30 volcanoes, used for simulation G17, adapted from Höpfner et al. (2015). SO_2 masses are given for three altitude ranges (for example (1): 10–14, 14–15, 15–22 km). The total SO_2 mass is given in bold. The Names of the volcanoes are given in Table A.2. The latitudes of the volcanoes are colour-coded: 60°N–90°N; 30°N–60°N; 00°N–30°N; 00°S–30°S; 30°S–60°S

	Name	Eruption date	SO_2 / Gg				altitude / km			
1	Ny	25.07.2002	22	15	0	**37**	10	14	15	22
2	Ru	25.09.2002	36	55	10	**101**	10	14	17	19
3	Rev	03.11.2002	54	45	12	**111**	10	14	17	19
4	So	12.06.2003	68	40	2	**110**	10	14	17	19
5	Ma	27.01.2005	79	105	39	**223**	10	14	17	20
6	An	06.04.2005	34	45	0	**79**	10	14	16	22
7	Tr	mid 07.2005	38	30	0	**68**	10	14	16	22
8	Tr	mid 08.2005	61	35	0	**96**	10	14	15	22
9	Ma	27.02.2006	21	58	1	**80**	10	14	17	22
10	So	20.05.2006	40	38	85	**163**	10	12.5	16.5	19
11	Ra	07.10.2006	90	118	12	**220**	10	14	17.5	19
12	Ny	27.11.2006	49	58	0	**107**	10	14	17	22
13	Fo	04.04.2007	57	14	0	**71**	10	14	15	22
14	Ta	30.09.2007	30	60	0	**90**	10	14	16	22
15	Ch	02.05.2008	30	2	2	**34**	10	14	18	22
16	Ok	12.07.2008	85	33	0	**118**	10	14	16	22
17	Ka	07.08.2008	518	124	35	**677**	10	14	18	19
18	Da	03.11.2008	40	70	1	**111**	10	14	18	19
19	Re	23.03.2009	182	18	0	**200**	10	14	15	22
20	Fe	10.04.2009	14	11	2	**27**	10	14	17	20
21	Sa	12.06.2009	401	362	5	**768**	10	14	18	19
22	Ny	02.01.2010	17	3	2	**22**	10	14	16.5	19
23	So	11.02.2010	11	20	5	**35**	10	14	17	20
24	Pa	28.05.2010	0	25	0	**25**	10	14	18	19
25	Me	04.11.2010	0	263	13	**378**	10	14	17	19
26	Sh	12.12.2010	18	1	0	**19**	10	13	17	22
27	Kar	01.01.2011	0	0	1	**1**	10	14	16	18
28	Gr	21.05.2011	273	2	0	**275**	10	13	15	22
29	Pu	04.06.2011	270	0	0	**270**	10	14	18	22
30	Na	12.06.2011	131	450	55	**636**	10	14.5	17	19.5

TABLE A.2: Abbreviations for volcanoes as seen in Fig.4.3, together with their locations. Colour-coding: 60°N–90°N; 30°N–60°N; 00°N–30°N; 00°S–30°S; 30°S–60°S

Abbrev.	Name	Country	Lat °N	Lon °E
Ny	Nyamuragira	Democratic Republic of the Congo	-1.4	29.2
Ru	Ruang	Indonesia	2.3	125.4
Rev	Reventador	Equador	-0.1	-77.7
So	Soufrière Hills	The Caribbean	16.7	-62.2
Ma	Manam	Papua New Guinea	-4.1	145.0
An	Anatahan	Northern Mariana Islands, USA	16.4	145.7
Ra	Rabaul	Papua New Guinea	-4.3	152.2
Fo	Piton de la Fournaise	La Réunion, France	-21.2	55.7
Ta	Jebel at Tair	Yemen	15.6	41.8
Ch	Chaitén	Chile	-42.8	-72.7
Ok	Okmok	Aleutian Islands, USA	53.4	-168.1
Ka	Kasatochi	Aleutian Islands, USA	52.2	-175.5
Da	Dalaffilla	Ethiopia	13.8	40.5
Re	Redoubt	Alaska, USA	60.5	-152.7
Fe	Fernandina	Galápagos Islands, Ecuador	-0.4	-91.6
Sa	Sarychev Peak	Kuril Islands, Russia	48.1	153.2
Pa	Pacaya	Guatemala	14.4	-90.6
Me	Mount Merapi	Indonesia	-7.5	110.4
Sh	Shiveluch	Kamchatka, Russia	56.7	161.4
Kar	Karymsky	Kamchatka, Russia	54.0	159.4
Gr	Grímsvötn	Iceland	64.4	-17.3
Pu	Puyehue-Cordón Caulle	Chile	-40.6	-72.1
Na	Nabro	Eritrea	13.4	41.7
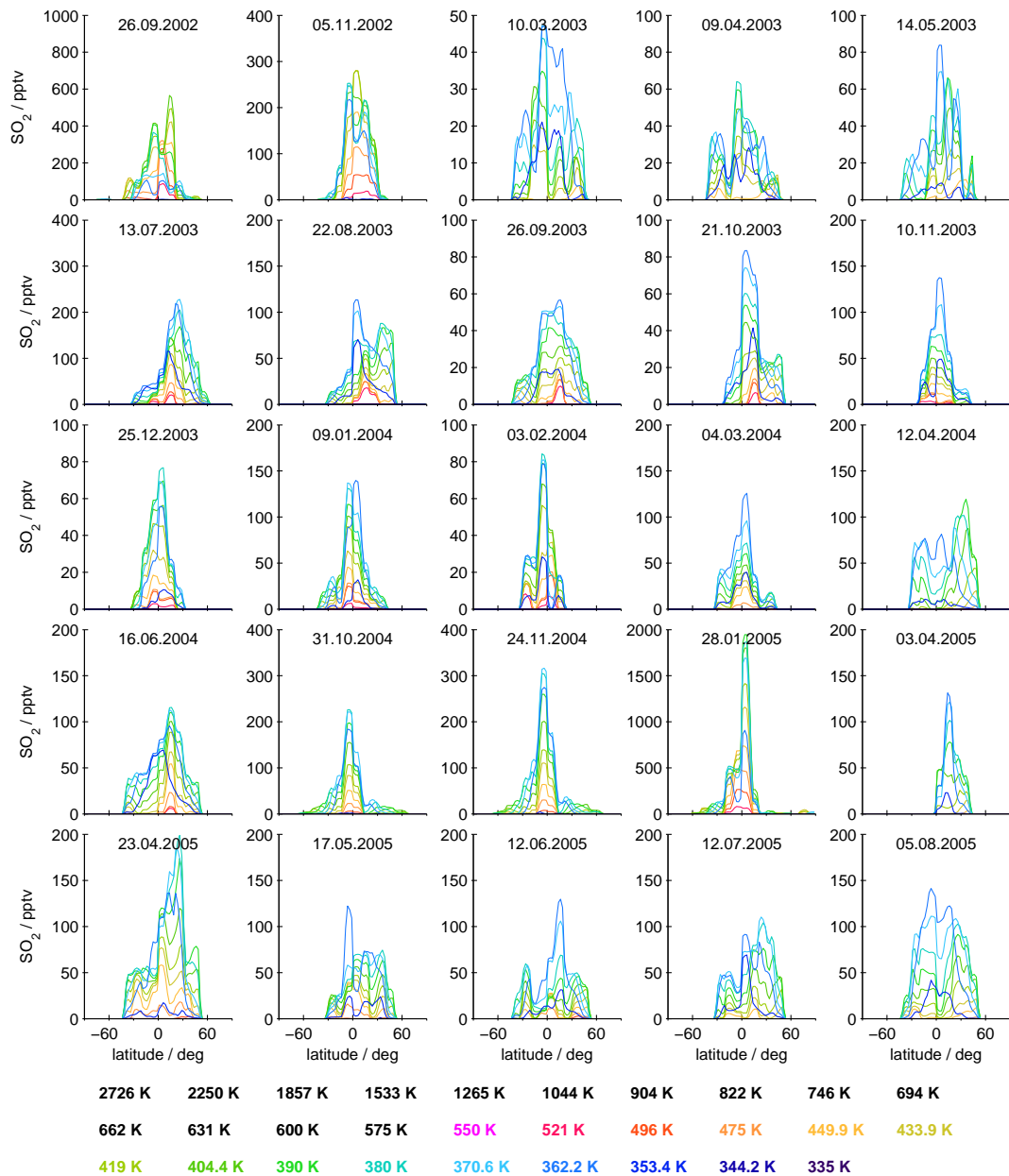
FIGURE A.1: Sulphur dioxide volume mixing ratios used as input for the CTM simulation B15. Shown are meridional distributions of SO₂ volume mixing ratios per isentropic level. Consider the varying ordinate limits. A list of the volcanoes is given in Brühl et al. (2015) (Table 1 therein). The date of the volcanic input is given per panel.
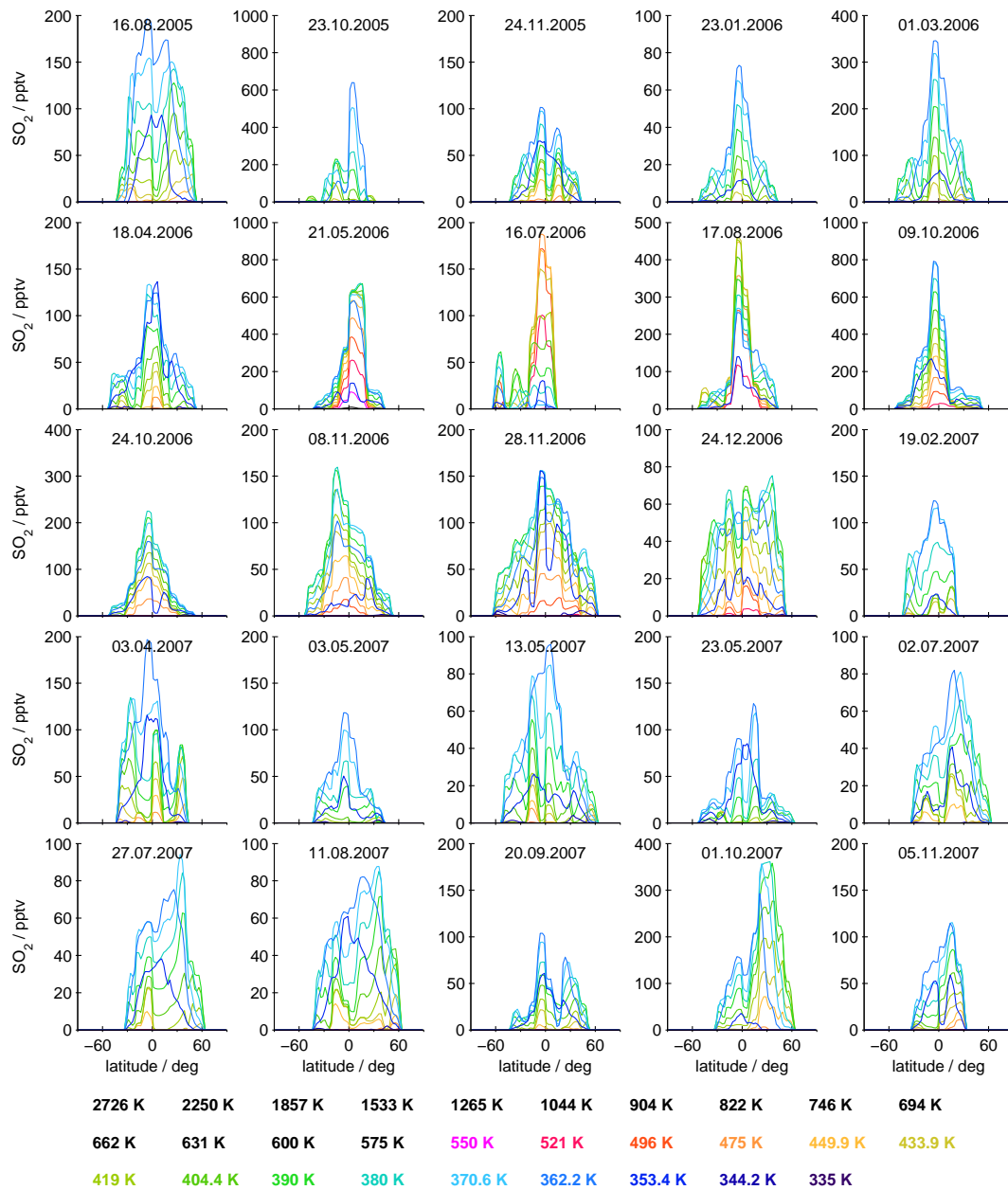
FIGURE A.2: Continuation of Fig. A.1.
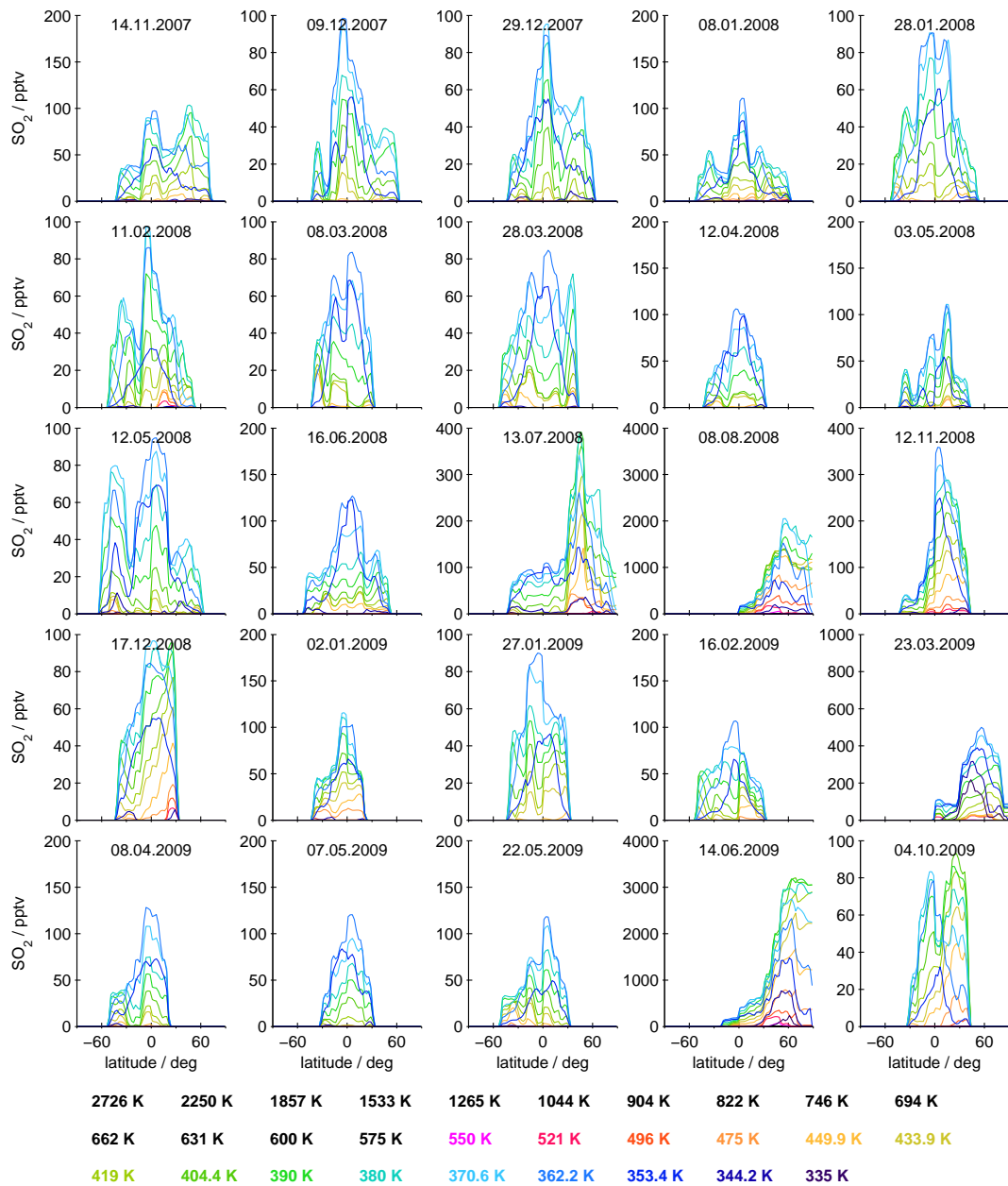
FIGURE A.3: Continuation of Fig. A.1.
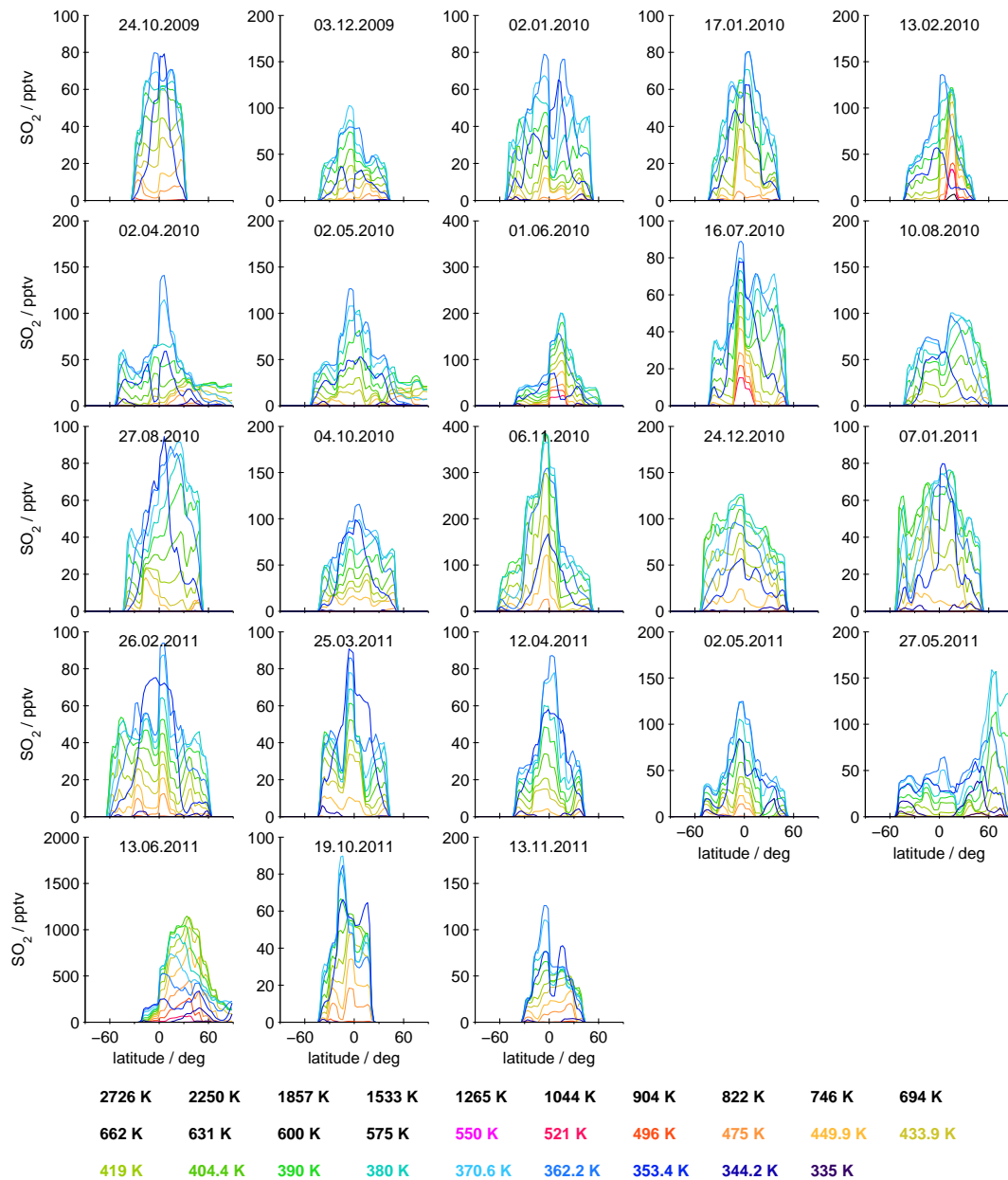
FIGURE A.4: Continuation of Fig. A.1.

A.3   MIPAS sulphate aerosol: de-selected data for background conditions
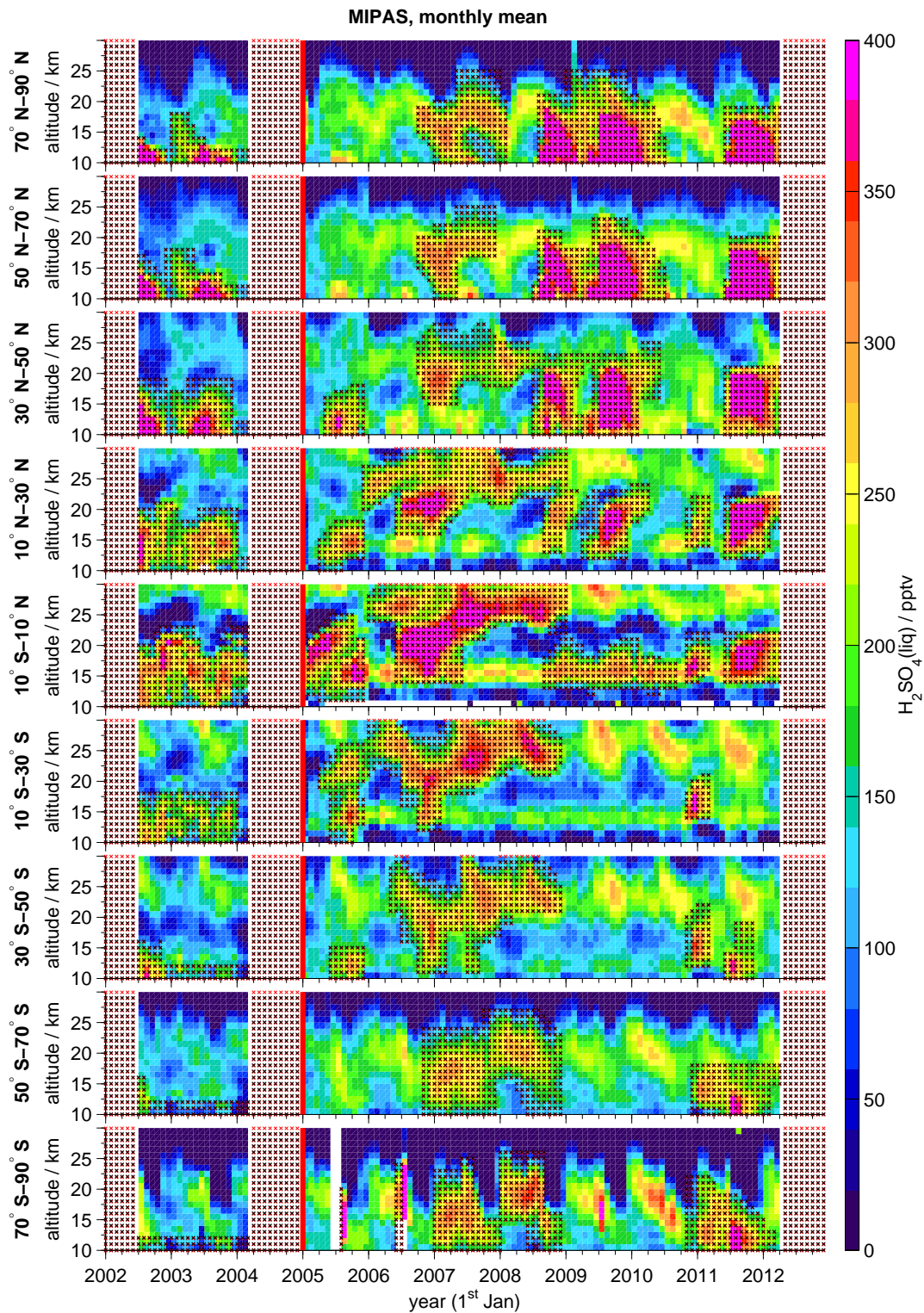
FIGURE A.5: Time series of MIPAS sulphate aerosol volume mixing ratios (2002–2012), with data being marked that are not considered when analysing 'non-volcanic' data. Data are vertically resolved time series of monthly averages for 20° latitude bins (area weighted averages). A vertical red line indicates the transition between the MIPAS measurement periods. Values exceeding the colour-scales are assigned with the limiting values.

A.4   Stratospheric sulphur mass

Stratospheric sulphur mass (≥ 10 km), 60°S–60°N
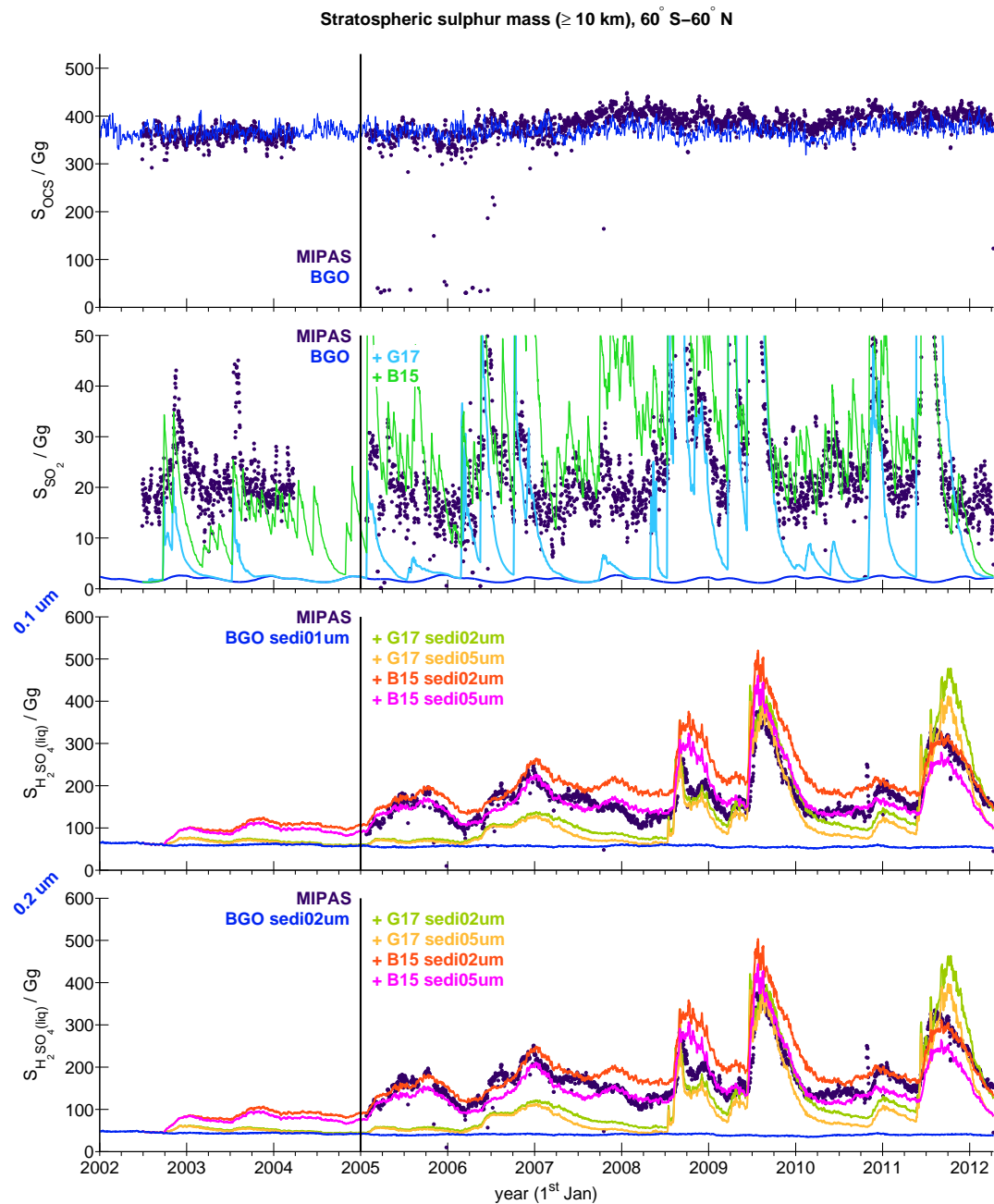
FIGURE A.6: Time series of stratospheric sulphur masses from MIPAS and CTM (60°S–60°N; 2002–2012). MIPAS: OCS, SO_2sgl, liquid-phase H_2SO_4; CTM: OCS (BGO), SO_2 (BGO, G17, B15), liquid-phase H_2SO_4 (BGO with ESRad 0.1 and 0.2 μm, G17 and B15 with ESRad 0.2 and 0.5 μm). The sulphur masses are based on stratospheric data only (filtered with NCEP tropopause heights). Minimal available altitude: 10 km. Maximal altitude: for OCS and H_2SO_4(liq) 30 km, for SO_2sgl 23 km. Masses are calculated from 5 d running zonal means for ~10° latitude bins, as in Sect. 4.3.1. Measured sulphate aerosol for P1 is not shown due to retrieval problems at low altitudes. Panel 1: sulphur mass in OCS from MIPAS and CTM (BGO). Panel 2: sulphur mass in SO_2 from MIPAS (SO_2sgl) and CTM (BGO, BGO + G17 and BGO + B15). Panel 3&4: sulphur mass in sulphate aerosol from MIPAS and CTM (BGO with ESRad 0.1 μm in panel 3, and with ESRad 0.2 μm in panel 4). Additionally in panels 3&4 are the sulphur masses from G17 and B15 (both with ESRad 0.2 and 0.5 μm). These masses are added to the masses from BGO.

Bibliography

Andersson, S. M., Martinsson, B. G., Vernier, J.-P., Friberg, J., Brenninkmeijer, C. A. M., Hermann, M., van Velthoven, P. F. J., and Zahn, A.: Significant radiative impact of volcanic aerosol in the lowermost stratosphere, Nature Communications, 6, 7692, doi: 10.1038/ncomms8692, URL `https://doi.org/10.1038/ncomms8692`, 2015.

Aschmann, J.: B3DCTM Manual, University of Bremen, 2014.

Aschmann, J., Sinnhuber, B.-M., Atlas, E. L., and Schauffler, S. M.: Modeling the transport of very short-lived substances into the tropical upper troposphere and lower stratosphere, Atmospheric Chemistry and Physics, 9, 9237–9247, doi:10.5194/acp-9-9237-2009, URL `https://www.atmos-chem-phys.net/9/9237/2009/`, 2009.

Ayers, G. P., Gillett, R. W., and Gras, J. L.: On the vapor pressure of sulfuric acid, Geophysical Research Letters, 7, 433–436, doi:10.1029/GL007i006p00433, URL `http://dx.doi.org/10.1029/GL007i006p00433`, 1980.

Baldwin, M. P., Gray, L. J., Dunkerton, T. J., Hamilton, K., Haynes, P. H., Randel, W. J., Holton, J. R., Alexander, M. J., Hirota, I., Horinouchi, T., Jones, D. B. A., Kinnersley, J. S., Marquardt, C., Sato, K., and Takahashi, M.: The quasi-biennial oscillation, Reviews of Geophysics, 39, 179–229, doi:10.1029/1999RG000073, URL `http://dx.doi.org/10.1029/1999RG000073`, 2001.

Barkley, M. P., Palmer, P. I., Boone, C. D., Bernath, P. F., and Suntharalingam, P.: Global distributions of carbonyl sulfide in the upper troposphere and stratosphere, Geophysical Research Letters, 35, n/a–n/a, doi:10.1029/2008GL034270, URL `http://dx.doi.org/10.1029/2008GL034270`, l14810, 2008.

Bekki, S.: Oxidation of volcanic SO_2: A sink for stratospheric OH and H_2O, Geophysical Research Letters, 22, 913–916, doi:10.1029/95GL00534, URL `http://dx.doi.org/10.1029/95GL00534`, 1995.

Bourassa, A. E., Robock, A., Randel, W. J., Deshler, T., Rieger, L. A., Lloyd, N. D., Llewellyn, E. J., and Degenstein, D. A.: Large Volcanic Aerosol Load in the Stratosphere Linked to Asian Monsoon Transport, Science, 337, 78–81, doi:10.1126/science.1219371, URL `https://doi.org/10.1126/science.1219371`, 2012.

Brasseur, G. P. and Solomon, S.: Aeronomy of the middle atmosphere: chemistry and physics of the stratosphere and mesosphere, 2006.

Brock, C. A., Hamill, P., Wilson, J. C., Jonsson, H. H., and Chan, K. R.: Particle Formation in the Upper Tropical Troposphere: A Source of Nuclei for the Stratospheric Aerosol, Science, 270, 1650–1653, doi:10.1126/science.270.5242.1650, URL `http://science.sciencemag.org/content/270/5242/1650`, 1995.

Brühl, C., Lelieveld, J., Crutzen, P. J., and Tost, H.: The role of carbonyl sulphide as a source of stratospheric sulphate aerosol and its impact on climate, Atmospheric Chemistry and Physics, 12, 1239–1253, doi:10.5194/acp-12-1239-2012, URL `https://doi.org/10.5194/acp-12-1239-2012`, 2012.

Brühl, C., Lelieveld, J., Tost, H., Höpfner, M., and Glatthor, N.: Stratospheric sulfur and its implications for radiative forcing simulated by the chemistry climate model EMAC, Journal of Geophysical Research: Atmospheres, 120, 2103–2118, doi:10.1002/2014jd022430, URL https://doi.org/10.1002/2014jd022430, 2015.

Burkholder, J. B., Sander, S. P., Abbatt, J., Barker, J. R., Huie, R. E., Kolb, C. E., Kurylo, M. J., Orkin, V. L., Wilmouth, D. M., and Wine, P. H.: Chemical Kinetics and Photochemical Data for Use in Atmospheric Studies, Evaluation Number 18, vol. JPL Publication 15–10, Jet Propulsion Laboratory, Jet Propulsion Laboratory, Pasadena, URL http://gpldataeval.jpl.nasa.gov, 2015.

Butchart, N.: The Brewer-Dobson circulation, Reviews of Geophysics, 52, 157–184, doi:10.1002/2013RG000448, URL http://dx.doi.org/10.1002/2013RG000448, 2014.

Cammas, J.-P., Brioude, J., Chaboureau, J.-P., Duron, J., Mari, C., Mascart, P., Nédélec, P., Smit, H., Pätz, H.-W., Volz-Thomas, A., Stohl, A., and Fromm, M.: Injection in the lower stratosphere of biomass fire emissions followed by long-range transport: a MOZAIC case study, Atmospheric Chemistry and Physics, 9, 5829–5846, doi:10.5194/acp-9-5829-2009, URL http://www.atmos-chem-phys.net/9/5829/2009/, 2009.

Campbell, P. and Deshler, T.: Condensation nuclei measurements in the midlatitude (1982-2012) and Antarctic (1986-2010) stratosphere between 20 and 35 km, Journal of Geophysical Research: Atmospheres, 119, 137–152, doi:10.1002/2013jd019710, URL https://doi.org/10.1002/2013jd019710, 2014.

Carn, S., Clarisse, L., and Prata, A.: Multi-decadal satellite measurements of global volcanic degassing, Journal of Volcanology and Geothermal Research, 311, 99 – 134, doi:https://doi.org/10.1016/j.jvolgeores.2016.01.002, URL http://www.sciencedirect.com/science/article/pii/S0377027316000032, 2016.

Carslaw, K. S., Luo, B., and Peter, T.: An analytic expression for the composition of aqueous HNO_3-H_2SO_4 stratospheric aerosols including gas phase removal of HNO_3, Geophysical Research Letters, 22, 1877–1880, doi:10.1029/95GL01668, URL http://dx.doi.org/10.1029/95GL01668, 1995.

Chagnon, C. W. and Junge, C. E.: THE VERTICAL DISTRIBUTION OF SUB-MICRON PARTICLES IN THE STRATOSPHERE, Journal of Meteorology, 18, 746–752, doi:10.1175/1520-0469(1961)018<0746:TVDOSM>2.0.CO;2, URL https://doi.org/10.1175/1520-0469(1961)018<0746:TVDOSM>2.0.CO;2, 1961.

Chin, M. and Davis, D. D.: A reanalysis of carbonyl sulfide as a source of stratospheric background sulfur aerosol, Journal of Geophysical Research, 100, 8993, doi:10.1029/95jd00275, URL https://doi.org/10.1029/95jd00275, 1995.

Clarisse, L., Hurtmans, D., Clerbaux, C., Hadji-Lazaro, J., Ngadi, Y., and Coheur, P.-F.: Retrieval of sulphur dioxide from the infrared atmospheric sounding interferometer (IASI), Atmospheric Measurement Techniques, 5, 581–594, doi:10.5194/amt-5-581-2012, URL https://doi.org/10.5194/amt-5-581-2012, 2012.

Corradini, S., Merucci, L., Prata, A. J., and Piscini, A.: Volcanic ash and SO_2 in the 2008 Kasatochi eruption: Retrievals comparison from different IR satellite sensors, Journal of Geophysical Research, 115, doi:10.1029/2009jd013634, URL https://doi.org/10.1029/2009jd013634, 2010.

Crutzen, P. J.: The possible importance of CSO for the sulfate layer of the stratosphere, Geophysical Research Letters, 3, 73–76, doi:10.1029/GL003i002p00073, URL http://dx.doi.org/10.1029/GL003i002p00073, 1976.

Crutzen, P. J.: Albedo Enhancement by Stratospheric Sulfur Injections: A Contribution to Resolve a Policy Dilemma?, Climatic Change, 77, 211, doi:10.1007/s10584-006-9101-y, URL `https://doi.org/10.1007/s10584-006-9101-y`, 2006.

Damoah, R., Spichtinger, N., Servranckx, R., Fromm, M., Eloranta, E. W., Razenkov, I. A., James, P., Shulski, M., Forster, C., and Stohl, A.: A case study of pyro-convection using transport model and remote sensing data, Atmospheric Chemistry and Physics, 6, 173–185, doi:10.5194/acp-6-173-2006, URL `http://www.atmos-chem-phys.net/6/173/2006/`, 2006.

Dee, D. P., Uppala, S. M., Simmons, A. J., Berrisford, P., Poli, P., Kobayashi, S., Andrae, U., Balmaseda, M. A., Balsamo, G., Bauer, P., Bechtold, P., Beljaars, A. C. M., van de Berg, L., Bidlot, J., Bormann, N., Delsol, C., Dragani, R., Fuentes, M., Geer, A. J., Haimberger, L., Healy, S. B., Hersbach, H., Hólm, E. V., Isaksen, L., Kållberg, P., Köhler, M., Matricardi, M., McNally, A. P., Monge-Sanz, B. M., Morcrette, J.-J., Park, B.-K., Peubey, C., de Rosnay, P., Tavolato, C., Thépaut, J.-N., and Vitart, F.: The ERA-Interim reanalysis: configuration and performance of the data assimilation system, Quarterly Journal of the Royal Meteorological Society, 137, 553–597, doi:10.1002/qj.828, URL `https://doi.org/10.1002/qj.828`, 2011.

Deshler, T.: A review of global stratospheric aerosol: Measurements, importance, life cycle, and local stratospheric aerosol, Atmospheric Research, 90, 223 – 232, doi:http://dx.doi.org/10.1016/j.atmosres.2008.03.016, URL `http://www.sciencedirect.com/science/article/pii/S0169809508000598`, 17th International Conference on Nucleation and Atmospheric Aerosols, 2008.

Deshler, T., Hervig, M. E., Hofmann, D. J., Rosen, J. M., and Liley, J. B.: Thirty years of in situ stratospheric aerosol size distribution measurements from Laramie, Wyoming (41°N), using balloon-borne instruments, Journal of Geophysical Research: Atmospheres, 108, n/a–n/a, doi:10.1029/2002JD002514, URL `http://dx.doi.org/10.1029/2002JD002514`, 4167, 2003.

Diallo, M., Legras, B., and Chédin, A.: Age of stratospheric air in the ERA-Interim, Atmospheric Chemistry and Physics, 12, 12 133–12 154, doi:10.5194/acp-12-12133-2012, URL `http://www.atmos-chem-phys.net/12/12133/2012/`, 2012.

Doeringer, D., Eldering, A., Boone, C. D., Abad, G. G., and Bernath, P. F.: Observation of sulfate aerosols and SO_2 from the Sarychev volcanic eruption using data from the Atmospheric Chemistry Experiment (ACE), Journal of Geophysical Research: Atmospheres, 117, n/a–n/a, doi:10.1029/2011jd016556, URL `https://doi.org/10.1029/2011jd016556`, 2012.

Eisinger, M. and Burrows, J. P.: Tropospheric sulfur dioxide observed by the ERS-2 GOME instrument, Geophysical Research Letters, 25, 4177–4180, doi:10.1029/1998GL900128, URL `http://dx.doi.org/10.1029/1998GL900128`, 1998.

Fischer, H., Birk, M., Blom, C., Carli, B., Carlotti, M., von Clarmann, T., Delbouille, L., Dudhia, A., Ehhalt, D., Endemann, M., Flaud, J. M., Gessner, R., Kleinert, A., Koopman, R., Langen, J., López-Puertas, M., Mosner, P., Nett, H., Oelhaf, H., Perron, G., Remedios, J., Ridolfi, M., Stiller, G., and Zander, R.: MIPAS: an instrument for atmospheric and climate research, Atmospheric Chemistry and Physics, 8, 2151–2188, doi:10.5194/acp-8-2151-2008, URL `https://doi.org/10.5194/acp-8-2151-2008`, 2008.

Fromm, M., Bevilacqua, R., Servranckx, R., Rosen, J., Thayer, J. P., Herman, J., and Larko, D.: Pyro-cumulonimbus injection of smoke to the stratosphere: Observations and impact

of a super blowup in northwestern Canada on 3–4 August 1998, Journal of Geophysical Research: Atmospheres, 110, n/a–n/a, doi:10.1029/2004JD005350, URL `http://dx.doi.org/10.1029/2004JD005350`, d08205, 2005.

Fromm, M., Lindsey, D. T., Servranckx, R., Yue, G., Trickl, T., Sica, R., Doucet, P., and Godin-Beekmann, S.: The Untold Story of Pyrocumulonimbus, Bulletin of the American Meteorological Society, 91, 1193–1209, doi:10.1175/2010BAMS3004.1, URL `https://doi.org/10.1175/2010BAMS3004.1`, 2010.

Fyfe, J. C., Gillett, N. P., and Zwiers, F. W.: Overestimated global warming over the past 20 years, Nature Climate Change, 3, 767–769, doi:10.1038/nclimate1972, URL `https://doi.org/10.1038/nclimate1972`, 2013.

Gao, C., Oman, L., Robock, A., and Stenchikov, G. L.: Atmospheric volcanic loading derived from bipolar ice cores: Accounting for the spatial distribution of volcanic deposition, Journal of Geophysical Research, 112, doi:10.1029/2006jd007461, URL `https://doi.org/10.1029/2006jd007461`, 2007.

Gettelman, A., Hoor, P., Pan, L. L., Randel, W. J., Hegglin, M. I., and Birner, T.: THE EXTRATROPICAL UPPER TROPOSPHERE AND LOWER STRATOSPHERE, Reviews of Geophysics, 49, n/a–n/a, doi:10.1029/2011RG000355, URL `http://dx.doi.org/10.1029/2011RG000355`, rG3003, 2011.

Giauque, W. F., Hornung, E. W., Kunzler, J. E., and Rubin, T. R.: The Thermodynamic Properties of Aqueous Sulfuric Acid Solutions and Hydrates from 15 to 300°K.1, Journal of the American Chemical Society, 82, 62–70, doi:10.1021/ja01486a014, URL `http://dx.doi.org/10.1021/ja01486a014`, 1960.

Glanville, A. A. and Birner, T.: Role of vertical and horizontal mixing in the tape recorder signal near the tropical tropopause, Atmospheric Chemistry and Physics, 17, 4337–4353, doi:10.5194/acp-17-4337-2017, URL `https://doi.org/10.5194/acp-17-4337-2017`, 2017.

Glatthor, N., Höpfner, M., Baker, I. T., Berry, J., Campbell, J. E., Kawa, S. R., Krysztofiak, G., Leyser, A., Sinnhuber, B.-M., Stiller, G. P., Stineciphe, J., and von Clarmann, T.: Tropical sources and sinks of carbonyl sulfide observed from space, Geophysical Research Letters, 42, 10,082–10,090, doi:10.1002/2015GL066293, URL `http://dx.doi.org/10.1002/2015GL066293`, 2015GL066293, 2015.

Glatthor, N., Höpfner, M., Leyser, A., Stiller, G. P., von Clarmann, T., Grabowski, U., Kellmann, S., Linden, A., Sinnhuber, B.-M., Krysztofiak, G., and Walker, K. A.: Global carbonyl sulfide (OCS) measured by MIPAS/Envisat during 2002–2012, Atmospheric Chemistry and Physics, 17, 2631–2652, doi:10.5194/acp-17-2631-2017, URL `https://doi.org/10.5194/acp-17-2631-2017`, 2017.

Green, B., Marshall, J., and Donohoe, A.: Twentieth century correlations between extratropical SST variability and ITCZ shifts, Geophysical Research Letters, 44, 9039–9047, doi:10.1002/2017GL075044, URL `http://dx.doi.org/10.1002/2017GL075044`, 2017GL075044, 2017.

Griessbach, S., Hoffmann, L., Spang, R., and Riese, M.: Volcanic ash detection with infrared limb sounding: MIPAS observations and radiative transfer simulations, Atmospheric Measurement Techniques, 7, 1487–1507, doi:10.5194/amt-7-1487-2014, URL `http://www.atmos-meas-tech.net/7/1487/2014/`, 2014.

Griessbach, S., Hoffmann, L., Spang, R., von Hobe, M., Müller, R., and Riese, M.: Infrared limb emission measurements of aerosol in the troposphere and stratosphere, Atmospheric

Measurement Techniques, 9, 4399–4423, doi:10.5194/amt-9-4399-2016, URL `http://www.atmos-meas-tech.net/9/4399/2016/`, 2016.

Griffith, D. W. T., Jones, N. B., and Matthews, W. A.: Interhemispheric ratio and annual cycle of carbonyl sulfide (OCS) total column from ground-based solar FTIR spectra, Journal of Geophysical Research: Atmospheres, 103, 8447–8454, doi:10.1029/97JD03462, URL `http://dx.doi.org/10.1029/97JD03462`, 1998.

Günther, A., Höpfner, M., Sinnhuber, B.-M., Griessbach, S., Deshler, T., von Clarmann, T., and Stiller, G.: MIPAS observations of volcanic sulfate aerosol and sulfur dioxide in the stratosphere, Atmospheric Chemistry and Physics, 18, 1217–1239, doi:10.5194/acp-18-1217-2018, URL `https://www.atmos-chem-phys.net/18/1217/2018/`, 2018.

Haenel, F. J.: Variability of age of air derived from MIIPAS SF_6 measurements, Ph.D. thesis, Karlsruhe Institute of Technology, doi:10.545/IR/1000074409, URL `https://publikationen.bibliothek.kit.edu/1000074409`, 2017.

Haenel, F. J., Stiller, G. P., von Clarmann, T., Funke, B., Eckert, E., Glatthor, N., Grabowski, U., Kellmann, S., Kiefer, M., Linden, A., and Reddmann, T.: Reassessment of MIPAS age of air trends and variability, Atmospheric Chemistry and Physics, 15, 13 161–13 176, doi:10.5194/acp-15-13161-2015, URL `https://www.atmos-chem-phys.net/15/13161/2015/`, 2015.

Hall, T. M. and Plumb, R. A.: Age as a diagnostic of stratospheric transport, Journal of Geophysical Research: Atmospheres, 99, 1059–1070, doi:10.1029/93JD03192, URL `http://dx.doi.org/10.1029/93JD03192`, 1994.

Hamill, P., Cadle, R. D., and Kiang, C. S.: The Nucleation of H_2SO_4-H_2O Solution Aerosol Particles in the Stratosphere, Journal of the Atmospheric Sciences, 34, 150–162, doi:10.1175/1520-0469(1977)034<0150:TNOHHS>2.0.CO;2, URL `https://doi.org/10.1175/1520-0469(1977)034<0150:TNOHHS>2.0.CO;2`, 1977.

Hansen, J. E. and Travis, L. D.: Light scattering in planetary atmospheres, Space Science Reviews, 16, 527–610, doi:10.1007/BF00168069, URL `https://doi.org/10.1007/BF00168069`, 1974.

Haywood, J. M., Jones, A., Clarisse, L., Bourassa, A., Barnes, J., Telford, P., Bellouin, N., Boucher, O., Agnew, P., Clerbaux, C., Coheur, P., Degenstein, D., and Braesicke, P.: Observations of the eruption of the Sarychev volcano and simulations using the HadGEM2 climate model, Journal of Geophysical Research, 115, doi:10.1029/2010jd014447, URL `https://doi.org/10.1029/2010jd014447`, 2010.

Haywood, J. M., Jones, A., and Jones, G. S.: The impact of volcanic eruptions in the period 2000–2013 on global mean temperature trends evaluated in the HadGEM2-ES climate model, Atmospheric Science Letters, 15, 92–96, doi:10.1002/asl2.471, URL `http://dx.doi.org/10.1002/asl2.471`, 2014.

Hofmann, D., Barnes, J., O'Neill, M., Trudeau, M., and Neely, R.: Increase in background stratospheric aerosol observed with lidar at Mauna Loa Observatory and Boulder, Colorado, Geophysical Research Letters, 36, n/a–n/a, doi:10.1029/2009gl039008, URL `https://doi.org/10.1029/2009gl039008`, 2009.

Hofmann, D. J., Rosen, J. M., Pepin, T. J., and Pinnick, R. G.: Stratospheric Aerosol Measurements I: Time Variations at Northern Midlatitudes, Journal of the Atmospheric Sciences, 32, 1446–1456, doi:10.1175/1520-0469(1975)032<1446:SAMITV>2.0.CO;2, URL `https://doi.org/10.1175/1520-0469(1975)032<1446:SAMITV>2.0.CO;2`, 1975.

Hofmann, D. J., Rosen, J. M., and Gringel, W.: Delayed production of sulfuric acid condensation nuclei in the polar stratosphere from El Chichon volcanic vapors, Journal of Geophysical Research: Atmospheres, 90, 2341–2354, doi:10.1029/JD090iD01p02341, URL `http://dx.doi.org/10.1029/JD090iD01p02341`, 1985.

Holton, J. R. and Lindzen, R. S.: An Updated Theory for the Quasi-Biennial Cycle of the Tropical Stratosphere, Journal of the Atmospheric Sciences, 29, 1076–1080, doi: 10.1175/1520-0469(1972)029<1076:AUTFTQ>2.0.CO;2, URL `https://doi.org/10.1175/1520-0469(1972)029<1076:AUTFTQ>2.0.CO;2`, 1972.

Holton, J. R., Haynes, P. H., McIntyre, M. E., Douglass, A. R., Rood, R. B., and Pfister, L.: Stratosphere-troposphere exchange, Reviews of Geophysics, 33, 403–439, doi: 10.1029/95RG02097, URL `http://dx.doi.org/10.1029/95RG02097`, 1995.

Höpfner, M.: Study on the impact of polar stratospheric clouds on high resolution midIR limb emission spectra, Journal of Quantitative Spectroscopy and Radiative Transfer, 83, 93–107, doi:10.1016/s0022-4073(02)00299-6, URL `https://doi.org/10.1016/s0022-4073(02)00299-6`, 2004.

Höpfner, M., Glatthor, N., Grabowski, U., Kellmann, S., Kiefer, M., Linden, A., Orphal, J., Stiller, G., von Clarmann, T., Funke, B., and Boone, C. D.: Sulfur dioxide (SO_2) as observed by MIPAS/Envisat: temporal development and spatial distribution at 15–45 km altitude, Atmospheric Chemistry and Physics, 13, 10 405–10 423, doi:10.5194/acp-13-10405-2013, URL `http://www.atmos-chem-phys.net/13/10405/2013/`, 2013.

Höpfner, M., Boone, C. D., Funke, B., Glatthor, N., Grabowski, U., Günther, A., Kellmann, S., Kiefer, M., Linden, A., Lossow, S., Pumphrey, H. C., Read, W. G., Roiger, A., Stiller, G., Schlager, H., von Clarmann, T., and Wissmüller, K.: Sulfur dioxide (SO_2) from MIPAS in the upper troposphere and lower stratosphere 2002–2012, Atmospheric Chemistry and Physics, 15, 7017–7037, doi:10.5194/acp-15-7017-2015, URL `http://www.atmos-chem-phys.net/15/7017/2015/`, 2015.

Hoskins, B. J.: Towards a PV-theta view of the general circulation, Tellus A, 43, 27–35, doi: 10.1034/j.1600-0870.1991.t01-3-00005.x, URL `https://doi.org/10.1034/j.1600-0870.1991.t01-3-00005.x`, 1991.

Hudson, R. D.: Measurements of the movement of the jet streams at mid-latitudes, in the Northern and Southern Hemispheres, 1979 to 2010, Atmospheric Chemistry and Physics, 12, 7797–7808, doi:10.5194/acp-12-7797-2012, URL `https://www.atmos-chem-phys.net/12/7797/2012/`, 2012.

Jacobson, M. Z.: Fundamentals of atmospheric modeling, Cambridge University Press, Cambridge, 1999.

Jensen, E. J., Toon, O. B., Pfister, L., and Selkirk, H. B.: Dehydration of the upper troposphere and lower stratosphere by subvisible cirrus clouds near the tropical tropopause, Geophysical Research Letters, 23, 825–828, doi:10.1029/96GL00722, URL `http://dx.doi.org/10.1029/96GL00722`, 1996.

Junge, C. E. and Manson, J. E.: Stratospheric aerosol studies, Journal of Geophysical Research, 66, 2163–2182, doi:10.1029/JZ066i007p02163, URL `http://dx.doi.org/10.1029/JZ066i007p02163`, 1961.

Kalnay, E., Kanamitsu, M., Kistler, R., Collins, W., Deaven, D., Gandin, L., Iredell, M., Saha, S., White, G., Woollen, J., Zhu, Y., Leetmaa, A., Reynolds, R., Chelliah, M., Ebisuzaki, W., Higgins, W., Janowiak, J., Mo, K. C., Ropelewski, C., Wang, J., Jenne, R., and Joseph,

D.: The NCEP/NCAR 40-Year Reanalysis Project, Bulletin of the American Meteorological Society, 77, 437–471, doi:10.1175/1520-0477(1996)077<0437:TNYRP>2.0.CO;2, URL `https://doi.org/10.1175/1520-0477(1996)077<0437:TNYRP>2.0.CO;2`, 1996.

Karagulian, F., Clarisse, L., Clerbaux, C., Prata, A. J., Hurtmans, D., and Coheur, P. F.: Detection of volcanic SO_2, ash, and H_2SO_4 using the Infrared Atmospheric Sounding Interferometer (IASI), Journal of Geophysical Research, 115, doi:10.1029/2009jd012786, URL `https://doi.org/10.1029/2009jd012786`, 2010.

Kiesewetter, G., Sinnhuber, B.-M., Weber, M., and Burrows, J. P.: Attribution of stratospheric ozone trends to chemistry and transport: a modelling study, Atmospheric Chemistry and Physics, 10, 12073–12089, doi:10.5194/acp-10-12073-2010, URL `https://doi.org/10.5194/acp-10-12073-2010`, 2010.

Kleinschmitt, C., Boucher, O., Bekki, S., Lott, F., and Platt, U.: The Sectional Stratospheric Sulfate Aerosol module S3A-v1 withinthe LMDZ general circulation model: Description and evaluationagainst stratospheric aerosol observations, Geoscientific Model Development Discussions, pp. 1–34, doi:10.5194/gmd-2017-31, URL `https://doi.org/10.5194/gmd-2017-31`, 2017.

Koop, T., Carslaw, K. S., and Peter, T.: Thermodynamic stability and phase transitions of PSC particles, Geophysical Research Letters, 24, 2199–2202, doi:10.1029/97GL02148, URL `http://dx.doi.org/10.1029/97GL02148`, 1997.

Kravitz, B., Robock, A., and Bourassa, A.: Negligible climatic effects from the 2008 Okmok and Kasatochi volcanic eruptions, Journal of Geophysical Research: Atmospheres, 115, n/a–n/a, doi:10.1029/2009JD013525, URL `http://dx.doi.org/10.1029/2009JD013525`, d00L05, 2010.

Kremser, S., Jones, N. B., Palm, M., Lejeune, B., Wang, Y., Smale, D., and Deutscher, N. M.: Positive trends in Southern Hemisphere carbonyl sulfide, Geophysical Research Letters, 42, 9473–9480, doi:10.1002/2015GL065879, URL `http://dx.doi.org/10.1002/2015GL065879`, 2015GL065879, 2015.

Kremser, S., Thomason, L. W., von Hobe, M., Hermann, M., Deshler, T., Timmreck, C., Toohey, M., Stenke, A., Schwarz, J. P., Weigel, R., Fueglistaler, S., Prata, F. J., Vernier, J.-P., Schlager, H., Barnes, J. E., Antuña-Marrero, J.-C., Fairlie, D., Palm, M., Mahieu, E., Notholt, J., Rex, M., Bingen, C., Vanhellemont, F., Bourassa, A., Plane, J. M. C., Klocke, D., Carn, S. A., Clarisse, L., Trickl, T., Neely, R., James, A. D., Rieger, L., Wilson, J. C., and Meland, B.: Stratospheric aerosol–Observations, processes, and impact on climate, Reviews of Geophysics, 54, 278–335, doi:10.1002/2015RG000511, URL `http://dx.doi.org/10.1002/2015RG000511`, 2015RG000511, 2016.

Kristiansen, N. I., Stohl, A., Prata, A. J., Richter, A., Eckhardt, S., Seibert, P., Hoffmann, A., Ritter, C., Bitar, L., Duck, T. J., and Stebel, K.: Remote sensing and inverse transport modeling of the Kasatochi eruption sulfur dioxide cloud, Journal of Geophysical Research, 115, doi:10.1029/2009jd013286, URL `https://doi.org/10.1029/2009jd013286`, 2010.

Krotkov, N. A., Schoeberl, M. R., Morris, G. A., Carn, S., and Yang, K.: Dispersion and lifetime of the SO_2 cloud from the August 2008 Kasatochi eruption, Journal of Geophysical Research, 115, doi:10.1029/2010jd013984, URL `https://doi.org/10.1029/2010jd013984`, 2010.

Laakso, A., Kokkola, H., Partanen, A.-I., Niemeier, U., Timmreck, C., Lehtinen, K. E. J., Hakkarainen, H., and Korhonen, H.: Radiative and climate impacts of a large volcanic eruption during stratospheric sulfur geoengineering, Atmospheric

Chemistry and Physics, 16, 305–323, doi:10.5194/acp-16-305-2016, URL `https://www.atmos-chem-phys.net/16/305/2016/`, 2016.

Lane, J. R. and Kjaergaard, H. G.: Calculated Electronic Transitions in Sulfuric Acid and Implications for Its Photodissociation in the Atmosphere, The Journal of Physical Chemistry A, 112, 4958–4964, doi:10.1021/jp710863r, URL `http://dx.doi.org/10.1021/jp710863r`, pMID: 18470974, 2008.

Lejeune, B., Mahieu, E., Vollmer, M. K., Reimann, S., Bernath, P. F., Boone, C. D., Walker, K. A., and Servais, C.: Optimized approach to retrieve information on atmospheric carbonyl sulfide (OCS) above the Jungfraujoch station and change in its abundance since 1995, Journal of Quantitative Spectroscopy and Radiative Transfer, 186, 81 – 95, doi:https://doi.org/10.1016/j.jqsrt.2016.06.001, URL `http://www.sciencedirect.com/science/article/pii/S0022407316300899`, satellite Remote Sensing and Spectroscopy: Joint ACE-Odin Meeting, October 2015, 2017.

Liu, J., Logan, J. A., Murray, L. T., Pumphrey, H. C., Schwartz, M. J., and Megretskaia, I. A.: Transport analysis and source attribution of seasonal and interannual variability of CO in the tropical upper troposphere and lower stratosphere, Atmospheric Chemistry and Physics, 13, 129–146, doi:10.5194/acp-13-129-2013, URL `https://doi.org/10.5194/acp-13-129-2013`, 2013.

López-Puertas, M., García-Comas, M., Funke, B., Bermejo-Pantaleón, D., Höpfner, M., Grabowski, U., Stiller, G. P., von Clarmann, T., and von Savigny, C.: Measurements of polar mesospheric clouds in infrared emission by MIPAS/ENVISAT, Journal of Geophysical Research, 114, doi:10.1029/2009jd012548, URL `https://doi.org/10.1029/2009jd012548`, 2009.

Maturilli, M., Neuber, R., Massoli, P., Cairo, F., Adriani, A., Moriconi, M. L., and Di Donfrancesco, G.: Differences in Arctic and Antarctic PSC occurrence as observed by lidar in Ny-Ålesund (79°N, 12°E) and McMurdo (78°S, 167°E), Atmospheric Chemistry and Physics, 5, 2081–2090, doi:10.5194/acp-5-2081-2005, URL `https://www.atmos-chem-phys.net/5/2081/2005/`, 2005.

McCormick, M. P., Thomason, L. W., and Trepte, C. R.: Atmospheric effects of the Mt Pinatubo eruption, Nature, 373, 399–404, doi:10.1038/373399a0, URL `https://doi.org/10.1038/373399a0`, 1995.

McIntyre, M. and Palmer, T.: The 'surf zone' in the stratosphere, Journal of Atmospheric and Terrestrial Physics, 46, 825 – 849, doi:https://doi.org/10.1016/0021-9169(84)90063-1, URL `http://www.sciencedirect.com/science/article/pii/0021916984900631`, 1984.

Meijer, E. W., Bregman, B., Segers, A., and van Velthoven, P. F. J.: The influence of data assimilation on the age of air calculated with a global chemistry-transport model using ECMWF wind fields, Geophysical Research Letters, 31, n/a–n/a, doi:10.1029/2004GL021158, URL `http://dx.doi.org/10.1029/2004GL021158`, l23114, 2004.

Mills, M. J.: Stratospheric sulfate aerosol: a microphysical model, Ph.D. thesis, University of Colorado, 1996.

Mills, M. J., Toon, O. B., Vaida, V., Hintze, P. E., Kjaergaard, H. G., Schofield, D. P., and Robinson, T. W.: Photolysis of sulfuric acid vapor by visible light as a source of the polar stratospheric CN layer, Journal of Geophysical Research: Atmospheres, 110, n/a–n/a, doi:10.1029/2004JD005519, URL `http://dx.doi.org/10.1029/2004JD005519`, d08201, 2005.

Murphy, D. M., Froyd, K. D., Schwarz, J. P., and Wilson, J. C.: Observations of the chemical composition of stratospheric aerosol particles, Quarterly Journal of the Royal Meteorological Society, 140, 1269–1278, doi:10.1002/qj.2213, URL https://doi.org/10.1002/qj.2213, 2013.

Neely, R. R., Toon, O. B., Solomon, S., Vernier, J.-P., Alvarez, C., English, J. M., Rosenlof, K. H., Mills, M. J., Bardeen, C. G., Daniel, J. S., and Thayer, J. P.: Recent anthropogenic increases in SO_2 from Asia have minimal impact on stratospheric aerosol, Geophysical Research Letters, 40, 999–1004, doi:10.1002/grl.50263, URL https://doi.org/10.1002/grl.50263, 2013.

Neu, J. L. and Plumb, R. A.: Age of air in a "leaky pipe" model of stratospheric transport, Journal of Geophysical Research: Atmospheres, 104, 19 243–19 255, doi:10.1029/1999JD900251, URL http://dx.doi.org/10.1029/1999JD900251, 1999.

Niedziela, R. F., Norman, M. L., DeForest, C. L., Miller, R. E., and Worsnop, D. R.: A Temperature- and Composition-Dependent Study of H_2SO_4 Aerosol Optical Constants Using Fourier Transform and Tunable Diode Laser Infrared Spectroscopy, The Journal of Physical Chemistry A, 103, 8030–8040, doi:10.1021/jp991323o, URL http://dx.doi.org/10.1021/jp991323o, 1999.

Niemeier, U. and Timmreck, C.: What is the limit of climate engineering by stratospheric injection of SO_2?, Atmospheric Chemistry and Physics, 15, 9129–9141, doi:10.5194/acp-15-9129-2015, URL https://doi.org/10.5194/acp-15-9129-2015, 2015.

Ploeger, F., Gottschling, C., Griessbach, S., Grooß, J.-U., Guenther, G., Konopka, P., Müller, R., Riese, M., Stroh, F., Tao, M., Ungermann, J., Vogel, B., and von Hobe, M.: A potential vorticity-based determination of the transport barrier in the Asian summer monsoon anticyclone, Atmospheric Chemistry and Physics, 15, 13 145–13 159, doi:10.5194/acp-15-13145-2015, URL https://www.atmos-chem-phys.net/15/13145/2015/, 2015.

Plumb, R. A.: A "tropical pipe" model of stratospheric transport, Journal of Geophysical Research: Atmospheres, 101, 3957–3972, doi:10.1029/95JD03002, URL http://dx.doi.org/10.1029/95JD03002, 1996.

Plumb, R. A. and Eluszkiewicz, J.: The Brewer–Dobson Circulation: Dynamics of the Tropical Upwelling, Journal of the Atmospheric Sciences, 56, 868–890, doi:10.1175/1520-0469(1999)056<0868:TBDCDO>2.0.CO;2, URL https://doi.org/10.1175/1520-0469(1999)056<0868:TBDCDO>2.0.CO;2, 1999.

Pommrich, R., Müller, R., Grooß, J.-U., Günther, G., Konopka, P., Riese, M., Heil, A., Schultz, M., Pumphrey, H.-C., and Walker, K. A.: What causes the irregular cycle of the atmospheric tape recorder signal in HCN?, Geophysical Research Letters, 37, n/a–n/a, doi:10.1029/2010GL044056, URL http://dx.doi.org/10.1029/2010GL044056, l16805, 2010.

Pope, F., Braesicke, P., Grainger, R., Kalberer, M., Watson, I., Davidson, P., and Cox, R.: Stratospheric aerosol particles and solar radiation management, Nature Climate Change, 2, 713–719, doi:10.1038/NCLIMATE1528, 2012.

Prata, A. J., Gangale, G., Clarisse, L., and Karagulian, F.: Ash and sulfur dioxide in the 2008 eruptions of Okmok and Kasatochi: Insights from high spectral resolution satellite measurements, Journal of Geophysical Research, 115, doi:10.1029/2009jd013556, URL https://doi.org/10.1029/2009jd013556, 2010.

Prather, M. J.: Numerical advection by conservation of second-order moments, Journal of Geophysical Research: Atmospheres, 91, 6671–6681, doi:10.1029/JD091iD06p06671, URL http://dx.doi.org/10.1029/JD091iD06p06671, 1986.

Pumphrey, H. C., Read, W. G., Livesey, N. J., and Yang, K.: Observations of volcanic SO$_2$ from MLS on Aura, Atmospheric Measurement Techniques, 8, 195–209, doi:10.5194/amt-8-195-2015, URL `https://doi.org/10.5194/amt-8-195-2015`, 2015.

Randel, W. J. and Park, M.: Deep convective influence on the Asian summer monsoon anticyclone and associated tracer variability observed with Atmospheric Infrared Sounder (AIRS), Journal of Geophysical Research: Atmospheres, 111, n/a–n/a, doi:10.1029/2005JD006490, URL `http://dx.doi.org/10.1029/2005JD006490`, d12314, 2006.

Rasch, P. J., Tilmes, S., Turco, R. P., Robock, A., Oman, L., Chen, C.-C., Stenchikov, G. L., and Garcia, R. R.: An overview of geoengineering of climate using stratospheric sulphate aerosols, Philosophical Transactions of the Royal Society A: Mathematical, Physical and Engineering Sciences, 366, 4007–4037, doi:10.1098/rsta.2008.0131, URL `https://doi.org/10.1098/rsta.2008.0131`, 2008.

Ridley, D. A., Solomon, S., Barnes, J. E., Burlakov, V. D., Deshler, T., Dolgii, S. I., Herber, A. B., Nagai, T., Neely, R. R., Nevzorov, A. V., Ritter, C., Sakai, T., Santer, B. D., Sato, M., Schmidt, A., Uchino, O., and Vernier, J. P.: Total volcanic stratospheric aerosol optical depths and implications for global climate change, Geophysical Research Letters, 41, 7763–7769, doi:10.1002/2014gl061541, URL `https://doi.org/10.1002/2014gl061541`, 2014.

Rinsland, C. P., Gunson, M. R., Ko, M. K. W., Weisenstein, D. W., Zander, R., Abrams, M. C., Goldman, A., Sze, N. D., and Yue, G. K.: H$_2$SO$_4$ photolysis: A source of sulfur dioxide in the upper stratosphere, Geophysical Research Letters, 22, 1109–1112, doi:10.1029/95GL00917, URL `http://dx.doi.org/10.1029/95GL00917`, 1995.

Robock, A.: 20 reasons why geoengineering may be a bad idea, Bulletin of the Atomic Scientists, 64, 14–18, doi:10.2968/064002006, URL `https://doi.org/10.2968/064002006`, 2008.

Rodgers, C. D.: Inverse methods for atmospheric sounding : theory and practice, World Scientific Publishing, 2000.

Rollins, A. W., Thornberry, T. D., Watts, L. A., Yu, P., Rosenlof, K. H., Mills, M., Baumann, E., Giorgetta, F. R., Bui, T. V., Höpfner, M., Walker, K. A., Boone, C., Bernath, P. F., Colarco, P. R., Newman, P. A., Fahey, D. W., and Gao, R. S.: The role of sulfur dioxide in stratospheric aerosol formation evaluated by using in situ measurements in the tropical lower stratosphere, Geophysical Research Letters, 44, 4280–4286, doi:10.1002/2017GL072754, URL `http://dx.doi.org/10.1002/2017GL072754`, 2017GL072754, 2017.

Rosen, J. M.: The Boiling Point of Stratospheric Aerosols, Journal of Applied Meteorology (1962-1982), 10, 1044–1046, URL `http://www.jstor.org/stable/26175603`, 1971.

Rothman, L., Gordon, I., Babikov, Y., Barbe, A., Benner, D. C., Bernath, P., Birk, M., Bizzocchi, L., Boudon, V., Brown, L., Campargue, A., Chance, K., Cohen, E., Coudert, L., Devi, V., Drouin, B., Fayt, A., Flaud, J.-M., Gamache, R., Harrison, J., Hartmann, J.-M., Hill, C., Hodges, J., Jacquemart, D., Jolly, A., Lamouroux, J., Roy, R. L., Li, G., Long, D., Lyulin, O., Mackie, C., Massie, S., Mikhailenko, S., Müller, H., Naumenko, O., Nikitin, A., Orphal, J., Perevalov, V., Perrin, A., Polovtseva, E., Richard, C., Smith, M., Starikova, E., Sung, K., Tashkun, S., Tennyson, J., Toon, G., Tyuterev, V., and Wagner, G.: The HITRAN2012 molecular spectroscopic database, Journal of Quantitative Spectroscopy and Radiative Transfer, 130, 4 – 50, doi:https://doi.org/10.1016/j.jqsrt.2013.07.002, URL `http://www.sciencedirect.com/science/article/pii/S0022407313002859`, hITRAN2012 special issue, 2013.

Santer, B. D., Bonfils, C., Painter, J. F., Zelinka, M. D., Mears, C., Solomon, S., Schmidt, G. A., Fyfe, J. C., Cole, J. N. S., Nazarenko, L., Taylor, K. E., and Wentz, F. J.: Volcanic contribution to decadal changes in tropospheric temperature, Nature Geoscience, 7, 185–189, doi:10.1038/ngeo2098, URL `https://doi.org/10.1038/ngeo2098`, 2014.

Schoeberl, M. R., Douglass, A. R., Newman, P. A., Lait, L. R., Lary, D., Waters, J., Livesey, N., Froidevaux, L., Lambert, A., Read, W., Filipiak, M. J., and Pumphrey, H. C.: QBO and annual cycle variations in tropical lower stratosphere trace gases from HALOE and Aura MLS observations, Journal of Geophysical Research: Atmospheres, 113, n/a–n/a, doi:10.1029/2007JD008678, URL `http://dx.doi.org/10.1029/2007JD008678`, d05301, 2008.

Sheng, J.-X., Weisenstein, D. K., Luo, B.-P., Rozanov, E., Arfeuille, F., and Peter, T.: A perturbed parameter model ensemble to investigate Mt. Pinatubo's 1991 initial sulfur mass emission, Atmospheric Chemistry and Physics, 15, 11 501–11 512, doi:10.5194/acp-15-11501-2015, URL `https://doi.org/10.5194/acp-15-11501-2015`, 2015.

Sinnhuber, B.-M., Weber, M., Amankwah, A., and Burrows, J. P.: Total ozone during the unusual Antarctic winter of 2002, Geophysical Research Letters, 30, n/a–n/a, doi:10.1029/2002GL016798, URL `http://dx.doi.org/10.1029/2002GL016798`, 1580, 2003.

Solomon, A., Richter, J. H., and Bacmeister, J. T.: An objective analysis of the QBO in ERA-Interim and the Community Atmosphere Model, version 5, Geophysical Research Letters, 41, 7791–7798, doi:10.1002/2014GL061801, URL `http://dx.doi.org/10.1002/2014GL061801`, 2014.

Solomon, S., Daniel, J. S., Neely, R. R., Vernier, J.-P., Dutton, E. G., and Thomason, L. W.: The Persistently Variable "Background" Stratospheric Aerosol Layer and Global Climate Change, Science, 333, 866–870, doi:10.1126/science.1206027, URL `https://doi.org/10.1126/science.1206027`, 2011.

Spang, R., Remedios, J., and Barkley, M.: Colour indices for the detection and differentiation of cloud types in infra-red limb emission spectra, Advances in Space Research, 33, 1041 – 1047, doi:http://dx.doi.org/10.1016/S0273-1177(03)00585-4, URL `http://www.sciencedirect.com/science/article/pii/S0273117703005854`, climate Change Processes in the Stratosphere, Earth-Atmosphere-Ocean Systems, and Oceanographic Processes from Satellite Data, 2004.

Steck, T.: Methods for determining regularization for atmospheric retrieval problems, Appl. Opt., 41, 1788–1797, doi:10.1364/AO.41.001788, URL `http://ao.osa.org/abstract.cfm?URI=ao-41-9-1788`, 2002.

Stein, B., Wedekind, C., Wille, H., Immler, F., Müller, M., Wöste, L., del Guasta, M., Morandi, M., Stefanutti, L., Antonelli, A., Agostini, P., Rizi, V., Readelli, G., Mitev, V., Matthey, R., Kivi, R., and Kyrö, E.: Optical classification, existence temperatures, and coexistence of different polar stratospheric cloud types, Journal of Geophysical Research: Atmospheres, 104, 23 983–23 993, doi:10.1029/1999JD900064, URL `http://dx.doi.org/10.1029/1999JD900064`, 1999.

Stiller, G. P., ed.: The Karlsruhe Optimized and Precise Radiative Transfer Algorithm (KOPRA), vol. FZKA 6487 of *Wissenschaftliche Berichte*, Forschungszentrum Karlsruhe, 2000.

Stiller, G. P., von Clarmann, T., Haenel, F., Funke, B., Glatthor, N., Grabowski, U., Kellmann, S., Kiefer, M., Linden, A., Lossow, S., and López-Puertas, M.: Observed temporal evolution of global mean age of stratospheric air for the 2002 to 2010 period, Atmospheric Chemistry and Physics, 12, 3311–3331, doi:10.5194/acp-12-3311-2012, URL `https://www.atmos-chem-phys.net/12/3311/2012/`, 2012.

Tabazadeh, A., Toon, O. B., Gary, B. L., Bacmeister, J. T., and Schoeberl, M. R.: Observational constraints on the formation of type ia polar stratospheric clouds, Geophysical Research Letters, 23, 2109–2112, doi:10.1029/96GL01998, URL http://dx.doi.org/10.1029/96GL01998, 1996.

Textor, C., Graf, H.-F., Timmreck, C., Robock, A., Granier, E. C., Artaxo, P., and Reeves, C.: Emissions from volcanoe, Chapter 7 of Emissions of Atmospheric Trace Compounds, Kluwer, Dordreacht, 2004.

Thomas, H. E., Watson, I. M., Carn, S. A., Prata, A. J., and Realmuto, V. J.: A comparison of AIRS, MODIS and OMI sulphur dioxide retrievals in volcanic clouds, Geomatics, Natural Hazards and Risk, 2, 217–232, doi:10.1080/19475705.2011.564212, URL https://doi.org/10.1080/19475705.2011.564212, 2011.

Thomason, L. and Peter, T.: SPARC Assessment of Stratospheric Aerosol Properties (ASAP), Tech. rep., SPARC, URL http://www.sparc-climate.org/publications/sparc-reports/, 2006.

Thomason, L. W. and Poole, L. R.: Use of stratospheric aerosol properties as diagnostics of Antarctic vortex processes, Journal of Geophysical Research, 98, 23 003, doi:10.1029/93jd02461, URL https://doi.org/10.1029/93jd02461, 1993.

Thomason, L. W., Burton, S. P., Luo, B.-P., and Peter, T.: SAGE II measurements of stratospheric aerosol properties at non-volcanic levels, Atmospheric Chemistry and Physics, 8, 983–995, doi:10.5194/acp-8-983-2008, URL https://www.atmos-chem-phys.net/8/983/2008/, 2008.

Tikhonov, A. N.: On the Solution of Incorrectly Posed Problem and the Method of Regularization, vol. 4, Soviet Mathematics, 1963.

Toon, O. B. and Pollack, J. B.: Physical properties of the stratospheric aerosols, Journal of Geophysical Research, 78, 7051–7056, doi:10.1029/JC078i030p07051, URL http://dx.doi.org/10.1029/JC078i030p07051, 1973.

Tweedy, O. V., Kramarova, N. A., Strahan, S. E., Newman, P. A., Coy, L., Randel, W. J., Park, M., Waugh, D. W., and Frith, S. M.: Response of trace gases to the disrupted 2015–2016 quasi-biennial oscillation, Atmospheric Chemistry and Physics, 17, 6813–6823, doi:10.5194/acp-17-6813-2017, URL https://www.atmos-chem-phys.net/17/6813/2017/, 2017.

Vaida, V., Kjaergaard, H. G., Hintze, P. E., and Donaldson, D. J.: Photolysis of Sulfuric Acid Vapor by Visible Solar Radiation, Science, 299, 1566–1568, doi:10.1126/science.1079297, URL http://science.sciencemag.org/content/299/5612/1566, 2003.

Vernier, J., Fairlie, T., Natarajan, M., Wienhold, F., Bian, J., Martinsson, B., Crumeyrolle, S., Thomason, L., and Bedka, K.: Increase in upper tropospheric and lower stratospheric aerosol levels and its potential connection with Asian pollution, Journal of Geophysical Research: Atmospheres, 120, 1608–1619, doi:10.1002/2014JD022372, 2015.

Vernier, J.-P., Thomason, L. W., and Kar, J.: CALIPSO detection of an Asian tropopause aerosol layer, Geophysical Research Letters, 38, n/a–n/a, doi:10.1029/2010GL046614, URL http://dx.doi.org/10.1029/2010GL046614, l07804, 2011a.

Vernier, J.-P., Thomason, L. W., Pommereau, J.-P., Bourassa, A., Pelon, J., Garnier, A., Hauchecorne, A., Blanot, L., Trepte, C., Degenstein, D., and Vargas, F.: Major influence of tropical volcanic eruptions on the stratospheric aerosol layer during the last decade, Geophysical Research Letters, 38, n/a–n/a, doi:10.1029/2011gl047563, URL https://doi.org/10.1029/2011gl047563, 2011b.

von Clarmann, T., Glatthor, N., Grabowski, U., Höpfner, M., Kellmann, S., Kiefer, M., Linden, A., Tsidu, G. M., Milz, M., Steck, T., Stiller, G. P., Wang, D. Y., Fischer, H., Funke, B., Gil-López, S., and López-Puertas, M.: Retrieval of temperature and tangent altitude pointing from limb emission spectra recorded from space by the Michelson Interferometer for Passive Atmospheric Sounding (MIPAS), Journal of Geophysical Research: Atmospheres, 108, n/a–n/a, doi:10.1029/2003JD003602, URL `http://dx.doi.org/10.1029/2003JD003602`, 4736, 2003.

von Clarmann, T., Höpfner, M., Kellmann, S., Linden, A., Chauhan, S., Funke, B., Grabowski, U., Glatthor, N., Kiefer, M., Schieferdecker, T., Stiller, G. P., and Versick, S.: Retrieval of temperature, H_2O, O_3, HNO_3, CH_4, N_2O, $ClONO_2$ and ClO from MIPAS reduced resolution nominal mode limb emission measurements, Atmospheric Measurement Techniques, 2, 159–175, doi:10.5194/amt-2-159-2009, URL `https://doi.org/10.5194/amt-2-159-2009`, 2009.

von Clarmann, T., Stiller, G., Grabowski, U., Eckert, E., and Orphal, J.: Technical Note: Trend estimation from irregularly sampled, correlated data, Atmospheric Chemistry and Physics, 10, 6737–6747, doi:10.5194/acp-10-6737-2010, URL `https://www.atmos-chem-phys.net/10/6737/2010/`, 2010.

Waugh, D. and Hall, T.: Age of Stratospheric Air: Theory, Observations, and Models, Reviews of Geophysics, 40, 1–1–1–26, doi:10.1029/2000RG000101, URL `http://dx.doi.org/10.1029/2000RG000101`, 1010, 2002.

Wetzel, G., Oelhaf, H., Berthet, G., Bracher, A., Cornacchia, C., Feist, D. G., Fischer, H., Fix, A., Iarlori, M., Kleinert, A., Lengel, A., Milz, M., Mona, L., Müller, S. C., Ovarlez, J., Pappalardo, G., Piccolo, C., Raspollini, P., Renard, J.-B., Rizi, V., Rohs, S., Schiller, C., Stiller, G., Weber, M., and Zhang, G.: Validation of MIPAS-ENVISAT H_2O operational data collected between July 2002 and March 2004, Atmospheric Chemistry and Physics, 13, 5791–5811, doi:10.5194/acp-13-5791-2013, URL `https://www.atmos-chem-phys.net/13/5791/2013/`, 2013.

Wu, X., Griessbach, S., and Hoffmann, L.: Equatorward dispersion of high-latitude volcanic plume and its relation to the Asian summer monsoon: a case study of the Sarychev eruption in 2009, Atmospheric Chemistry and Physics Discussions, pp. 1–27, doi:10.5194/acp-2017-425, URL `https://doi.org/10.5194/acp-2017-425`, 2017.

Xu, W. and Zipser, E. J.: Properties of deep convection in tropical continental, monsoon, and oceanic rainfall regimes, Geophysical Research Letters, 39, n/a–n/a, doi:10.1029/2012GL051242, URL `http://dx.doi.org/10.1029/2012GL051242`, l07802, 2012.

Yu, P., Murphy, D. M., Portmann, R. W., Toon, O. B., Froyd, K. D., Rollins, A. W., Gao, R.-S., and Rosenlof, K. H.: Radiative forcing from anthropogenic sulfur and organic emissions reaching the stratosphere, Geophysical Research Letters, 43, 9361–9367, doi:10.1002/2016gl070153, URL `https://doi.org/10.1002/2016gl070153`, 2016.